

**AN ULTRA-LOW-VIBRATION FACILITY FOR HOUSING A DILUTION
TEMPERATURE SCANNING TUNNELING MICROSCOPE**

by

Benjamin MacLeod

B.A.Sc. , The University of British Columbia, 2013

A THESIS SUBMITTED IN PARTIAL FULFILLMENT OF
THE REQUIREMENTS FOR THE DEGREE OF

MASTER OF APPLIED SCIENCE

in

THE FACULTY OF GRADUATE AND POSTDOCTORAL STUDIES
(Engineering Physics)

THE UNIVERSITY OF BRITISH COLUMBIA

(Vancouver)

August 2015

© Benjamin MacLeod, 2015

Abstract

This thesis details the specification, design and characterization of an ultra-low vibration facility and aspects of the design and performance of an ultra-high-vacuum dilution temperature scanning tunneling microscope (STM) housed within this facility.

The basic principles of vibration isolation and STM are introduced. Existing ultra-low-vibration facilities and dilution temperature scanning tunneling microscopy experiments are reviewed.

A specification for the vibration isolation performance of the facility is developed based on a simple model of the vibrational mechanics of a STM head. The experimental techniques of accelerometry and microphony are introduced. A survey of the acoustic and vibrational conditions at the site of the facility prior to its construction leads into a detailed description of the facility design. This is followed by an experimental characterization of the facility performance.

Acoustic transmission functions of double-walled acoustic isolation vaults are reported; the dominant ambient sounds inside these vaults are found to coincide substantially with the acoustic modes of the vaults. Massive pneumatically supported concrete inertia blocks are found to perform approximately as ideal 2nd order damped spring mass systems below 10-15 Hz. Above these frequencies, acoustic forces are found to cause additional motion of the pneumatically supported stages. It is found that these systems must be carefully adjusted and monitored to ensure low resonant frequencies are maintained. Inertia blocks optimized for flexural resonant frequencies above 200Hz are presented; these vibrations are found to be poorly damped and to degrade isolation performance at the flexural resonance frequencies. Experiments mounted on light-load pneumatic isolators on top of the inertia blocks are found to be very

susceptible to acoustic forces and as a result exhibit non-ideal isolation behavior above approximately 7 Hz.

The design of a rigid STM head for use in the ultra-high-vacuum dilution refrigerator experiment is detailed and an overview of the supporting experimental system is given. The results of preliminary commissioning of the microscope are given and poorly damped vibrations of the dilution refrigerator structure at ~20 Hz are found to be the dominant contribution to the noise in the tunneling current signal when the instrument is operated at dilution temperature.

Preface

The development of the UBC ultra-high-vacuum dilution refrigerator STM is a massive and ongoing undertaking in which I have had the privilege of playing a small part. Many people have contributed to the development and characterization of both this instrument and its home in the Laboratory for Atomic Imaging Research (LAIR) ultra-low-vibration facility at UBC. The design and experimental work detailed in this thesis is therefore the result of numerous collaborative efforts. My decision to focus my Master's research on vibration issues was an organic one and I take credit for the overall design of my research program while acknowledging the direction and support of my supervisors Professors Doug Bonn and Jenny Hoffman as well as from Dr. Yan Pennec and Professor Sarah Burke.

My contributions and the contributions of my collaborators to the present work are as follows:

- I researched and wrote all of chapter 1 by myself.
- Chapter 2:
 - I carried out and analyzed the data from the site survey detailed in section 2.3 under the supervision of Dr. Yan Pennec and with the assistance of Baptiste Goubert. Dr. Pennec and I developed the facility vibration isolation specification.
 - The design of the LAIR facility detailed in section 2.5 was carried out primarily by Dr. Yan Pennec and Professors Sarah Burke and Doug Bonn in collaboration with Maples Argo architects, RWDI vibration consultants and Integrated Dynamics Engineering. My contribution to this design was to begin using finite-element simulations to study the inertia block resonant frequencies; the final optimization of the inertia block geometry was carried out by Dr. Yan Pennec.

- I performed and analyzed all the acoustic measurements in section 2.6 with the exception of the reverberation time measurement which was carried out by Professor Murray Hodgson and his students Shira Daltrop and James Higgins.
- The initial commissioning of the LAIR detailed in section 2.7.2.2 of this thesis was performed by Dr. Yan Pennec and Vincent Wong from UBC as well as Steve Shedd from Integrated Dynamics Engineering; the resulting data was summarized by Vincent Wong. Except where indicated, I produced all the plots presented in this thesis.
- The laborious measurements of the flexural modes of the inertia blocks detailed in section 2.7.2.3 were performed by Vincent Wong, who also produced the plots of the resulting mode-shape data. I performed the finite element simulations of the inertia block flexural modes for comparison with the measured data.
- The 3D models of the LAIR used throughout this thesis were originally drawn by Graeme Adamson but I created all drawings and renderings presented in this thesis.
- The data from St Andrews University presented in section 2.8 was taken by Matthew Neat, one of Peter Wahl's PhD students.
- I performed and analyzed all the other experiments in section 2.7 and did all the modelling of the acoustic forces.
- Chapter 3:
 - The overall experiment design was led by Dr. Yan Pennec. The low vibration dilution refrigerator was designed by Dr. Vladimir Shvarts of the Janis Research Company in collaboration with Dr. Pennec and with minor input from me. Janis

was the integrator of the dilution fridge with the American Magnetics magnet system, which uses a Kadel dewar. Solid models of the dilution fridge, magnet and dewar were provided by their respective manufacturers. The cryogenic Z-manipulator was designed by Dr. Pennec, Graeme Adamson and Urs Maier (at Ferrovac GmbH). The experiment was principally assembled by Dr. Pennec, Dr. James Day, Rob Delaney, Dr. David Fournier, Dr. Piotr Forysinski and Graeme Adamson. All drawings and rendering used here were produced by me.

- Under the close direction of Dr. Pennec, I developed the microscope head and sample plate geometry and produced all the 3D models and drawings of the final microscope assembly. The microscope head was assembled and initial testing was performed by Kirill Sapchuk and Dr. Pennec.
- Under the direction of Dr. Pennec I designed the custom piping and pipe supports for connecting the dilution fridge to the gas handling system, which were assembled by Dr. Day, Robert Delaney and me. The vibration decoupling gimbals were designed by Dr. Pennec and Wesley Fritzke and assembled by myself and Robert Delaney.
- The frame vibration data presented in section 3.3 were taken by Robert Delaney and I. I performed all the analysis of this data.

Table of Contents

Abstract.....	ii
Preface.....	iv
Table of Contents	vii
List of Tables	xi
List of Figures.....	xiii
List of Symbols	xxiii
List of Abbreviations	xxiv
Acknowledgements	xxv
Dedication	xxx
Chapter 1: Introduction	1
1.1 Overview of this thesis.....	2
1.2 Scanning tunneling microscopy principles and instrumentation	4
1.2.1 Basic theory and instrumentation.....	4
1.2.2 STM vibration criteria.....	7
1.2.3 STM head optimization.....	8
1.2.4 Motivation for studying matter under extreme conditions and associated technical difficulties	9
1.3 Fundamentals of low vibration facilities.....	11
1.3.1 Mass-spring-damper vibration isolators	12
1.3.2 Real pneumatic vibration isolators.....	15
1.3.3 Low-vibration foundations.....	17

vii

1.3.4	Rigid body vibrations of inertia blocks.....	18
1.3.5	Flexural vibrations of inertia blocks	19
1.3.6	Acoustic isolation.....	19
1.4	Existing UHV dilution temperature STM experiments and low vibration facilities	21
Chapter 2: Specification, design and characterization of the laboratory for atomic imaging research ultra-low-vibration facility		25
2.1	Facility overview	26
2.2	Techniques	28
2.2.1	Experimental techniques.....	28
2.2.1.1	Accelerometry.....	28
2.2.1.2	Microphony.....	34
2.2.2	Analytical techniques.....	36
2.2.2.1	Spectral analysis.....	36
2.2.2.2	Finite element simulations	44
2.3	Facility site survey	45
2.4	Vibration isolation specification	54
2.5	Facility design.....	60
2.5.1	Building substrate and foundations.....	60
2.5.2	Acoustic enclosures	64
2.5.3	Inertia blocks.....	67
2.5.4	Heavy load pneumatic isolators	72
2.6	Simulation, measurement and analysis of acoustic vibrations.....	72
2.6.1	Acoustic transmission functions	73

2.6.2	Reverberation time.....	77
2.6.3	Short and long-time measurements of ambient acoustic spectra.....	77
2.6.4	Room modes	83
2.7	Simulation, measurement and analysis of solid vibrations.....	95
2.7.1	Foundations.....	95
2.7.1.1	Simulation of vibrations of the foundations and acoustic enclosure walls.....	96
2.7.1.2	Measurement of foundation vibrations	101
2.7.2	Inertia blocks.....	121
2.7.2.1	Simulation of inertia block vibrational mode frequencies.....	121
2.7.2.2	Initial commissioning of inertia blocks.....	125
2.7.2.3	Flexural motion of inertia blocks	139
2.7.2.4	Long term vibration measurements	147
2.7.2.5	Off-resonance acoustic excitation of inertia block rigid body motion	168
2.7.3	Experiment frames supported by light load pneumatic isolators.....	177
2.8	Comparison to St. Andrews university ultra-low-vibration labs	183
Chapter 3: A high-bandwidth, dilution temperature ultra-high-vacuum scanning tunneling microscopy experiment.....		185
3.1	Microscope head	185
3.2	Experiment overview	189
3.3	Experiment structure vibrations and microscope head performance	197
Chapter 4: Conclusion.....		209
4.1	Regarding instrumentation for characterizing low-vibration facilities.....	209
4.1.1	Conclusions.....	209

4.1.2	Recommendations and future research directions	210
4.2	Regarding acoustic effects on the performance of low-vibration facilities	211
4.2.1	Conclusions.....	211
4.2.2	Recommendations and future research directions	213
4.3	Regarding vibrations of solid bodies relevant to the performance of low-vibration facilities.....	216
4.3.1	Conclusions.....	216
4.3.2	Recommendations and future research directions	219
4.4	Identified shortcomings of the present work	222
Bibliography		223
Appendices.....		229
Appendix A : Lists of the lowest 30 FEA-predicted vibrational frequencies for the monolithic isolation enclosures		229
Appendix B : Linear spectral density calculation MATLAB script		230

List of Tables

Table 1.1: Preamplifier noise referred to variations in the tunneling junction width	7
Table 2.1 : Characteristics of the Wilcoxon 731A and PCB 393B04 piezoelectric accelerometers	31
Table 2.2: Measured noise parameters for the ECM8000 microphone	35
Table 2.3 : Calculated properties of the LAIR inertia blocks as designed	70
Table 2.4 : Summary of the specifications of the heavy load isolators selected	72
Table 2.5 : Approximate analytical room mode frequencies for the Nano-g acoustic enclosure.	85
Table 2.6 : Approximate analytical room mode frequencies for the C-pod acoustic enclosure ...	86
Table 2.7: Comparison of calculated and measured room mode frequencies for the Nano-g pod.	92
Table 2.8: Comparison of calculated and measured room mode frequencies for the C-pod. With the addition of the inertia block to the simulation, the refraction downshifting of the horizontal acoustic modes appears again, but the filling in of the vertical axis by the block also seems to upshift the vertical mode.....	93
Table 2.9 : Geometric and material properties used for FEA of the LAIR monolithic concrete isolation boxes	98
Table 2.10: FEA-predicted pseudo-rigid-body modes of the Nano-g monolithic concrete isolation box.....	99
Table 2.11: FEA-predicted pseudo-rigid-body modes of the Omega/C-pod monolithic concrete isolation box.....	100
Table 2.12 : Material properties used in FEM simulations of the inertia block resonant frequencies	122

Table 2.13 : Summary of the results of finite element simulations of the rigid and flexural vibrational modes of the LAIR inertia blocks.....	123
Table 2.14: Summary of rigid-body vibration characteristics of the three LAIR inertia blocks upon commissioning in 2012.....	126

List of Figures

Figure 1.1 : Simple conceptual models of a STM head and of the vacuum tunneling of electrons between the STM tip and sample.....	5
Figure 1.2 : Schematic of a typical layout for a low-vibration facility for STM experiments.	11
Figure 1.3 : 1-D model of a vibration isolated stage subject to base excitation and force excitation.....	12
Figure 1.4: Normalized velocity responses of a mass-spring-damper system to base and force excitations.	14
Figure 1.5: Simplified diagram of a pneumatic isolator.	15
Figure 2.1: Simplified schematic of the LAIR facility and inertia blocks.....	27
Figure 2.2: Conceptual schematic of a compression-mode piezoelectric accelerometer.	30
Figure 2.3: Accelerometry measurement noise floors, in velocity units.	33
Figure 2.4: Theoretical noise floor curve for the WM60A microphone compared to a very quiet ambient noise spectrum measured with the ECM8000 microphone.	35
Figure 2.5: Example time-series data for the Omegapod block and foundation.	37
Figure 2.6: Example time-series data for Omegapod shown with finer time resolution.	37
Figure 2.7: Raw periodogram of the Omegapod foundation and inertia block time series data shown in Figure 2.5.....	40
Figure 2.8 : Average of 100 raw periodograms taken on the Omegapod foundation and inertia block.....	41
Figure 2.9 : The raw periodogram from Figure 2.7 after smoothing with a 0.5 Hz wide moving average.	42

Figure 2.10: Empirical transfer function and coherence between the omegapod inertia block and the underlying foundation. Each curve is the average of 100 consecutive 30-s data segments. .	44
Figure 2.11: Simplified plan view of the AMPEL basement prior to the construction of the LAIR facility.	46
Figure 2.12 : X-direction floor velocity spectra in the AMPEL basement prior to construction of the LAIR	47
Figure 2.13: Y-direction floor velocity spectra in the AMPEL basement prior to construction of the LAIR	48
Figure 2.14: Z-direction floor velocity spectra in the AMPEL basement prior to construction of the LAIR	48
Figure 2.15: Asynchronously acquired RMS Z-direction acceleration map of the AMPEL basement prior to construction of the LAIR	49
Figure 2.16 : Tri-axial velocity floor velocity spectra measured in the center of the AMPEL basement prior to construction of the LAIR.	50
Figure 2.17 : Sound pressure spectra measured in the AMPEL basement prior to construction of the LAIR	51
Figure 2.18 : Running integrals of the seismic and acoustic spectra measured at point A prior to construction of the LAIR facility showing the weighting of the environmental vibrational energy predominantly to frequencies below 100 Hz.	53
Figure 2.19 : 1 degree-of-freedom model of a Scanning Tunneling Microscope head	55
Figure 2.20 : Response of the tunnel junction tip/sample displacement to base displacements for a model STM head with a resonant frequency of 1000 Hz and a damping ratio of 1%.	57

Figure 2.21: Floor velocity criterion for the STM experimental platform compared to the measured pre-construction floor velocity and theoretical floor velocities for ideal 1- and 2-stage passive vibration isolators.....	59
Figure 2.22 : Dimensioned drawing of the LAIR foundations and map of foundation vibration measurement positions. The isolators which support the inertia blocks (but not the inertia blocks themselves) are shown in red.....	62
Figure 2.23: Dimensioned drawing of the LAIR acoustic isolation enclosures	66
Figure 2.24: Acoustic wall treatments in the interstitial between the south acoustic walls of the Nano-g pod.....	66
Figure 2.25: Photo of the inside of the Nano-g pod.....	67
Figure 2.26 : Finite element stress analysis of the C-pod inertia block under gravitational loading.	68
Figure 2.27: Dimensioned drawings of the three inertia blocks constructed in the LAIR.	71
Figure 2.28: Microphone and subwoofer locations for the acoustic measurements.....	73
Figure 2.29 : Direct transmission acoustic transfer function and coherence for the C-pod back wall and doors, as measured with subwoofer sine sweep transmission experiments.	75
Figure 2.30 : Ambient acoustic spectra measured in the Nano-g and C- pods.....	78
Figure 2.31 : Acoustic pressure spectrogram (top) and RMS pressure (bottom) from late afternoon until 9 am in the C-pod acoustic isolation vault near the south surface of the inertia block	79
Figure 2.32 : Long term acoustic spectra recorded in the C-pod acoustic isolation vault near the south surface of the inertia block.	80
Figure 2.33: Acoustic pressure spectrum as a function of time in the Nano-g acoustic isolation vault near the south surface of the inertia block.	81

Figure 2.34: Long term acoustic spectra recorded in the Nano-g acoustic isolation vault near the south surface of the inertia block.	82
Figure 2.35: Raw response of the Nano-g acoustic enclosure to sine sweep excitation compared to approximate analytical resonance frequencies for the enclosure.....	88
Figure 2.36: Raw response of the C-pod acoustic enclosure to sine sweep excitation compared to approximate analytical resonance frequencies for the enclosure.....	89
Figure 2.37 : Comparison of raw room response (dashed curves) and ambient sound pressure spectra (solid curves) in the Nano-g and C- pods.	90
Figure 2.38 : Finite element analysis of acoustic mode downshifting due to acoustic refraction around the Nano-g inertia block	94
Figure 2.39: Examples of high-order FEA-predicted flexural modes of the monolithic isolation enclosures.....	101
Figure 2.40 : Vertical velocity spectrum and RMS velocity on the C-pod foundation vs time at the beginning of a workday.....	104
Figure 2.41 : Vertical velocity spectrum and RMS velocity on the foundation under the Omegapod inertia block over a period of just under 24 hours.....	105
Figure 2.42 : Vertical velocity spectrum and RMS velocity on the Nano-g foundation	106
Figure 2.43 : Long-term vertical velocity spectra for the isolated foundation underneath the C-pod inertia block.	107
Figure 2.44 : Long-term vertical velocity spectra for the isolated foundation underneath the Omegapod inertia block.....	108
Figure 2.45 : Long-term vertical velocity spectra for the isolated foundation underneath the Nano-g inertia block.	109

Figure 2.46 : Comparison of the long-run linear mean vertical foundation velocities at the three measurement locations on the two isolated foundations.....	110
Figure 2.47 : Comparison of the average of the 10 quietest 30-s long vertical foundation velocity spectra at the three measurement locations on the two isolated foundations.	111
Figure 2.48 : Comparison of the long run peak-hold vertical velocity spectra at the three measurement locations on the two isolated foundations.....	112
Figure 2.49 : Horizontal (X i.e. North-South) velocity spectrum and RMS velocity on the C-pod foundation vs time overnight into early morning	114
Figure 2.50: Horizontal (X i.e. North-South) velocity spectrum and RMS velocity on the Nano-g pod foundation vs time overnight, through a weekday and into a weekend morning.	115
Figure 2.51: Long-term horizontal velocity spectra for the isolated foundation underneath the C-pod inertia block	116
Figure 2.52: Long-term horizontal velocity spectra for the isolated foundation underneath the Nano-g pod inertia block	117
Figure 2.53 : Comparison of the long run mean horizontal velocity spectra on the two isolated foundations.....	118
Figure 2.54 : Comparison of the average of the 10 quietest 30-s horizontal velocity spectra on the two isolated foundations	119
Figure 2.55 : Comparison of the long run peak-hold horizontal velocity spectra on the two isolated foundations	120
Figure 2.56: Plan and isometric views of the FEA-predicted fundamental flexural mode shapes for the three LAIR inertia block.....	124
Figure 2.57: Vertical inertia block velocities on the three inertia blocks.	127

Figure 2.58: Horizontal inertia block velocities on the three inertia blocks.....	128
Figure 2.59 : C-Pod inertia block vertical axis transfer function showing a resonant frequency of 1.42 Hz and 20.5 dB amplification at resonance.	129
Figure 2.60: C-Pod inertia block East-West-axis transfer function showing a resonant frequency of 1.02 Hz and 30.1 dB amplification at resonance.	130
Figure 2.61: C-Pod inertia block North-South axis transfer function showing a resonant frequency of 1.02 Hz and 26.7 dB amplification.	131
Figure 2.62: Omegapod inertia block vertical axis transfer function showing a resonant frequency of 1.16 Hz and 17.9 dB amplification at resonance.	132
Figure 2.63 : Omegapod inertia block North-South axis transfer function showing a resonant frequency of 0.74 Hz and 24.2 dB amplification at resonance.	133
Figure 2.64: Omegapod inertia block East-West axis transfer function showing a resonant frequency of 0.74 Hz and 28.2 dB amplification at resonance.	134
Figure 2.65 : Nano-g inertia block vertical axis transfer function showing a highly damped resonance a 0.7 Hz.	135
Figure 2.66 : Nano-g inertia block East-West axis transfer function showing a resonant frequency of 0.65 Hz and 25.5 dB of amplification at resonance.	136
Figure 2.67 : Nano-g inertia block North-South axis transfer function showing a 0.65 Hz resonant frequency and 23.6 dB of amplification at resonance.	137
Figure 2.68: Accelerometer and excitation locations for the inertia block mode shape experiments.	140
Figure 2.69: Time-series of the response of the C-pod inertia block measured at the south-west corner of the block to an impulse near the north-east corner of the block.	141

Figure 2.70: Linear spectral density of the impulse response of the C-pod inertia block at the southwest corner to an impulse in the northeast corner.	142
Figure 2.71 : Comparison of symmetrized experimental mode shapes and frequencies with FEA predictions for the C-pod inertia block.	143
Figure 2.72: Comparison of symmetrized experimental mode shapes and frequencies with FEA predictions for the Omegapod inertia block.....	144
Figure 2.73: Comparison of symmetrized experimental mode shapes and frequencies with FEA predictions for the Nano-g inertia block	145
Figure 2.74: Vertical velocity spectrum and RMS velocity on the C-pod inertia block vs time at the beginning of a workday.....	149
Figure 2.75: Vertical velocity spectrum and RMS velocity on the Omegapod inertia block vs time over nearly 24 hours during the work week.	150
Figure 2.76: Vertical velocity spectrum and RMS velocity vs time on the Nano-g inertia block over more than 24 hours during the work week.	151
Figure 2.77 : Long term vertical velocity spectra for the C-pod inertia block.	152
Figure 2.78: Long term vertical velocity spectra for the Omegapod inertia block.....	153
Figure 2.79 : Long-term vertical velocity spectra for the Nano-g inertial block.....	154
Figure 2.80: Horizontal velocity spectrogram for the C-pod inertia block.....	155
Figure 2.81: Horizontal velocity spectrogram for the C-pod inertia block.....	156
Figure 2.82: Long term horizontal velocity spectra on the C-pod inertia block.....	157
Figure 2.83: Long term horizontal velocity spectra on the Nano-g inertia block.....	158
Figure 2.84: Long-term mean vertical axis empirical transfer functions from the foundations to the inertia blocks.	159

Figure 2.85: Long-term horizontal axis empirical transfer functions for the C-pod and Nano-g inertia blocks	160
Figure 2.86: Comparison of the average of the 10 quietest 30-s long vertical velocity spectra on the three inertia blocks	161
Figure 2.87: Comparison of the long term mean vertical velocity spectra on the three inertia blocks	162
Figure 2.88: Comparison of the long term peak hold vertical velocity spectra on the three inertia blocks	163
Figure 2.89: Comparison of the average of the 10 quietest 30-s long horizontal velocity spectra on the three inertia blocks	164
Figure 2.90: Comparison of the long-run mean horizontal velocity spectra on the Nano-g and C-pod inertia blocks	165
Figure 2.91: Comparison of long term peak-hold horizontal velocities on the C-Pod and Nano-g inertia blocks	166
Figure 2.92: Long-term average horizontal velocity spectra on the Nano-g inertia block and foundation compared to the sound pressure level measured near the south surface of the inertia block.....	169
Figure 2.93 : Non-dimensional plot of the acoustic force an inertia block as a function of the length of the block and of the frequency of the acoustic wave.....	171
Figure 2.94 : Schematic of the spatial variation in the acoustic pressure of the fundamental acoustic mode of a room containing an inertia block.	172
Figure 2.95: Long-term average horizontal axis empirical transfer function and fitted transfer function for the Nano-g inertia block pneumatic isolators.	174

Figure 2.96: Modelled acoustic forcing and base-excitation contributions to the velocity of the Nano-g inertia block	175
Figure 2.97: Comparison of modelled base excitation and total velocity with the measured velocity of the Nano-g inertia block.	176
Figure 2.98: Long run linear mean velocity spectra on the Omegapod foundation, inertia block and STM experiment frame.	178
Figure 2.99: Empirical transfer function between the Omegapod inertia block and the Omegapod STM experiment frame	179
Figure 2.100: Vibration spectra on the Omegapod STM experiment when floating on its light load isolators for different states of the inertia block	181
Figure 2.101: Empirical transfer function from the Omegapod inertia block to the frame of the Omicron 4K STM experiment through the experiment's light load pneumatic isolators.....	182
Figure 2.102 : Comparison of peak-hold and averaged velocity spectra for an inertia block at St Andrews with similar data for the Nano-g inertia block at the UBC LAIR facility.....	184
Figure 3.1 : Schematic overview of the microscope head used in the UBC dilution refrigerator STM experiment	186
Figure 3.2 : Schematic of the moving stage and scanner tube assembly of the STM	187
Figure 3.3 : Schematic of sample plate design, transfer mechanism and scheme for locking the sample plate into the head.....	188
Figure 3.4: A photograph of the dilution refrigerator taken underneath the experiment frame in the access pit of the Nano-g inertia block.	190
Figure 3.5: Section view of the helium dewar, superconducting magnet, dilution refrigerator and scanning tunneling microscope.....	191

Figure 3.6: Dewar visible underneath experiment frame.....	192
Figure 3.7: Annotated photograph of the UBC dilution fridge STM system on top of the Nano-g inertia block.	193
Figure 3.8: Gas handling system pumping line connected to dilution fridge still	194
Figure 3.9: Vibration isolating gimbal for dilution fridge pumping line	195
Figure 3.10: 2 nd vibration isolating gimbal for dilution fridge pumping line	196
Figure 3.11: Vibration levels measured on the central plate of the dilution refrigerator STM frame under different frame mounting conditions.	198
Figure 3.12: Empirical transfer functions from the inertia block to the experiment frame for large (inertia block not floating) and small (inertia block floating) levels on input vibration.....	200
Figure 3.13: Modelled velocity of the dilution STM frame due to acoustic forcing.	201
Figure 3.14: Modelled velocity of the dilution STM frame due to combined acoustic and base excitation compared to the ideal base-excitation only modelled velocity.	202
Figure 3.15: Vibration spectra measured at the end of the DR vacuum can compared to the vibration criterion for the STM base established in section 2.4.	204
Figure 3.16: Relative Z-velocity of the STM tip to sample while tunneling onto graphite at a 50pA setpoint, 600 mV bias, proportional gain of 20 pm and time constant of 1 ms.	204
Figure 3.17 Comparison of the empirical transfer functions from the vacuum can to the STM head to the simple model developed in section 2.4	205
Figure 3.18 : Tunnel current noise-spectrum with and without heat switch rod mechanically connecting the 4K, still and mixing chamber plates.	206
Figure 3.19 : Finite element analysis of the fundamental cantilever mode of the dilution refrigerator with and without the heat-switch engaged.....	207

List of Symbols

k ...spring constant

b ...coefficient of linear viscous damping

m ...mass

ξ ... damping ratio

f ...frequency in Hertz

f_0 ...natural frequency of vibration in Hertz

ω ... angular frequency in radians per second

ω_0 ...natural angular frequency of vibration in radians per second

p ...pressure

V ...volume

A ...area

L ...length

h ...height

List of Abbreviations

Scanning Tunneling Microscope (STM)

Dilution refrigerator (DR)

Ultra high Vacuum (UHV)

milli-Kelvin (mK)

picometers (pm)

femtometers (fm)

nanometers (nm)

Hertz (Hz)

Pascals (Pa)

Acknowledgements

When I first joined the lab in the summer of 2010, I was an inexperienced undergraduate and the basement of AMPEL was a just a big empty room with a blue painted floor. So many things have changed since then, and while they have not all been positive, I feel very fortunate to have spent a large part of the last five years in an environment which has promoted my growth both as a person and as a scientist. I am grateful to the huge number of kind, wise, dedicated and passionate people whom I have had the privilege of working with and alongside in this time.

Yan Pennec brought me into the lab and showed me that a small team of driven, passionate people can accomplish big things. Yan was a great mentor to me when I was, as he put it, a “junior scientist”. Largely thanks to Yan I learned the skills to help bring my own and other people’s ideas to life and had a major role in designing a microscope that can image atoms! Yan is one of the most productive people I have ever met and I remain in awe of his ability to filter out the noise and focus on the truly important aspects of a problem.

Doug Bonn, as my principal supervisor, has provided invaluable personal, intellectual and material support for my vibration research. The freedom and resources Doug gave me to explore my topic, combined with the right amount of guidance to keep me on track, taught me how to go about doing scientific research (and left me eager to do more of it!). I am thankful to Doug for this, as well as for his analytical and editorial support during the writing of my thesis and his flexibility in accommodating my overly ambitious writing timeline.

Jenny Hoffman was generous enough to agree to become my co-supervisor while still fully engaged with her duties at Harvard and to take the time to give me valuable advice and feedback both long-distance and during her extremely busy trips to UBC. She also bought one of the best (and most expensive) accelerometers in the world so I could study details that were

invisible with other instruments. Participating in the design of Jenny's new low-vibration labs helped motivate my research and her enthusiasm for understanding these kinds of facilities and how to optimize them was infectious. As I write this, they are building the formwork for the foundations of the new labs outside my window. I can't wait until the labs are ready so I can help Jenny's students measure how quiet they are and then help make them even quieter!

Sarah Burke, while not formally my supervisor, has also been extremely supportive of my research and of my development as a scientist. Her organization of regular talks during our group meetings induced me to present my research at many different stages throughout its development and I especially appreciate all the questions and feedback she has had for me at those times and in general.

Rob Delaney, who has invested more hours in bringing the beast (a.k.a the dilution refrigerator STM) to life than I can believe, has been an amazing colleague to work with over the past several years. Rob's positive attitude and perseverance in the face of even the most daunting of technical setbacks have taught me a lot and his technical courage and competence never cease to amaze me. I am grateful to Rob for his enormous contributions to the STM project; for listening patiently to my endless thinking out loud and then contributing his sharp technical insights, and for keeping me in the loop with the project even when I moved over to mostly working on my vibration research. Few, if any, of the interesting results regarding the dilution STM in chapter 3 of this work would have been possible without Rob.

James Day brought not only low-temperature expertise but great camaraderie to the dilution STM team and to the group in general. His good nature, broad skill set and mentorship – not just in science but in writing and in other areas of life – have helped make these last few years really pleasant. I owe many thanks to James for his willingness to edit things for me at the

last minute, for all the rides to and from the lab, for his tireless work to keep the helium flowing among a huge number of other responsibilities, and for making AMPEL a fun place to be.

Murray Hodgson provided me with valuable advice and references on acoustics, as well as extended loans of various pieces of crucial measurement equipment and the support of his group members in making reverberation time and other measurements.

Chris Waltham gave generously of his time to help me develop a richer understanding of some core ideas in acoustics and mechanical vibrations through a directed studies course. Chris opened my eyes to the variety of things I could do with finite elements and experimental modal analysis, and he was the person who really got me started on writing this thesis when he asked me to prepare a literature review for him.

Pinder Dosanjh is another person whose patience, cheerfulness and seemingly magical ability to manipulate 40 AWG wires into any necessary configuration have made my life around the lab that much better over the five years. Pinder's philosophy of steady, careful work – and doing everything under the microscope - has helped me and will continue to help me to build better scientific instruments.

Graeme Adamson, a Solidworks master and all around great guy, did much of the CAD in the early days of the dilution STM project. His excellent solid models of the experiment (and of the LAIR facility) were enormously helpful to me in producing clear diagrams for this thesis.

Vincent Wong did much of the initial commissioning work for the LAIR and his thorough and well-documented results were a large and invaluable starting point for me in my own experimental work and in preparing this thesis.

There are so many other wonderful people who have worked on the STM project and who helped create a wonderful working environment in AMPEL, I am afraid to list them all in case I leave someone out. On the STM project, Damien Quentin, Greg McMurtrie, Ben Xu, David Fournier, Piotr Forysinski, Andrew Cote, Walter Wasserman, Wesley Fritzke and Sebastian Munoz all made important contributions and were, without exception, wonderful to work with. Beyond campus, I am grateful for the support of our commercial partners: Vladimir Shvarts from Janis – who led the design of our dilution fridge and made the trip from Boston to personally fix it when it had a leak; Seth Rector at AMI, and Tim Weiss at Kadel who graciously stood behind their products when we were having difficulties.

I owe a big thanks to my current and past lab mates for all the science talks, jokes, help with any and all tasks, advice, good times and generally making AMPEL a nice place to work: Andrew Macdonald, Agustin Shiffrin, Katherine Cochrane, Martina Capsoni, Shun Chi, Damien Quentin, Nathan Evetts, Tanya Roussy, Sebastien Tremblay-Johnston and Stephanie Grothe, who is deeply missed.

There are many others around AMPEL and around campus who helped me in various ways. I owe many thanks to Walter Hardy for sharing his wisdom on many electronics and cryogenics topics, Josh Folk and his group for advice on dilution temperature thermalization and electronics, Doug Wong for expert advice on UHV and other issues, Harish Guatam for opening his shop to me and making many crucial parts for the project, Pavel Trochtchanovitch for his excellent electronics advice, Jon Nakane and Bernhard Zender for advice and support and letting me use the project lab, Martin O’Keane and the PHAS machine shop staff for help, advice and loans of tooling and stores manager Mark Reynolds for all the times he made the hike down to the basement to get me the metal stock I needed.

I would also like to thank Dr. Ram Aluru, Matthew Neat and Professor Peter Wahl from St Andrews university for helping me make what I feel is one of the first relatively rigorous comparisons between the performance of two ultra-low-vibration facilities as well as Nic Ontiveros for his valiant data collection efforts at Harvard.

I never would have completed my undergraduate, not to mention my master's without the support of my loving parents and sister. I am forever grateful to my mom and dad for raising me to want to learn and for the generous emotional, logistical and financial support they have given me which has allowed me to do so.

My wonderful girlfriend Belle has helped me in countless ways through the entirety of my degree; most importantly, I think, she has taught me to be sensitive to the subtleties of the world and the people in it – a skill which I am finding invaluable both in science and in life. Her love, patience and support have been crucial in helping me get to where I am today and her kindness – not just to me, but to everyone – inspires me to keep working towards something good that I too can share with the world.

I dedicate this thesis to two very special people:

My grandfather John, who gave me my first microscope and helped me grow my first crystal

and

Dr. Stephanie Grothe, a ray of sunshine who was taken from us far too soon

Chapter 1: Introduction

Scanning Tunneling Microscopes (STMs) can probe the local density of states of conducting materials with an energy resolution proportional to the experiment temperature and with sub-angstrom spatial resolution. Concomitant to their high spatial resolution, these microscopes are extremely sensitive to vibrations, which contribute noise to the measured signal. For STMs operating at liquid helium temperatures, substantial immunity from vibrations is readily achieved by mounting the microscope head to an eddy-current-damped, spring suspended plate inside the cryostat. Below this temperature range, however, the increasingly poor thermal link such spring suspensions provide between the microscope head and the experiment cold plate makes this simple and effective means of vibration isolation impractical.

As experimental condensed matter physicists seek finer energy resolution by decreasing experiment temperatures below 300 mK using dilution refrigerators (DRs), the vibration problems which were substantially solved for helium temperature STMs by eddy-current-damped spring suspensions must be solved in new ways. The most common approach is to rigidly bolt the microscope head to the mixing chamber plate of the DR and to mitigate the effects of vibrations in three areas:

1. Vibration immunity of the microscope head
2. Low-vibration design of the dilution refrigerator and other experiment structures
3. Isolation of the experiment from external vibrations

The goal of this thesis was to research these three factors and feed the results into the design and ongoing operational optimization of:

1. A ultra-high-vacuum dilution-refrigerator STM experiment developed at UBC
2. The purpose-built ultra-low-vibration facility that houses this experiment

1.1 Overview of this thesis

STM heads become increasingly immune to vibrations as the frequencies of their fundamental mechanical resonances are increased. Accordingly, optimized designs tend to be compact and extremely rigid. In Section 1.2 of this thesis, the principle of Scanning Tunneling Microscopy and the nature of the sensitivity of this instrument to vibrations are introduced. The applications and experimental conditions under which these instruments operate are surveyed and some principles relevant to their vibrational optimization are discussed.

Even heavily optimized STM heads are not fully immune to vibrations and therefore the reduction of vibrations at the STM mounting point is essential. These include both vibrations produced by the experiment and vibrations of other origins which propagate through the vibration isolation system and experiment structure to the microscope head. Accordingly, section 1.4 reviews existing dilution temperature STM experiments with a focus on design features relevant to vibration and the impact of vibrations on the ultimate performance of these instruments. Meanwhile, section 0 introduces the theory of vibration isolation and reviews the state of the art in ultra-low-vibration facilities.

Chapter 2 focuses on the design and characterization of the Laboratory for Atomic Imaging Research ultra-low-vibration facility and is the core of this work. The experimental techniques of accelerometry and microphony and the analytical tools of spectrograms, modal analysis and finite-element simulations are introduced. The initial site vibration survey and the development of the vibration isolation specification for the facility are documented. The facility design is reviewed and the characterization and analysis of the propagation of the acoustic and solid-borne vibrations through the facility are presented in detail.

First, the properties of the acoustic isolation vaults are studied. Acoustic transfer functions, low frequency acoustic room modes and ambient noise spectra are reported. The results of finite element simulations of the room modes are presented. The key results of this section are that the room modes strongly affect the ambient acoustic spectra inside the isolation vaults and that these room modes are downshifted from the frequencies predicted by the simplest analytical formula due to the perturbation of the cuboidal geometry of the room by the large inertia blocks.

Second, the rigid body and flexural vibrations of the relevant building and experiment structures are studied. The rigid and flexural motions of the building's foundations are modelled and measured, as are the motions of the facility's massive, pneumatically isolated inertia blocks. The transfer functions of these pneumatically supported inertia blocks are found to deviate from the ideal. This deviation is attributed to acoustic forces and this conclusion is supported by a simple analytical model.

Chapter 3 details some aspects of the design and performance of the UBC dilution fridge STM. An overview of the system and of the design of the STM head are presented. The vibrations of the dilution fridge experiment structure are measured in several configurations and the noise performance of the microscope is compared to the vibration levels measured near the microscope mount position. The transfer functions of the pneumatically supported experiment frame is found to deviate even more strongly from the ideal than was the case for the inertia blocks, and this is attributed to larger relative importance of acoustic forces for a pneumatically supported experiment frame resting on an already very still floor.

Conclusions which may be of use in the planning and design of future dilution refrigerator STM experiments and low-vibration facilities are drawn in chapter 4.

1.2 Scanning tunneling microscopy principles and instrumentation

The scanning tunneling microscope (STM) exploits the quantum mechanical phenomenon of electron tunneling to approximately measure the local density of electronic states as a function of position and of energy at the surface of a conducting sample. In this section, the basic principle of operation of these microscopes is introduced, leading into a discussion of the sensitivity of these instruments to mechanical vibrations. Thereafter, vibration criteria for STM operation are discussed and the mechanical modelling, design and optimization of STM heads are surveyed. The motivation for building an STM which operates under ultra-high-vacuum (UHV, $< 10^{-9}$ torr) at dilution refrigerator temperatures (< 100 mK) and in a high magnetic field (up to 7 T) is discussed and a survey of relevant experiments is given.

1.2.1 Basic theory and instrumentation

In a scanning tunneling microscope a conductive tip is brought to within ~ 0.5 nm of a conductive sample, a bias voltage is applied between the two and the resulting current of electrons tunneling through the vacuum gap between tip and sample is measured. Information about the sample is obtained by measuring this tunneling current as a function of position (topography) or as a function of the bias voltage (spectroscopy). The tunneling current has an exponential dependence on the width of the vacuum gap such that the majority of the tunneling current flows through the tip atom closest to the sample, yielding a spatial resolution on the atomic scale. This length scale can be readily accessed by the flexural deformations of a piezoelectric scanner tube. Meanwhile, many condensed matter phenomena of interest occur over energy scales easily and precisely probed with readily available bias voltage sources. A diagram of these concepts is shown in Figure 1.1.

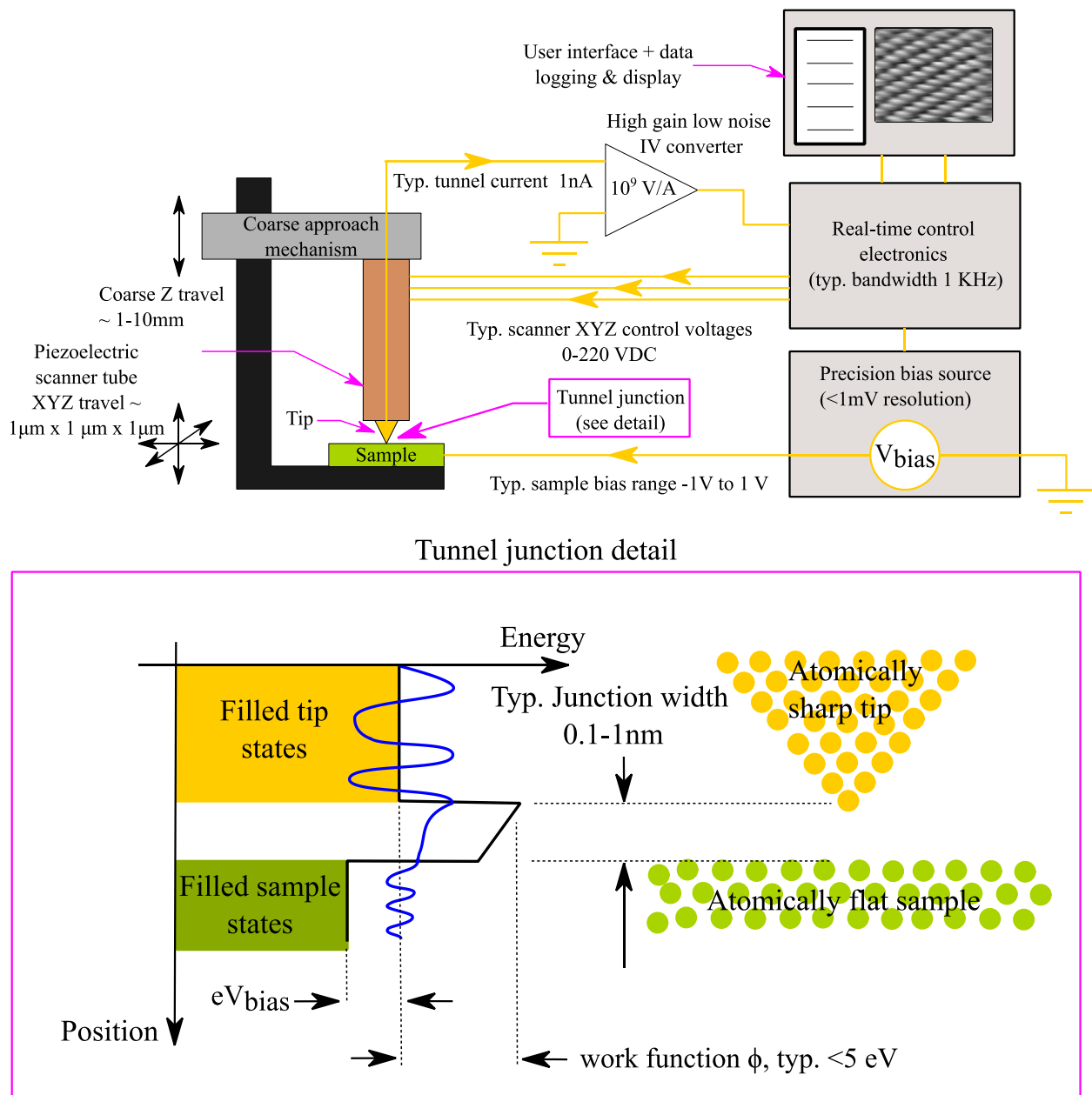


Figure 1.1 : Simple conceptual models of a STM head and of the vacuum tunneling of electrons between the STM tip and sample. The coarse approach mechanism must have a position resolution smaller than scan range of the piezoelectric scanner tube in order to successfully navigate the tip to within range of the sample. The values and ranges given for important parameters are typical but are not necessarily representative of all STM instruments or experiments.

A simple model which gives reasonable absolute values for the tunneling current in terms of the bias voltage and tunnel junction width is summarized in [1]. This can be written as

$$I_t = V_b \cdot G_0 \cdot e^{-\frac{2\sqrt{2 \cdot m_e \cdot \phi}}{\hbar} \cdot Z} \quad 1.1$$

where I_t is the net tunneling current, V_b is the bias voltage, $G_0 \approx 77.48 \mu S$ is the quantum of conductance, ϕ is the work function (taken to be the same for both tip and sample in this simplified model), m_e is the electron mass and Z is the relative tip-sample distance as defined in [1].

Following [1] and taking $\phi = 5 \text{ eV}$ as an upper bound to the work function of a metallic tip and sample¹, this model gives a reasonable relative tip-sample distance of $Z = 0.64 \text{ nm}$ for a typical tunneling current set point of $I_{t,0} = 1 \text{ nA}$ at $V_b = 100 \text{ mV}$.

Taking the derivative of the tunnel current with Z immediately reveals the origin of the sensitivity of the STM to changes in the tunnel junction width:

$$\begin{aligned} \frac{\partial I_t}{\partial Z} &= -\frac{2\sqrt{2 \cdot m_e \cdot \phi}}{\hbar} \cdot V_b \cdot G_0 \cdot e^{-\frac{2\sqrt{2 \cdot m_e \cdot \phi}}{\hbar} \cdot Z} \\ &= -\frac{2\sqrt{2 \cdot m_e \cdot \phi}}{\hbar} I_{t,0} \approx 23 I_{t,0} / \text{nm} = 2.3 I_{t,0} / \text{\AA} \end{aligned} \quad 1.2$$

where the evaluation is for $\phi = 5 \text{ eV}$ as before. The tunneling current more than doubles for a one-angstrom change in the tunnel junction width. This extreme spatial sensitivity allows scanning tunneling microscopes to measure features with heights on the atomic scale but also makes the tunneling current signal extremely susceptible to corruption by any environmental mechanical vibrations which disturb the tunnel junction.

¹ This gives a model with the most vibration sensitive tunnel junction, which is conservative

1.2.2 STM vibration criteria

Several discussion of vibration criteria for STM in the literature conclude that the amplitude of relative vibration between the tip and sample of an STM should be below 1pm for the instrument to function properly[1][2][3]. The very sensible reasoning behind this number is that the atomic corrugation of an atomically flat sample can be as low as 10 pm, and so the vibrational disturbance should be at least ten times smaller.

A different but practical criterion can be developed by considering the noise floor of the tunneling current IV converter (or preamplifier) as referred to the motion of tip. The utility of this approach is that it sets a scale beyond which further reductions in the vibrational noise are not productive. The instruments in the LAIR have been found to typically have electronic noise floors of approximately $\delta I_t = 20 \text{ fA}/\sqrt{\text{Hz}}$. In a linear approximation, the equivalent vibrational motion at the tip is

$$\delta Z = \delta I_t \cdot \frac{dZ}{dI_t} \approx \frac{\delta I_t}{2.3E10 \cdot I_{t,0}} [m/\sqrt{\text{Hz}}] \quad 1.3$$

Where $I_{t,0}$ is the tunneling current set-point. The importance of the electronic noise decreases as the set point is increased and above a certain set point, the vibrational noise will dominate. The referred amplifier noise is tabulated for a range of practical set points in Table 1.1.

Current set-point	Tunnel junction width variation δZ equivalent to $20 \text{ fA}/\sqrt{\text{Hz}}$
1 pA	$870 \text{ fm}/\sqrt{\text{Hz}}$
10 pA	$87 \text{ fm}/\sqrt{\text{Hz}}$
100 pA	$8.7 \text{ fm}/\sqrt{\text{Hz}}$
1 nA	$0.87 \text{ fm}/\sqrt{\text{Hz}}$
10 nA	$0.087 \text{ fm}/\sqrt{\text{Hz}}$

Table 1.1: Preamplifier noise referred to variations in the tunneling junction width

Based on experience and consideration of the set points normally used for probing samples of interest, a $10 \text{ fm}/\sqrt{\text{Hz}}$ criterion for mechanical vibrations of the tunneling junction was set for the dilution refrigerator STM experiment described in this thesis. Table 1.1 shows that – based on the preceding analysis - with this level of mechanical noise, the amplifier noise will dominate for set points below approximately 100 pA. The 1 kHz bandwidth of our preamplifiers [4] motivates the consideration of this criterion only within the 0-1000 Hz band. From experience, this is an ambitious criterion; it is also 10 – 100 times lower than the tunnel junction width variations reported for a state-of-the-art dilution refrigerator STM [5] within the 0-1 kHz band.

1.2.3 STM head optimization

A key factor in achieving low levels of vibration of the tunneling junction is the design of the STM head. As will be treated mathematically in section 2.4, the higher the fundamental mechanical resonant frequency of the STM head, the greater the immunity of that instrument to vibrational perturbations. This is essentially because in a more rigid head, the tip and sample move together instead of relative to each other when the head is subject to external sources of vibration. This principal applies to all types of scanning probe microscope (SPM) heads. It is important to keep in mind that this may not hold if substantial vibrations can be transmitted to the tip or sample through paths other than the STM head body, for example by the wires which provide voltages to the scanner tube electrode or the coaxial cable which carries the tunneling current.

To develop ever-stiffer STM head designs, analytical [6] and finite-element [7] optimizations of the resonant frequencies of microscope bodies and scanner tubes [8] have been

carried out. Typical resonance frequencies for high-performance STM heads are in the 1-5 kHz range. When the microscope body has been optimized, the piezoelectric scanner tube can become the vibrational weak point in common designs. One extreme optimization which employs a new type of piezoelectric scanner – based on stack elements rather than a tube scanner – resulted in an AFM head with a fundamental resonant frequency of 23.4 kHz and which resolved nanometer sized objects even when placed on the seat of a idling motorcycle [9].

1.2.4 Motivation for studying matter under extreme conditions and associated technical difficulties

The motivation for building a dilution temperature STM is simple: at lower temperatures, the thermal broadening of the Fermi-Dirac distribution of electron occupancies is reduced and finer energy resolution can be achieved with scanning tunneling spectroscopy (STS). The thermal-broadening driven lower limit to the energy resolution of STS performed with a metallic tip at an electronic temperature T is $\Delta E = \frac{7}{2}k_B T$ [10] where k_B is the Boltzmann constant. This is equivalent to $0.3 \mu\text{eV}$ per mK, $30 \mu\text{eV}$ at 100 mK or 1.26 meV at 4.2 K. With access to the tiny energy scales below liquid helium temperature, minute but important details of quantum mechanical objects can be examined. Many experimental difficulties arise, however, in pursuing STM at dilution refrigerator temperatures. The decreasing thermal conductivities of materials make proper thermalization of the microscope head and sample increasingly difficult. The decoupling of the electron and phonon baths means that the effective temperature of the electrons under study can be driven well above the temperature of the dilution fridge by broad band Johnson and technological noise sources. The extremely low cooling powers of dilution refrigerators necessitate thermally weak – and therefore mechanically weak – support structures

for the mixing chamber plate to which the STM is mounted; this results in structures which have low resonant frequencies readily excited by ambient vibrations.

Pairing low temperatures with high magnetic fields so that the magnetic energy scale dominates the thermal energy scale opens the door to further interesting physics, but also introduces constraints that materials not be magnetic and even constrains the arrangement of non-magnetic conductors to minimize eddy current heating.

While crystals cleaved in the cold space of a helium cryostat or dilution refrigerator can present atomically flat, uncontaminated surfaces ideal for study with a STM, successful experiments on a broader range of materials typically require high-temperature sample preparations techniques such as molecular beam epitaxy. To load samples prepared with such technique into a cryogenic STM – a mechanical process which can easily take minutes -without substantial surface contamination, the intervening space must be kept under ultra-high-vacuum (UHV). The materials and design constraints associated with achieving and maintaining UHV are especially onerous for STM systems as turbopumps generate too much vibration to be operated at the same time as the microscope head.

1.3 Fundamentals of low vibration facilities

The following sections survey the literature and give details on the key components of a typical low-vibration facility for high-performance STM experiments as shown in Figure 1.2. First, the transfer functions of a linear mass spring damper system to excitations of the base and to forces acting on the mass are derived. Real pneumatic vibration isolators – which are approximated by such a mass spring system are then introduced. Next, the literature on the vibrational properties of foundations that are either isolated or contiguous with the building foundation is then surveyed. Then the literature on the rigid body and flexural vibrations of pneumatically suspended inertia blocks is examined. Finally, the topic of acoustic isolation is discussed. Discussion of light load isolators and experiment structures – which are hardly treated in the literature - are deferred to later chapters.

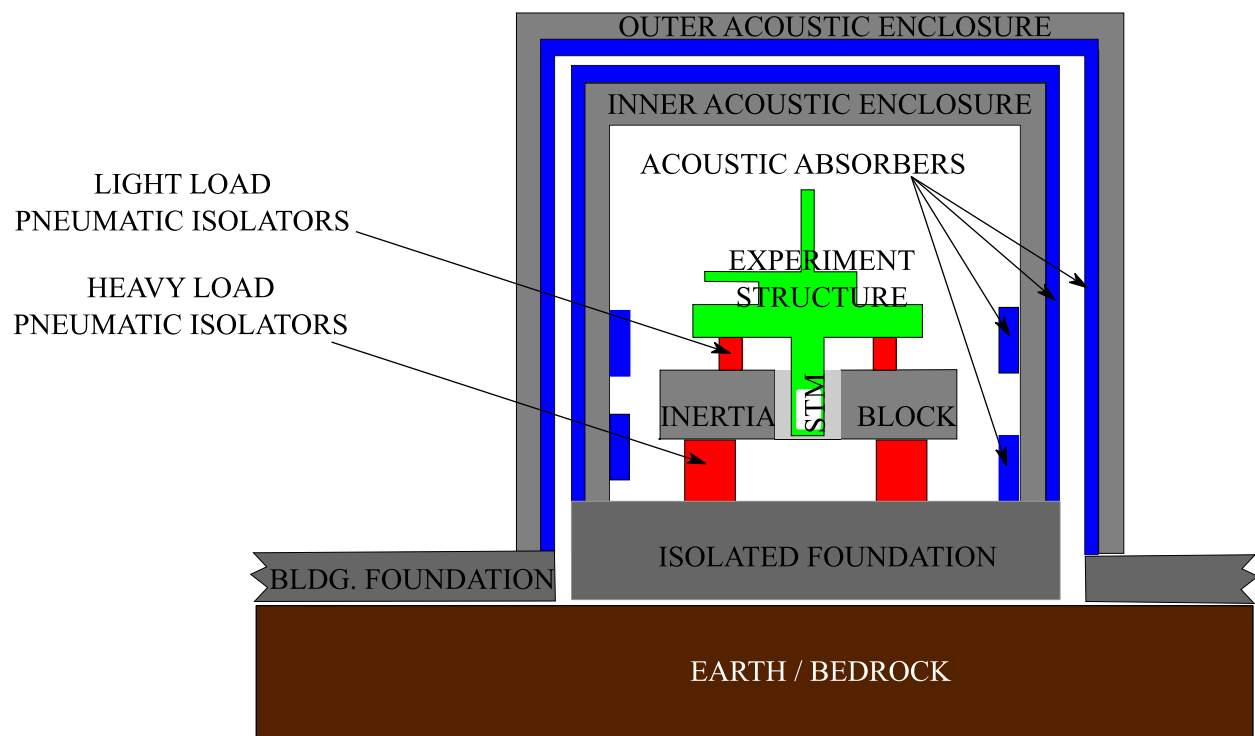


Figure 1.2 : Schematic of a typical layout for a low-vibration facility for STM experiments. The inertia block dimensions are typical on the order of 3-5 m and the mass typically tens of tons.

1.3.1 Mass-spring-damper vibration isolators

Many common types of passive vibration isolators can be modelled as a linear system comprised of a mass m supported from a base by a spring of stiffness k and a damper or dashpot of linear viscous damping coefficient b . The motion of the mass $x_{mass}(t)$ may be excited by one or both of two inputs : forces $F(t)$ acting directly on the mass (force excitation) and motions $x_{base}(t)$ of the base (base excitation). This system is depicted in Figure 1.3

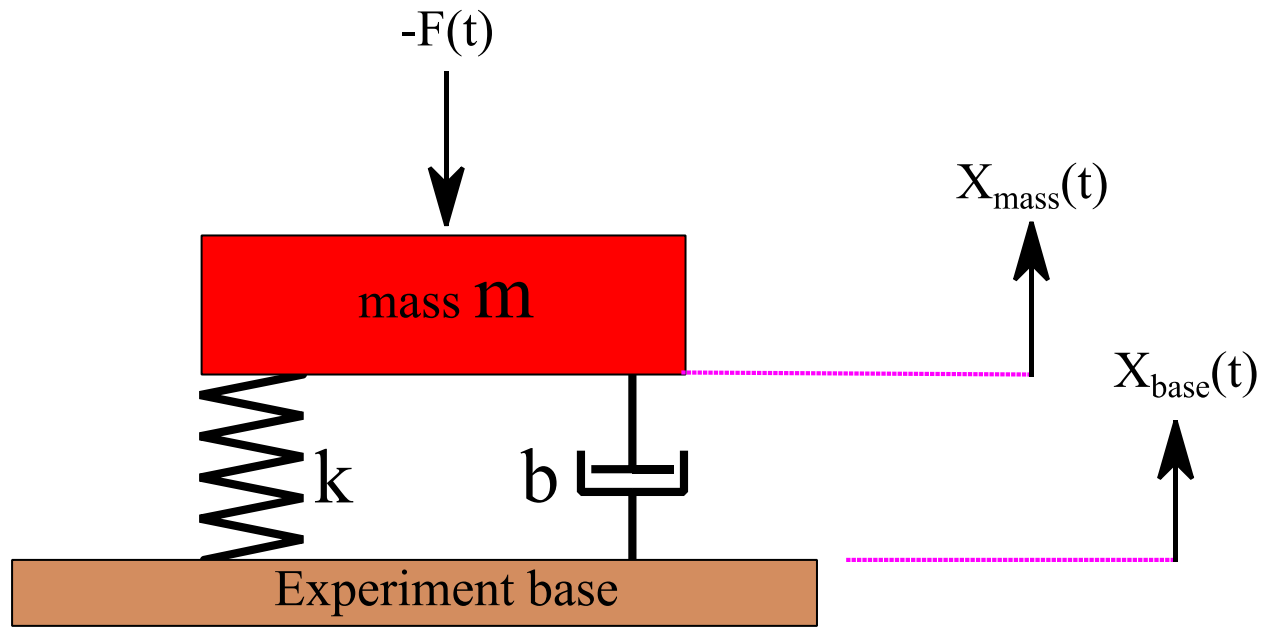


Figure 1.3 : 1-D model of a vibration isolated stage subject to base excitation and force excitation

The equation of motion of this system in the time domain can be shown to be:

$$m\ddot{x}_{mass} + b\dot{x}_{mass} + kx_{mass} = F + b\dot{x}_{base} + kx_{base} \quad 1.4$$

Fourier transforming yields

$$-m\omega^2 X_{mass} + j\omega b X_{mass} + k X_{mass} = F + j\omega b X_{base} + k X_{base}$$

where the capitals indicate functions in the frequency domain rather than the time domain and j is the imaginary number and ω is the angular frequency.

Considering only the base motion yields the base excitation transfer function

$$H_{base}(\omega) = \frac{X_{mass}(\omega)}{X_{base}(\omega)} = \frac{V_{mass}(\omega)}{V_{base}(\omega)} \frac{j\omega b + k}{-m\omega^2 + j\omega b + k} \quad 1.5$$

where $V(\omega)$ is a velocity spectrum.

Considering only the force acting on the mass yields the force excitation transfer function, which, cast in terms of velocity by frequency domain differentiation (multiplication by $j\omega$), is

$$H_{force}(\omega) = \frac{V_{mass}(\omega)}{F(\omega)} = \frac{j\omega X_{mass}(\omega)}{F(\omega)} = \frac{j\omega}{-m\omega^2 + j\omega b + k} \quad 1.6$$

Introducing the parameters of undamped natural resonant frequency $\omega_0 = \sqrt{k/m}$, damping ratio

$\xi = \frac{b}{\sqrt{4km}}$ and dimensionless frequency $r = \omega/\omega_0$ yields better structured expressions for the

magnitudes of these transfer functions

$$|H_{base}(\omega)| = \left| \frac{X_{mass}(\omega)}{X_{base}(\omega)} \right| = \left[\frac{1 + (2\xi r)^2}{(1 - r^2)^2 + (2\xi r)^2} \right]^{1/2} \quad 1.7$$

and

$$|H_{force}(\omega)| = \left| \frac{V_{mass}(\omega)}{F(\omega)} \right| = \left[\frac{r/\sqrt{mk}}{\sqrt{(1 - r^2)^2 + (2\xi r)^2}} \right] \quad 1.8$$

Normalized versions of the functions are shown in Figure 1.4 .

For base excitations, a quality factor $Q = \frac{1}{2\xi} \approx |H_{base}(\omega = \omega_0)|$ can be defined which is

approximately equal to the amplification at resonance for small values of the damping ratio.

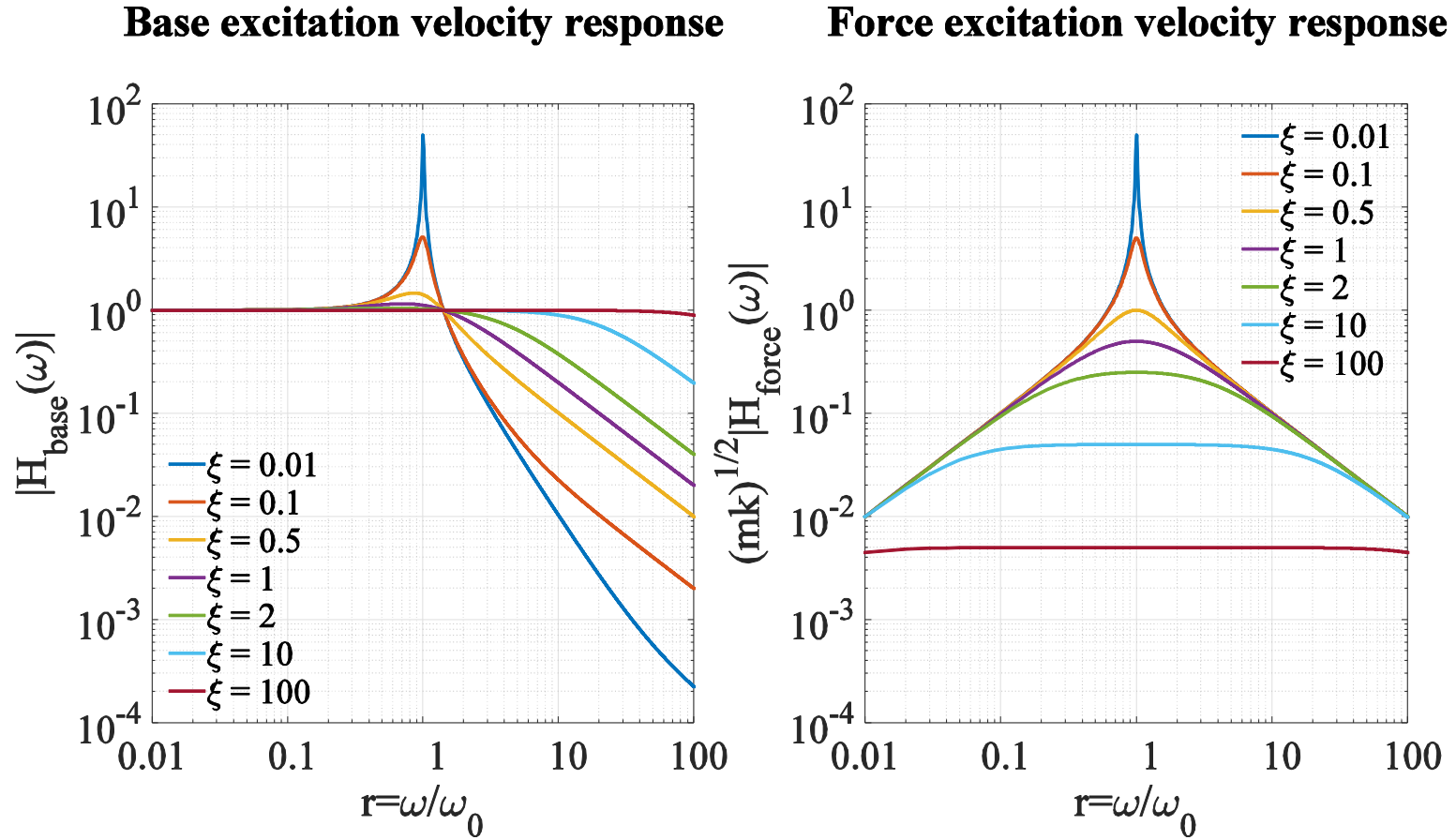


Figure 1.4: Normalized velocity responses of a mass-spring-damper system to base and force excitations. For base excitations, higher damping ratios reduce the amplification at resonance ($r=1$) but decreases the slope of the response roll off in the isolation region above resonance. For force excitations, the asymptotic slope of the response above resonance is independent of damping ratio. This means that while using more damping is a trade-off for isolating base excitations, more damping is always better for isolating from force excitations.

1.3.2 Real pneumatic vibration isolators

Real pneumatic isolators typically work by combining a pendulum with a vertically directed air-spring to provide isolation of vibrations in both horizontal and vertical directions. A simplified diagram of a pneumatic isolator and an explanation of its function are given in Figure 1.5

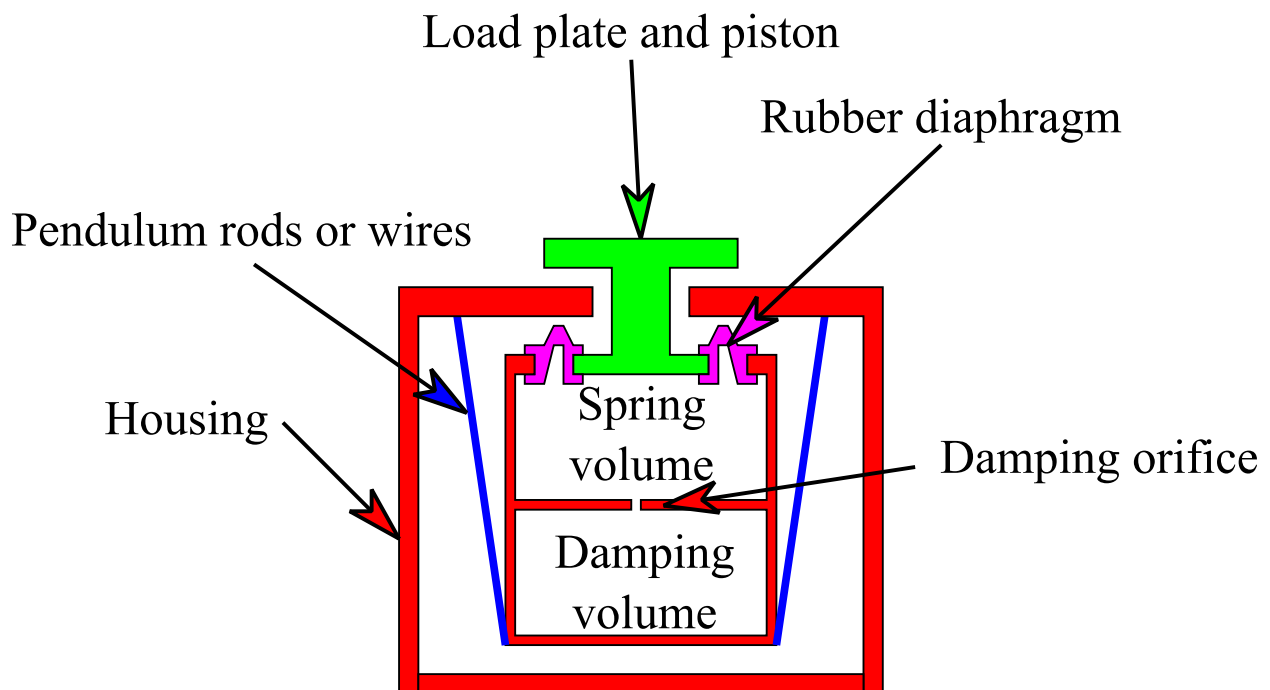


Figure 1.5: Simplified diagram of a pneumatic isolator. The mass (not shown) rests on the load plate; the spring volume and damping volume are filled with compressed air, supporting the mass on what is effectively an air-spring. Vertical vibration isolation is provided by the axial degree of freedom of this air spring and horizontal vibration isolation by the degrees of freedom of the pendulum formed by the suspension of the air-spring assembly by wires or rods. Substantial damping of the vertical motion is provided by viscous losses through the damping orifice as the piston displaces air out of – or aspirates it into – the spring volume. Without additional horizontal damping mechanism, the horizontal axis damping of the design shown here would be very low; poor horizontal damping is common even in commercial pneumatic vibration isolators.

The pneumatic isolator acts as a spring and damper both in the horizontal and vertical directions. The horizontal resonant frequency is set by the length l of the pendulum:

$$\omega_0 = \sqrt{\frac{g}{l}} \quad 1.9$$

In the absence of an intentional horizontal damping mechanism, the horizontal damping ratio will be set by small amounts of mechanical dissipation in the rubber diaphragm or elsewhere in the mechanism. Typical horizontal resonant frequencies for commercially available isolators are on the order 1 Hz while quality factors may easily be 10 or more without specific horizontal damping mechanisms in place [11].

The simplest model of the vertical stiffness of a pneumatic isolator is a single-chamber cylinder of height h and cross-sectional area A such that the working volume is $V = Ah$. At equilibrium the weight of the mass is balanced by the pressure acting on the piston so that

$$p_0 A = mg \quad 1.10$$

where the 0 subscript indicates the value of a property at equilibrium. Then - working in the isothermal limit for simplicity – the pressure and volume in the air spring are given by

$$pV = pAh = p_0 V_0 \quad 1.11$$

Thus the pressure as a function of the height of this piston is

$$p(h) = \frac{p_0 V_0}{Ah} = \frac{p_0 Ah_0}{Ah} = \frac{p_0 h_0}{h} \quad 1.12$$

And so the stiffness in the vicinity of the equilibrium point $h = h_0$ is

$$k(h = h_0) = -\left. \frac{df}{dh} \right|_{h=h_0} = -\left. \frac{d}{dh} Ap(h) \right|_{h=h_0} = \frac{Ap_0}{h_0} = \frac{mg}{h_0} \quad 1.13$$

And the resonant frequency of the mass-spring system is

$$\omega_0 = \sqrt{\frac{k}{m}} = \sqrt{\frac{mg/h_0}{m}} = \sqrt{\frac{g}{h_0}} \quad 1.14$$

Suprisingly, the mass drops out of the resonant frequency and the height of the cylindrical air-spring volume is found to be the parameters which controls the resonant frequency. This behavior holds qualitatively for real, double-chambered pneumatic isolators: taller isolators have lower resonant frequencies. These frequencies and also damping coefficients can be predicted with reasonable accuracy for real isolators by more sophisticated models such as the one presented in [12]. Typically resonant frequencies for commercial isolators are a function of their size but are typically on the order of 1 Hz while for axial vibrations of the piston, damping ratios near unity can be achieved if desired [11], keeping in mind that the non-linear characteristics of viscous damping may give different effective damping ratios at different frequencies.

1.3.3 Low-vibration foundations

In their rigid-body modes, concrete slab-on-grade foundation act as masses on earth-springs resonating at frequencies typically in the range 5-30Hz [13]. The damping of these rigid motions is driven by radiation of acoustic waves into the earth and this leads to a design trade-off between having a low resonant frequency – achieved with a high ratio of foundation mass to surface area - and a high level of radiation damping (achieved with a high surface area)[13]. Further design trade-offs exist between slabs not connected to the surrounding building foundation (“isolated slabs”) and monolithic slabs spanning the entire floor space of a building. As shown in [14], isolated slabs tend to exhibit slightly improved relative isolation from vertical

vibrations but substantially worse isolation from horizontal vibrations. This is likely explained by their inherently smaller size, which does not allow them to benefit as much from the averaging out of long wavelength horizontal vibrations, resulting in increased levels of horizontal vibrations in isolated slabs relative to monolithic slabs [15][16].

The relevance of foundation flexural modes to the design of low-vibration slab-on-grade foundations does not appear to be discussed in the literature. The larger flexibility of foundation slabs in the vertical direction relative to the horizontal direction means that the lowest frequency (most detrimental) flexural modes of the slabs are likely to bending modes which might be improved with a ribbed slab design.

1.3.4 Rigid body vibrations of inertia blocks

The pneumatic isolators used to support inertia blocks typically have resonant frequencies in the range 0.75-1.5 Hz in the Z direction and 0.7-3 Hz in the horizontal directions [11]. Active vibration isolators appear to provide some additional performance relative to passive isolators [5][16]. Placement of inertia block center of mass at plane of isolator heads minimizes coupling of horizontal rigid body vibrations to rocking mode rigid body vibrations.

Minimization of direct coupling of vibrations via pumping lines and other service connections is minimized by careful employment of highly compliant couplings such as gimbals [5], [17] and long hoses.

The role of acoustic forces in causing rigid body motion of inertia blocks is not well documented in the literature. This so-called “sail effect” is briefly mentioned in the paper describing the NIST low-vibration facility [5] where an acoustic enclosure was placed on, rather

than around, the inertia blocks. This additional surface area is hypothesized to increase the strength of the acoustic interactions.

Placing inertia blocks too close to fixed surfaces such as foundations or walls may also add undesirable additional stiffness to the isolator system due to the air entrapped between such surfaces and the inertia block [18].

1.3.5 Flexural vibrations of inertia blocks

Flexural vibration frequencies and mode shapes of suspended inertia slabs have been predicted with reasonable accuracy using FEA and measured experimentally [19]. Moreover, these resonances are found to degrade isolation system performance at certain frequencies [19]. Reported fundamental resonant frequencies for flexural modes of inertia blocks range from 34 HZ [19] to 328 Hz [20]

These problems are exacerbated by the fact that ordinary reinforced concrete structures are poorly damped ($\xi \approx 0.01$)[21]. A study carried out in the context of damping the flexural vibrations in inertia blocks found that the damping ratio of concrete can be increased to ~ 0.05 through the addition of various materials to the aggregate mix, although detrimental effects on concrete strength and other properties may be a concern [22]. To the authors' knowledge, no inertia blocks cast with specially damped concretes have been reported.

1.3.6 Acoustic isolation

Sufficiently large acoustic pressure fluctuations are predicted to directly drive rigid body motion of compliantly suspended inertia blocks or experiment frames [23]. Since the response of pneumatically supported equipment to forces is maximal near to the isolator resonant frequency

(typically $\sim 1\text{Hz}$), acoustically driven motion is likely to be the largest at low frequencies, especially since low frequency acoustic waves are not well attenuated by even very heavy acoustic enclosures. The flexural modes of resonant structures can also be acoustically excited [24] and high-quality resonators such as aluminum experiment frames and stainless steel cryostats may be particularly vulnerable to these excitations. For these reasons, attenuation of ambient acoustic noise is a key factor in achieving low levels of vibration.

While portable acoustic enclosures are commercially available [25] and have been characterized experimentally [26], these units provide little isolation at frequencies below $\sim 20\text{ Hz}$. Meanwhile, few details of heavily acoustically isolated rooms are available. Ambient acoustic conditions in such rooms are typically characterized by an equivalent sound pressure level (SPL) which is a weighted integral of the sound pressure spectrum as defined in International Electrotechnical Commission Standard IEC 61672-1. These single number measures give very little information about the spectral distribution of the noise in the critical low-frequency region. Ultra-quiet rooms with reported sound levels include:

- Orfield laboratories : -9.4dBA^2 according to [20]
- Cornell electron microscopy lab : $< 6.3e - 4 \text{ Pa}/\sqrt{\text{Hz}}$ from 20-500 Hz[27]
- IBM Zurich labs : 21 dBC^3 [20]

In general, the transmission of sound through even a single wall into a room is a complex one. The acoustic modes of the transmitting and receiving rooms, as well as the flexural mode shapes of the wall must be considered [28]. The additional resonant cavity introduced by a second

² dBA indicates an A-weighted SPL, which is a weighting intended to mimic the frequency response of the human ear

³ dBC indicates a C-weighted SPL, which is a flatter weighting at low frequencies than the A-weighting

acoustic wall leads to mass-air-mass resonances of the double wall and resonant dips in the attenuation at some frequencies [29].

1.4 Existing UHV dilution temperature STM experiments and low vibration facilities

Low vibration facilities for scanning tunneling microscope experiments utilizing large concrete inertia blocks exist at Cornell[30], NIST [5], MPI-Stuttgart, Harvard, IBM Zurich [20], Princeton [17], Purdue [31] and elsewhere. Despite the number of such facilities, few details and little analysis of their characteristics is available in the literature. Most of these facilities appear to have comparable performance although the three stage partially active system at NIST may confer some additional isolation. A key design difference between facility designs is whether the inner acoustic enclosure is mounted on the inertia block or not. Increasing the surface area of the inertia block significantly in this way without a meaningful increase in its mass is thought to increase the susceptibility of the inertia block to acoustic forces. On the other hand, an acoustic enclosure mounted to a vibration isolated stage will not produce acoustic radiation driven by ground-borne vibrations in the way that an enclosure anchored to a foundation might.

Another difference is that not all facilities make use of the isolated foundation concept, some use a foundation coupled directly to the building foundation.

Scanning tunneling microscopes operating at dilution temperature under ultra-high vacuum conditions started appearing around 2010 with the publication of an extensive review on a sophisticated dilution STM facility at NIST [5]. In 2013, dilution STM experiments at Princeton [17] and MPI-Stuttgart were described [10]. These systems all allow various degrees of in-situ sample growth and preparation beyond cleaving. Although all three of these experiments employ multi-stage vibration isolation system, the impact of vibrations on the STM

measurements is still apparent to varying degrees. The circulation of the helium mixture in the dilution refrigerators employing a 1K pot appears to be a significant source of vibration.

The NIST dilution refrigerator STM experiment [5] employs a three-stage vibration isolation system consisting of a passive experiment frame supported by passive pneumatic isolators on a 6 ton granite slab; the granite slab is supported by active pneumatic isolators from a 110 ton concrete inertia block which in turn is supported by active pneumatic isolators sitting on the foundation of the building. A double acoustic enclosure with the outer enclosure mounted on the foundation and the inner enclosure mounted on the inertia block are used to diminish acoustic pressure fluctuations that might excite vibrations on the experiment stage. In the crucial low frequency band 0-100 Hz the stability of the STM tip was reported to approach $100 \text{ fm}/\sqrt{\text{Hz}}$ and the Z-height spectrum is very smooth with only a single small peak around 16 Hz appearing which might be ascribed to mechanical noise. A dilution fridge design allowing the use of either a 1K pot or Joule-Thompson condenser allowed comparative testing which shows that the 1K pot is significant source of vibration while the Joule-Thompson stage is not. Vibrational decoupling of the dilution fridge pumping lines is accomplished through a system of compliant edge-welded bellows mounted into gimbals.

The dilution STM experiment at Princeton [17] employs a two stage passive vibration isolation system with the experiment frame mounted rigidly to a 4 ton granite block which is pneumatically supported from a 30 ton inertia block. The inertia block in turn is pneumatically supported by isolators resting on large concrete posts cast into the floor of the building. An outer acoustic enclosure made of grout-filled concrete blocks and an inner acoustic enclosure which appears to be of a light-weight variety are anchored to the building floor. Pumping lines for the DR still are decoupled vibrationally from the experiment with vacuum gimbals similar to those

used at NIST. These pumping lines are additionally anchored by concrete blocks to the building foundation and to the inertia block to further reduce the vibrations propagating towards the STM. Despite achieving low levels of vibration on the granite block to which the experiment frame was anchored, the tunneling current signal reported for this STM experiment shows a number of conspicuous mechanical peaks below 100 Hz. At some frequencies, these peaks are more than an order of magnitude above the otherwise excellent broad-band current noise level of $\sim 20\text{--}30 \text{ fA}/\sqrt{\text{Hz}}$ at a 100pA setpoint and -200mV bias with the Z-feedback turned off). Tests suggest that helium flow through the 1K pot is likely the dominant source of vibrations affecting this STM although the circulation of the He3/4 mixture may also contribute.

The UHV dilution STM at MPI-Stuttgart does not employ a massive concrete inertia block for vibration isolation. Rather, a metal cradle is supported on active dampers which isolate between 0.6 and 100 Hz. The experiment is supported from this actively isolated stage by a second set of passive isolators and spans two floors. The isolators supporting the experiment assembly reside on an upper floor while the cryostat penetrates downward through an opening in the floor for user access on a lower floor. No tunnel current or tip Z-height noise spectra are shown, nor are any direct measurements of the vibration levels achieved with this setup. However, topographic measurements made on Au(111) are used to estimate the Z-noise to have an amplitude of approximately 3pm and another experiment on Cu(111) estimates the Z-noise at $4.2\text{pm} \pm 0.5\text{pm}$ when averaging for $T_{avg} = 3.5\text{ms}$ at each data point. Assuming that this noise is all in the not-averaged-out band $0 - 1/T_{avg} = 0 - 285 \text{ Hz}$ would suggest an average Z-spectral noise in this band of $250 \text{ fm}/\sqrt{\text{Hz}}$ which is larger than might be desired but certainly not an unreasonable number. While vibration data is lacking from this paper, it is clear that a smaller active system can provide sufficient vibration isolation to achieve at least a basic level of

functionality for a STM. With the extremely impressive $11.4 \mu\text{eV}$ energy resolution reported for this system, further results are eagerly awaited.

Chapter 2: Specification, design and characterization of the laboratory for atomic imaging research ultra-low-vibration facility

The Laboratory for Atomic Imaging Research (LAIR) is an ultra-low-vibration facility located on the Vancouver campus of the University of British Columbia. The LAIR was built for the purpose of providing an environment with extremely low levels of ambient acoustic and mechanical vibration for three high performance Scanning Tunneling Microscopy experiments including the dilution temperature experiment discussed in the next chapter. The facility was built as an extensive renovation to the unfinished basement of the Advanced Materials and Process Engineering Laboratory (AMPEL) building and was completed in 2012.

In this chapter the specification, design and experimental characterization of the Laboratory for Atomic Imaging Research ultra-low-vibration facility are detailed. First a brief overview of the facility design is given. Then the experimental and analytical techniques used to assess the pre-construction levels of vibration and to characterize the completed facility are introduced. Then the results of a vibration survey of the AMPEL building basement conducted prior to the design of the facility are presented. From this vibration survey, a specification for the required vibration isolation is developed. The design of the features of the facility relevant to vibration isolation are then presented including the foundation design, inertia block design, isolator selection and the design of the acoustic isolation vaults. The results of the experimental characterization of the facility are then given. Finally, the vibration levels in the LAIR facility are compared to similar facilities worldwide and to other locations on campus.

2.1 Facility overview

The LAIR facility consists of three acoustically and vibrationally isolated vaults or “pods”. Each pod contains a massive inertia block supported by pneumatic isolators on an “isolated” foundation which is connected to the foundation of the surrounding building only indirectly through the underlying earth. On top of each inertia block, a STM experiment is mounted on a second set of smaller pneumatic isolators. Surrounding the experiment and inertia block in each pod is a thick, double-walled acoustic enclosure. The inner walls of these enclosures are reinforced concrete anchored to the isolated foundations while the outer walls are concrete block anchored to the building foundation. Large volumes of acoustically absorptive material have been placed inside the vaults as well as between the inner and outer enclosures to damp the acoustic resonances of the hard concrete surfaces. Access to the pods is through two sets of acoustics doors (in the outer and inner acoustic walls) and suspended aluminum decks provide convenient operator access to the experiments without coupling the inertia blocks to the foundations. A graphical overview of the design of the facility and inertia blocks is shown in Figure 2.1. For simplicity, the double acoustic doors are not shown in this image.

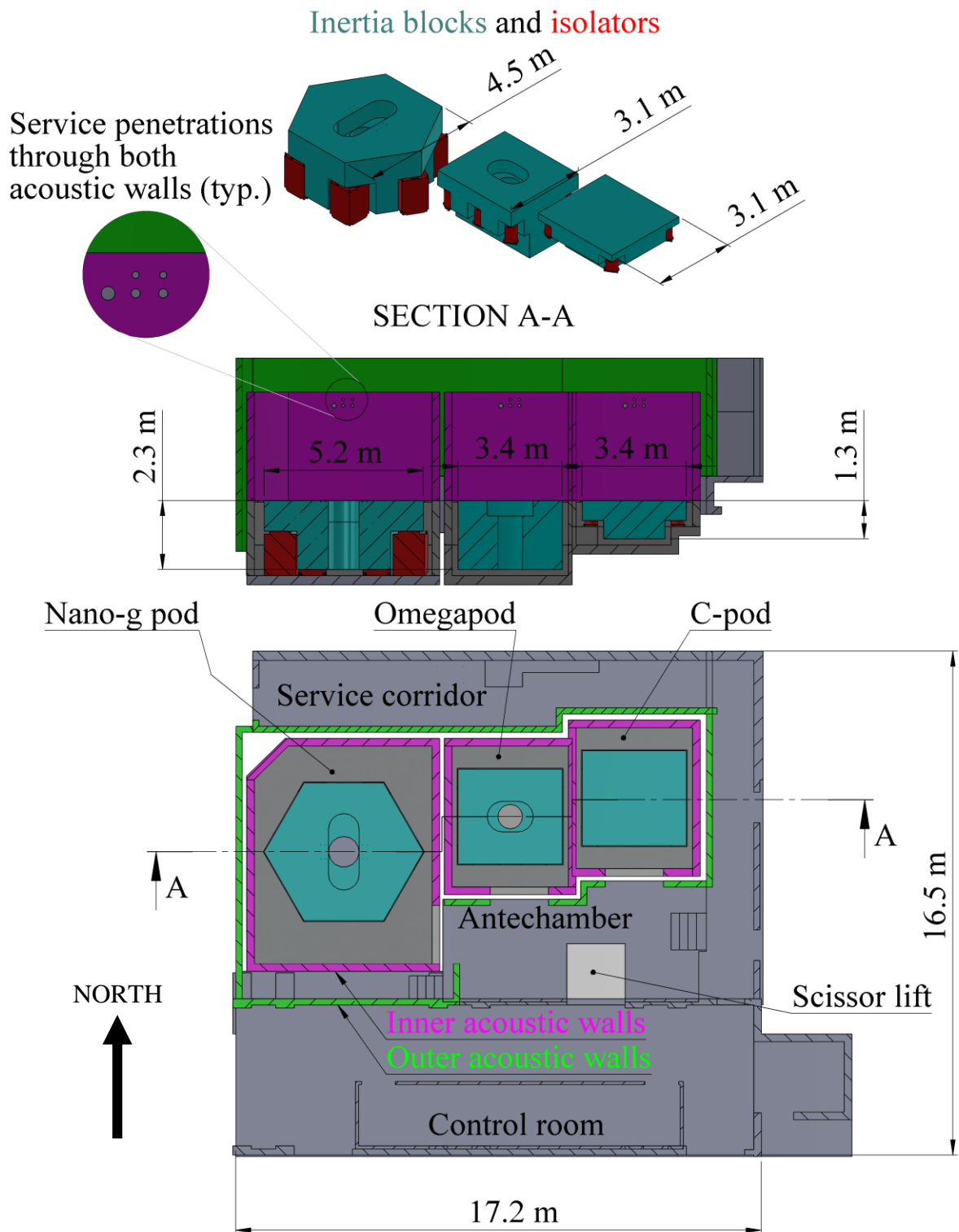


Figure 2.1: Simplified schematic of the LAIR facility and inertia blocks

2.2 Techniques

The following subsections introduce the techniques used to measure, analyze and simulate the mechanical and acoustic vibrations studied in this work.

2.2.1 Experimental techniques

The primary experimental techniques employed in the following studies were accelerometry (the measurement of accelerations) and microphony (the measurement of acoustic air pressure fluctuations). A brief technical background and details of the measurement equipment used are given in the following subsections. Due to the low-levels of mechanical and acoustic vibrations measured here, the discussion of sensor noise floors is emphasized. Details of the experimental set-ups for the various results presented in this chapter are presented as needed alongside the results.

2.2.1.1 Accelerometry

There are dozens of ways to measure the motion of an object. The most appropriate technique depends on the amplitude and bandwidth of the motion to be studied. In the context of ultra-low-vibration facilities and scanning tunneling microscopes, the frequency range of interest is from below the ~ 1 Hz timescale of the tunneling current signal in spectroscopic and topographic modes up to at least the bandwidth of the tunneling current amplifier - 1 KHz in the case of the FEMTO DLPCA-200 amplifier used here at a gain setting of 10^9 [4].

Within this band, the amplitude range of interest is from extreme broad-band ground vibrations of order $10^{-3} \text{ m/s}/\sqrt{\text{Hz}}$ caused by heavy excavation machinery operating

approximately 50m away to the quietest levels measured on well-isolated inertia blocks late at night of approximately $10^{-6} \text{ m/s}/\sqrt{\text{Hz}}$ at 1 Hz and dropping below $10^{-10} \text{ m/s}/\sqrt{\text{Hz}}$ at 1000 Hz. For measuring vibrations in this frequency/amplitude window, two types of instruments are commonly used: geophones and accelerometers. A conventional geophone uses a spring-suspended coil and magnet to induce a voltage on the coil proportional to the applied velocity while an accelerometer, depending on its type, will employ one of many possible mechanisms to measure the applied acceleration.

While geophones have been used to characterize both ultra-low-vibration facilities [19] and low-vibration dilution refrigerators [5], only piezoelectric accelerometers were used to measure mechanical vibrations in the present study and therefore only this type of vibration sensor will be discussed here. A detailed introduction to modern piezoelectric accelerometers and an analysis of their frequency response and noise characteristics can be found in [32].

Piezoelectric accelerometers exploit a property known as the direct piezoelectric effect - wherein a mechanically stressed material accumulates a surface charge – to measure the inertial force on a proof mass, which is proportional to the applied acceleration. A conceptual schematic of a compression-mode piezoelectric accelerometer is shown in Figure 2.2.

The fundamental limit on the low-frequency response of piezoelectric accelerometers is set by the filtering of the voltage produced by the piezo element (V_p in Figure 2.2) by the RC circuit formed by the element's capacitance (C_p) and its leakage resistance (R_p). The minimum low-corner cutoff frequency of the piezoelectric accelerometer response is thus:

$$f_c = \frac{1}{2\pi R_p C_p} \quad 2.1$$

In practice, however, this fundamental limit on the low-corner frequency is typically superseded by the low-corner frequency of the charge amplifier. For high performance piezoelectric accelerometers such as those used in this study, the low-frequency cutoffs are typically of order 10 mHz.

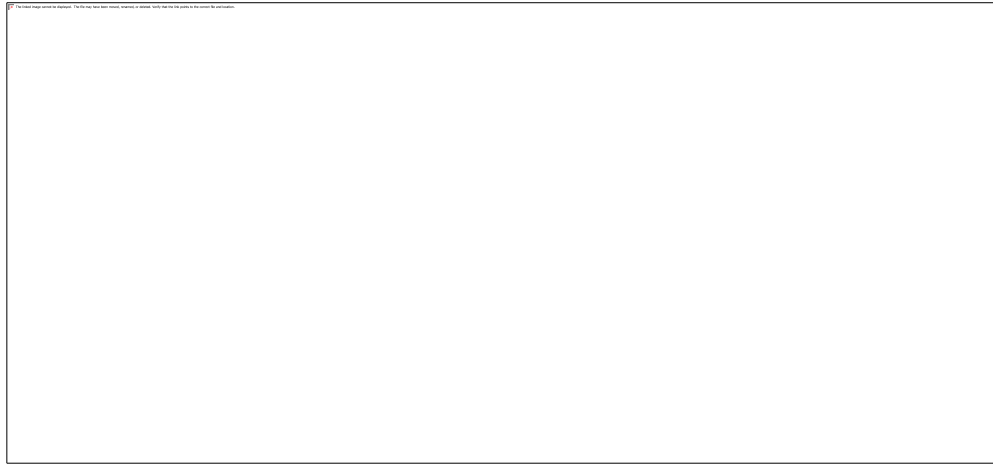


Figure 2.2: Conceptual schematic of a compression-mode piezoelectric accelerometer. A compression mechanism keeps the proof mass in contact with the piezoelectric element during both upwards and downwards accelerations. The electrical response of the piezoelectric element to the varying compressional stresses exerted upon it by the accelerating proof mass can be modelled as a voltage source V_p - which produces a voltage proportional to the strain – in series with the capacitance of the piezo element. The high-input-impedance charge amplifier outputs an AC voltage proportional to the amplitude of these motions.

The highest useful frequency of a piezoelectric accelerometer is set by the lowest mechanical resonance of the proof-mass/piezoelectric system. When the accelerometer is excited near or beyond this resonant frequency, the amplitude of motion of the proof mass is strongly frequency dependent and the accelerometer no longer exhibits the necessary characteristic of approximately frequency-independent acceleration sensitivity. Typical resonant frequencies for piezoelectric accelerometers range from several hundreds to several thousands of Hz, depending on the application for which the accelerometer was designed.

The working amplitude limits for a piezoelectric accelerometer are set from above by the saturation of the output voltage of the signal conditioning electronics and from below by the noise floor of the sensor. The fundamental lower limit to the noise floor of a piezoelectric accelerometer is set by the combined thermo-mechanical and Johnson noise of the piezoelectric element. In practice, only in state-of-the-art accelerometers are these intrinsic noise sources comparable to the electrical noise of the amplifier electronics [33]. The major implication of this is that $1/f$ noise from the input transistor of the charge amplifier stage dominates the piezo accelerometer's noise at low frequencies and limits the usefulness of these sensors for measuring low-amplitude vibration signals at low frequencies.

Two different types of piezoelectric accelerometer were used in the experimental work detailed here: a large, very sensitive, low-noise Wilcoxon 731A [34] and several smaller, lower performance PCB 393B04's [35]. The relevant properties of these accelerometers are summarized in Table 2.1.

Accelerometer	Sensitivity [$V/m/s^2$]	Maximum acceleration amplitude [m/s^2]	Noise floor [$m/s^2/\sqrt{Hz}$]	± 3 dB frequency limits [Hz]
PCB 393B04[35]	0.102	49	2.9e-6 @ 1 Hz 1e-6 @ 10 Hz 4e-7 @ 100 Hz 4e-7 @ 1000 Hz	.02 - 1700
Wilcoxon 731A[34]	102	4.9	2.9e-7 @ 2 Hz 9.8e-8 @ 10 Hz 3.9e-8 @ 100 Hz	0.05 - 450

Table 2.1 : Characteristics of the Wilcoxon 731A and PCB 393B04 piezoelectric accelerometers

For the low-level vibration measurements made here, it is important to compare the sensor noise floors to the measured signals. Figure 2.3 shows the noise floors of the two types of

accelerometers, as well as measurements made with these accelerometers on the same inertia block; this figure illustrates how features that can be clearly seen with the Wilcoxon 731A are hidden by the higher noise floor of the PCB 393B04. Additionally plotted is the electrical noise of the National Instruments PCI 4462 DAQ card used to acquire the signals from the accelerometers, referred to the input of the accelerometers [36].

This DAQ card was used to acquire the voltage signal from the 731A's P31 signal conditioner which was always set to 1000V/g gain and 450 Hz bandwidth. Additionally, the same DAQ card was used to provide a 4mA excitation current and to measure the returned voltage signal directly from the PCB accelerometers.

A major shortcoming of this experimental set up was that the PCI 4462 card has a 3Hz high-pass filter on its inputs, which attenuated the low frequency signals measured by approximately -11dB (a factor of 0.28) at 1Hz. This had the effect of dropping the amplitude of the low-frequency low-amplitude vibration signals from the PCB 393B04 accelerometers very close to the noise floor of the PCI 4462; this likely explains the poor coherence at low-frequencies of the many vibration transfer functions measured using the PCB 393B04 accelerometers.

The second shortcoming of the experimental set up was that no anti-aliasing filters were used for the PCB accelerometers (the P31 provides a filter for the Wilcoxon accelerometer). All accelerometer signals were sampled at 5 KHz unless otherwise noted. While the environmental vibration amplitudes above the 2.5 KHz Nyquist frequency are likely small enough to contribute negligible aliased signals to the 1-1000Hz band of interest, clusters of peaks evident around harmonics of 60 Hz in several of the reported measurements suggest aliasing of electrical noise.

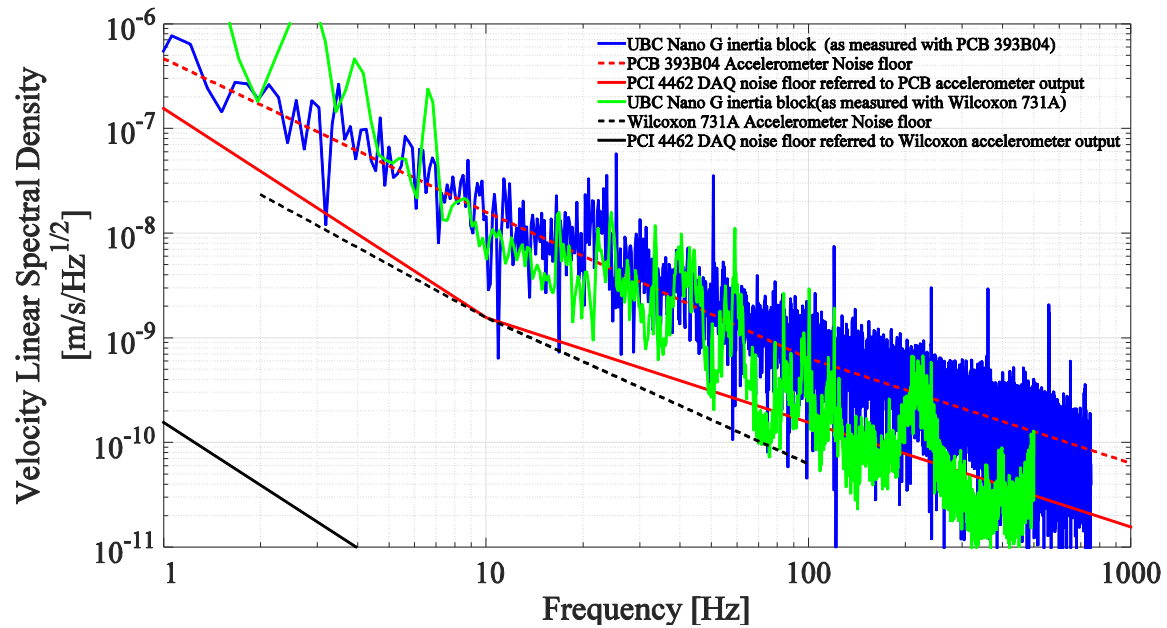


Figure 2.3: Accelerometry measurement noise floors, in velocity units.

A final relevant experimental detail is the method by which the accelerometers were mounted to the objects under study. A mounting method resulting in a low resonant frequency for the accelerometer/mount system will mechanically filter the vibrations detected by the accelerometer and artificially reduce the signal at frequencies beyond this resonance. Ideally, accelerometers should be rigidly bolted to the vibration surface in question. Unfortunately this is not always possible or convenient. In the present work, heavy, rigid accelerometer mounts were manufactured for both the PCB and Wilcoxon accelerometers and the frequency response of these was found to be satisfactory when these were simply placed on the surfaces under study. These mounts were employed when bolting was not possible; details of the accelerometer mounting for each particular experiment are given in the following sections.

2.2.1.2 Microphony

The low frequencies and low amplitudes of the ambient acoustic signals of interest in this work are nearly outside the envelope accessible with readily available measurement equipment.

The acoustic measurements detailed here were made using Behringer ECM8000 omni-directional electret condenser microphones [37] powered by a Yorkville PGM8 mixer board [38] with the gain set to zero and with the output fed directly into the PCI-4462 by way of a ¼” phono to BNC adapter. The information provided by Behringer on the performance of the ECM8000 microphone is limited, however an independent calibration carried out by another company found a single unit of the ECM8000 to have a sensitivity of 11mV/Pa, -3 dB frequency response range of approximately 20Hz – 15KHz and an A-weighted noise floor of 32 dBA [39] . No experimental information about the narrow-band noise spectrum of these microphones appears to be available, and indeed very little information about the noise-spectra of electret microphones at the low frequencies of interest to this work is available in the literature. In [40], a Panasonic WM60A miniature electret condenser microphone similar to the ECM8000 was characterized between 650 and 30,000 Hz : the sensitivity was measured to be 18.5 mV/P at 250 Hz and the noise floor was found to be approximately described by the equation

$$\sqrt{J(f)} = \sqrt{b_0 + \frac{b_1}{f} + \frac{b_2}{f^2}} \quad 2.2$$

where the coefficients were $b_0 = 3.5 \pm 0.2 \times 10^{-11}$, $b_1 = 1.1 \pm 0.1 \times 10^{-7}$ and $b_2 = 9.7 \pm 8.5 \times 10^{-6}$. The important $1/f$ and $1/f^2$ terms are attributed to random mechanical motion of the microphone diaphragm and shot noise in the gate of preamplifier FET, respectively. This function is plotted in Figure 2.4 down to 10 Hz. Although this curve is an extrapolation from measured data, the shape of an apparent background of the ambient acoustic spectrum measured

in one of the very quiet acoustic vaults in the LAIR facility with the ECM8000 is similar in magnitude and shape. This suggests that electret microphone noise floors do follow equation 2.2 for frequencies below 650 Hz. Fitting a function of the form of equation 2.2 to the apparent background results yielded the noise parameters for the ECM 8000 microphone in Table 2.2.

Parameter	$b_0 [Pa^2/\sqrt{Hz}]$	$b_1 [Pa^2]$	$b_2 [Pa^2 \cdot Hz]$
Value (95 % confidence bounds)	7.9e-12 (no confidence bounds returned from fit – fixed at bound)	3.5e-08 (1.8e-08, 5.2e-08)	1.2e-05 (7.4e-06, 1.6e-05)

Table 2.2: Measured noise parameters for the ECM8000 microphone

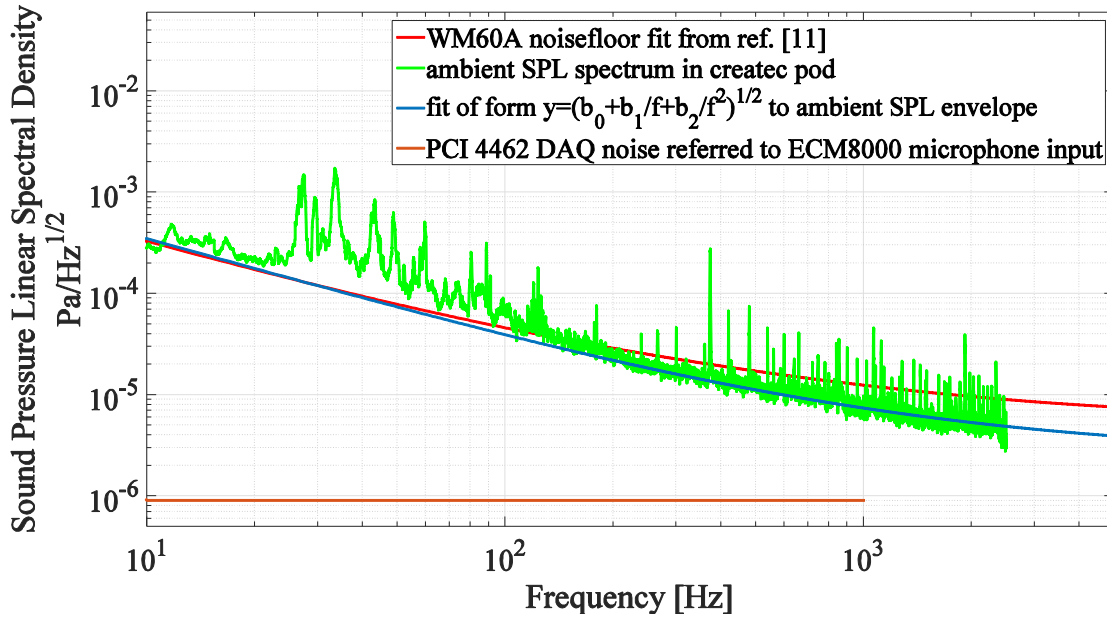


Figure 2.4: Theoretical noise floor curve for the WM60A microphone compared to a very quiet ambient noise spectrum measured with the ECM8000 microphone. A 0.5 Hz wide moving average filter has been applied to this SPL measurement in the frequency domain. A fit of equation 2.2 to the apparent background of this smooth SPL curve and the PCI-4462 DAQ noise as referred to the input of the microphone are also shown.

Electronic noise is also present in the acoustic measurements carried out here. Primarily this is observed in the form of narrow band pickup noise peaks at 60 Hz and its harmonics

present in the low-level acoustic measurements. Although the PGM8 mixer board and the PCI 4462 DAQ card must contribute additional electronic noise, the preceding analysis suggests that this electronic noise is negligible relative to the ECM8000 microphone's intrinsic noise.

2.2.2 Analytical techniques

Two common types of mathematical tools have been employed in the present work: *spectral analysis* for characterizing broad-band vibration signals and *finite element analysis* for modelling the vibrations of mechanical and acoustic resonators.

2.2.2.1 Spectral analysis

Consider the first two seconds of a 30-s long segment of vibration data acquired simultaneously on the Omegapod inertia block and foundation as shown in Figure 2.5. Looking at the number of peaks in one second of either curve shows a vibration with a frequency of roughly 20 Hz. The motion of the block at this frequency also appears roughly out of phase with the motion of the foundation but it is difficult to tell for sure. The block is also clearly undergoing some motion at a frequency of order 1 Hz but the exact frequency of this motion is difficult to estimate by inspection. The blurring of both curves suggests that high-frequency vibrations are present and when the same data is examined at a shorter time scale - as seen in Figure 2.6 - higher frequency oscillations are indeed evident. Clearly this time-series contains information about a number of vibrations which are taking place. Accurately quantifying the frequencies, amplitudes and phase relations of these vibrations, however, is much better accomplished using the tools of spectral analysis rather than by direct inspection of the time-series.

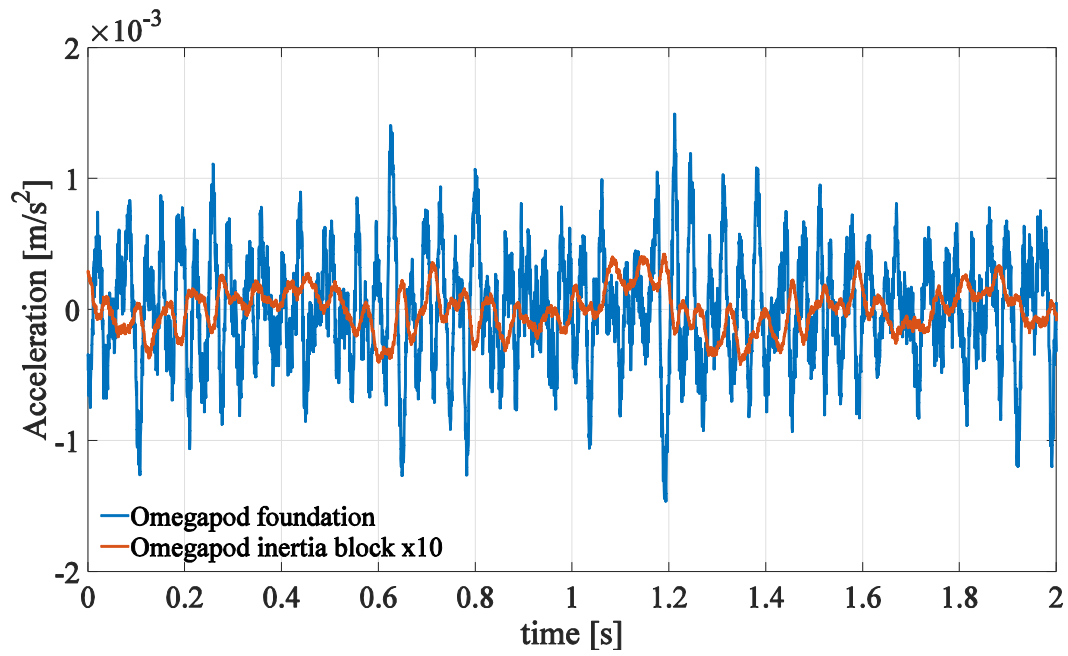


Figure 2.5: Example time-series data for the Omegapod block and foundation. The inertia block curve has been multiplied by ten to make both curves legible on the same scale.

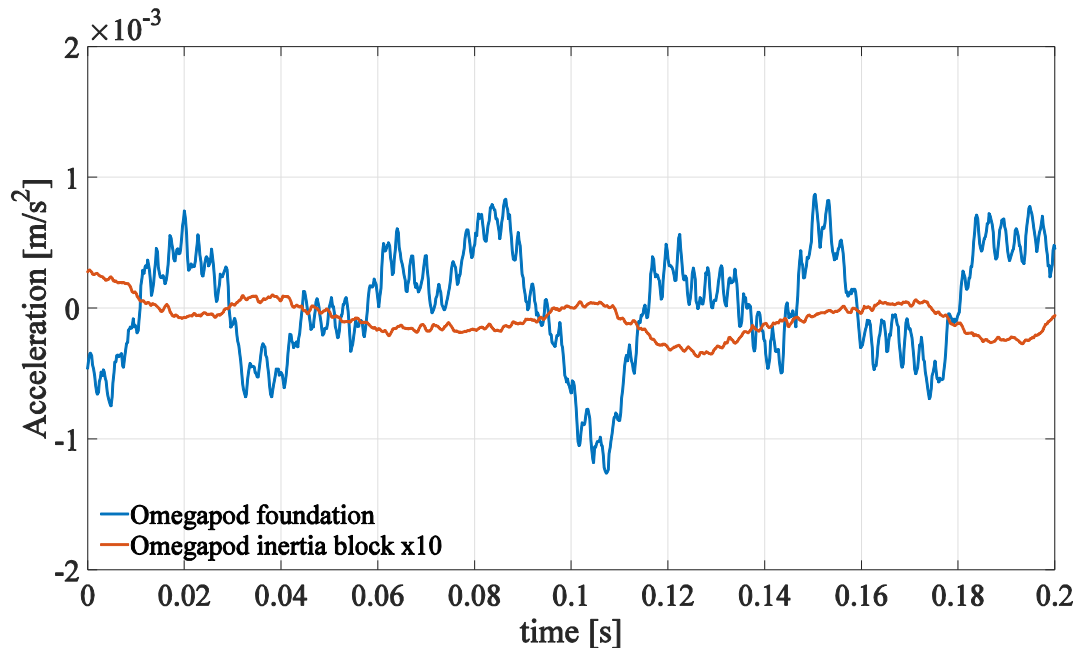


Figure 2.6: Example time-series data for Omegapod shown with finer time resolution.

The power spectral density (PSD) of a discrete wide-sense stationary⁴ random process $x(n)$ can be defined as the Fourier transform of the autocorrelation sequence [41] .

$$PSD(f) = \sum_{k=-\infty}^{\infty} \left[\lim_{N \rightarrow \infty} \frac{1}{2N+1} \sum_{n=-N}^N x(n+k)x^*(n) \right] e^{-2\pi f k i} \quad 2.3$$

The PSD describes the distribution of the power of the signal as a function of frequency. A closely related quantity is the linear spectral density (LSD), denoted here by (f) :

$$X(f) = \sqrt{PSD(f)} \quad 2.4$$

The PSD and LSD have a convenient physical interpretation in terms of the RMS value of a signal in a given frequency band [42]:

$$X_{RMS} = \sqrt{\left[\int_{f_1}^{f_2} PSD(f) df \right]} = \sqrt{\left[\int_{f_1}^{f_2} X^2(f) df \right]} \quad 2.5$$

Moreover, for a linear time-invariant system described by a transfer function $H(f)$, and excited by an input $X(f)$, the system response $Y(f)$ is given by:

$$Y(f) = |H(f)|X(f) \quad 2.6$$

This convenient relation is the principal reason why the LSD is used over the PSD throughout this thesis.

In practice, only finite segments of data sampled at finite sampling rates are available, and the true linear spectral density can only be estimated. Following the excellent practical

⁴ Discrete wide-sense stationary random processes have a mean and autocovariance sequence which are independent of the time at which they are computed

introduction given in [42], the linear spectral densities of vibration signals are estimated throughout this thesis by:

$$X(f) \approx X_{rp}(f) = \sqrt{\frac{2}{N}} \left| \sum_{n=1}^N x(n) e^{-\frac{2\pi i}{N} \cdot (f-1) \cdot (n-1)} \right| \quad 2.7$$

where $X(f)$ is the true LSD, $X_{rp}(f)$ is the estimated LSD, N is the number of samples in the time-series, $x(n)$ is the n^{th} sample and i is the imaginary number. This basic estimate, with no window function applied to the time-series data, is known as an unmodified or raw periodogram – hence the subscript rp . While easy to implement, this estimate suffers from at least two shortcomings.

The first of these shortcomings is that when the linear spectral density of a finite time-series is computed, some degree of spectral leakage of the signals from narrow peaks into adjacent frequency bins occurs. The distribution of this leakage into the adjacent bins depends on the type of window-function applied to deal with the discontinuity of the data at the ends of the finite data segment. The use of no window – also called a rectangular window - causes substantial leakage into far away bins. This can result in leakage from large peaks obscuring small spectral features nearby. Much of the data in this thesis is acquired in 30-s long time series; these provide a high frequency resolution - 33 mHz – that partially mitigates the loss of frequency resolution due to the lack of windowing (no windowing of time-series data was performed for any the analysis I performed during this thesis). To prevent spectral leakage from spurious low-frequency signals such as $1/f$ noise and DC offsets, the linear trend of every time-series analyzed was removed prior to the estimation of the spectral density. The MATLAB implementation of equation 2.7 used on the data in this thesis is given in appendix Appendix B

The second and more important shortcoming is that the raw periodogram is a poor estimator of the true linear spectral density. In Figure 2.7, a raw periodogram computed according to equation 2.3 is shown. This periodogram is calculated from the 30-s time-series data partially shown in Figure 2.5 and presents some immediately useful information: the low frequency motion of the block appears to be driven by four large peaks below 5 Hz and there are at least two definite frequency peaks between 10 and 20 Hz. Overall, however, the raw periodogram is very noisy and, like the time-series, somewhat difficult to read. The reason for this is that although the expected value of the raw periodogram does converge to the true value of the LSD as the number of samples grows large, the variance of the estimate does not converge to zero but rather to a finite value [41]:

$$\text{Var}[X_{rp}(f)] \approx X^2(f) \quad 2.8$$

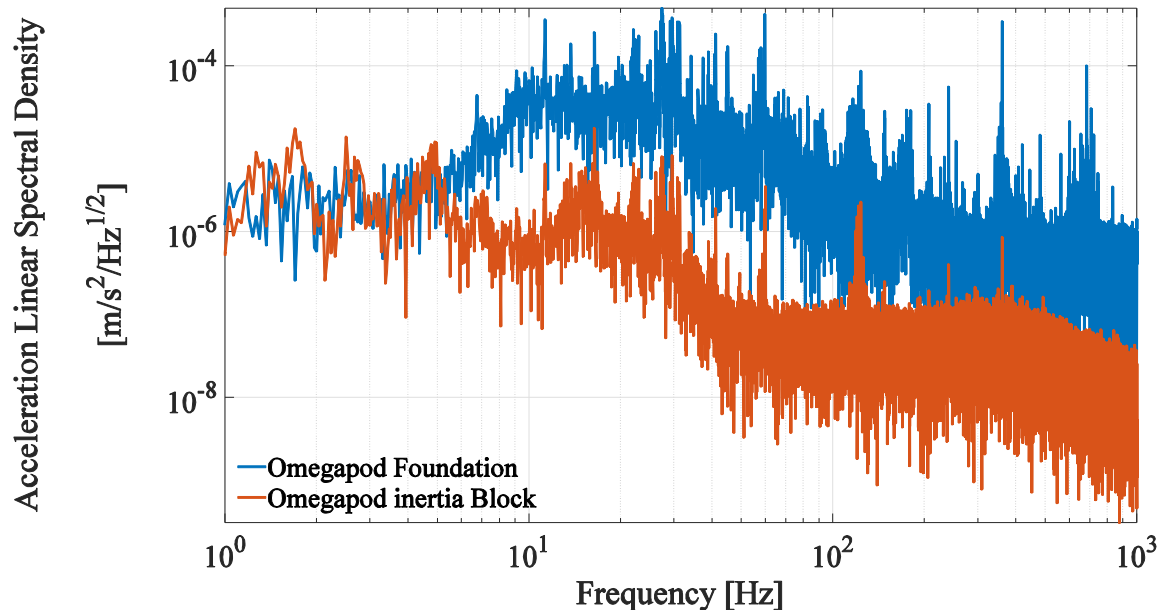


Figure 2.7: Raw periodogram of the Omegapod foundation and inertia block time series data shown in Figure 2.5

There are several methods to decrease the variance of the estimated linear spectral density below the variance of the raw periodogram. The simplest - Bartlett's method – reduces the variance of the estimate by averaging many independent raw periodograms:

$$Var[X_{Bartlett}(f)] = \frac{1}{N_{averages}} Var[X_{rp}(f)] = \frac{X^2(f)}{N_{averages}} \quad 2.9$$

An example of the improvement to the raw periodogram that can be accomplished with Bartlett's method can be seen in Figure 2.8.

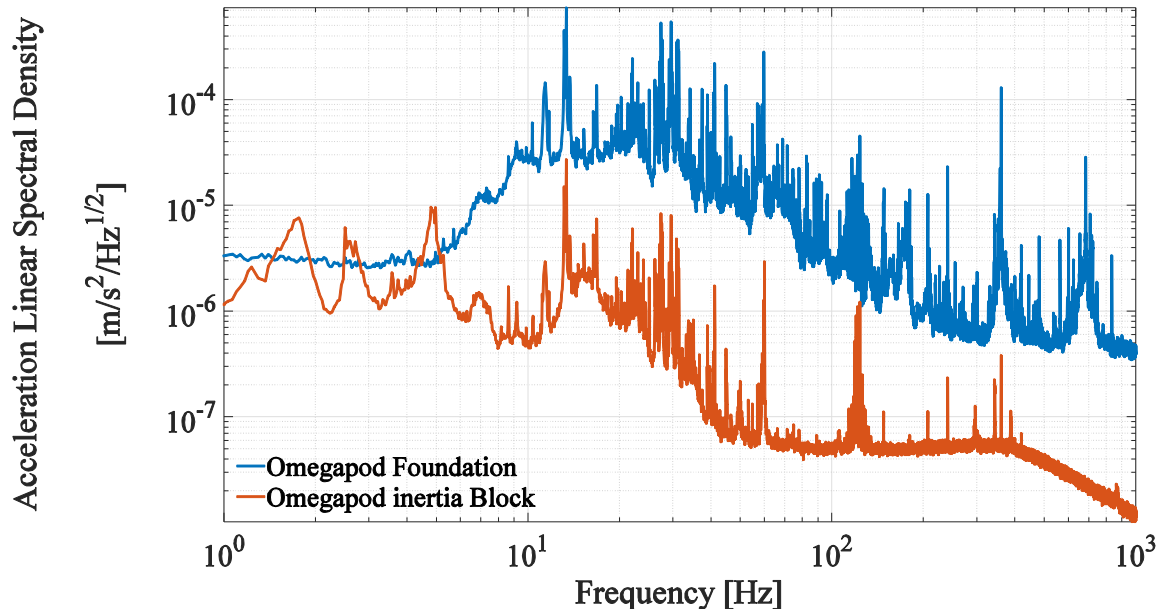


Figure 2.8 : Average of 100 raw periodograms taken on the Omegapod foundation and inertia block.

Several other methods of increasing complexity such as Welch's method or frequency-domain smoothing can also be used to reduce the variance of an estimated LSD and produce more legible plots. An example of the effect of a 0.5 Hz wide simple moving average filter on a raw periodogram is shown in Figure 2.9. This smoothing technique is used occasionally in this thesis to improve the legibility of short data sets when multiple runs were not taken for averaging purposes. Although the analysis of the reduction in variance is due to smoothing, intuitively, the

variance should go inversely with the number of bins spanned by the moving-average. The loss of frequency resolution inherent in this technique should be on the order of the frequency-width of the moving average.

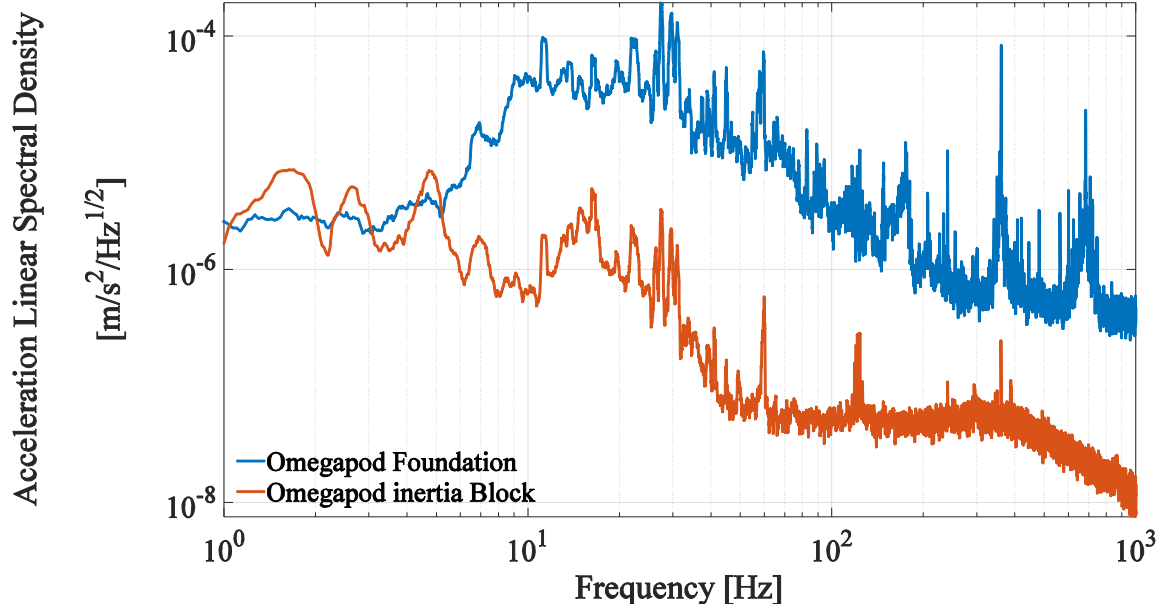


Figure 2.9 : The raw periodogram from Figure 2.7 after smoothing with a 0.5 Hz wide moving average.

Two tools related to spectral analysis which are helpful in understanding simultaneously acquired vibration signals are the empirical transfer function and the coherence. The empirical transfer function is calculated by measuring the input and output of a device and inverting equation 2.6 to yield:

$$H_{empirical}(f) = \frac{Y(f)}{X(f)} \quad 2.10$$

This function is particularly useful in characterizing the performance of isolation stages and other vibrating objects because it shows at what output frequencies the input is amplified or attenuated and by how much.

The coherence is a function of frequency which ranges between zero and one and indicates at which frequencies two time-series have constant phase and amplitude ratios. A high coherence between two time-series at a given frequency suggests that the components of both signals at that frequency are linearly related. The coherences reported in this thesis were calculated using the MATLAB function `mscohere`. This function computes the coherence $C_{xy}(f)$ between two time series $x(t)$ and $y(t)$ as

$$C_{xy}(f) = \frac{CSD_{xy}(f)}{PSD_x(f) \cdot PSD_y(f)} \quad 2.11$$

where $PSD_{x,y}$ are the power spectral density of the two time series and $CSD_{xy}(f)$ is the cross power spectral density :

$$CSD_{xy}(f) = \sum_{k=-\infty}^{\infty} \left[\frac{1}{2N+1} \sum_{n=-N}^N x(n+k)y^*(n) \right] e^{-2\pi f k i} \quad 2.12$$

The empirical transfer function and the coherence between acceleration signals acquired simultaneously on the Omegapod inertia block and on the underlying foundation are shown in Figure 2.10.

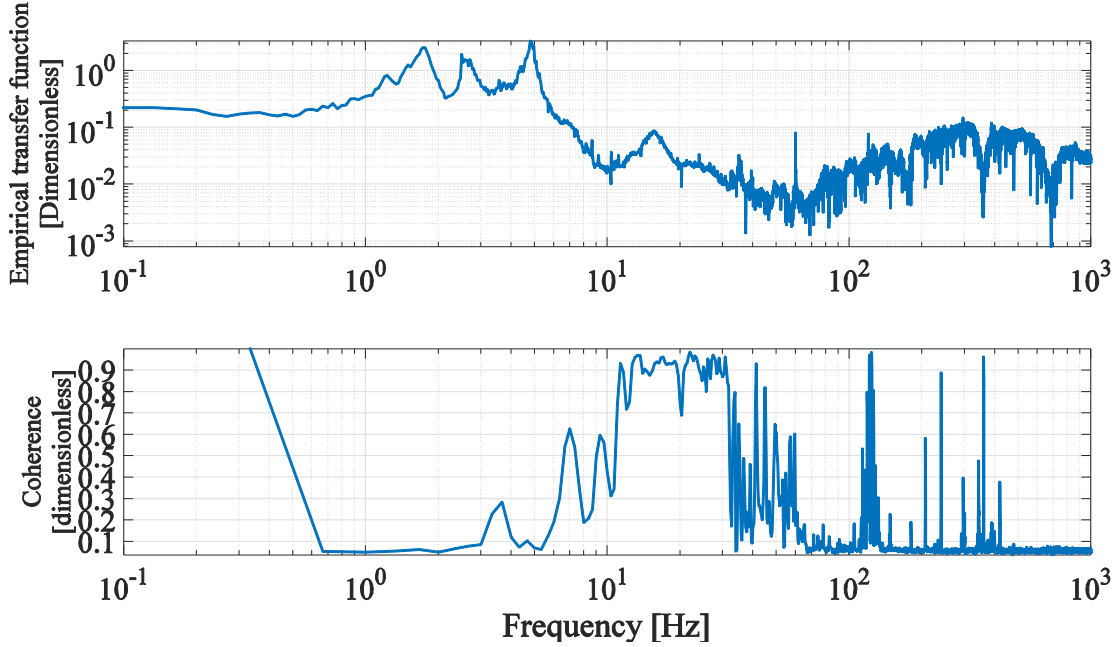


Figure 2.10: Empirical transfer function and coherence between the omegapod inertia block and the underlying foundation. Each curve is the average of 100 consecutive 30-s data segments.

2.2.2.2 Finite element simulations

The finite element method (FEM) is a powerful computational tool for approximately solving many kinds of differential equations when the geometry of the problem is too complicated for analytical approaches to be successful. An introduction to the finite element method for the study of mechanical vibrations can be found in [43]. The core idea underlying this method is the division of a complex geometry for which an analytical solution may not exist into an aggregation of simple objects such as beams, plates or cubes for which analytical solutions do exist. The application of continuity and boundary conditions to this aggregate structure (known as a mesh) results in a system of readily-solvable linear equations, the solutions of which approximate solutions to the original problem.

In this work, the COMSOL finite-element software package [44] was used to calculate the resonant frequencies and mode shapes of solid objects (microscope heads, experiment

structures, inertia blocks and building foundations) as well the frequencies and pressure distributions of the low-frequency acoustic modes of the acoustic isolation vaults containing the inertia blocks.

2.3 Facility site survey

In this section, the results of vibration and acoustic measurements made in the AMPEL basement prior to the construction of the LAIR are presented. In section 2.4, some of these results are used to generate a specification for the level of vibration isolation required from the LAIR vibration isolation systems.

A simplified plan view of the AMPEL basement prior to the renovation is shown in Figure 2.11. Vibration and acoustic noise measurements were made at three locations, marked A, B and C.

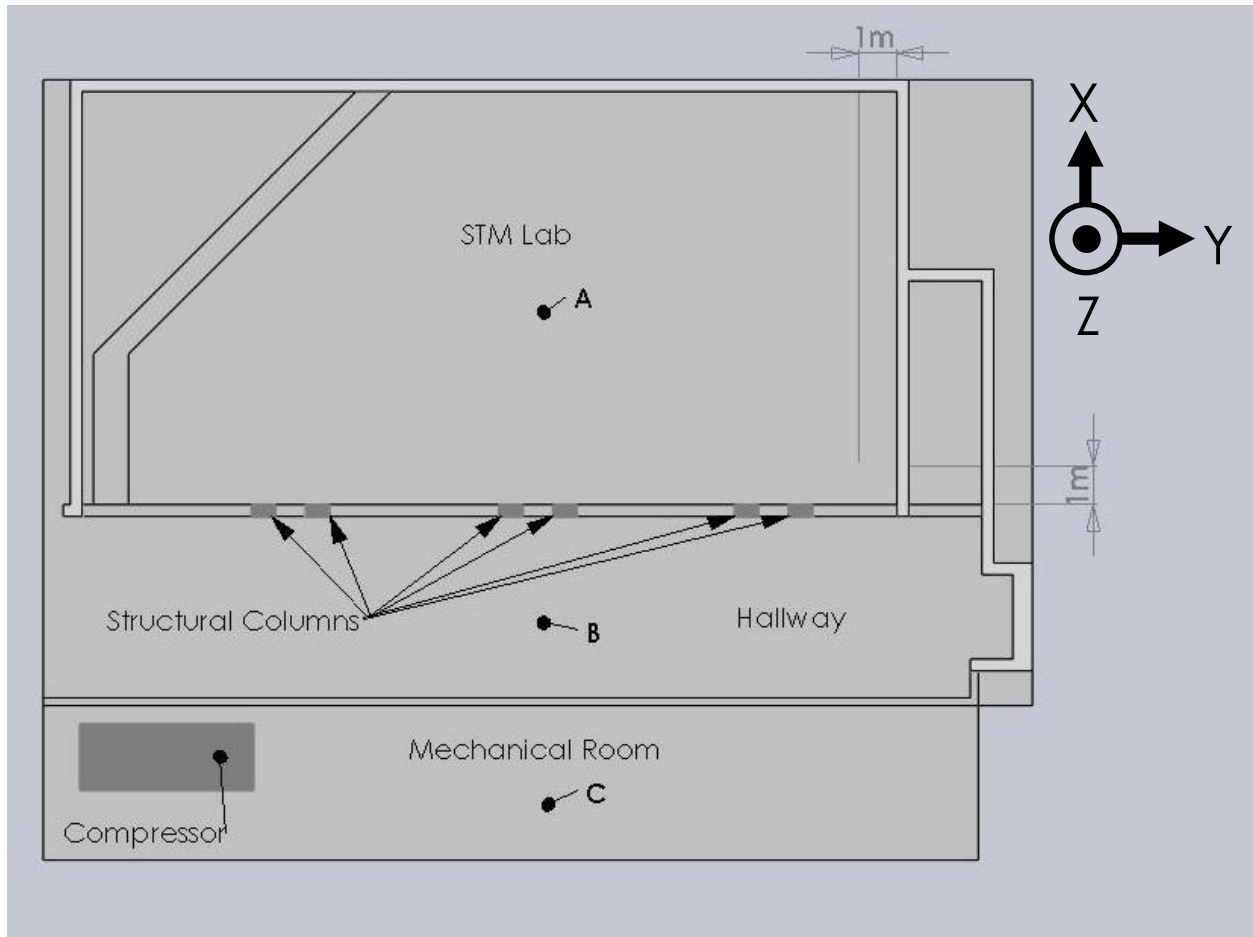


Figure 2.11: Simplified plan view of the AMPEL basement prior to the construction of the LAIR facility.

Acceleration measurements were made simultaneously in the X,Y and Z directions denoted in Figure 2.11 with three PCB 393B04 accelerometers mounted orthogonally via 10-32 threaded studs to an approximately 2" x 2" x 1" steel block. The steel block had three nuts epoxied in a triangular pattern to its base to allow it to rest on a flat surface without wobbling. This tri-axial accelerometer setup was placed on the concrete building floor at each of the three measurement locations with no additional attachment mechanism. As only one 30-s long, 1500 Hz vibration measurement was made at each location, smoothing of the resulting velocity spectra was accomplished by the application of a 0.25 Hz wide moving average filter rather than through

the use of Bartlett's method. The X, Y and Z direction floor velocities are compared between locations in Figure 2.12, Figure 2.13 and Figure 2.14. Although the short measurement times used make this set of measurements vulnerable to the conflation of transient vibration events with the true stationary background, the much higher levels of vibration measured in the mechanical room are likely not a coincidence.

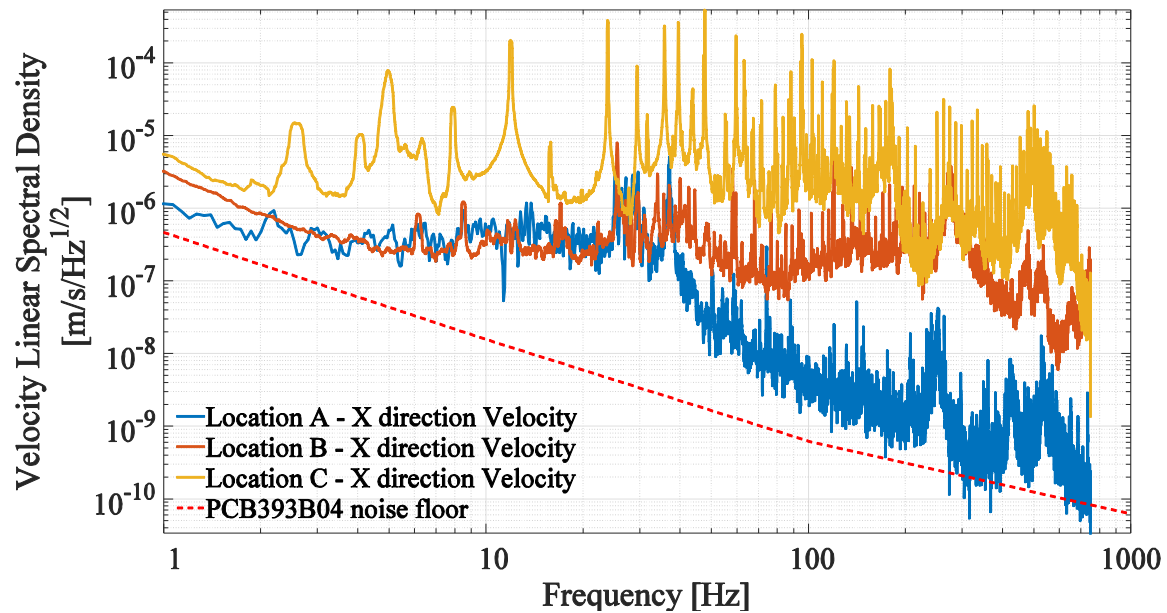


Figure 2.12 : X-direction floor velocity spectra in the AMPEL basement prior to construction of the LAIR

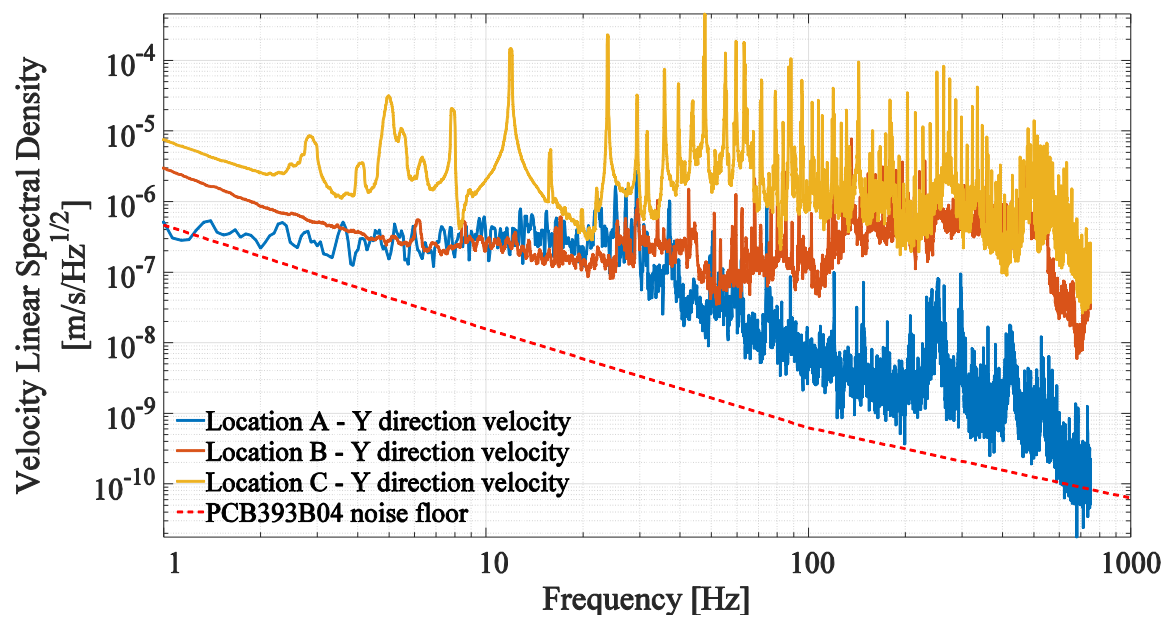


Figure 2.13: Y-direction floor velocity spectra in the AMPEL basement prior to construction of the LAIR

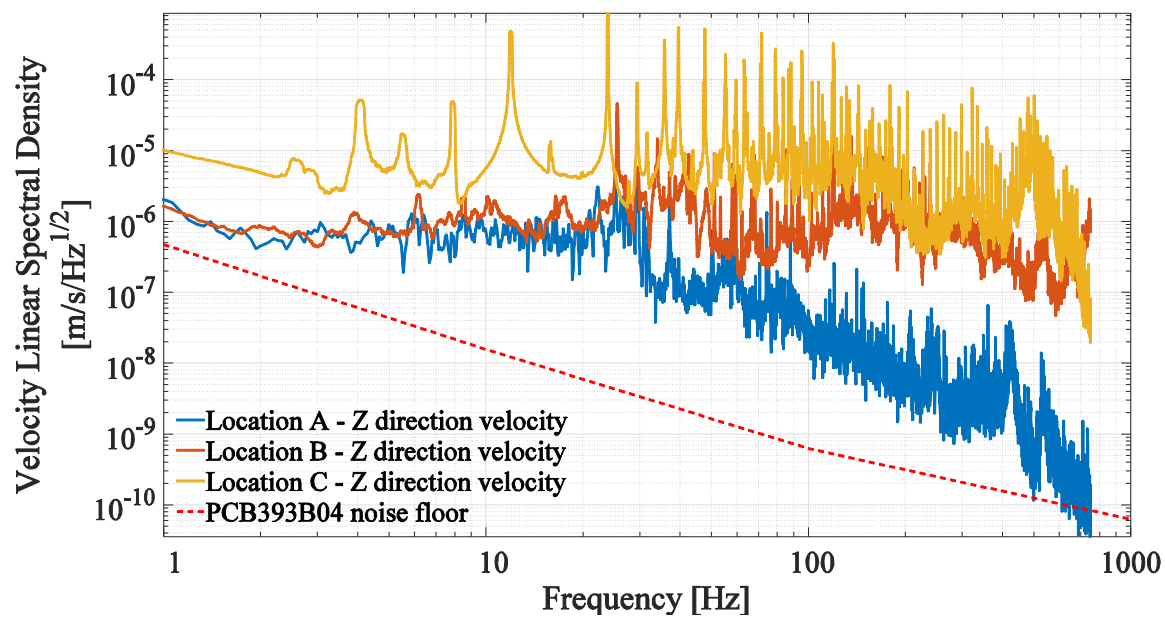


Figure 2.14: Z-direction floor velocity spectra in the AMPEL basement prior to construction of the LAIR

The data set shown in Figure 2.15 – although similarly flawed due to the data acquisition being performed asynchronously - also suggests increased levels of vibration in the mechanical room. Some amount of vibration may also be conducted into the floor from the structural column supporting the four-story laboratory building above the basement. This data set was acquired by moving a single accelerometer on the same steel mount to points on a grid and calculating the RMS acceleration over 5 seconds. As there were fewer large signals in the north-west corner of the basement, only some of the grid points were measured in this region; the remaining grid point values were interpolated.

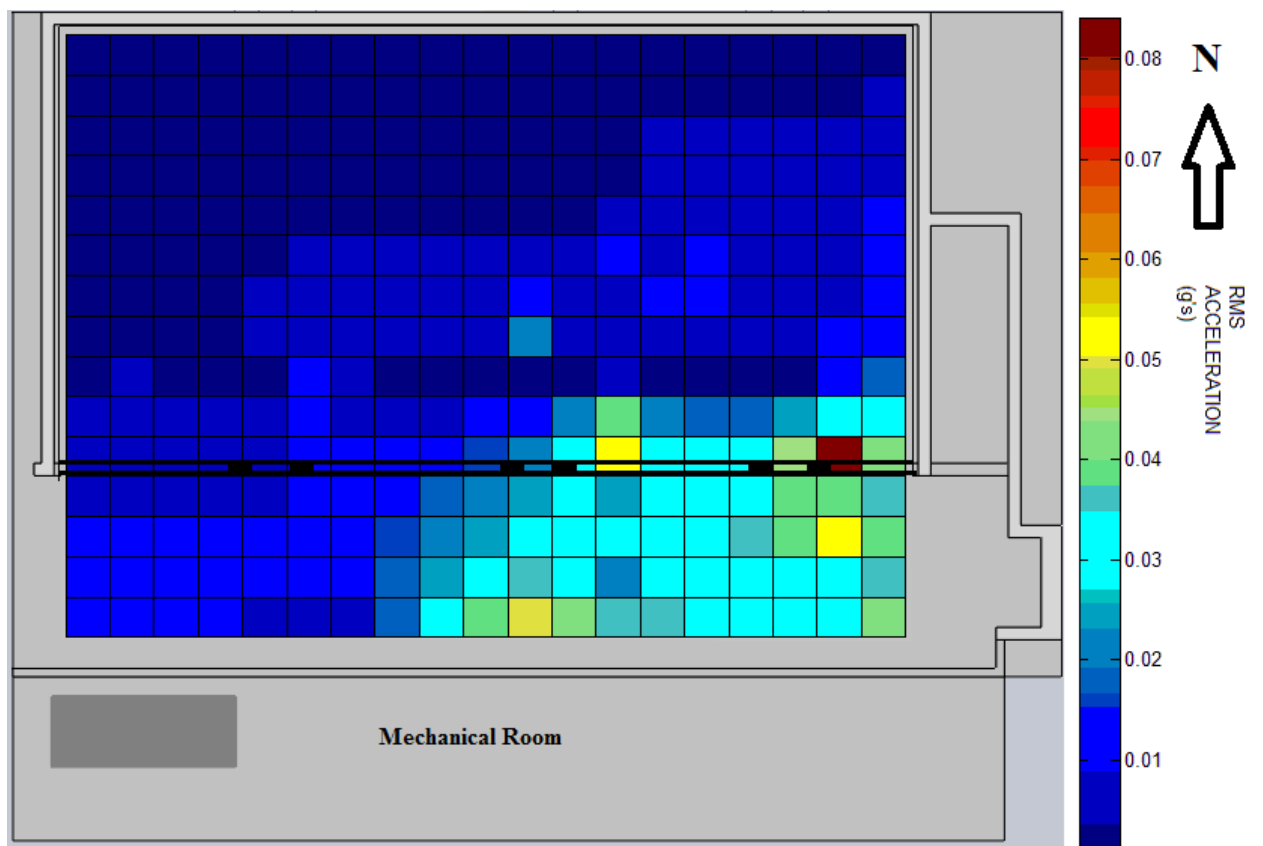


Figure 2.15: Asynchronously acquired RMS Z-direction acceleration map of the AMPEL basement prior to construction of the LAIR

As it was established prior to the beginning of detailed design of the LAIR that the low-vibration vaults would be built in the main unfinished room of the basement (location A and surroundings as indicated in Figure 2.11) the vibration levels measured at that location A were used in the development of the vibration isolation specification for the facility detailed in the next section. Figure 2.16 compares the velocity spectra in all three directions at location A. Because the Z-direction is thought to be the principle direction in which STM heads are sensitive to vibrational perturbations, because the Z-vibrations measured at location A were the largest of all three directions and for simplicity, the Z-velocity spectrum from location A was used exclusively in the development of the facility vibration isolation specification.

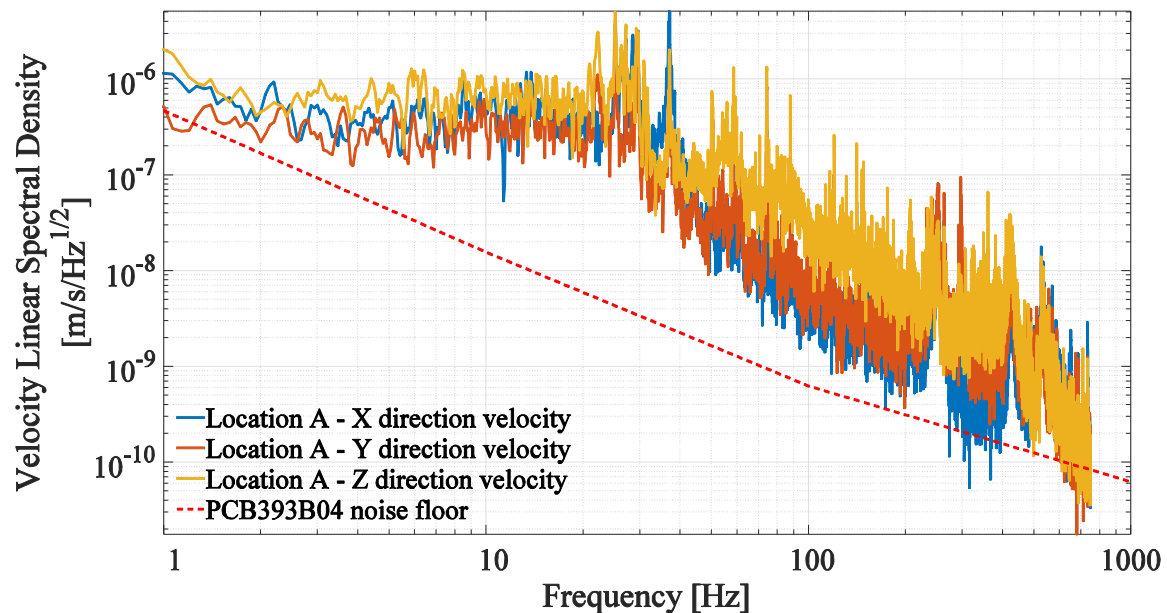


Figure 2.16 : Tri-axial velocity floor velocity spectra measured in the center of the AMPEL basement prior to construction of the LAIR.

The pre-construction acoustic measurements were made with an APEX220 microphone [45] powered by a EURORACK MX602 mixer board [46] set to zero gain. The APEX220 microphone has a specified sensitivity of $-63 \text{ dB} \pm 3\text{dB}$ relative to 1V/microbar (0.71mV/Pa) and a specified bandwidth of 20Hz to 20 KHz. This acoustic measurement set up is very similar to the Behringer/York setup detailed in the Techniques section and was used for this one set of measurements only. One 10-s measurement sampled at 100 KHz was made at each location; the results of these measurements are shown in Figure 2.17. Although the short sampling time again makes these results unreliable, the higher level of noise in the mechanical room and the comparable levels of noise in the other parts of the basement suggest these measurements are at least a plausible snapshot of the acoustic conditions in the AMPEL basement.

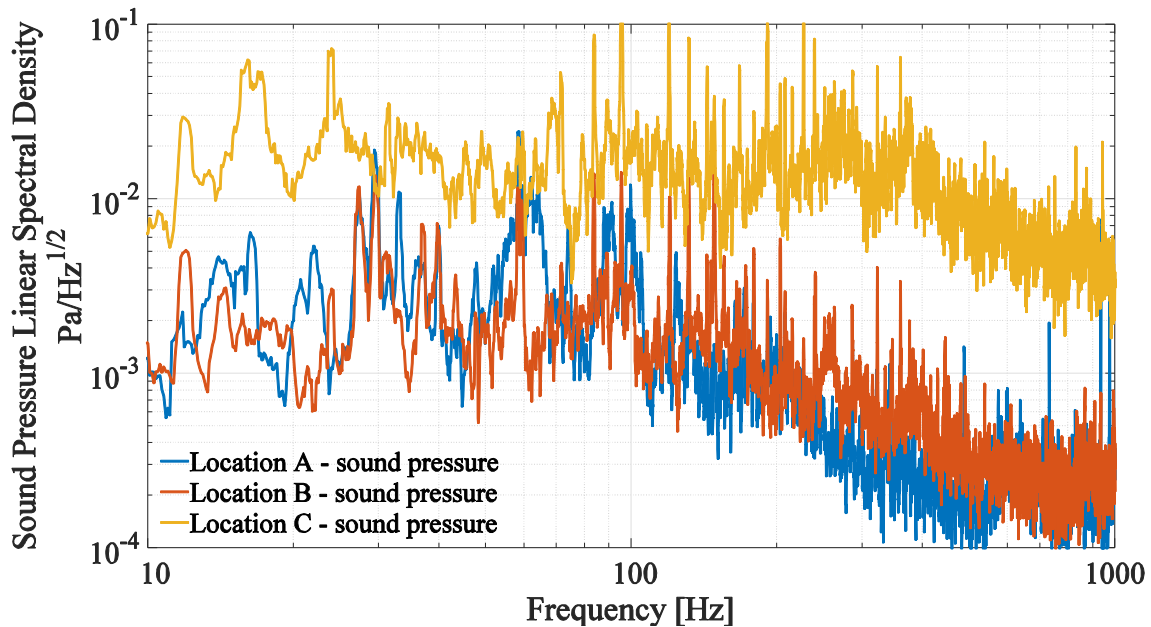


Figure 2.17 : Sound pressure spectra measured in the AMPEL basement prior to construction of the LAIR

It is important to recognize how heavily weighted to low frequencies the ambient sound and vibration are. Figure 2.18 shows the vibration and sound spectra measured at point A alongside running normalized integrals of the spectra. This plot shows that essentially all the measured ambient vibration velocity and approximately 80% of the sound pressure is in the first 100 Hz of the spectrum. This puts a large emphasis on the need to design an isolation system which is effective beginning at very low frequencies.

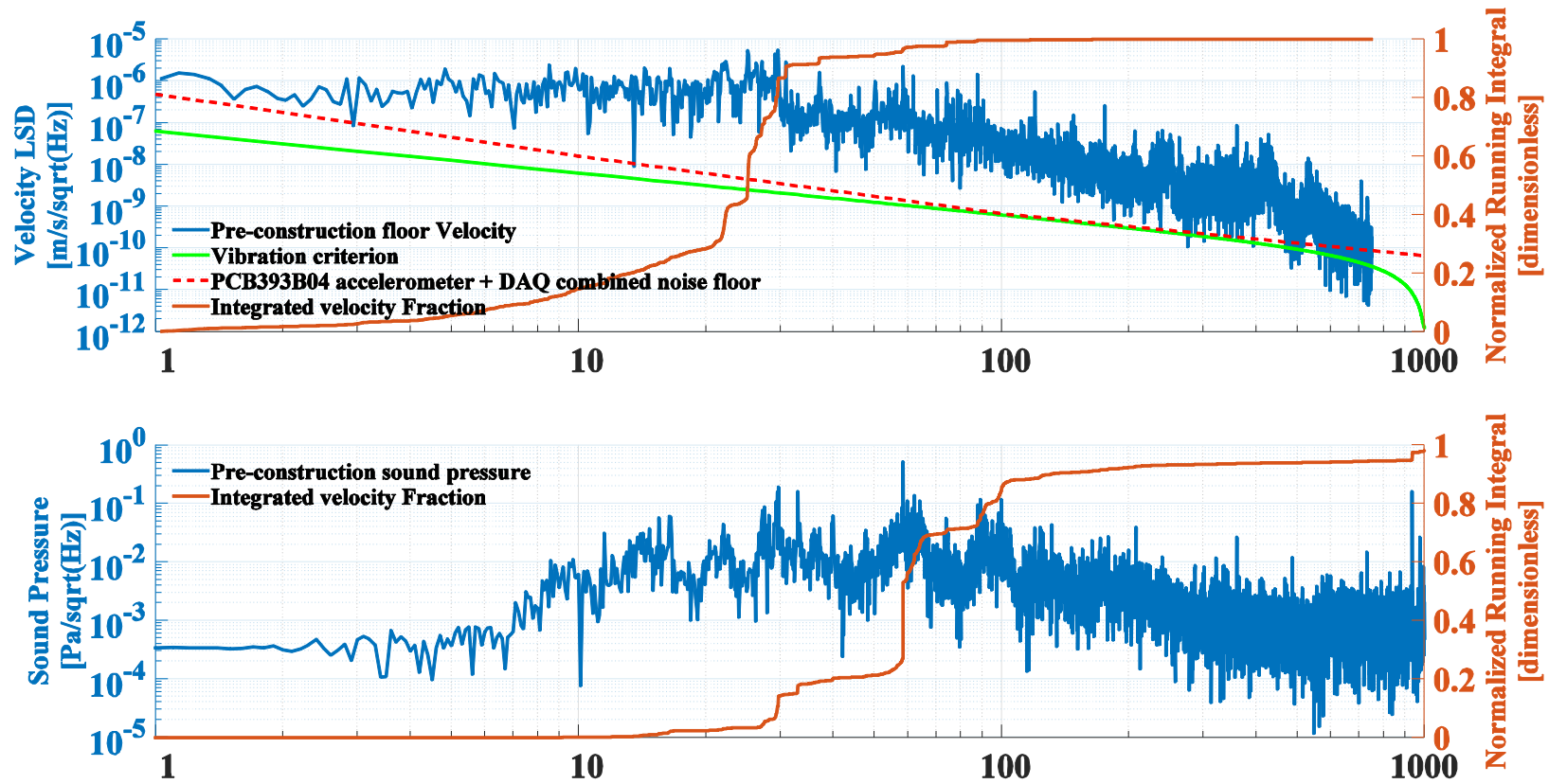


Figure 2.18 : Running integrals of the seismic and acoustic spectra measured at point A prior to construction of the LAIR facility showing the weighting of the environmental vibrational energy predominantly to frequencies below 100 Hz.

2.4 Vibration isolation specification

In section 1.2.2. , $10fm/\sqrt{Hz}$ between 1 and 1000 Hz was established as a reasonable criterion for allowable variations in the width of the tunnel junction in a high-performance Scanning Tunneling Microscope. Following the approach employed in [23], this section uses this $10fm/\sqrt{Hz}$ motion budget and a simple model of an STM head as a damped 1-degree-of-freedom simple harmonic oscillator to derive a criterion for the allowable level of input vibration to the STM head. Based on vibration levels measured in the AMPEL basement prior to the construction of the LAIR facility, a specification for the vibration isolation needed to achieve this allowable level of input vibration is produced.

Following the modelling of a generic nanotechnology tool carried out in [23], a STM head can be modelled as a tip part of mass m coupled mechanically to a sample part by a spring of stiffness k and a dashpot with linear viscous damping coefficient b as shown in Figure 2.19 . The sample part is considered to be attached rigidly to the experiment base.

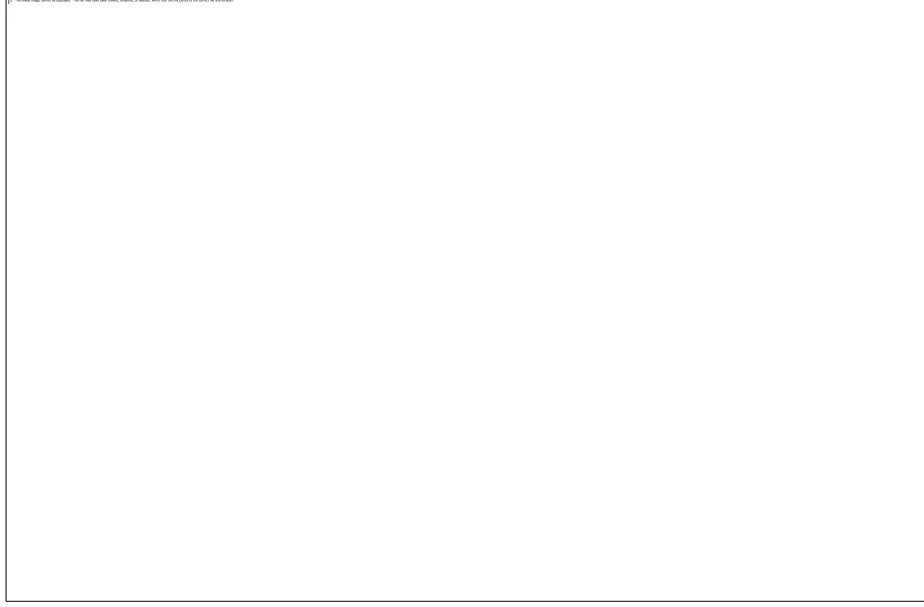


Figure 2.19 : 1 degree-of-freedom model of a Scanning Tunneling Microscope head

Based on the parameters of this spring-mass-damper system, the relative displacement between the tip and sample $z(t) = x_{tip}(t) - x_{base}(t)$ (i.e. the tunnel junction width) can be calculated as a function of the motion of the base. In particular, the transfer function between the base motion and the tunnel junction width variation $H_{relative}(\omega)$ can be calculated as follows:

$$m\ddot{x}_{tip} = b(\dot{x}_{base} - \dot{x}_{tip}) + k(x_{base} - x_{tip}) \quad (\text{force balance})$$

$$m\ddot{z} + b\dot{z} + kz = -m\ddot{x}_{base} \quad (\text{substitution})$$

$$H_{relative}(\omega) = \frac{Z(\omega)}{X_{base}(\omega)} = \frac{-m\omega^2}{-m\omega^2 + ib\omega + k} \quad (\text{Fourier transform})$$

This expression is more clearly cast in terms of the undamped natural frequency $\omega_0 = \sqrt{\frac{k}{m}}$ and

the damping ratio $\xi = \frac{b}{2m\omega_0}$:

$$H_{relative}(\omega) = \frac{\omega^2}{\omega^2 - \omega_0^2 + 2i\xi\omega_0\omega} \quad 2.13$$

The absolute value of this expression is:

$$|H_{relative}(\omega)| = \sqrt{\frac{\omega^4}{(\omega_0^2 - \omega^2)^2 + (2\xi\omega_0)^2}} \quad 2.14$$

With this transfer function the sensitivity of the tunnel junction to vibrational excitations of a STM head can be modelled with the choice of just two parameters: the resonant frequency ω_0 and the damping ratio ξ . These parameters were chosen to be 1000 Hz and 0.01 or 1% of critical damping. These parameters were chosen in an effort to represent a moderately rigid and weakly damped STM head. Equation 2.14 is plotted in Figure 2.20 with this choice of parameters. Three regimes of this transfer function can be identified: below 1 KHz the tip and sample move substantially together and the junction width is only weakly perturbed by the base excitations, the resonant amplification of the base excitations near 1 KHz, and the regime beyond 1 KHz where the tip ceases to move with the sample and the base excitations are transferred to the tunnel junction width directly.

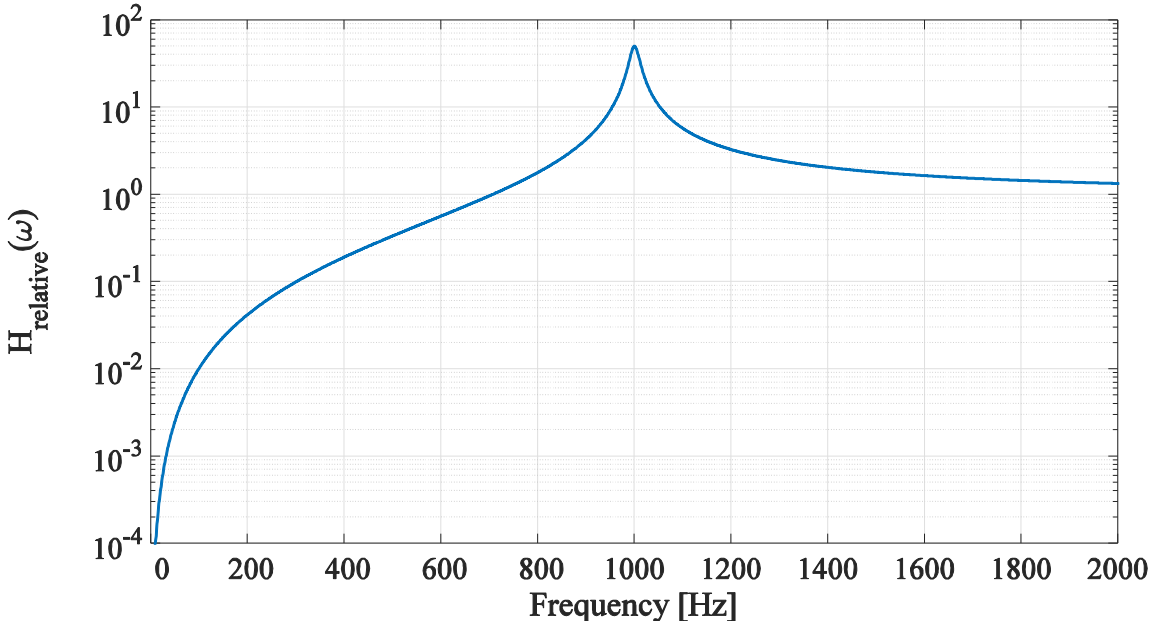


Figure 2.20 : Response of the tunnel junction tip/sample displacement to base displacements for a model STM head with a resonant frequency of 1000 Hz and a damping ratio of 1%. This function is also valid as the tip/sample velocity response to base velocities.

The justification for this choice of parameters deserves some discussion. FEA simulations suggest that 1 KHz is a very conservative underestimate for the fundamental resonant frequency of a compact Pan-style STM body built from macor [7] with a lead zirconate titanate scanner tube [8] such as the one detailed in chapter 3. On the other hand, available information suggests that the choice of 1% damping is likely an overestimate and therefore not conservative: reported Q factors for macor resonators range from 311 [47] to 5000 [48] while the EBL #4 lead zirconate titanate piezoelectric material used for the scanner tube in the STM described in the following chapter has a specified mechanical Q factor of 960 [49]. As $\xi = \frac{1}{2Q}$, these Q factors correspond to damping ratios below 0.2% of critical damping. As others have noted [50], material Q factors tend to increase at lower temperatures, aggravating this problem further at the cryogenic operating temperatures of interest. In mechanical assemblies, the friction

arising at the mechanical joints is often the dominant source of damping [51] and given the high Q factor of the materials used, this is likely the case in the STM detailed later in this thesis. Nevertheless, future improved STM head designs might benefit from the selection of materials with higher inherent damping properties, such as the EBL #3 piezoelectric ceramic which has a Q more than 10 times less than that of EBL #4 [49].

Moving forward with this simplified vibrational model of an STM head, an allowable vibration level for the experiment base onto which the STM is mounted can be calculated from the motion budget for the tunnel junction width $Z_{allowed}(\omega) = 10\text{fm}/\sqrt{Hz}$. The allowable displacement spectrum at the experiment base is then:

$$X_{base,allowed}(\omega) = \frac{Z_{allowed}(\omega)}{H(\omega)} \quad 2.15$$

Since it is conventional to work in velocity units, this displacement criterion can be converted into a velocity criterion:

$$V_{base,allowed}(\omega) = \frac{j\omega Z_{allowed}(\omega)}{H(\omega)} \quad 2.16$$

To explore the feasibility of achieving this criterion, the measured floor velocity at location A and the vibration levels that could be theoretically achieved with one and two stages of cascaded passive vibration isolation are compared to the criterion in Figure 2.21

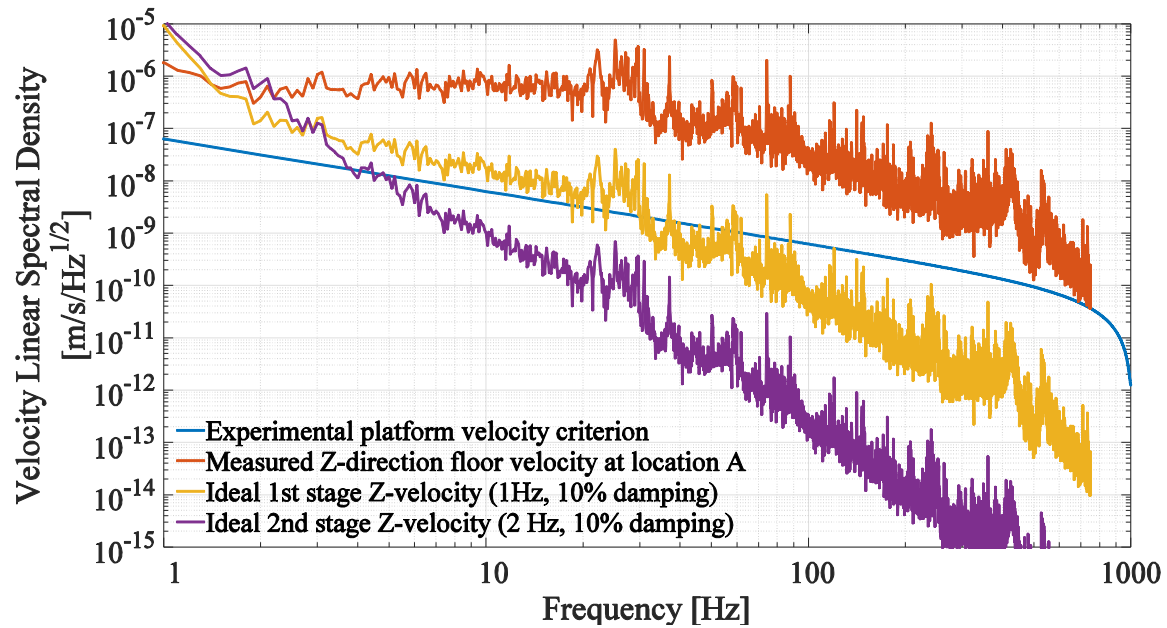


Figure 2.21: Floor velocity criterion for the STM experimental platform compared to the measured pre-construction floor velocity and theoretical floor velocities for ideal 1- and 2- stage passive vibration isolators.

Based on the results of this modelling, it was concluded that the specification for the microscope experimental platform velocity could be achieved at frequencies above approximately 4 Hz with two stages of passive isolation *if* relatively ideal behavior could be achieved. This approach was therefore pursued in the design of the LAIR facility.

Acoustic forcing of the isolated platform is the principally cited reason for degradation of isolator performance from the ideal behavior [52][5][53]. Acoustic vibrations may also excite resonances of experimental structures directly. For these reasons, it was determined that the experimental platforms should reside within heavily acoustically isolated rooms. Due to the limited design alternatives for achieving such isolation, and uncertainty as to potential severity of this issue, no detailed acoustic isolation specification was developed, although the NC-NT specification developed in [23] was considered as a guideline. Instead, it was decided that the experimental rooms should employ the largest amount of acoustic attenuation feasible within the design constraints of space, constructability and budget.

2.5 Facility design

As noted in the preface, the design of the LAIR facility was carried out by primarily by Dr. Pennec and Professors Bonn and Burke in close collaboration with Maples Argo architects and with consultation from RWDI and IDE. My major contribution to the facility design was to start doing FEM simulations on the early inertia block designs, a methodology which was adopted by Dr. Pennec to iteratively increase the resonant frequencies of the block geometries. As detailed in a later section, this optimization yielded unique inertia block designs with some of the highest resonant frequencies reported in the literature despite their large masses. Additionally, I proposed that the access pit in the Nano-g inertia block be elongated to provide two-sided access to the STM attachment point on the dilution refrigerator probe and justified this practical design feature by showing with FEA that the decrease in the resonant frequency of the inertia block resulting from this removal of material was negligible.

Despite my minimal involvement in the design phase of the development of the LAIR facility, substantial details of the facility are given in the following subsections to provide context and background information for the experimental results presented later in this chapter and in the next. First, geotechnical information about the site is presented and the design of the vault foundations are presented. Next, the design of the acoustic enclosures is detailed. Then the selection of the passive pneumatic isolators is discussed and finally the inertia block designs are presented. While reading these sections, it may be helpful to refer to Figure 2.11 at the beginning of this chapter.

2.5.1 Building substrate and foundations

In the LAIR, two isolated foundation slabs support the three inertia blocks. These foundations are isolated in that they are discontinuous both from the building foundation and

from each other. The two smaller inertia blocks (omegapod and cpod) share one of the two isolated slabs while the largest inertia block (nanog) occupies the other.

These two isolated foundations are 300mm thick concrete slabs poured on grade and reinforced with a 300mm pitch grid of 15M⁵ (16mm nom. OD) rebar near both the top and bottom of the slab. Fiber-reinforced plastic rebar was used in the Nano-g and Omega pods to avoid magnetic materials while mild steel rebar was used in C-pod. The concrete used had a specified compressive strength of 35 MPa and measured 28-day strength of 55 MPa. Measured air content in the concrete was 3.2%. To minimize the amount of excavation required, the slabs are stepped to different heights in some places.

The underlying soil is “dense to very dense till-like sand to sandy silt with some gravel” [54, p. 3] . Dynamic penetration tests required 30-50 blows per 0.3 M of deflection and the modulus of elasticity of this soil was estimated to be in the range 95-190 MPA [54] which is consistent with values in the literature for this type of soil [55].

⁵ M here stands for “Metric Bar Size” and is roughly approximate to the bar diameter in mm; 15M rebar has a nominal 16mm outer diameter.

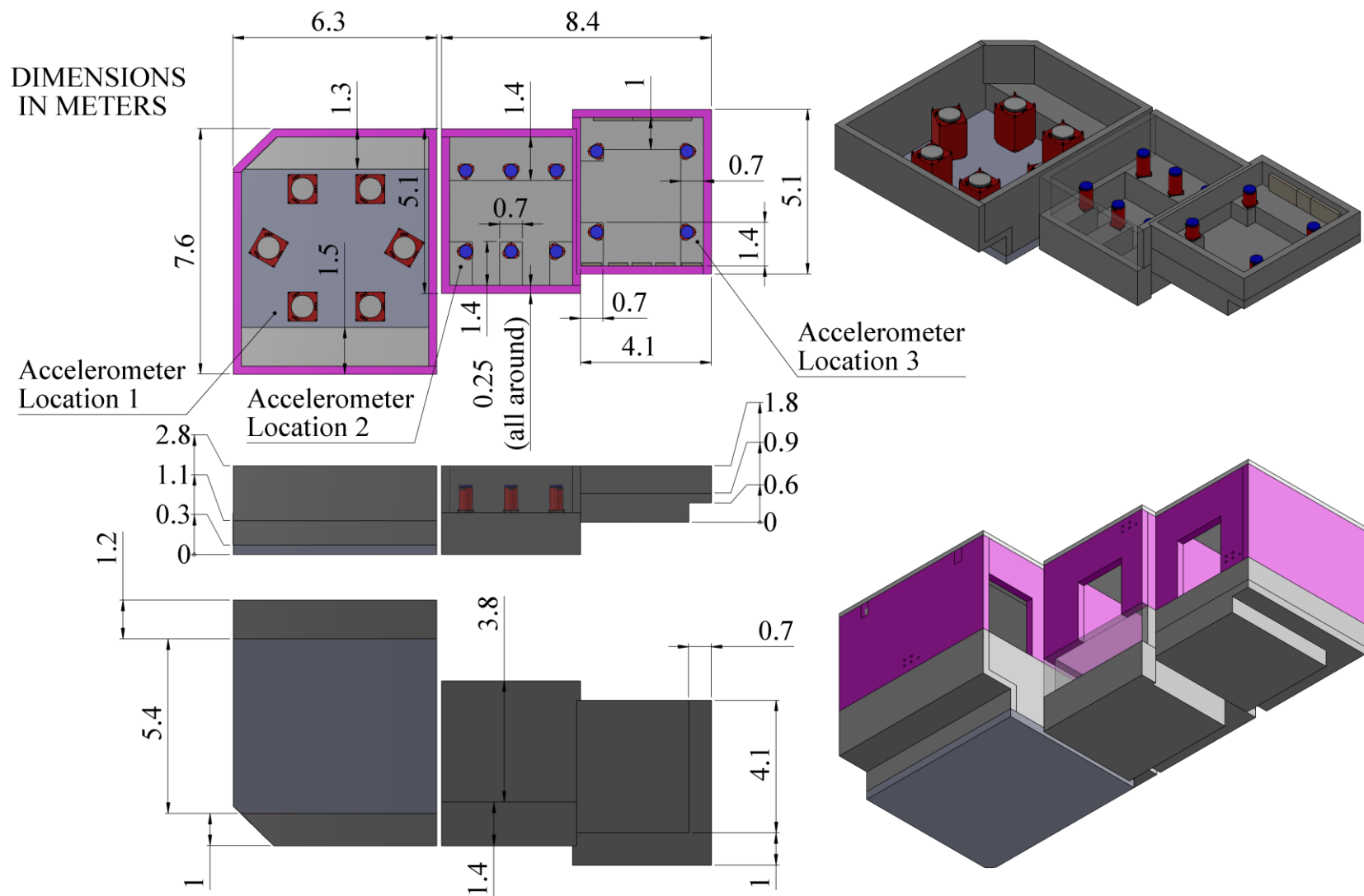


Figure 2.22 : Dimensioned drawing of the LAIR foundations and map of foundation vibration measurement positions. The isolators which support the inertia blocks (but not the inertia blocks themselves) are shown in red.

An additional point of practical importance is that the settlement of the foundations – predicted not to exceed 25mm total and 15mm differential settlement [54] is comparable to the pneumatic travel (~10mm) of the isolators. Over the first several years of operation of the LAIR facility, what appears to be settlement of the foundation under the concentrated loads of the isolator feet has required occasional increases to the isolator floating heights to fully lift the inertia blocks out of contact with their levelators⁶. On the largest inertia block, this has progressed to the point where no additional travel is available in the pneumatic mechanism. While it is straightforward in principle to add height to the pneumatic isolators by adjusting their levelling feet which have many cm of travel on threaded rods, restricted physical access to these feet under the inertia block can make this task difficult. Moreover, the unpredictable and possibly gradual decreases in inertia block isolation performance that can result from this can easily go unnoticed until they become severe. In every instance when one of the inertia blocks has stopped performing well in the LAIR it has resulted in at least several days of wasted experimental time before this trivial but unexpected cause of greatly reduced STM performance was uncovered. Implementation of a isolation performance monitoring system which continuously measures the transfer functions of the isolators in real time is recommend to avoid these problems entirely. An added benefit of such a system would be the possibility of quickly detecting new sources of vibration such as improperly installed or malfunctioning mechanical equipment.

⁶ When the inertia blocks are not suspended by their inflated pneumatic isolators, the rest on four Farrat LA-8 levelators. These are essentially high-load-capacity precision jacks that drive upwards-opening metal cups. When the inertia blocks are unfloated, metal cones on the bottom faces of the blocks mate with the cups of the levelators, safely supporting the mass of the block and also re-centering.

2.5.2 Acoustic enclosures

To isolate the inertia blocks and experiments from acoustic disturbances, the isolated, reinforced concrete foundations are wrapped upwards at a thickness of 250mm to form continuous acoustic isolation vaults surrounding the inertia blocks. The two small pods share one such vault with an inner acoustic wall separating the two pods, while the large inertia block, having its own isolated foundation, also has its own acoustic enclosure. All three pods share a second 200mm thick outer acoustic wall built from concrete blocks and lightly reinforced with vertical 15M rebars on 400mm centers. This outer acoustic wall is coupled to the building foundation. Each pod is accessible via two sets of double doors : steel doors rated STC-59 in the inner acoustic wall and solid core wood doors rated STC-42 in the outer wall.

To further improve the performance of the double acoustic enclosures, fiberglass acoustic insulation was placed in the interstitial space between the inner and outer concrete walls.

Acoustic absorbing pillows and foam corner bass-traps were placed on the inner surfaces of the inner walls of the enclosures. In the Nano-g and Omegapod enclosures, large fractions – perhaps 30% by volume – of the spaces around the inertia blocks underneath the cantilevered aluminum service floors were filled with large acoustic absorbers economically homebuilt from acoustically transparent mesh and fiberglass thermal insulation . As detailed in 2.6, the addition of this acoustically absorptive material inside the pods is especially important for reducing the reverberation time of what is otherwise a very reverberant hard-walled concrete room.

Service penetrations in the acoustic walls for gas lines, vacuum lines and user-installed electrical cabling were made by embedding a short section of plastic pipe into each of the inner and outer acoustic walls. These embedded pipe sections are coaxial with each other but do not

touch each other. This facilitates the insertion and removal of tubing, cables and the like while not providing a solid path for the flanking transmission of acoustic vibrations to the inside of the acoustically isolated vault. For the same reason, flexible couplings are employed for electrical and sprinkler connections. Ventilation within the pods has been eliminated entirely to prevent the introduction of duct-borne pressure fluctuations, acoustic noise and vibration into the vaults. Large directed vents exchange the air within the pods when the doors are opened and all pods are equipped with oxygen level monitors and alarms to alert users in the event of oxygen depletion. Additionally, helium gas from the three cryogenic STM experiments is recovered to the building helium reliquification facility for economic reasons and to avoid substantial accumulations of hypoxic gasses in the pods during experimental runs.

A dimensioned drawing of the acoustic enclosures is given in Figure 2.27; acoustic doors are not shown. Photos of the acoustic wall treatments are shown in Figure 2.24 and Figure 2.25

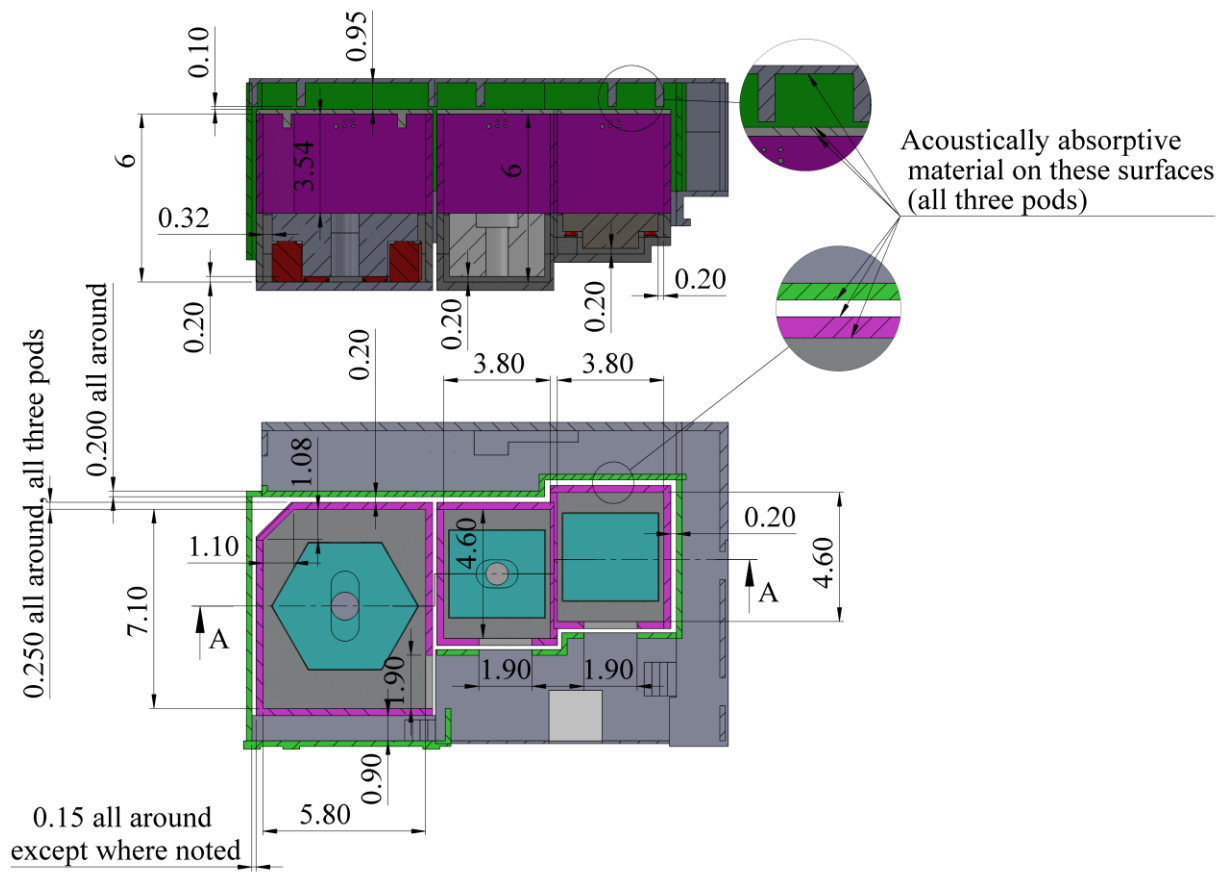


Figure 2.23: Dimensioned drawing of the LAIR acoustic isolation enclosures



Figure 2.24: Acoustic wall treatments in the interstitial between the south acoustic walls of the Nano-g pod



Figure 2.25: Photo of the inside of the Nano-g pod. The left heavy steel inner acoustic door, some of the acoustic treatments for the inner walls (red, white, blue and grey pads) and the aluminum walk-on floor are visible. The corner of the inertia block can also be seen in the bottom right corner of the frame.

2.5.3 Inertia blocks

Designing a large, heavy inertia block which does not fail catastrophically under its own weight when supported by pneumatic isolators at a limited number of positions is not a significant challenge. Figure 2.26 shows a FEA stress analysis carried out in Solidworks of the C-pod inertia block under gravitational loading (in the direction of the red arrow) when supported only by the four isolator support surfaces (demarcated by the clusters of green arrows). Although the lightest of the three blocks, this block has by far the thinnest flanges for support by the pneumatic isolators yet even at the stress concentration points in the internal sharp corners where

these flanges meet the bulk of the inertia block, the stress remains below even the low tensile strength of unreinforced concrete. Design freedom to additionally reinforce inertia blocks at crucial locations such as these – the C-pod block has embedded steel I-beams reinforcing the four corner flanges – means that structural strength, although an important consideration, is not a primary limitation in inertia block design.

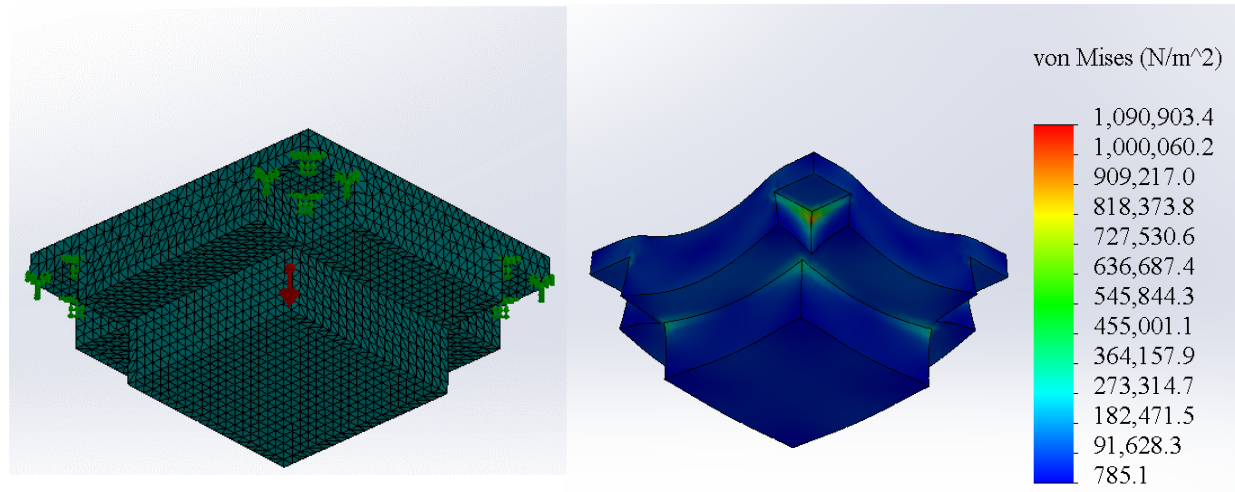


Figure 2.26 : Finite element stress analysis of the C-pod inertia block under gravitational loading.

While designing an inertia block with sufficient strength to support its own weight can readily be accomplished, achieving a high frequency for the fundamental flexural resonance of an inertia block as the mass is increased is not as straightforward. As discussed in chapter 1, inertia blocks with low flexural resonant frequencies are undesirable as their flexural modes will be more efficiently excited by ambient vibrations which are heavily weighted to frequencies below 100 Hz and which pass more easily through the pneumatic isolators and acoustic walls.

To maximize the fundamental resonant frequencies of the three inertia blocks, iterative shape and material optimizations were carried out using linear isotropic finite element simulations. These simulations led to compact, blocky shapes for the inertia blocks and to the specification of a concrete with a high Young's modulus. Although the inertia blocks were

heavily reinforced – partly to ensure ample strength against fracture – only relatively low volume fractions (less than 5%) of reinforcement are achievable due to constructability limitations⁷. Therefore, even the unusually high levels of reinforcement used in the inertia blocks likely have only a small impact on the flexural properties of the concrete at the small amplitudes of interest and it is predominantly important to choose a high performance concrete.

The inertia blocks were cast with a high strength concrete similar to the foundations; a cure-retarding agent was added to the mixture to minimize the possibility of cracking induced by differential thermal expansion or contraction during curing. All three blocks were heavily reinforced with 20M to 25M FRP rebar (to avoid magnetism) on 100-150 mm centers each way. Stainless steel embeds at corners, plates at the isolator support points and bent rebars were also used where required. Thorough vibrational consolidation of the poured concrete was performed.

This iterative simulation design approach was quite successful and yielded fundamental resonant frequencies around 200 Hz and above, as will be discussed further in later sections. These original simulations were not carried out by the author of this thesis and unfortunately full details are not available. However, details of recently performed simulations with similar results for the flexural modes, and which also capture the rigid-body rolling modes, are presented in section 2.7.2.1. The final inertia block designs are shown in Figure 2.27. Table 2.3 summarized many of the important geometrical and physical properties of the designed inertia blocks.

⁷ Beyond a certain density of embedded reinforcement bars, it becomes difficult to ensure that the liquid concrete reaches all the areas of the formwork. This imposes a practical limit on the density of reinforcement that can be used.

Inertia block	Nominal mass (nominal density * designed volume)	Projected surface areas			Principal moments of inertia			Unloaded COG distance from isolator support plane
		Vertical	North-South	East-West	About Vertical Axis	About North-South axis	About East-West axis	
C-pod	21,219 kg	10.54 m ²	3.41m ²	3.22 m ²	28469 kg · m ²	17761 kg · m ²	15592 kg · m ²	0.14 m below
Omegapod	36,681 kg	10.04 m ²	7.65 m ²	5.28 m ²	59344 kg · m ²	51443 kg · m ²	36150 kg · m ²	0.33 m below
Nano-g	71,566 kg	16.75 m ²	14.47 m ²	11.67 m ²	190379 kg · m ²	122731 ⁸ kg · m ²	127034 ⁹ kg · m ²	0.03 m below

Table 2.3 : Calculated properties of the LAIR inertia blocks as designed

⁸ The broken symmetry of the nano-g inertia block results in the principal axes of inertia not being aligned with the Cartesian axes of the basement. The principal moment of inertia in the North-South column is along an axis with normalized components 0.93 in the South direction and 0.37 in the East direction.

⁹ See the above footnote. The principal moment of inertia in the East-West column is along an axis with normalized components 0.37 in the North direction and 0.93 in the East direction.

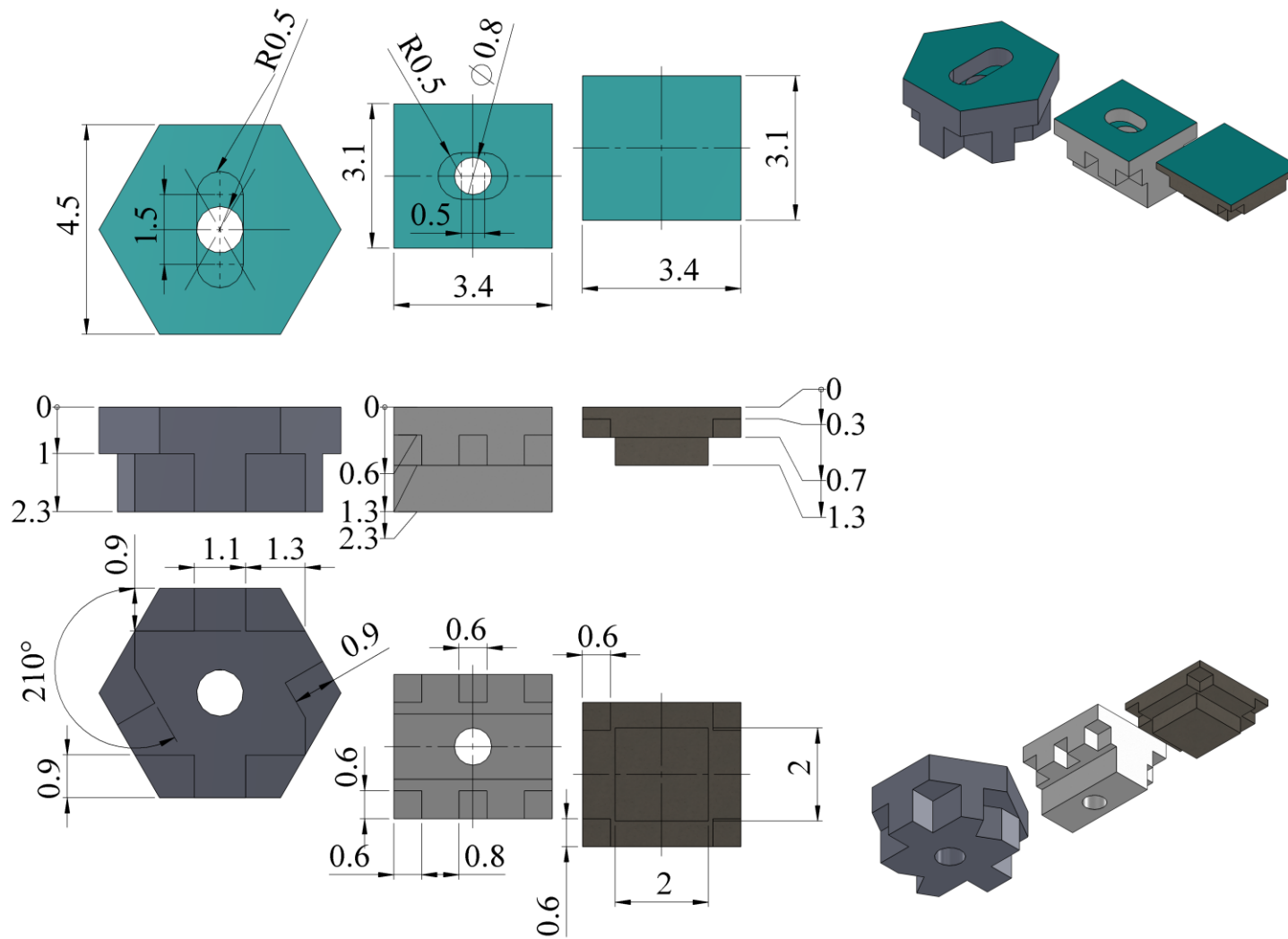


Figure 2.27: Dimensioned drawings of the three inertia blocks constructed in the LAIR. From left to right they are the Nano-g, Omegapod and C-pod inertia blocks. Ribs are employed to increase the rigidity of all three inertia blocks and dewar pits which penetrate the entire thickness of the Nano-g and Omegapod blocks are provided..

2.5.4 Heavy load pneumatic isolators

The heavy load pneumatic isolators selected to support the inertia blocks were manufactured by Integrated Dynamics Engineering. Their properties as specified by the manufacturer are summarized in Table 2.4.

Pod	Number of isolators x type	Vertical Resonant Frequency	Horizontal Resonant Frequency	Damping	Notes
C-pod	4 x IDE PD-1001H?	0.8 Hz	0.7 Hz	???	Stock item – height 595 mm
Omegapod	6 x IDE PD-1001H	0.8 Hz	0.7 Hz	Horizontal damping bladder	Customized – height increased to 900mm (from 595mm)
Nano-g	6 x IDE PD-3001H	0.8 Hz	0.7 Hz	Adjustable damping orifice	Customized – height increased to 1450mm (from 595mm)

Table 2.4 : Summary of the specifications of the heavy load isolators selected

2.6 Simulation, measurement and analysis of acoustic vibrations

In this section, the results of acoustic measurements made in the LAIR are presented. All of the measurements detailed in this section were carried out using the Behringer ECM8000 measurement microphones, the York PGM8 mixer board, the PCI-4462 DAQ and a large, homebuilt subwoofer borrowed from Professor Murray Hodgson of the Acoustics & Noise Research Group. A characterization of that subwoofer carried out by a student of Professor Hodgson's found that it had a relatively flat frequency response between 50 and 2500 Hz, with -10 dB points at 35 and 3000 Hz [56]. Microphone and subwoofer locations for the acoustic transmission and ambient level measurement experiments are shown in Figure 2.28.

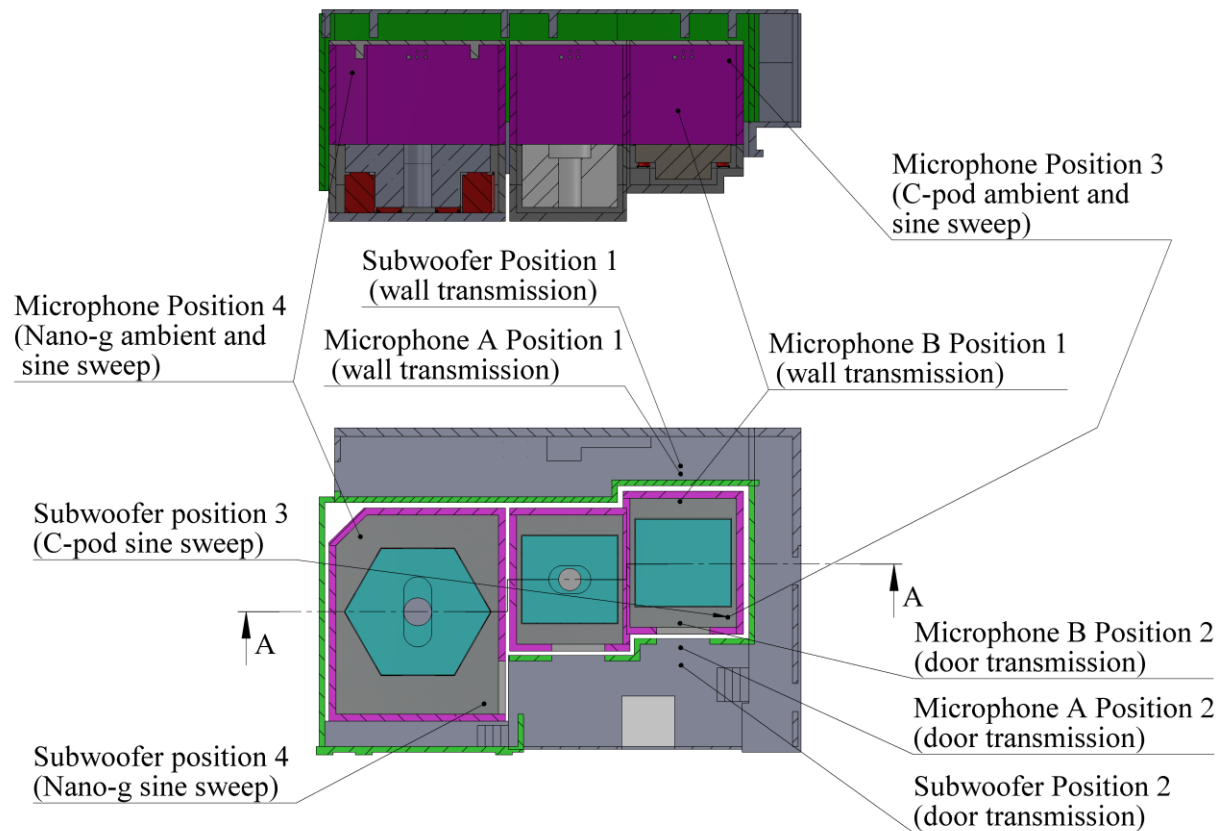


Figure 2.28: Microphone and subwoofer locations for the acoustic measurements

2.6.1 Acoustic transmission functions

As the true ambient sound pressure inside the pods was below the noise floor of the available microphones at many frequencies, it was not possible to properly characterize the acoustic attenuation of the vaults' walls and doors by simply measuring the ratio of sound pressures on either side under ambient conditions. Instead, a large subwoofer was used to provide a tone loud enough outside the pod that a coherent signal could be measured inside the pod, and sine-sweep transmission experiments performed.

These experiments were performed through the back wall (equipment positions 1 in Figure 2.28) and through the doors of the c-pod (equipment positions 2). In each case, a

microphone (“microphone A”) was placed between the subwoofer and the outer acoustic surface (wall or door), while a second microphone (“microphone B”) was placed at the same height inside the pod. The subwoofer was pointed directly along the line connecting the microphones and was driven at a current level of approximately 500mA by a Kepco BOP 15-20M bipolar power operational amplifier controlled by the audio output of the PC housing the PCI-4462 DAQ card. A tone was played and data was sampled at 5KHz for 1 second at frequencies of 10-100 Hz in 0.1 Hz steps and 100 – 1000Hz in 1 Hz steps. At frequencies below ~30Hz the tone from the subwoofer was very quiet but at the 500mA current drive level quickly become painfully loud as the drive signal moved into the flat region of the subwoofer’s frequency response above ~50 Hz. Because of this weak subwoofer response at low frequencies the transmission functions measured here have reduced coherence and thus validity below 40 Hz.

The results of these experiments are shown in Figure 2.29; the fine and coarse frequency step measurements have been joined into a single plot. The transfer function was calculated by dividing the pressure linear spectral density at the drive frequency as measured at microphone A by the same as measured at microphone B. The coherence was calculated using the MATLAB function `mscohere` with a Hanning window of 5000 samples width, overlap length of 2500 samples, an FFT length of 5000 samples and a sampling rate of 5 KHz (the experimental sampling rate).

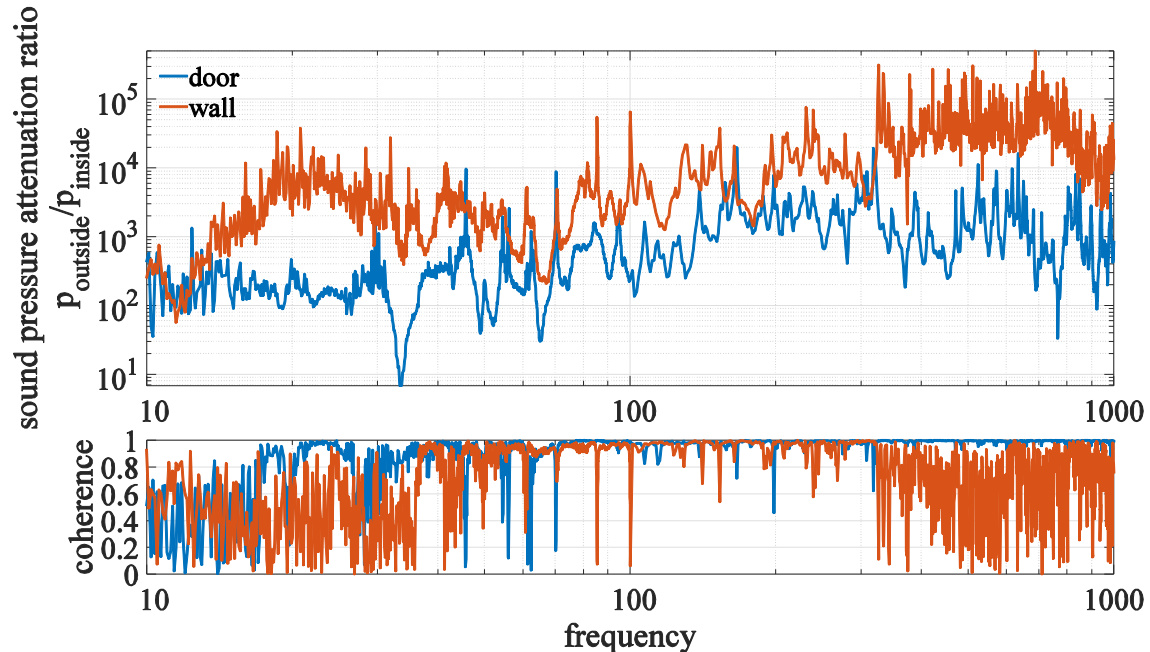


Figure 2.29 : Direct transmission acoustic transfer function and coherence for the C-pod back wall and doors, as measured with subwoofer sine sweep transmission experiments.

There are many weaknesses with this poorly designed experiment:

First, the acquisition time is short, which has several consequences. The frequency resolution of the FFT is coarser (1 Hz) than the 0.1 Hz frequency step size used in the 10-100 Hz part of the sweep. The length of this time window is also quite short relative to the period of the acoustic waves being studied especially at the low frequencies – at 10 Hz only ten cycles are being captured. These short segments – which are also not acquired multiple times - are not conducive to variance reduction methods such as Bartlett's method, Welch's method or even smoothing as the bin spacing is so large, so the variance in the spectra from which the transfer functions values at each frequency are calculated will be large. Finally the 1-second timescale is comparable to the reverberation time of the pod at some frequencies, so effects due to the acoustic ring up time of the room are included in a complicated, transient way which is undesirable.

Secondly, the measurement is a direct incidence measurement as opposed to random incidence measurement. As the transmission function of the wall will depend on the direction from which the incident sound is arriving, a single direct incidence measurement is at best an incomplete characterization of the wall. A random incidence measurement requires the use of a diffuse sound field in the transmitting room. Achieving such a condition with sufficient loudness to produce a useful signal at low frequencies inside the pod did not appear to be possible with the equipment available therefore the direct incidence measurement was pursued.

Lastly, even with a large subwoofer, at low frequencies (below ~20 Hz for the door transmission experiment and below ~40 Hz for the wall transmission experiment) the acoustic signal measured at the microphone inside the pod was small compared to the ambient noise and the self-noise of the microphone. This manifests itself in the low coherence of the measured empirical transfer functions at low frequencies and means that the data are unreliable below the above-noted frequencies. On the other hand, this also means that the measured transfer functions are likely lower bounds on the true attenuation. As the spurious noise sources inside the pod can be considered to have artificially raised the sound levels there, the true amplitude of the transmitted sound should be lower than reported.

Despite the weaknesses of this measurement, one intuitively appealing and practical inference can be drawn from it: the doors of the pod are likely the weak point of the acoustic isolation scheme by about an order of magnitude at most frequencies in the 10-1000Hz band.

2.6.2 Reverberation time

Reverberation time measurements and other measurements inside the nano-g pod were carried out by James Higgins, Shira Daltrop and Professor Murray Hodgson of the Acoustic & Noise Research Group in July and August 2012. These measurements were performed before and after the addition of acoustic absorption panels and corner bass traps to the inside of the pod. The effect of these materials was pronounced; the room went from being a highly reverberant space having an average reverberation time of 2.7 seconds in the band 40-8000Hz to a much more well damped state with an average reverberation time of 0.7 over the same band [57]

2.6.3 Short and long-time measurements of ambient acoustic spectra

Ambient acoustic spectra were measured for 100 seconds at 5KHz in both Nano-g and C- pods. In C-pod, the ECM8000 microphone was suspended in the upper south-west tri-corner of the room (location 3 in Figure 2.28) ; in Nano-g, the microphone was placed at the upper north-west tri-corner of the room (location 4). Measurement at tri-corner locations provides maximal sensitivity to all the acoustic modes of the room as all such modes have pressure maxima at the walls.

The results of this measurement are shown in Figure 2.30. A 0.2 Hz wide moving average filter was applied to this data in the frequency domain to reduce the variance of the spectrum. The comb of peaks above 200 Hz is almost entirely comprised of peaks at harmonics of 60 Hz. The presence of spectral features below 100 Hz is consistent with the weighting of the ambient sound levels outside the pods towards the 0-100 Hz frequency range and also with the relatively weaker acoustic attenuation of the acoustic enclosure and doors in this low frequency band.

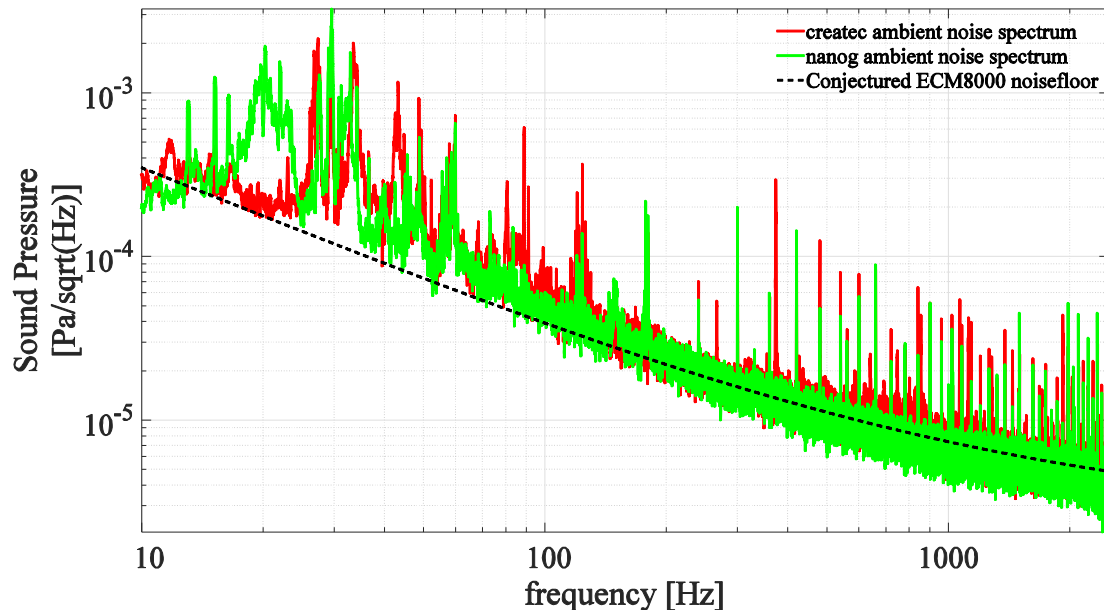


Figure 2.30 : Ambient acoustic spectra measured in the Nano-g and C- pods.

Long term acoustic spectra were also acquired in the Nano-g and C-pods with the ECM8000 microphone placed under the aluminum access deck on the south surface of the inertia blocks in each case. A 30 second time series sampled at 2 kHz was recorded every minute over several hours. In the C-pod, data was recorded between 4:12pm Wednesday July 15th and 9:00 am Thursday July 16th. Although not an ideal window, this period captures some overnight events that may be due to the mechanical functions of the building as well as increased sound level as the daily activities of the building begin in the morning. In the Nano-g pod, data was recorded between 8:36pm Thursday July 16th and 8:06 am, Saturday morning. This data set clearly shows the acoustic events over an entire weekday and throughout the night in the Nano-g pod

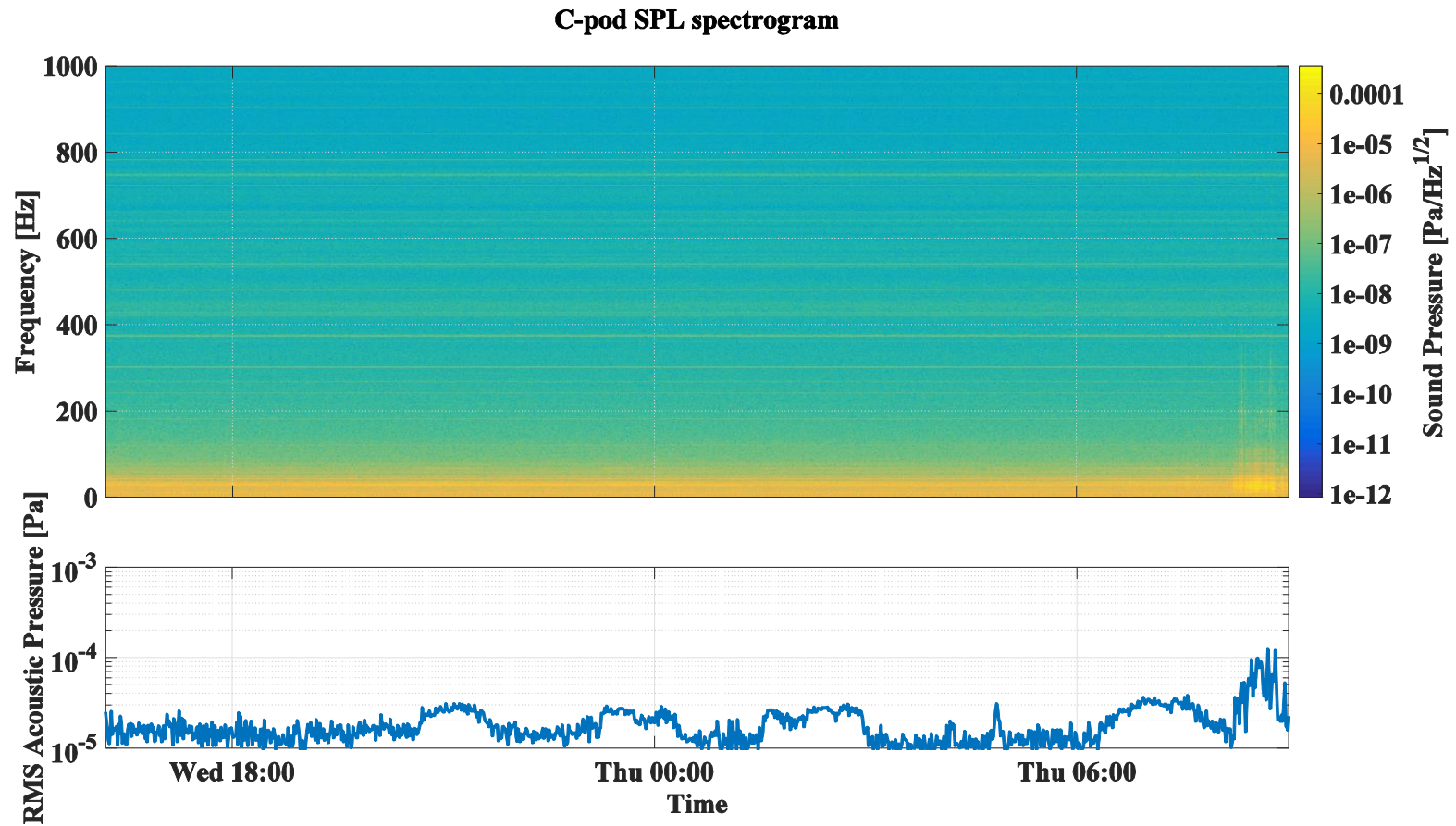


Figure 2.31 : Acoustic pressure spectrogram (top) and RMS pressure (bottom) from late after noon until 9 am in the C-pod acoustic isolation vault near the south surface of the inertia block At the far right, broadband acoustic events can be seen to begin occurring around 8 am in the morning while prolonged, ~1hr long events associated with narrow-band, low frequency features not clearly visible in the spectrogram occur several times throughout the night. The latter might be caused by the cycling on and off of HVAC equipment in the building while the former are due to people and possibly construction.

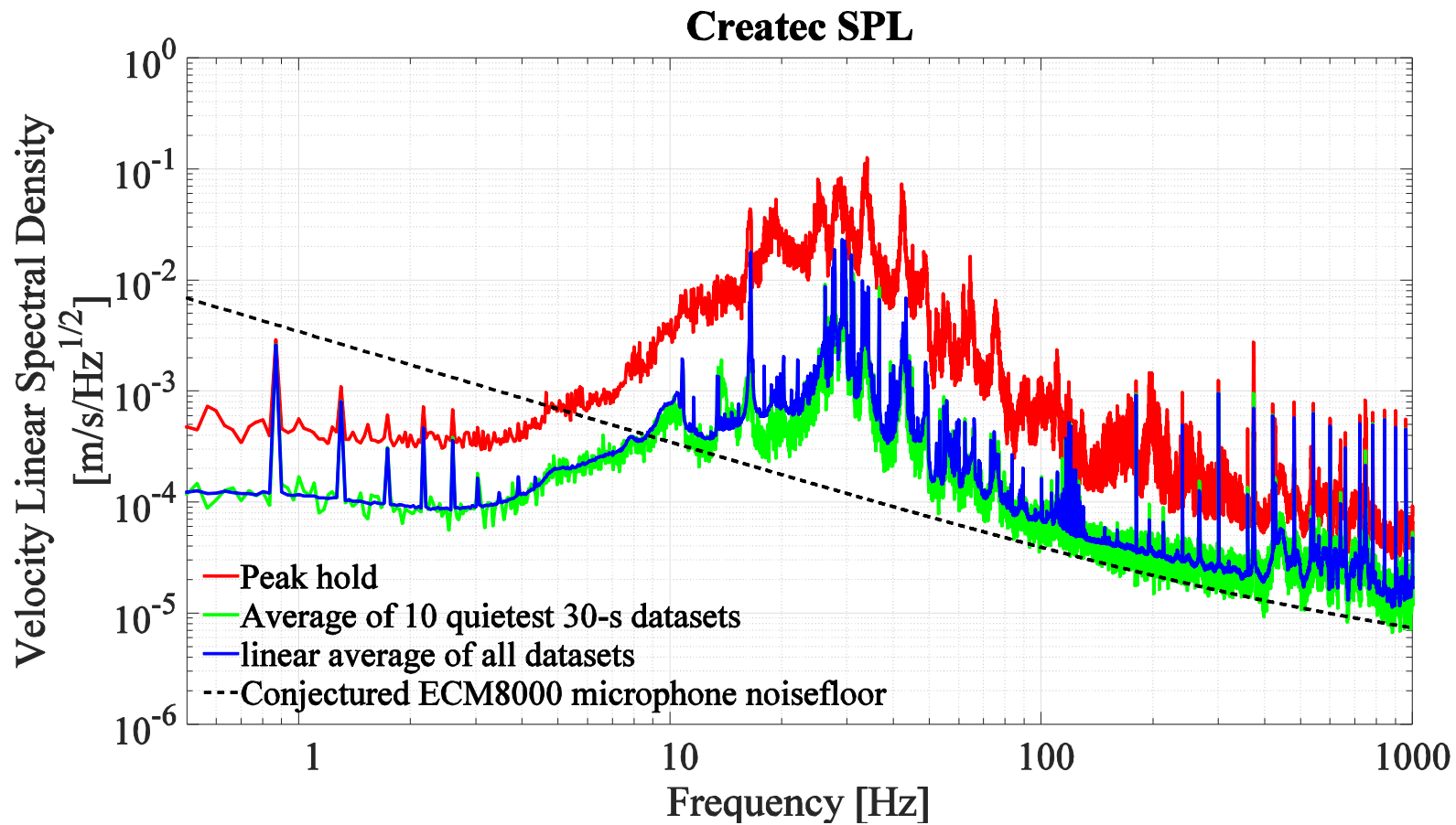


Figure 2.32 : Long term acoustic spectra recorded in the C-pod acoustic isolation vault near the south surface of the inertia block. The peak hold, linear mean and average-of-quietest curves are for a dataset many hours in length. The average of 10 quietest data sets is used to produce a smooth curve representative of the quietest condition; a “min-hold” tends to pick off random downwards fluctuations that are often below the noise floor and of unclear meaning.

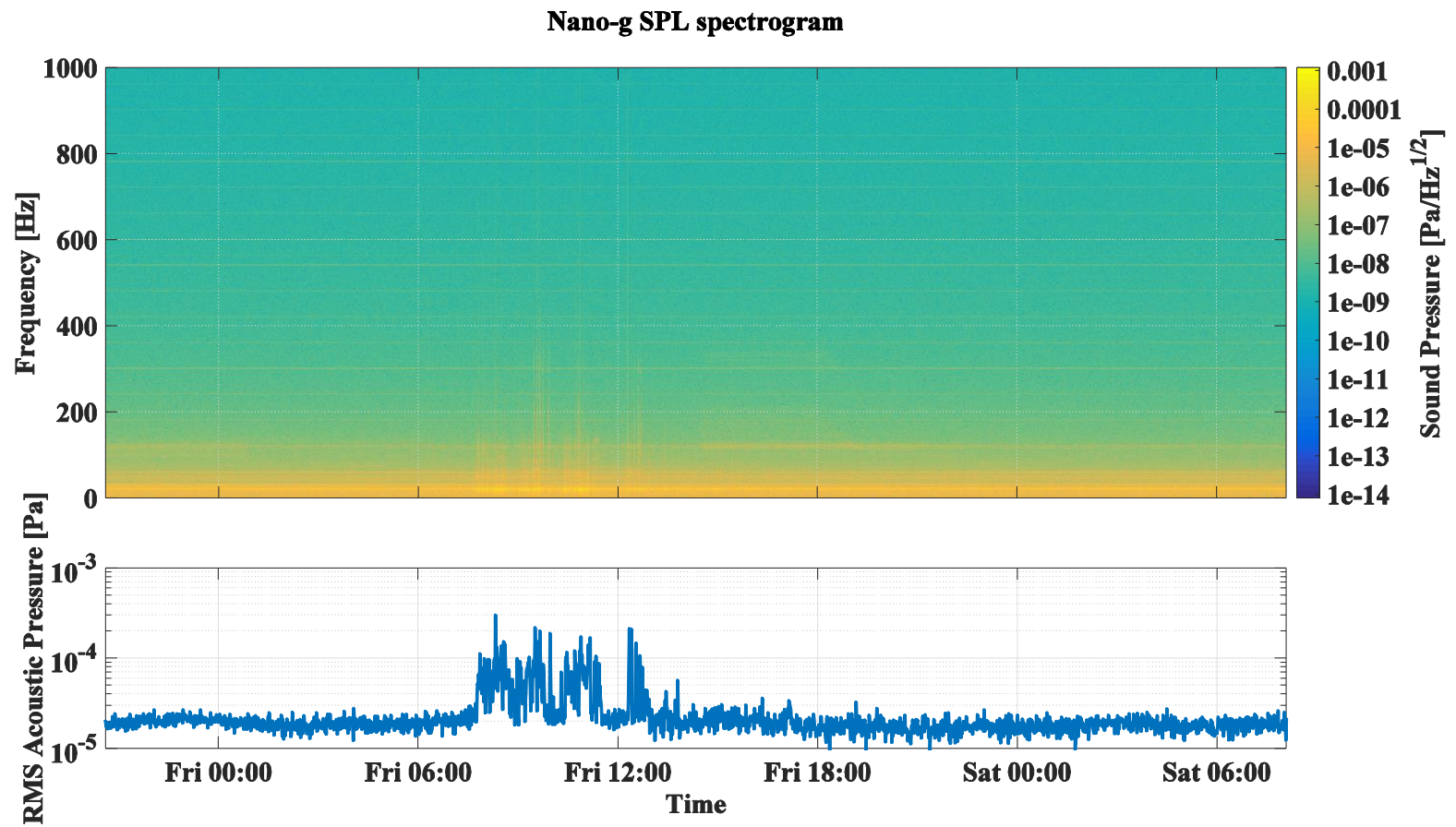


Figure 2.33: Acoustic pressure spectrum as a function of time in the Nano-g acoustic isolation vault near the south surface of the inertia block. A clear period of high-amplitude events start occurring early Friday morning; this was likely construction work at the nearby QMI building site.

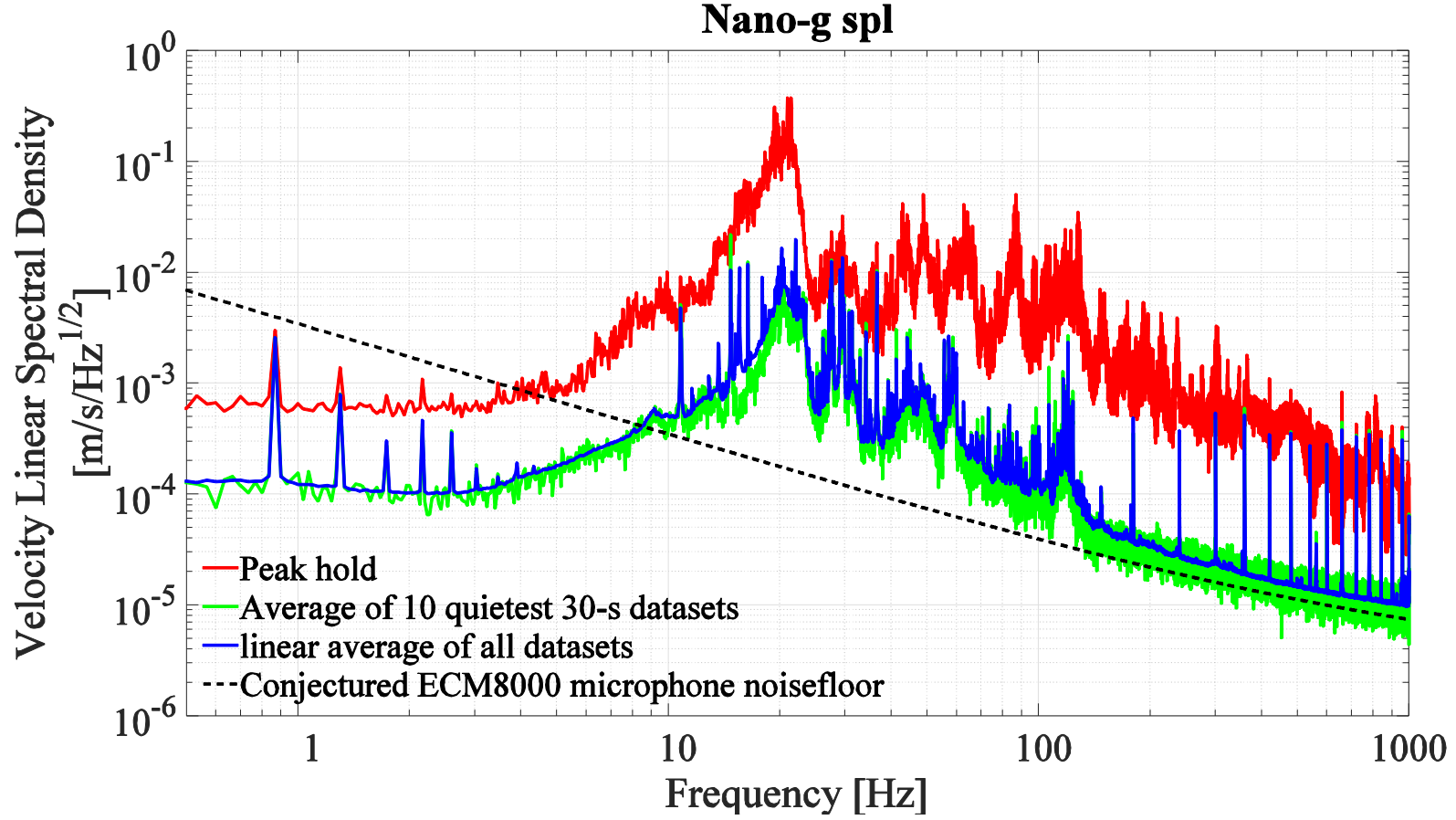


Figure 2.34: Long term acoustic spectra recorded in the Nano-g acoustic isolation vault near the south surface of the inertia block. The peaking of the spectrum around 20 Hz is likely due to amplification by the fundamental acoustic mode of the room.

2.6.4 Room modes

The three lowest frequency acoustic resonances— also known as room modes – of a cuboidal room occur at wavelengths $\lambda_{allowed}$ for which integer multiples the half-wavelengths coincide with distances between the parallel walls of the room (L_{room}) :

$$\frac{\lambda_{allowed}}{2} = L_{room} \quad 2.17$$

These wavelengths correspond to plane waves with perfectly constructive interference between the zero velocity boundary conditions which are imposed by the walls of the room. For the i – th set of parallel walls in the room separated by a distance $L_{room,i}$, the lowest frequency acoustic modes exists at frequencies

$$f_{mode}(n, i) = \frac{c_{sound}}{2L_{room,i}} \quad 2.18$$

More generally, the fundamental and higher order acoustic modes of a cuboidal room are given by:

$$f_{mode}(n_x, n_y, n_z, L_x, L_y, L_z) = \frac{c_{sound}}{2} \sqrt{\left(\frac{n_x}{L_x}\right)^2 + \left(\frac{n_y}{L_y}\right)^2 + \left(\frac{n_z}{L_z}\right)^2} \quad 2.19$$

where the modal indices $n_{x,y,z}$ are integers - up to two of which may be zero - and $L_{x,y,z}$ are the three dimensions between the parallel walls of the cuboidal room [58]. The discussion of room modes here is motivated by the influence these modes may have on the ambient acoustic spectra in the pods: any sound at the room's resonant frequencies that is produced within the pod or that enters through the acoustic walls will be amplified[58]. This is most likely to be problematic at

low frequencies where the acoustic isolation due to the walls is lower [59]. Moreover, low frequency acoustic modes are typically much more weakly damped than higher frequency ones as conventional fibrous acoustic damping treatments similar to those applied in the LAIR are not very effective at low frequency [60]. More modern absorber technologies with significantly improved low frequency attenuation - such as compound baffle absorbers [58] and perforated panel absorbers [61] - are likely much more appropriate alternatives in these type of laboratories.

As the features in the acoustic spectra measured within the pods are predominantly below 100 Hz, only the room modes in this frequency range were considered for the following analysis. All the resonant frequencies below 100 Hz calculated from equation 2.19 for cuboidal rooms approximating the slightly more complex geometry of the Nano-g and C- pod acoustic enclosures are tabulated in Table 2.7 and Table 2.8.

North-South Axis $L_x = 7.1m$ $n_x =$	East-West Axis $L_y = 5.8m$ $n_y =$	Vertical Axis $L_z = 6m$ $n_z =$	Calculated resonant frequency (Hz)	North-South Axis $L_x = 7.1m$ $n_x =$	East-West Axis $L_y = 5.8m$ $n_y =$	Vertical Axis $L_z = 6m$ $n_z =$	Calculated resonant frequency (Hz)
1	0	0	24.16	3	0	1	77.92
0	0	1	28.59	3	1	0	78.29
0	1	0	29.58	2	1	2	80.50
1	0	1	37.43	2	2	1	81.56
1	1	0	38.19	0	2	2	82.28
0	1	1	41.14	3	1	1	83.35
1	1	1	47.71	0	0	3	85.78
2	0	0	48.32	1	2	2	85.75
2	0	1	56.15	0	3	0	88.73
2	1	0	56.66	1	0	3	89.11
0	0	2	57.18	0	1	3	90.73
0	2	0	59.16	1	3	0	91.96
1	0	2	62.08	3	0	2	92.33
2	1	1	63.46	0	3	1	93.23
1	2	0	63.90	3	2	0	93.56
0	1	2	64.38	1	1	3	93.89
0	2	1	65.70	2	2	2	95.42
1	1	2	68.76	1	3	1	96.31
1	2	1	70.00	4	0	0	96.65
3	0	0	72.49	3	1	2	96.95
2	0	2	74.87	3	2	1	97.83
2	2	0	76.38	2	0	3	98.45

Table 2.5 : Approximate analytical room mode frequencies for the Nano-g acoustic enclosure

North-South Axis $L_x = 7.1m$ $n_x =$	East-West Axis $L_y = 5.8m$ $n_y =$	Vertical Axis $L_z = 6m$ $n_z =$	Calculated resonant frequency (Hz)
0	0	1	34.31
1	0	0	37.29
0	1	0	45.14
1	0	1	50.68
0	1	1	56.70
1	1	0	58.56
1	1	1	67.87
0	0	2	68.62
2	0	0	74.59
1	0	2	78.10
2	0	1	82.10
0	1	2	82.14
2	1	0	87.19
0	2	0	90.29
1	1	2	90.21
2	1	1	93.69
0	2	1	96.59
1	2	0	97.69

Table 2.6 : Approximate analytical room mode frequencies for the C-pod acoustic enclosure

Partial characterization of the room modes of the Nano-g and C-pods was carried out by sampling the sound pressure in the room at 5KHz while performing a 10 to 100 Hz sine-sweep in 0.1 Hz steps with large homebuilt subwoofer mentioned previously. At each step, data was acquired for 2 seconds. In Nano-g, the subwoofer was placed on the aluminum decking in the south-east corner of the room (subwoofer position 4 in Figure 2.28) and tilted to excite the room modes more evenly. The ECM8000 microphone was placed in the upper north-west tricorner (position 4). In C-pod the subwoofer was also placed on the decking in the south-east corner (subwoofer position 3) and the microphone in the south-east upper tri-corner (microphone position 3). The deviations of the geometry of the Nano-g and C- pod acoustic enclosures away from the ideal cuboid for which this theory is strictly valid – principally due to the large inertia

blocks filling major portions of the rooms – immediately indicates that these calculated frequencies will not match the measured modal frequencies exactly, and indeed they do not, as can be seen in Figure 2.35 and Figure 2.36.

Comparing the ambient noise spectrum to the measured room modes in Figure 2.37 suggests that the amplification of sound at the room modal frequencies may be a significant factor in determining the ambient acoustic level inside the acoustic enclosures.

The measured room resonances appear to have full-widths at half-maximum on the order of 1-3 Hz, yielding quality factors

$$Q = \frac{f_0}{\Delta f_{FWHM}} \quad 2.20$$

in the range of 5 to 100 for the room acoustic resonances, which correspond to non-negligible amplification of ambient noise. This suggests that the resonances of the room play a role in amplifying the low frequency ambient excitations that are making it through the acoustic enclosure. Improved damping of these low frequency acoustic modes using low frequency absorbers such as compound baffle absorbers [58] or perforated panel absorbers [61] may be appropriate.

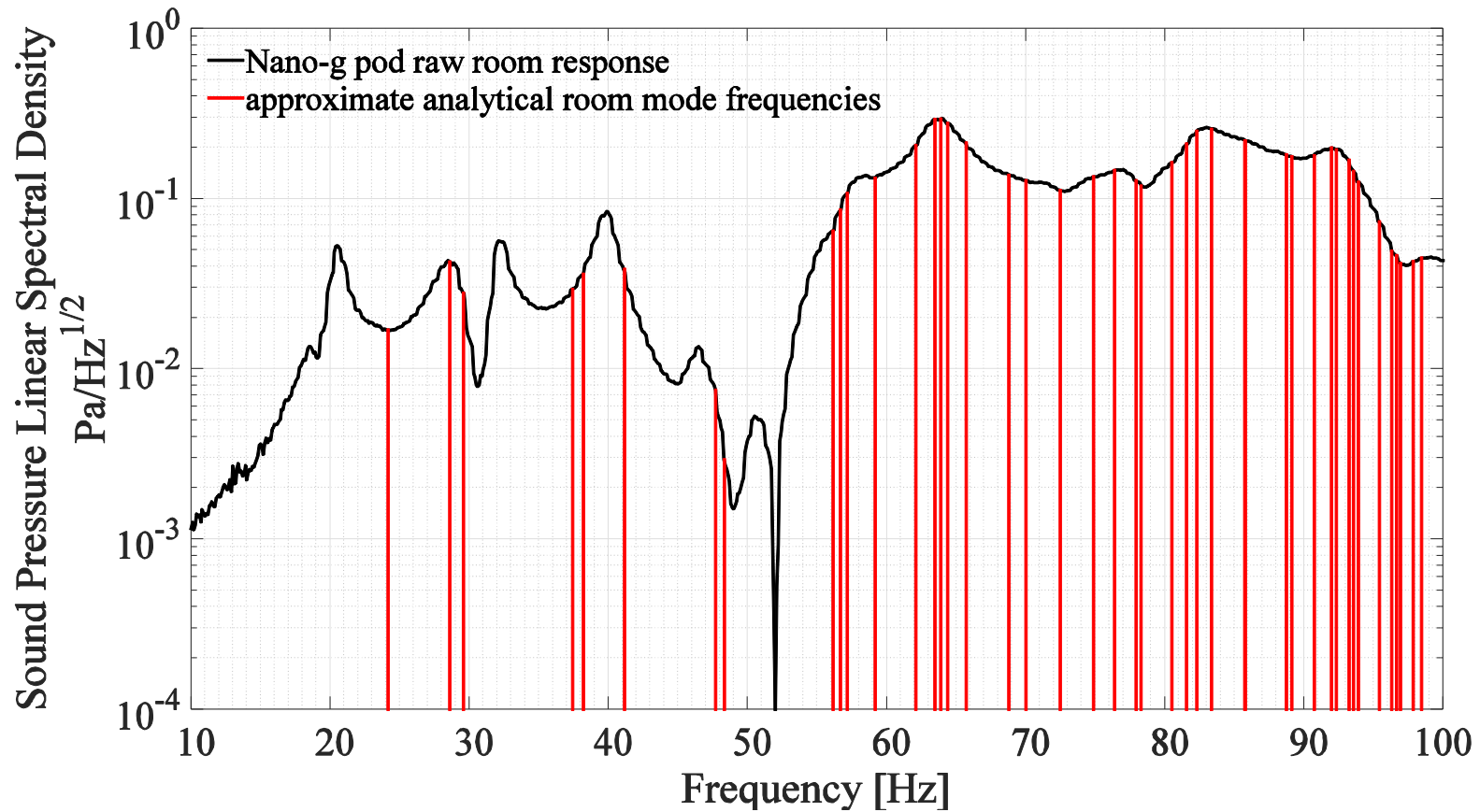


Figure 2.35: Raw response of the Nano-g acoustic enclosure to sine sweep excitation compared to approximate analytical resonance frequencies for the enclosure. The absolute amplitude of the response curve carries little meaning as the room response of the room has not been normalized by the subwoofer response which is changing steeply until approximately 50 Hz. The shape of these curves – in particular the widths and heights of the peaks – should carry information about the room modes. The increasing density of modes above ~55 Hz likely explains the increasingly smooth frequency response in that region.

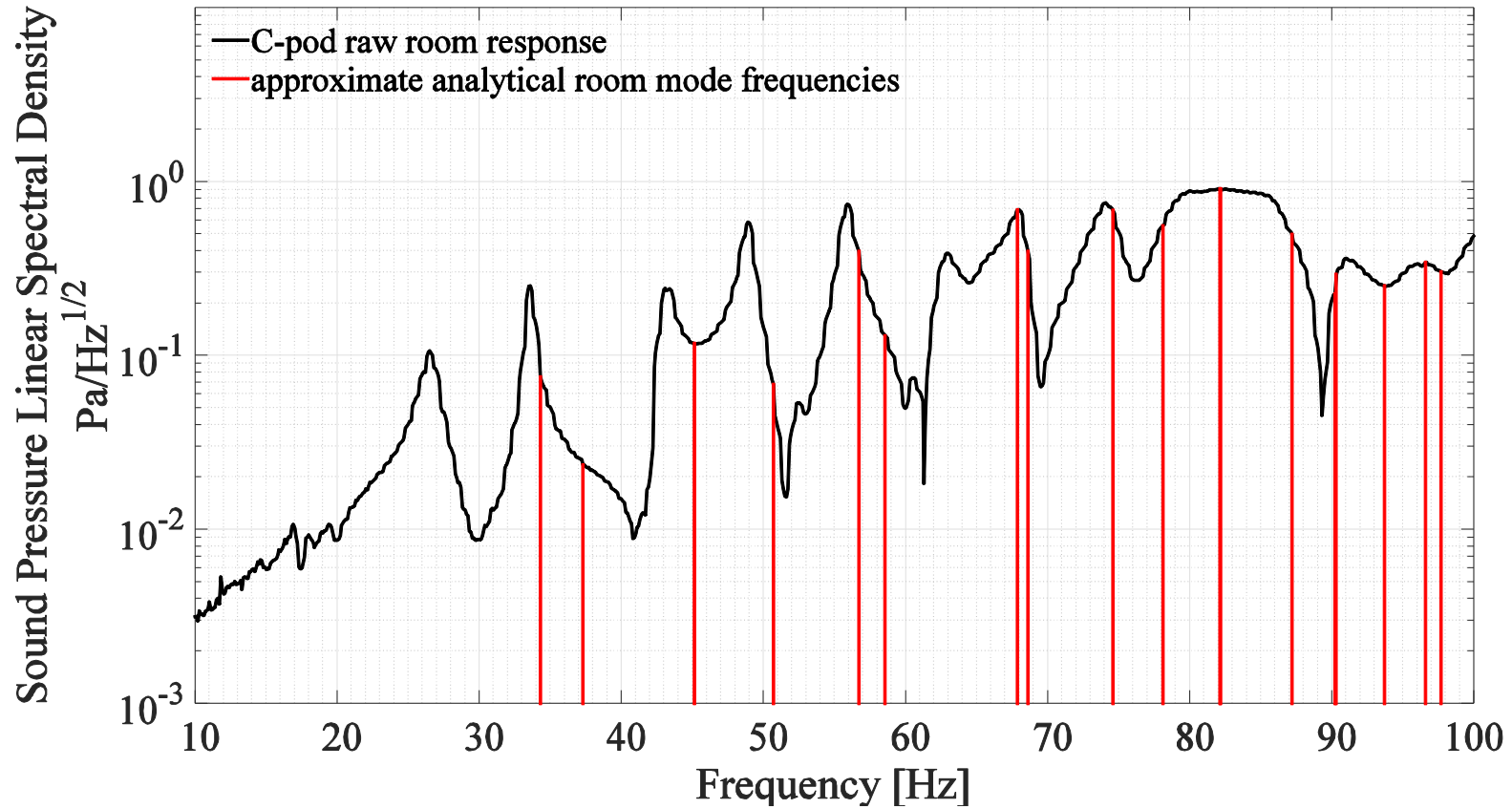


Figure 2.36: Raw response of the C-pod acoustic enclosure to sine sweep excitation compared to approximate analytical resonance frequencies for the enclosure. This smaller room has a much smaller density of modes in the frequency range considered and therefore a much less even response than the Nano-g pod enclosure in this range. This is one reason that large concert halls have superior acoustics for bass frequencies: as the density of acoustic modes grows large – which happens at lower frequencies in larger rooms – the room response becomes much smoother.

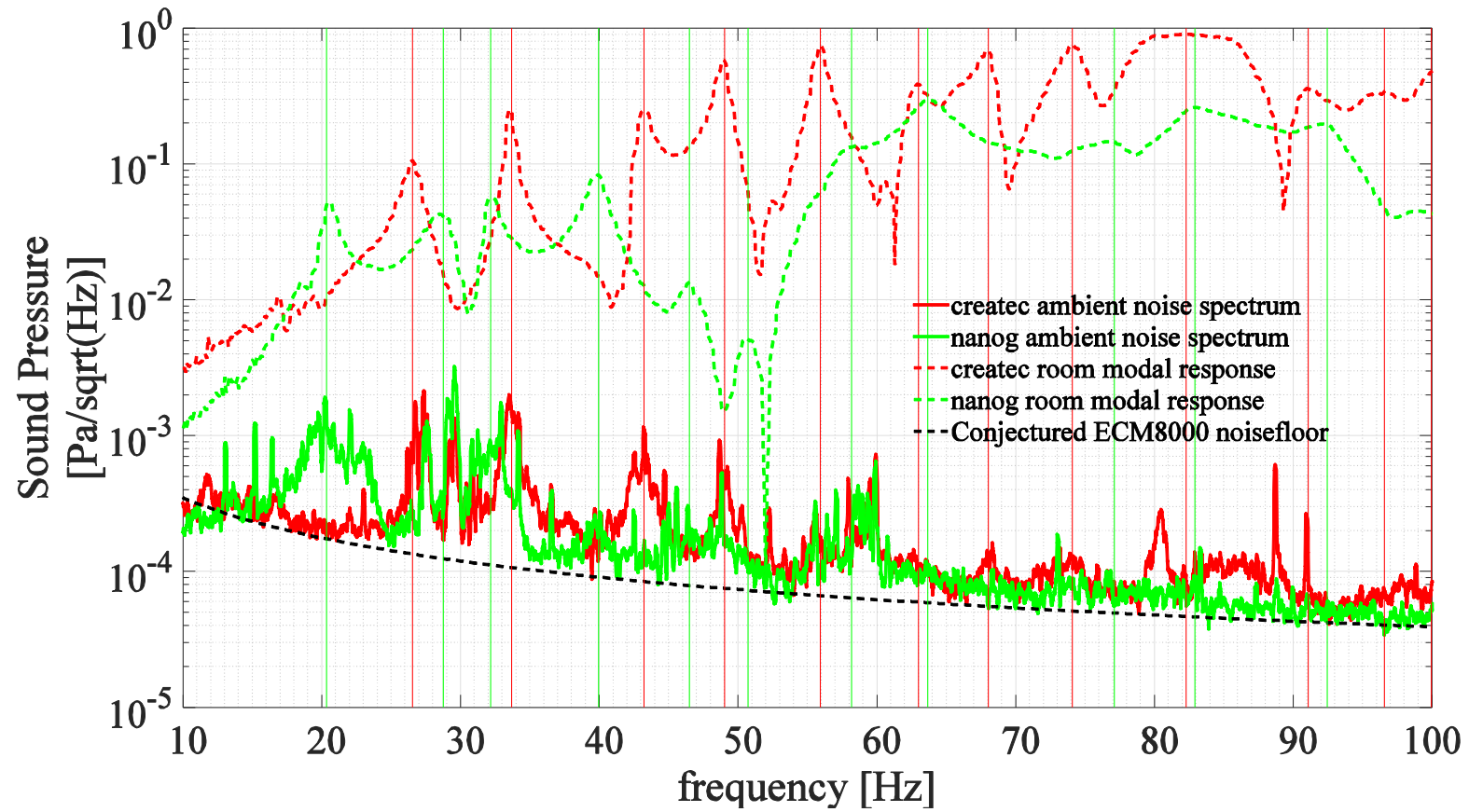


Figure 2.37 : Comparison of raw room response (dashed curves) and ambient sound pressure spectra (solid curves) in the Nano-g and C- pods. The coincidence of peaks in the ambient spectra with peaks in the excited room response suggests that significant amplification of sound due to room resonances may be occurring.

The lowest frequency room modes – which appear to correspond to some of the largest peaks in the ambient spectrum and may drive unwanted inertia block motion the most strongly – are deserving of particular attention. That the frequencies of these lowest modes do not coincide very well with the analytically predicted modes suggest that the influence of the inertia blocks in perturbing the mode shapes must be taken into account. A better understanding of these mode shapes may help in the strategic placement of tuned or broadband low frequency absorbers in the high air-pressure or velocity zones of these modes. Accurately predicting the frequencies of these fundamental resonances may also help guide designers away from room designs which have many nearly coincident resonances. To investigate the effect of the inertia blocks on the room modes further, finite element simulations of the approximate geometries of the rooms, both with and without the inertia blocks, were carried out in COMSOL. In these simulations, the mesh sequence type used was “Physics-controlled mesh” and the element size was set to “extra-fine”. The “sound hard” boundary condition was applied to all the surfaces of the vaults and the inertia blocks were modelled as rigid inclusions into the room. The results of these simulations are tabulated in Table 2.7 for the Nano-g pod and for C-pod in Table 2.8.

Refraction of sound waves around the inertia blocks – illustrated in Figure 2.38 – increasing the effective total acoustic path length between the walls, does appear to decrease the fundamental resonant frequencies of the rooms. While this may be sufficient to fully explain the lowering of the lowest mode of the Nano-g pod to about 20.37 Hz, the lowest frequency mode measured in the C-pod is substantially lower than even the refraction-downshifted frequency predicted by the FEA. The additional downshifting is likely due to the relatively large additional volume of the STM experiment in C-pod, which was not included in the FEA.

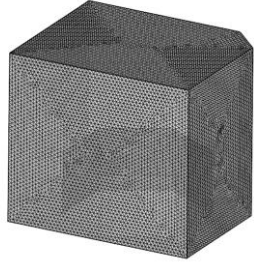
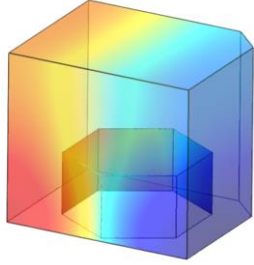
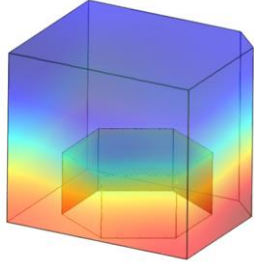
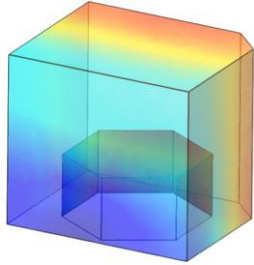
Measured and calculated room resonance frequencies (Hz)					
Nano-g pod					
Mode	Analytical formula	FEA (without block)	FEA (with block)	Potentially associated raw response peak	Picture of mesh / mode shape
					
South wall to North wall, $L=7.1$ m, $n=1$	24.17	24.46	20.69	20.37	
Floor underneath block to ceiling, $L=6$ m, $n=1$,	28.60	27.31	27.43	28.78	
West wall to East wall, $L=5.8$, $n=1$	29.59	30.14	26.718	32.17	

Table 2.7: Comparison of calculated and measured room mode frequencies for the Nano-g pod.

The measured raw response peak frequencies are included in the order which they are expected to correspond to the simulated modes. The addition of the inertia block to the FEA simulation decreases the frequencies of the modes in which the acoustic waves have to diffract around the inertia block.

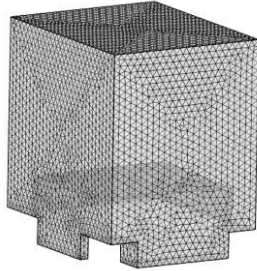
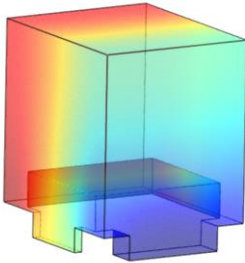
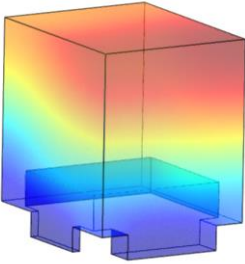
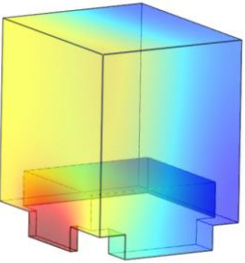
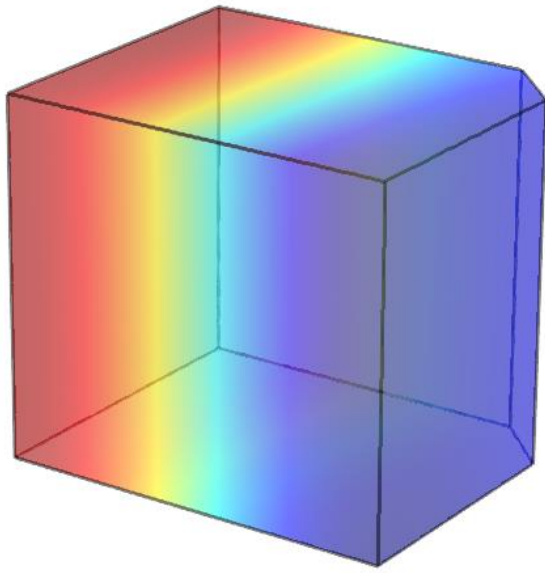
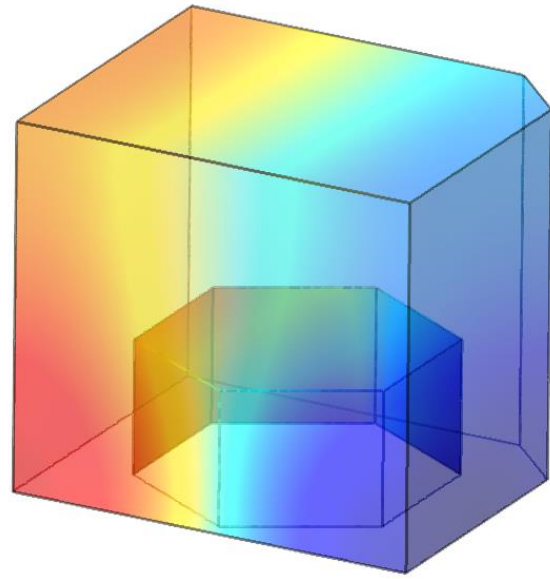
Measured and calculated room resonance frequencies (Hz)					
C-Pod					
Mode	Analytical formula	FEA (without block)	FEA (with block)	Potentially associated raw response peak	Picture of mesh / mode shape
					
South wall to North wall, L= 4.6 m, n=1	37.30	37.9	33.14	26.54	
Floor underneath block to ceiling, L=5 m, n=1,	34.32	35.7	40.74	33.68	
West wall to East wall, L=3.8, n=1	45.16	45.8	43.98	43.24	

Table 2.8: Comparison of calculated and measured room mode frequencies for the C-pod. With the addition of the inertia block to the simulation, the refraction downshifting of the horizontal acoustic modes appears again, but the filling in of the vertical axis by the block also seems to upshift the vertical mode.



$$f_0 = 24.46$$



$$f_0 = 20.69$$

Figure 2.38 : Finite element analysis of acoustic mode downshifting due to acoustic refraction around the Nano-g inertia block

2.7 Simulation, measurement and analysis of solid vibrations

In the following sections, the rigid and flexural vibrations of the pod foundations/acoustic enclosures and of the inertia blocks are treated. The performance of the large heavy-load pneumatic isolators supporting the inertia blocks is analyzed and the performance of 2nd stage light load pneumatic isolators discussed. The issue of experimental structure vibrations is touched upon but deferred substantially to chapter 3. The vibration performance of the LAIR is compared to other locations on campus and similar facilities around the world. Finally, simulations of the inertia block designs for the UBC Quantum Matter Institute Microscopy suite – all based on the Nano-g inertia block design – are briefly presented.

2.7.1 Foundations

The three LAIR inertia blocks rest on two isolated foundations cast so as to be disjoint with the foundations of the surrounding building. The inner acoustic enclosure of the Nano-g pod is built on one of these foundations while the shared inner acoustic enclosure of the Omegapod and C-pod is built on the other. These isolated foundations and the inner acoustic enclosures form two monolithic concrete isolation boxes: one containing the Nano-g inertia block and the other containing the other two inertia blocks. The vibrations of these monolithic boxes, with an emphasis on the modes which move the floor underneath the inertia block isolators at low frequencies, are treated in the following subsections.

2.7.1.1 Simulation of vibrations of the foundations and acoustic enclosure walls

With knowledge of the elastic properties of the underlying soil and of concrete, a FEM simulation can predict the rigid-body and flexural vibrational modes of the monolithic isolation boxes. The coupling of the flexural modes of the walls of these boxes with the acoustic modes of the cavities the boxes contain is an interesting and potentially important problem since the frequencies of the dominant acoustic modes in the room are near to the enclosures flexural frequencies and also near to problem frequencies for the STM as discussed in Chapter 3:. The analysis of this problem is beyond the scope of this thesis, however the literature suggests that only for very small (stiff) acoustic cavities or very flexible walls does the acoustic cavity significantly affect the modes of the walls (although the converse is not necessarily true) . The following finite element analysis does not consider structural-acoustic coupling whatsoever. Additionally, for simplicity, the inertia blocks have been neglected entirely. This is partially justified because the isolation box modes are found to lie above 5Hz, and when the inertia blocks are pneumatically suspended by their isolators the harmonic forces transmitted by the foundation to the blocks (and therefore the back-action of the blocks on the foundation) decreases quickly beyond the pneumatic isolator resonance ~1 Hz.

The modulus of elasticity of the glacial till – type soil underlying the AMPEL building is estimated to be in the range 95-190 MPA [54], which is consistent with values in the literature for this type of soil [55]. Following [62], the spring constant of the earth underneath the foundation can be approximated by considering the earth to be a semi-infinite elastic medium supporting a rigid-plate, with a subgrade modulus (i.e. spring constant per unit area) k of

$$k_s = \frac{k_{total}}{A} = 1.13 \frac{E}{1 - \nu^2} \frac{1}{\sqrt{A}} \left(\frac{n}{m} / m^2 \right) \quad 2.21$$

Where k_{total} is the total stiffness of the foundation in $/m$, E is the modulus of elasticity of the soil, ν is its Poisson's ratio and A is the area of the foundation. Taking the elastic modulus to be at the midpoint of the estimated range for the AMPEL building, 142.5 MPa, and taking the Poisson's ratio for glacial till to be 0.3 as reported in [55],

$$k_s = 1.77E8 \cdot A^{-\frac{1}{2}} \quad 2.22$$

Based on this distributed spring constant – and making the major assumption that horizontal deflections are resisted by the same spring constant per unit area as vertical ones – approximate frequencies and mode shapes for the rigid and flexural modes of the two concrete boxes in the LAIR can easily be calculated using COMSOL. As before, these simulations used extra-fine, physics-controlled meshes. The parameters used in these simulations are given in Table 2.9 while the important low frequency – essentially rigid-body - modes are summarized in Table 2.10 and Table 2.11. The first thirty FEA-predicted modal frequencies for the monolithic enclosures occur every few Hz up to ~100 Hz; most of the higher modes involve membrane-like deformations of the walls of the acoustic enclosures as exemplified in Figure 2.39. The mode frequencies predicted by the FEA are tabulated in appendix Appendix A .

Property	Nano-g monolithic box	Omegapod/C-pod monolithic box
Area of horizontal foundation surfaces in contact with the earth and used for COMSOL isotropic spring foundation	45.48 m ²	42.59 m ²
Horizontal and vertical spring constant per unit area used	26.2E6 ($\frac{n}{m}/m^2$)	27.1E6 ($\frac{n}{m}/m^2$)
Material model for concrete box	Concrete (from COMSOL material library): Density = 2300 kg/m ³ Young's modulus = 25E9 Pa Poisson Ratio = 0.33	Concrete (from COMSOL material library): Density = 2300 kg/m ³ Young's modulus = 25E9 Pa Poisson Ratio = 0.33
Mass of monolithic box	157,781 kg	162,000 kg
Principal axis ¹⁰ / moment of inertia # 1 (approximately along the NS axis)	Axis :(-0.21E,0.01Z,0.98S) Moment : 1.64E6	Axis :(0.14E,0.30Z,0.944S) Moment : 1.91E6
Principal axis / moment of inertia # 2 (approximately along vertical axis)	Axis :(-0.08E,0.97Z,0.04S) Moment : 1.75E6	Axis :(-0.37E,0.90Z,-0.23 S) Moment : 1.72E6
Principal axis / moment of inertia # 3 (approximately along the EW axis)	Axis :(0.98E,-0.08Z,0.21S) Moment : 1.83E6	Axis :(0.92E,0.32Z,-0.24 S) Moment : 1.19E6

Table 2.9 : Geometric and material properties used for FEA of the LAIR monolithic concrete isolation boxes

¹⁰ The principal axes here are given as normalized vectors with components in the East (E), upwards (Z), and South (S) directions

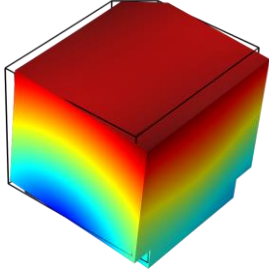
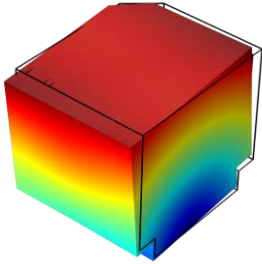
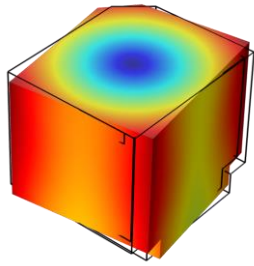
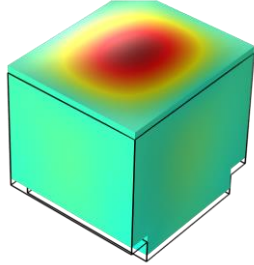
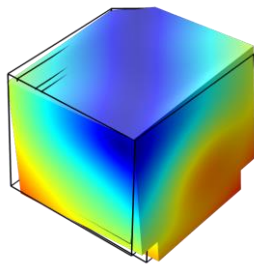
Mode #	Frequency	Description	Image
1	5.45 Hz	Rocking about NS axis	
2	6.1 Hz	Rocking about EW axis	
3	11.653 Hz	Twisting about vertical axis	
4	13.1 Hz	Vertical rigid body translation coupled to membrane modes of roof and floor	
5	19.9 Hz	Higher-order rocking about axis connecting NW and SE corners of pod	

Table 2.10: FEA-predicted pseudo-rigid-body modes of the Nano-g monolithic concrete isolation box

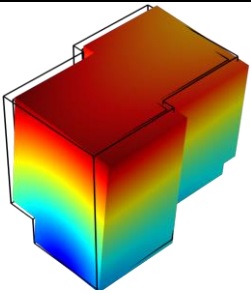
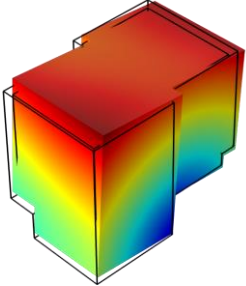
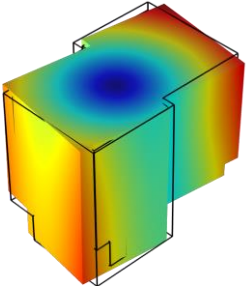
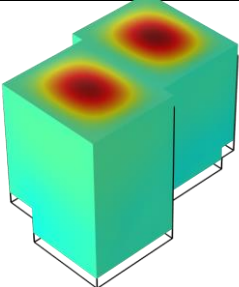
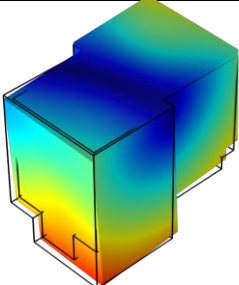
Mode #	Frequency	Description	Image
1	5.5 Hz	Rocking about EW axis	
2	7.5 Hz	Rocking about NW axis	
3	12.0 Hz	Twisting about vertical axis	
4	13.6 Hz	Vertical rigid body translation coupled to membrane modes of ceilings	
5	18.2 Hz	Higher order rocking about EW axis	

Table 2.11: FEA-predicted pseudo-rigid-body modes of the Omega/C-pod monolithic concrete isolation box

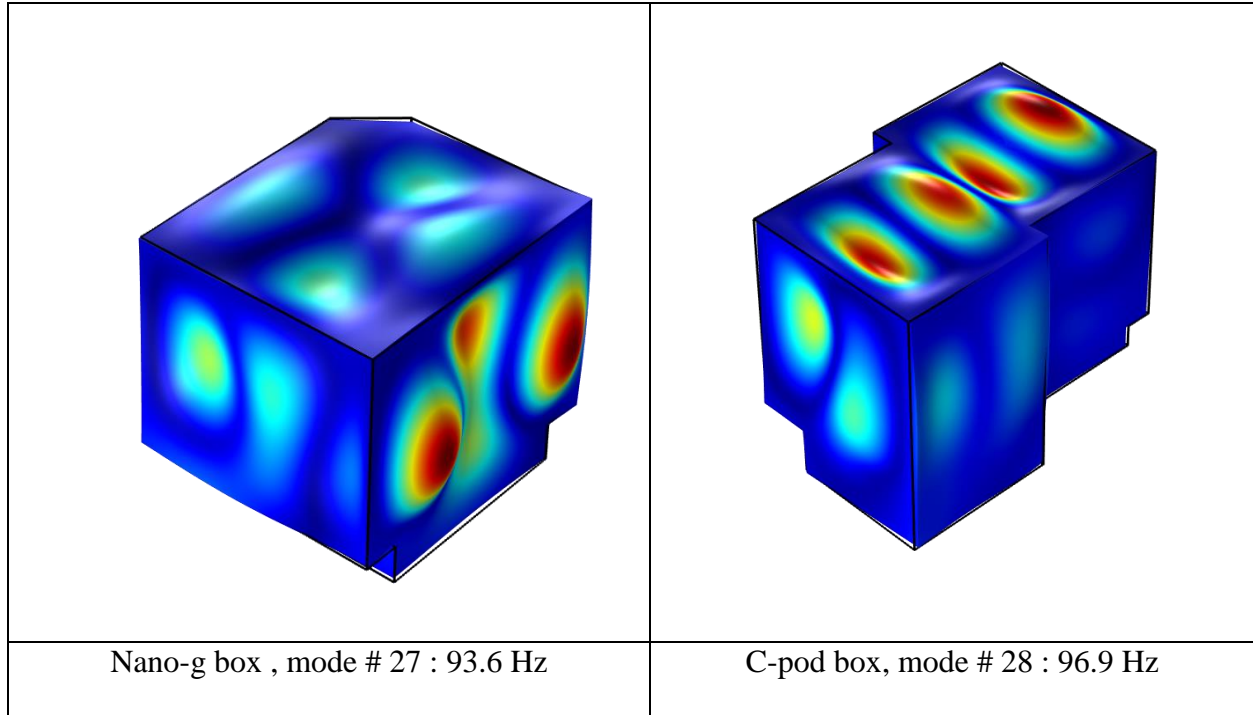


Figure 2.39: Examples of high-order FEA-predicted flexural modes of the monolithic isolation enclosures

2.7.1.2 Measurement of foundation vibrations

Long term measurements ranging from ~6 hours to over 24 hours in length were carried out in the three pods, using the PCB393B04 accelerometer to measure the vibrations on the foundations and the Wilcoxon 731A on the inertia blocks. The results of the foundation measurements are presented in this section while the block vibrations, and the transfer functions from the foundations to the blocks are presented in section 2.7.2. Due to the necessity of closing off the pods to measure the ambient levels of vibration on the inertia blocks without disturbances such as people walking on the blocks, it was necessary to work around the schedules of the STM experiments taking place. This resulted in data being taken over windows of different lengths and starting and ending at different times.

The PCB accelerometer was placed at points on the foundations underneath each of the three inertia blocks at locations indicated in Figure 2.22. The accelerometer was attached with a threaded stud to an aluminum block which was in turn epoxied to the concrete floor. Underneath the C-pod and Nano-g inertia blocks, measurements were made in the vertical (Z) and North-South (X) directions, while only vertical direction measurements were made under the Omegapod inertia block. Data was acquired at a sampling rate of 5 KHz for 30 seconds out of every minute (approximately) for long periods in the day and night during June and July, 2015 during which time violent excavation work for the construction of the UBC Quantum Matter Institute building was intermittently in progress immediately to the east of the AMPEL building.

An interesting finding was that the measured levels of vibration during the day were often an order of magnitude or larger than they were at night. That said, it is important to keep in mind the strong but intermittent vibrations created by the excavation work. These likely obscure to some extent the gentler variations in ambient vibrations levels from day to night that otherwise might be expected.

Spectrograms of the acquired vibration data are shown along with the RMS floor velocity as a function of time for each measurement location are shown in Figure 2.40, Figure 2.41 and Figure 2.42. Long-term peak hold, linear mean and averages of the 10 quietest spectra in the respective data sets are shown for C-pod in Figure 2.43, Omegapod in Figure 2.44 and Nano-g in Figure 2.45.

Due to the non-simultaneous acquisition of the data at the different locations, and the different lengths and start/end times of the acquired data, comparing the amplitude of the linear mean spectra is probably not very meaningful as the quantity of transient vibration events captured in each dataset is different, unfairly biasing the linear mean spectra up or down.

However, to help identify characteristic resonance frequencies of the different isolation boxes, the linear spectra are compared in Figure 2.46; these curves are the simple average of hundreds of spectra and are very smooth and show peaks clearly.

Comparing the quietest spectra – typically measured late at night or very early in the morning – is likely the best measure by which to compare the intrinsic vibration performance of the different foundations. Figure 2.47 compares these spectra. Instead of using the single quietest spectra, the average of the 10 quietest spectra is used to produce smoother curves which hopefully are somewhat representative of the extent to which the baseline of ambient vibrations in the AMPEL building is amplified and attenuated by the isolated foundations at different frequencies. Finally, the peak-hold amplitudes are compared in Figure 2.48 – although this comparison is also unfair, it approximates worst-case vibrations levels for each location.

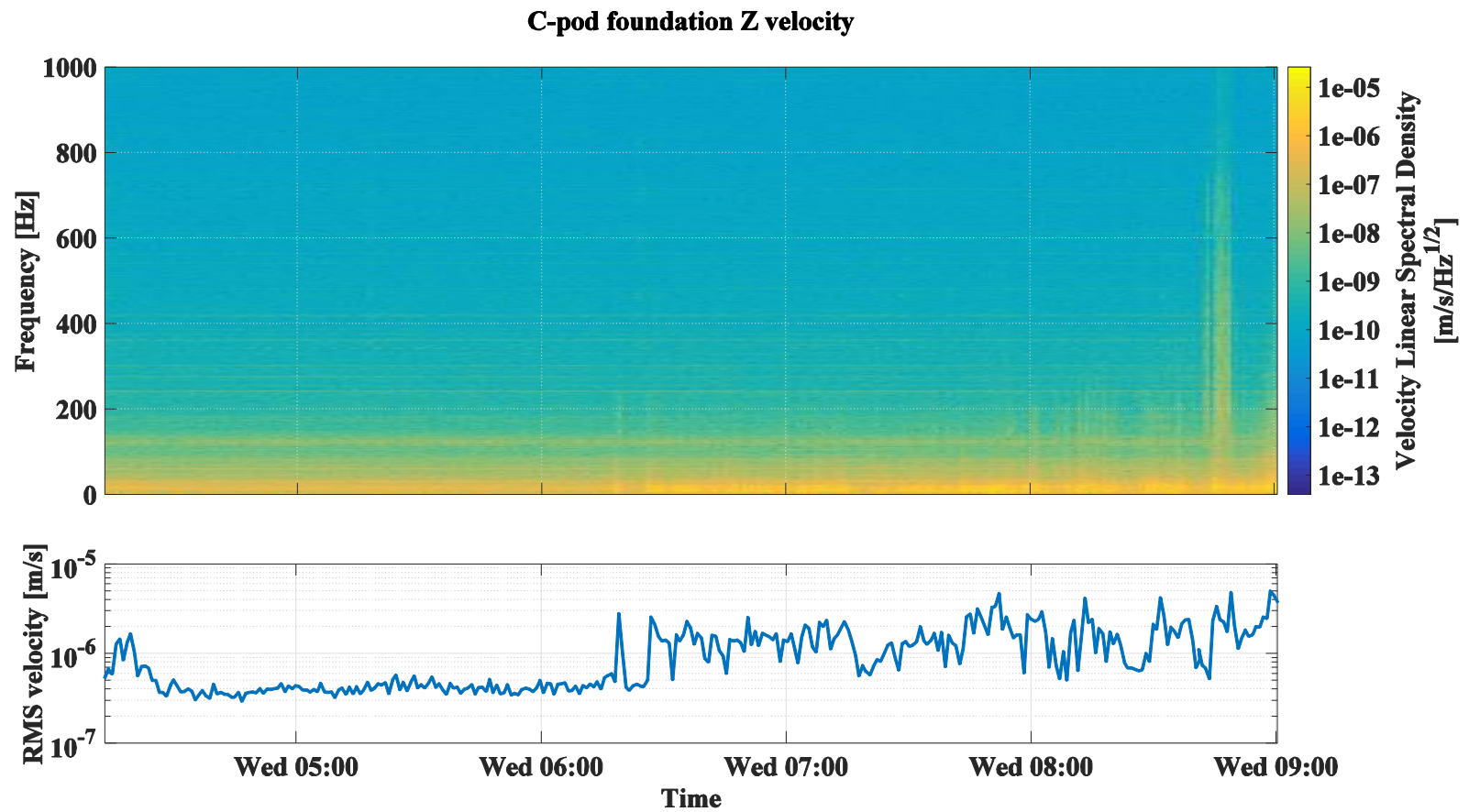


Figure 2.40 : Vertical velocity spectrum and RMS velocity on the C-pod foundation vs time at the beginning of a workday This data was acquired with a PCB 393B04 accelerometer mounted at location number 3 in Figure 2.22. Each column of pixels in the spectrogram represents the spectrum of 30 seconds of vibration data. The RMS velocity is the square root of the sum of the squares of the spectrogram values. The time is shown in 24-hr format. In this plot, increased vibrational activity can be seen beginning just before 6:30 am and continuing until the end of the data at 9:00 am

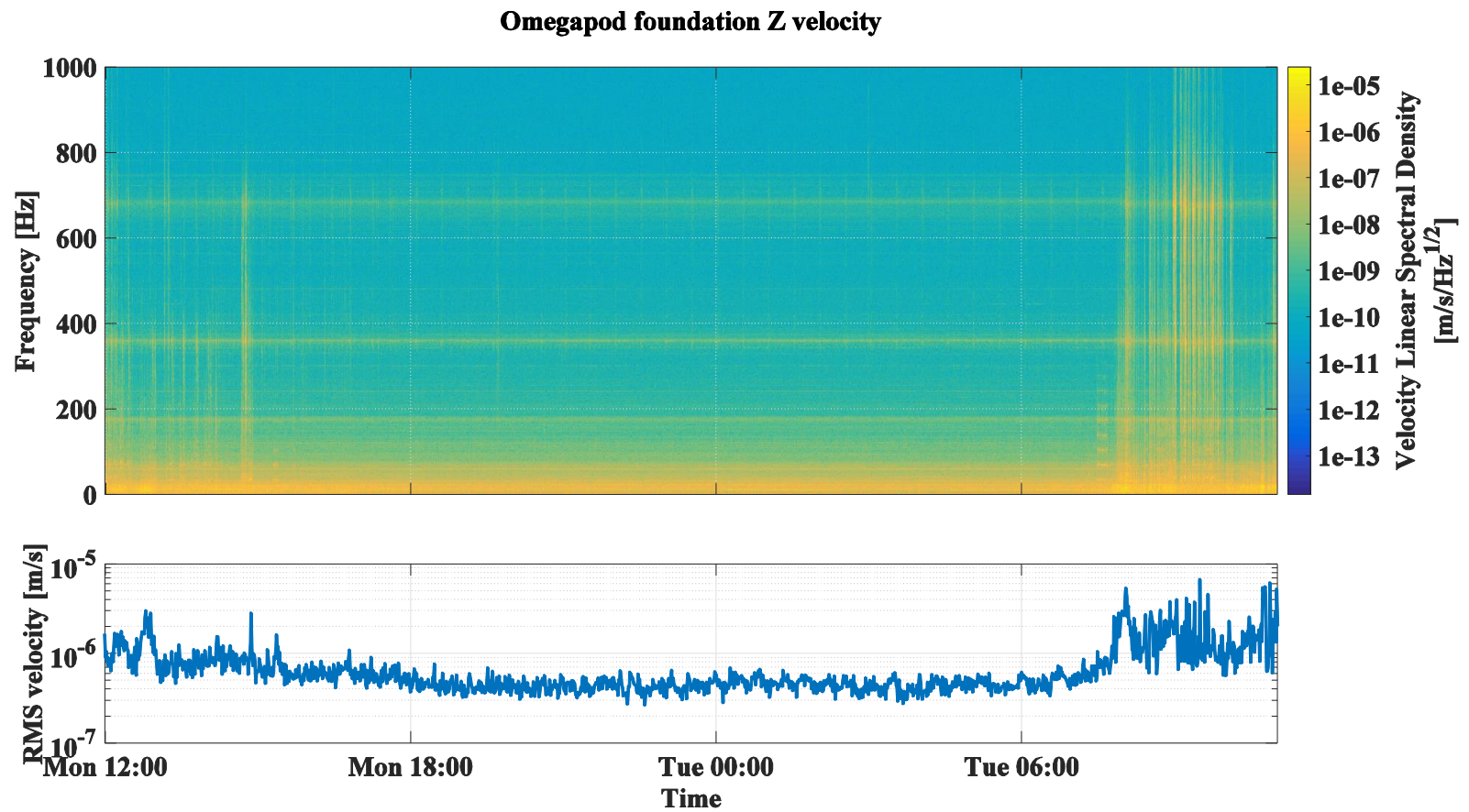


Figure 2.41 : Vertical velocity spectrum and RMS velocity on the foundation under the Omegapod inertia block over a period of just under 24 hours. This data was acquired with a PCB 393B04 accelerometer mounted at location number 2 in Figure 2.22. Lightly elevated levels of vibration can be seen in the afternoon on Monday and more violent events start occurring early Tuesday morning.

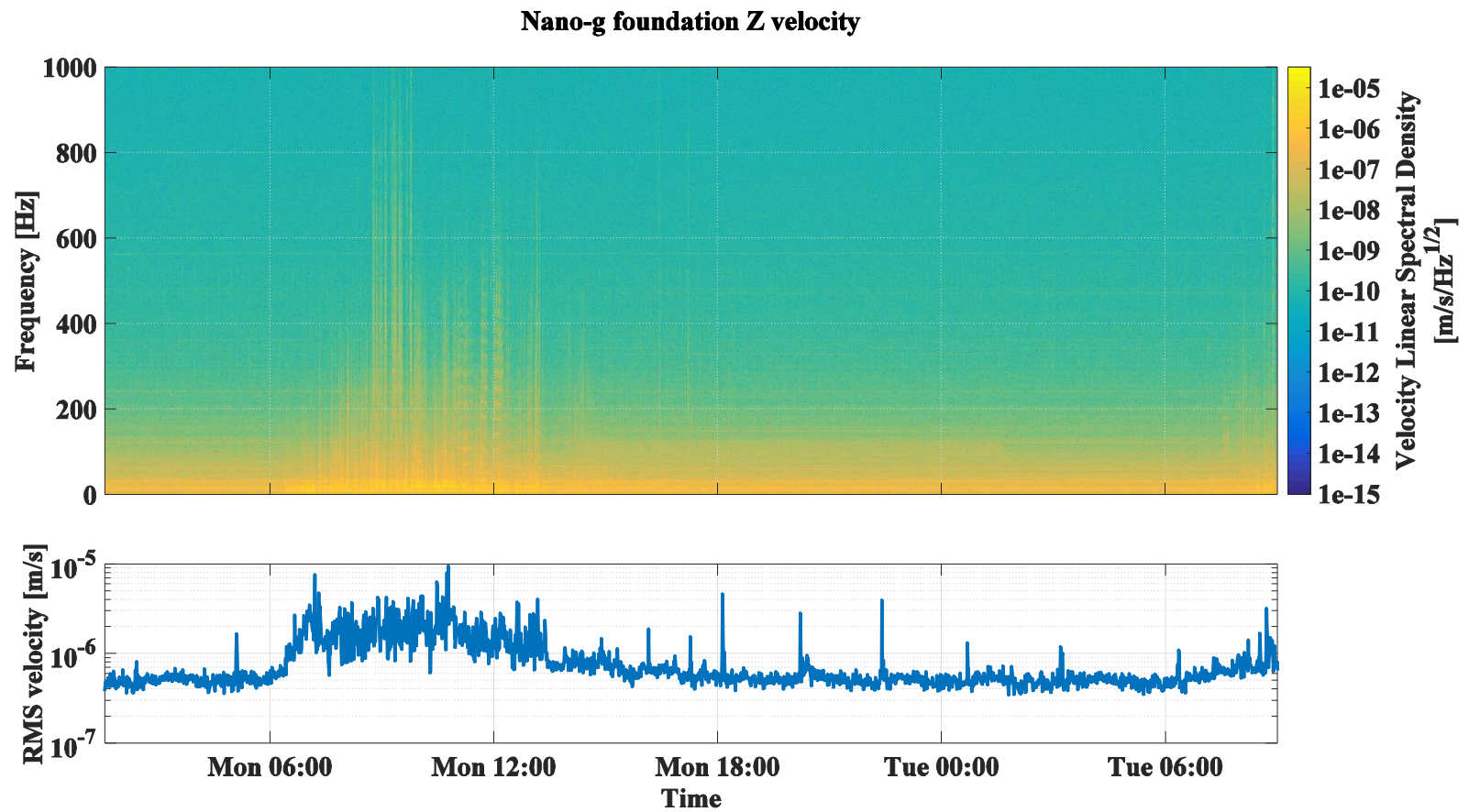


Figure 2.42 : Vertical velocity spectrum and RMS velocity on the Nano-g foundation This data was acquired with a PCB 393B04 accelerometer mounted at location number 1 in Figure 2.22. In this plot, increased vibrational activity can be seen beginning just after 6:00 am and fading away in the afternoon.

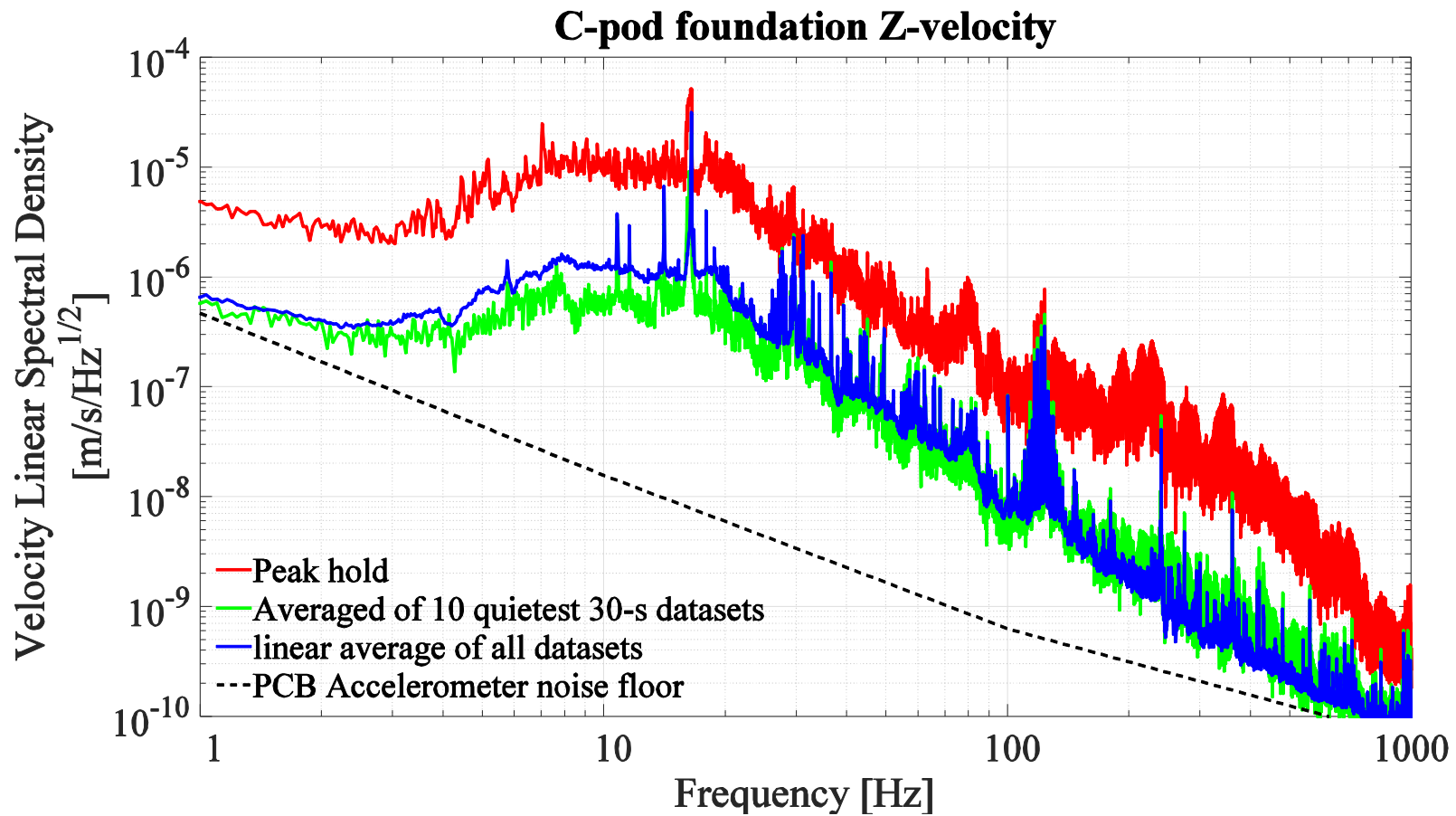


Figure 2.43 : Long-term vertical velocity spectra for the isolated foundation underneath the C-pod inertia block. For this and the other foundations, order of magnitude variations in the foundation velocity are apparent at most frequencies

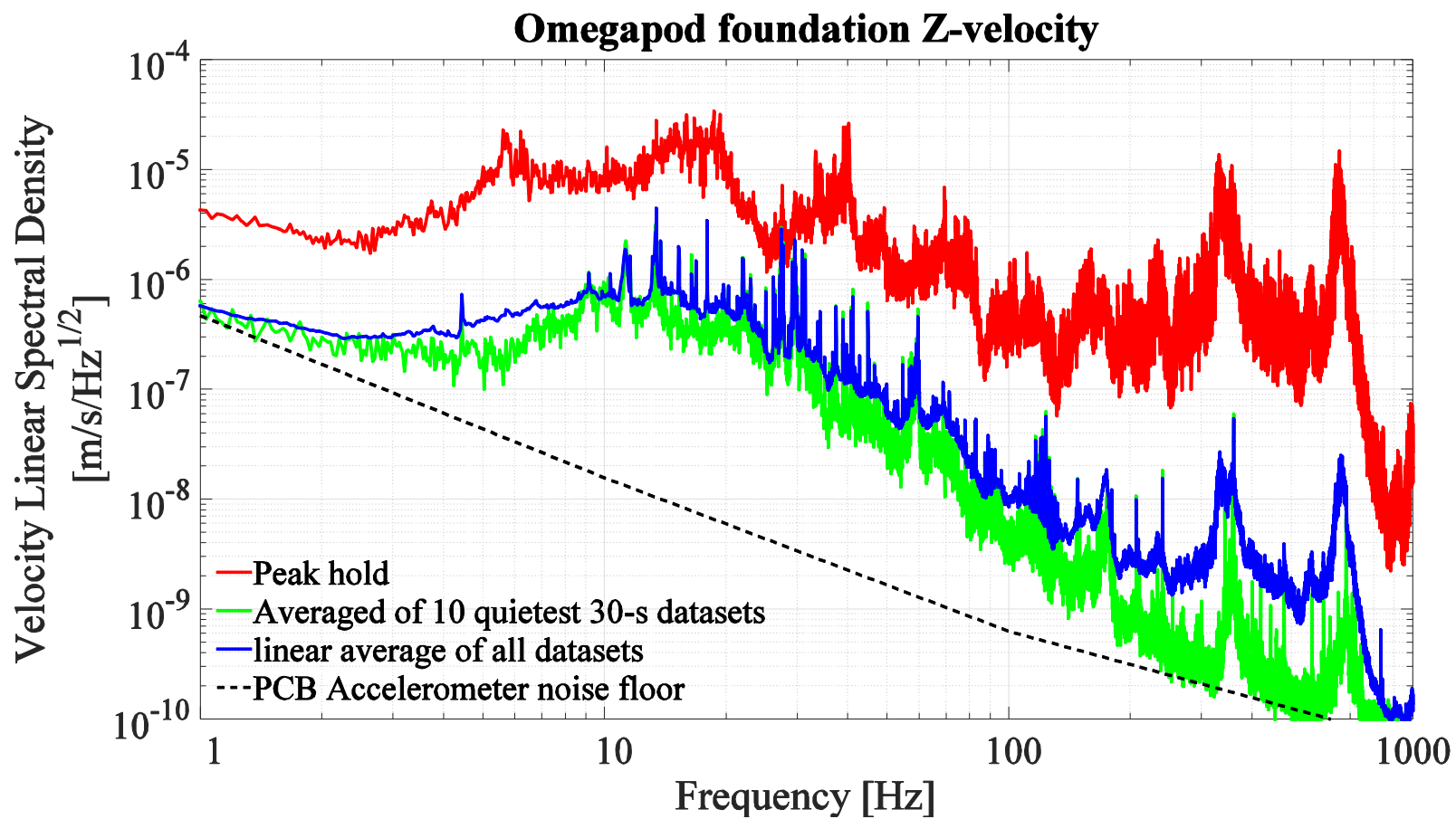


Figure 2.44 : Long-term vertical velocity spectra for the isolated foundation underneath the Omegapod inertia block.

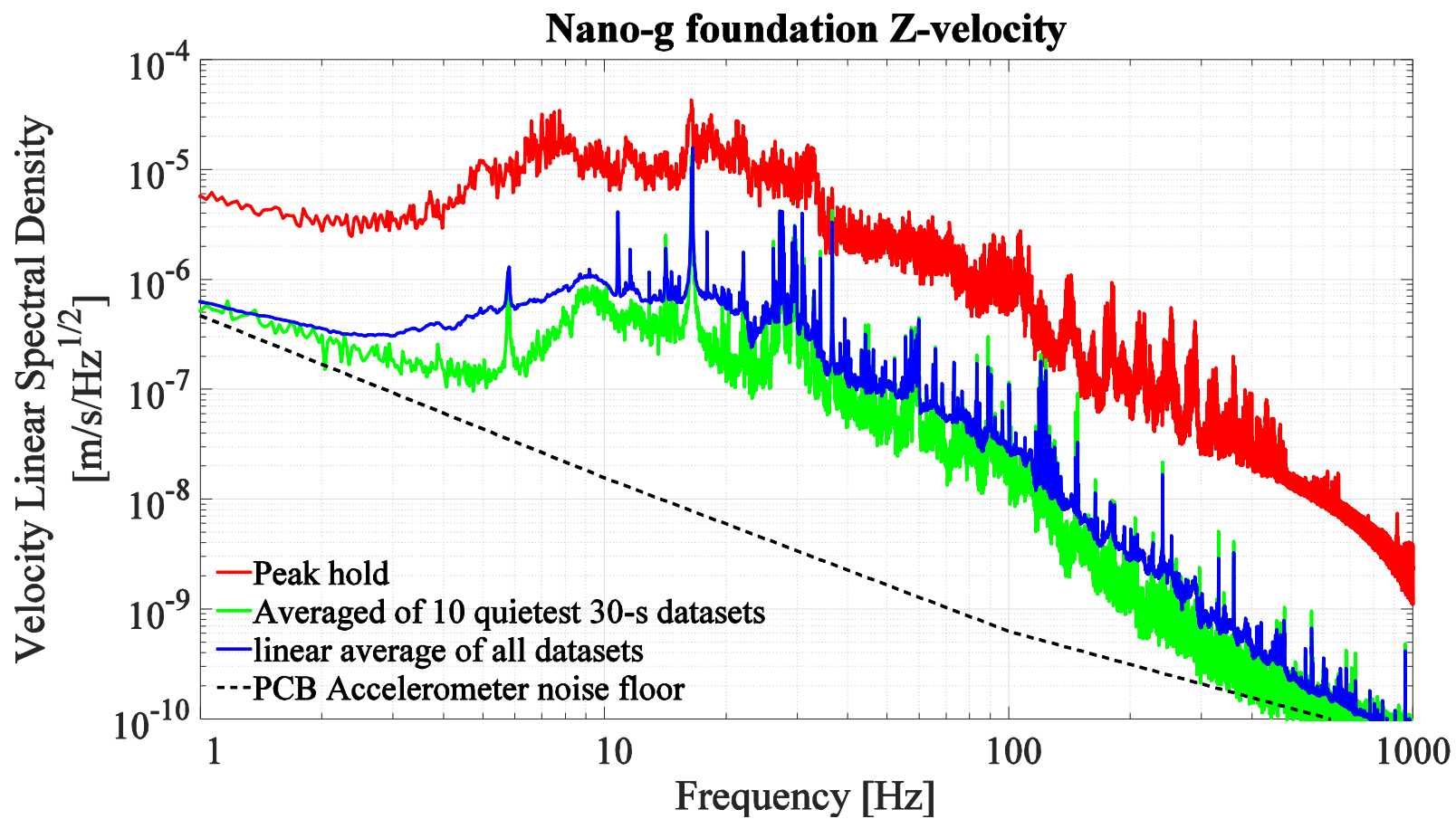


Figure 2.45 : Long-term vertical velocity spectra for the isolated foundation underneath the Nano-g inertia block.

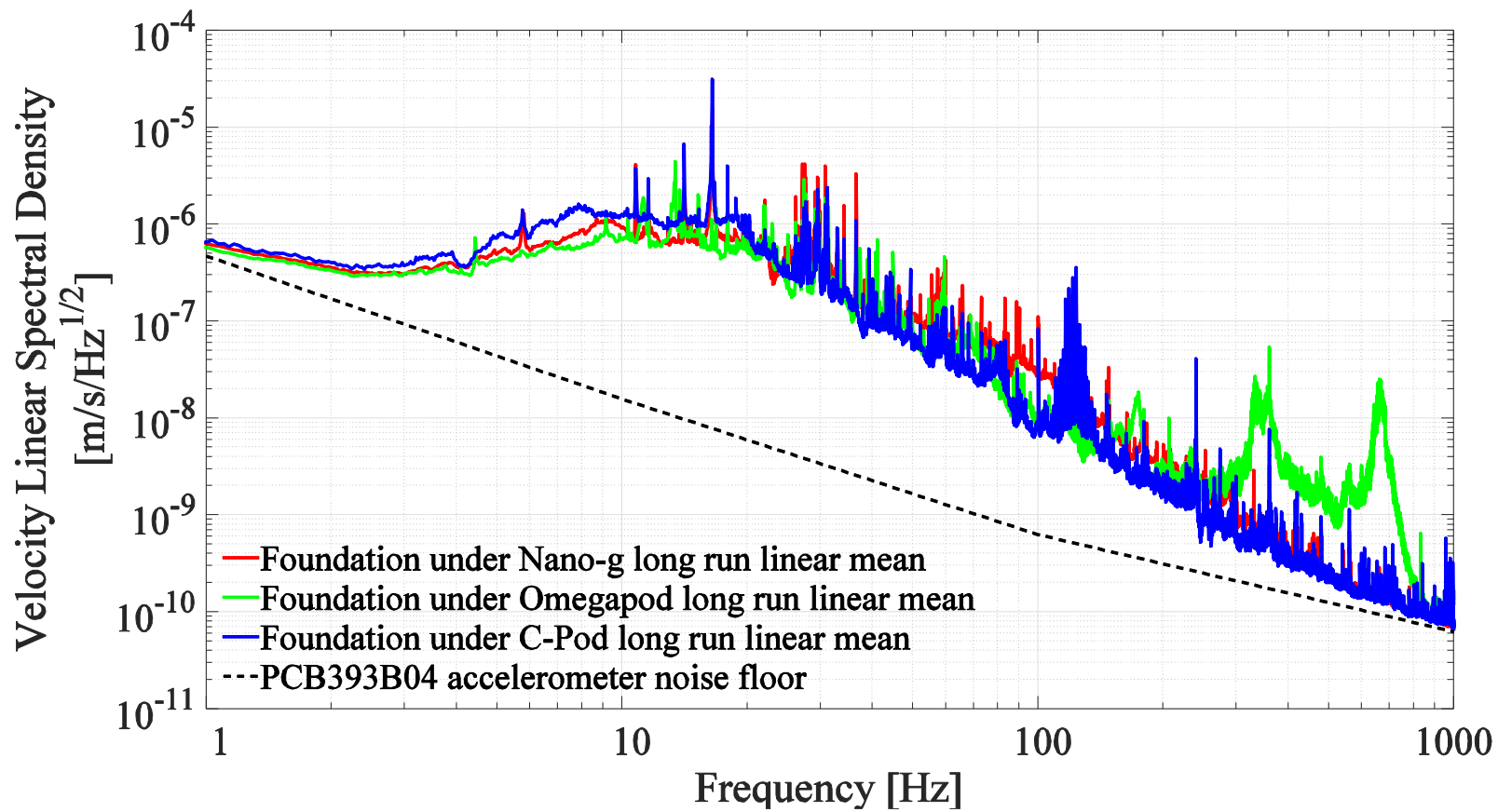


Figure 2.46 : Comparison of the long-run linear mean vertical foundation velocities at the three measurement locations on the two isolated foundations
 It is interesting to observe that the baseline level of vibration of both foundations begins a smooth, power-law like decrease above approximately 20 Hz, which is close to the FEA-predicted frequency of the highest rigid body mode.

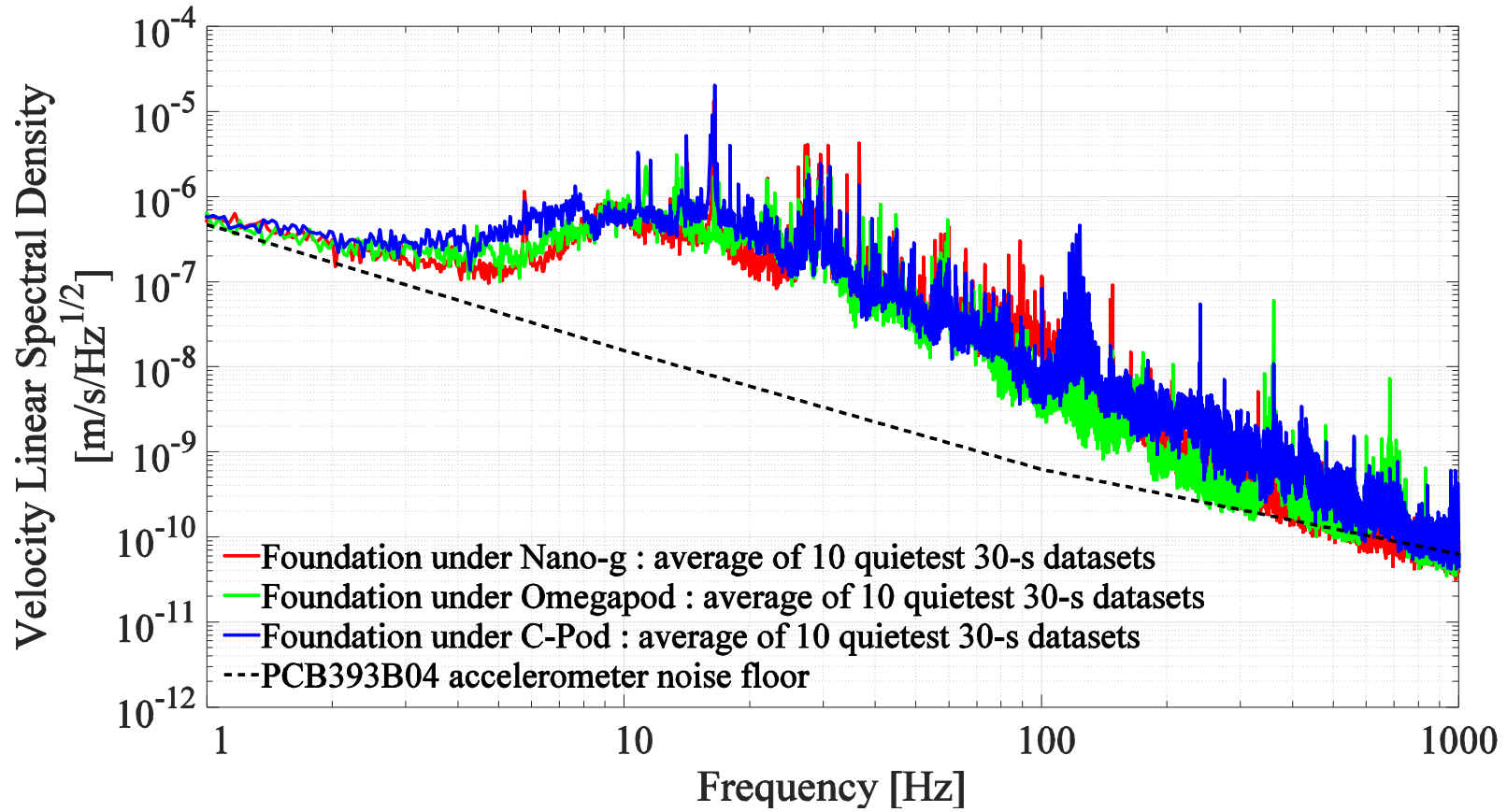


Figure 2.47 : Comparison of the average of the 10 quietest 30-s long vertical foundation velocity spectra at the three measurement locations on the two isolated foundations.

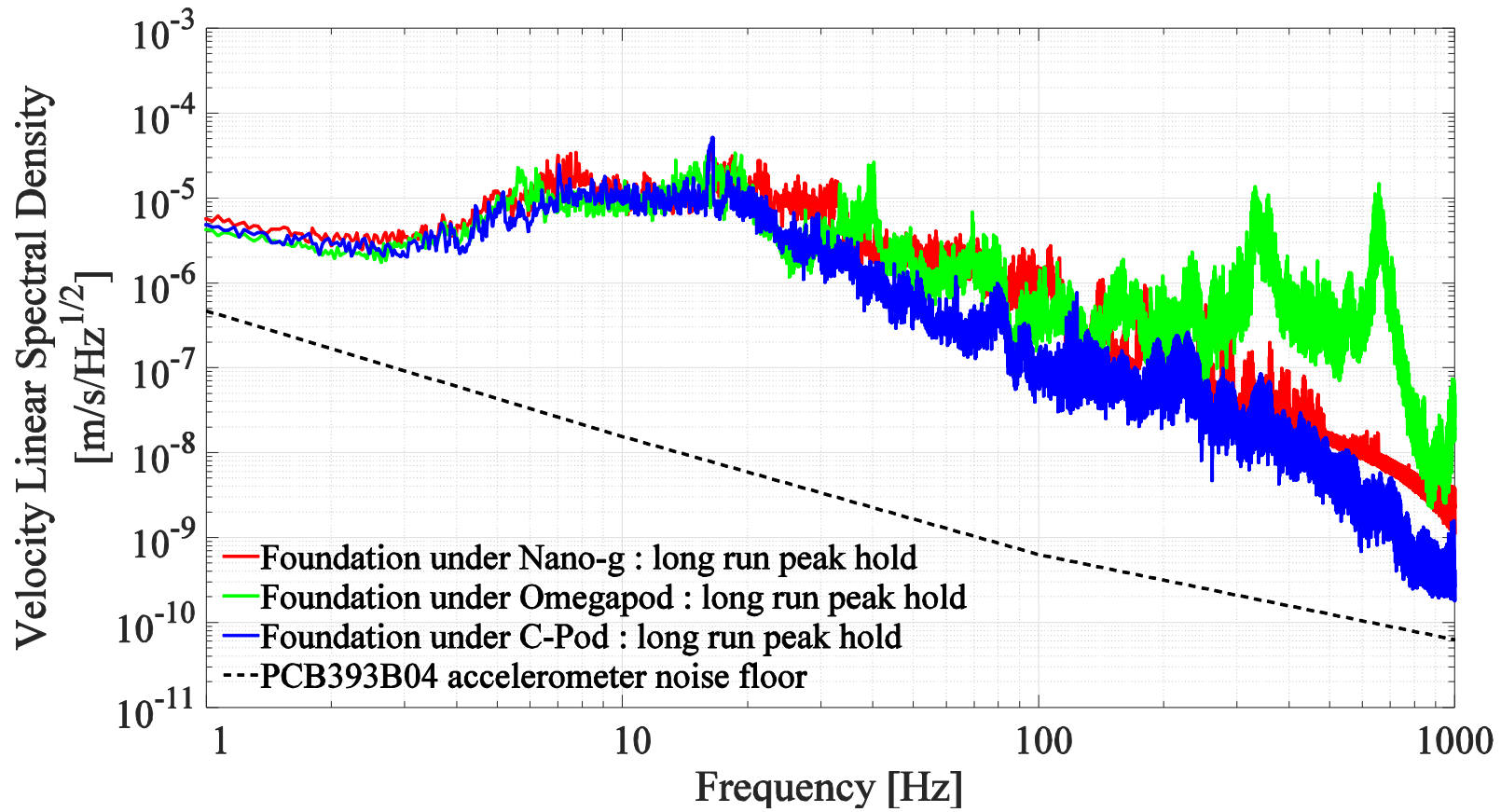


Figure 2.48 : Comparison of the long run peak-hold vertical velocity spectra at the three measurement locations on the two isolated foundations

The vertical direction foundation data above and the corresponding horizontal direction data (shown in Figures 2.49-2.55, below) show two interesting behaviours.

First, the spectrograms indicate that order-of-magnitude variations both in the RMS floor velocity and in the velocity level at any one frequency in the 1-1000 Hz band occur from night to day, at least when construction activity is taking place nearby.

Second, it is interesting to note the apparent roll off in the velocity spectrum on the isolated foundations of both monolithic isolation boxes above approximately 20 Hz. This is very near to the highest-frequency rigid body modes for the boxes predicted by the finite element analysis. Recalling that the pre-construction floor velocity spectra rolled off above 30Hz, this result suggests that the isolation boxes may be providing vibration isolation above the frequencies of their highest rigid body modes except perhaps at frequencies corresponding to their flexural resonances. This may explain some of the many sharp peaks on the downwards slope of the foundation velocity curves. This result appears to be consistent with the theory for the rigid vibrations of foundations developed in [13]. While achieving isolation boxes which have high flexural rigidity (and damping) is clearly desirable to avoid amplification of vibrations at the flexural resonances of these structures, the present data suggest that it may be desirable to place isolation boxes on much more compliant substrates to lower their fundamental resonant frequencies even further and achieve isolation at lower frequencies, effectively providing another stage of passive isolation prior to the inertia blocks.

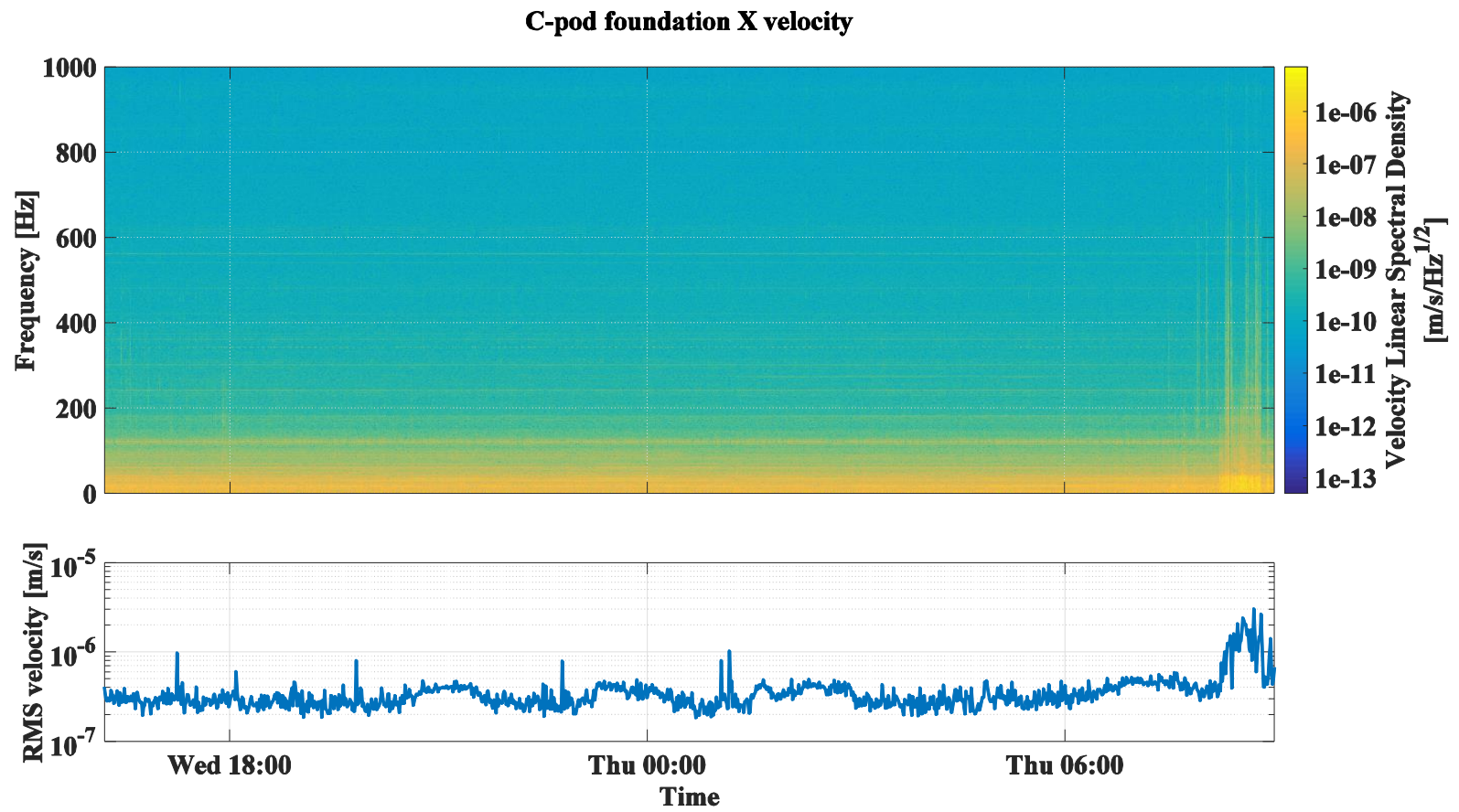


Figure 2.49 : Horizontal (X i.e. North-South) velocity spectrum and RMS velocity on the C-pod foundation vs time overnight into early morning

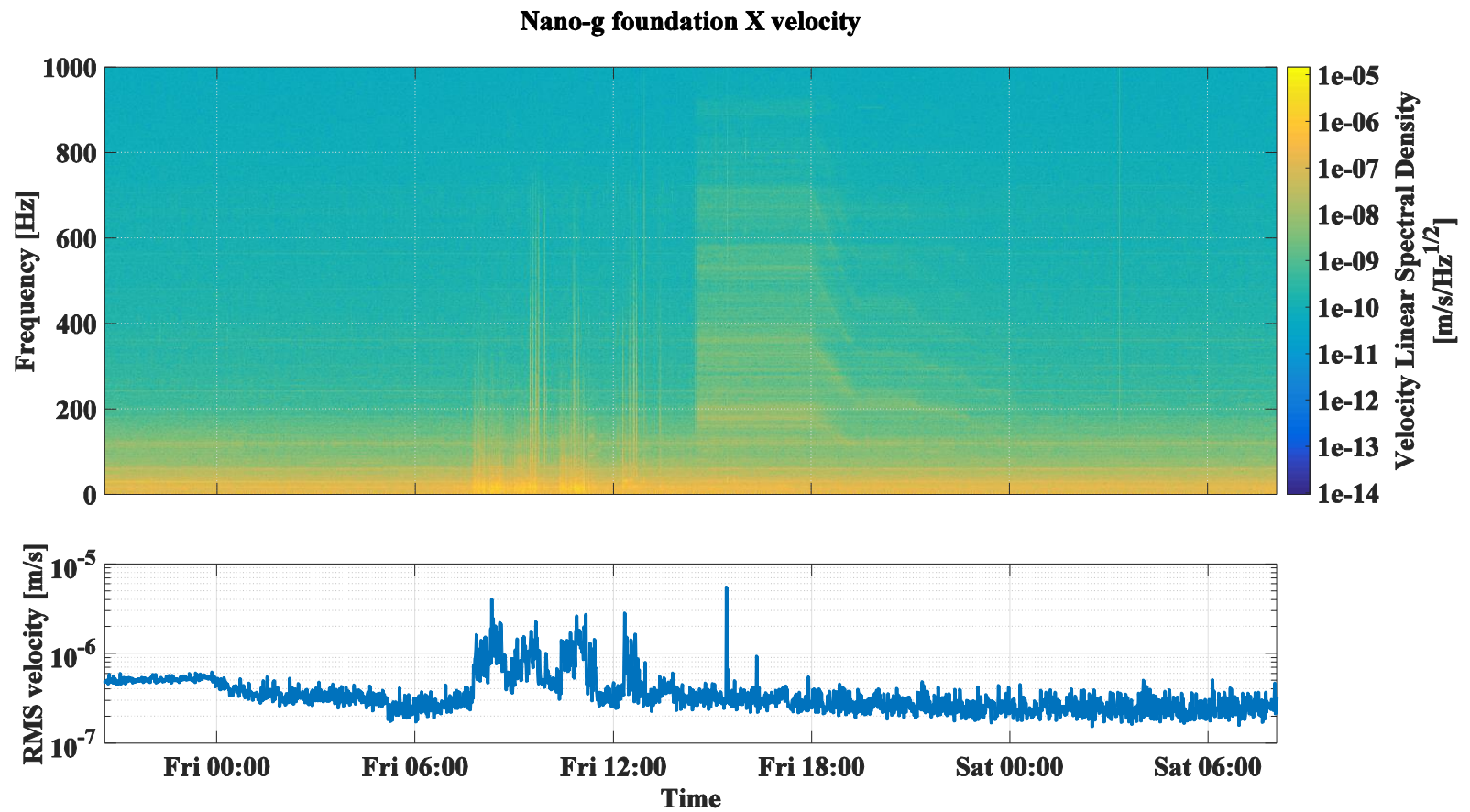


Figure 2.50: Horizontal (X i.e. North-South) velocity spectrum and RMS velocity on the Nano-g pod foundation vs time overnight, through a weekday and into a weekend morning.

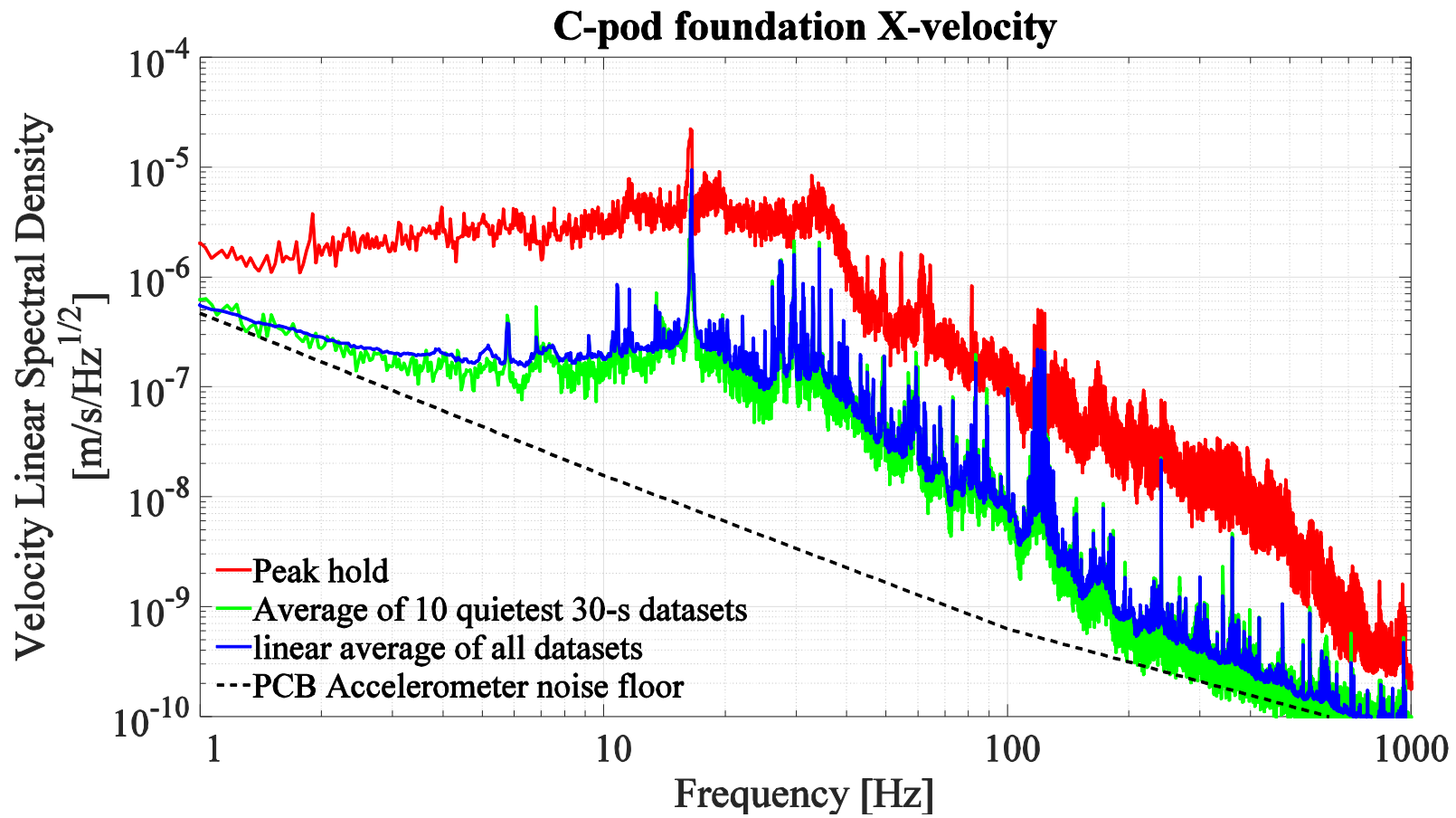


Figure 2.51: Long-term horizontal velocity spectra for the isolated foundation underneath the C-pod inertia block

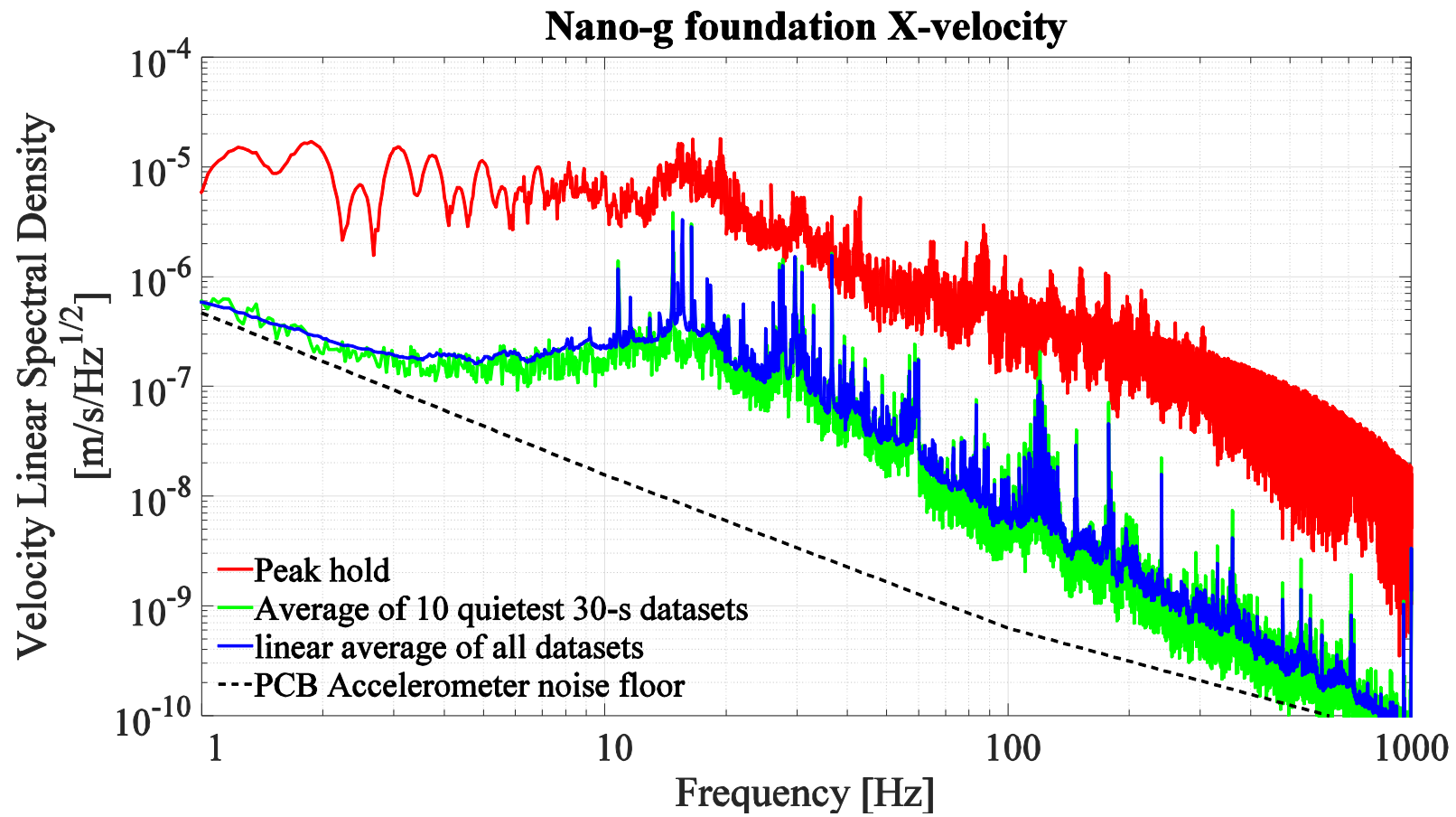


Figure 2.52: Long-term horizontal velocity spectra for the isolated foundation underneath the Nano-g pod inertia block

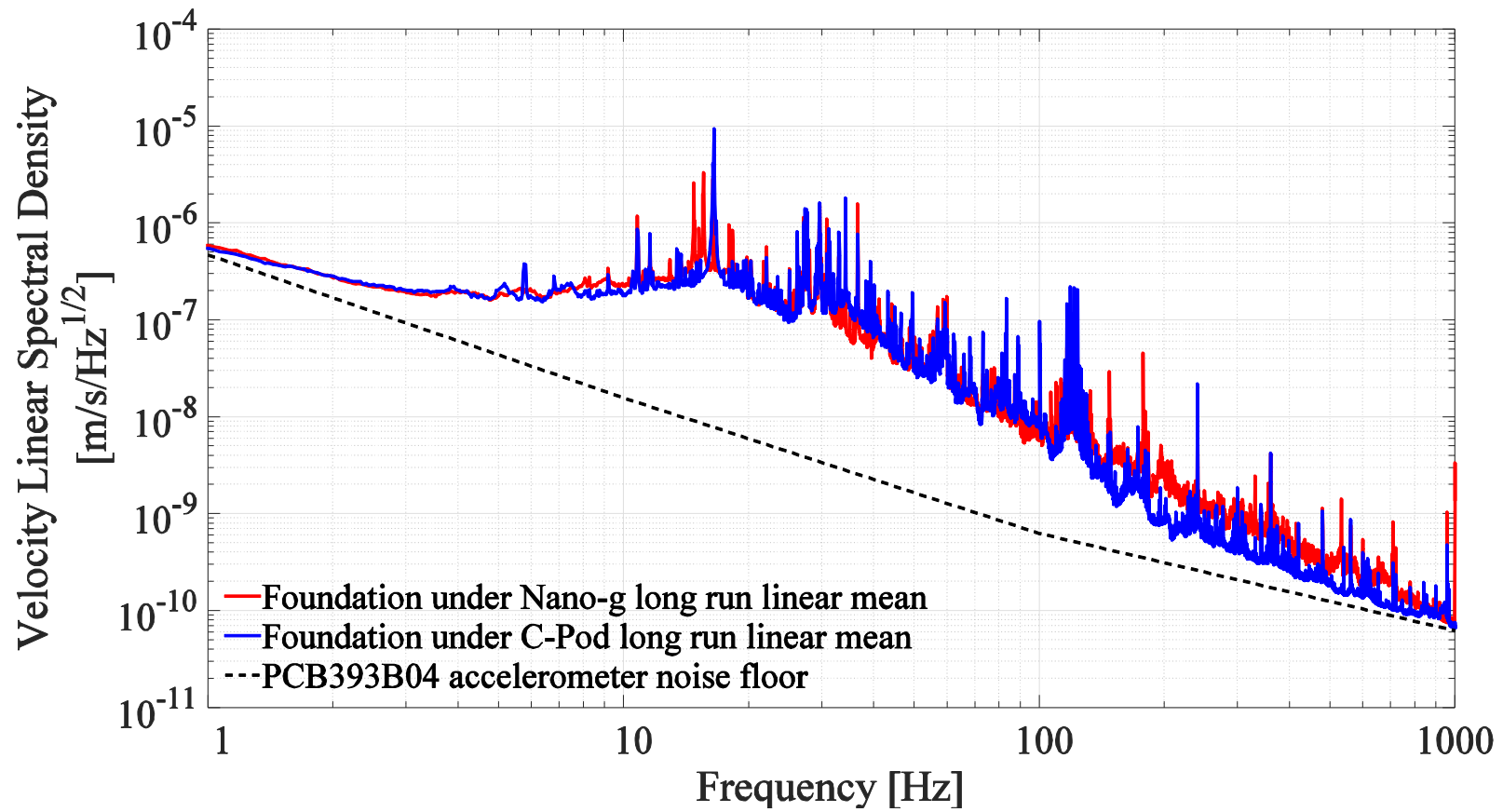


Figure 2.53 : Comparison of the long run mean horizontal velocity spectra on the two isolated foundations

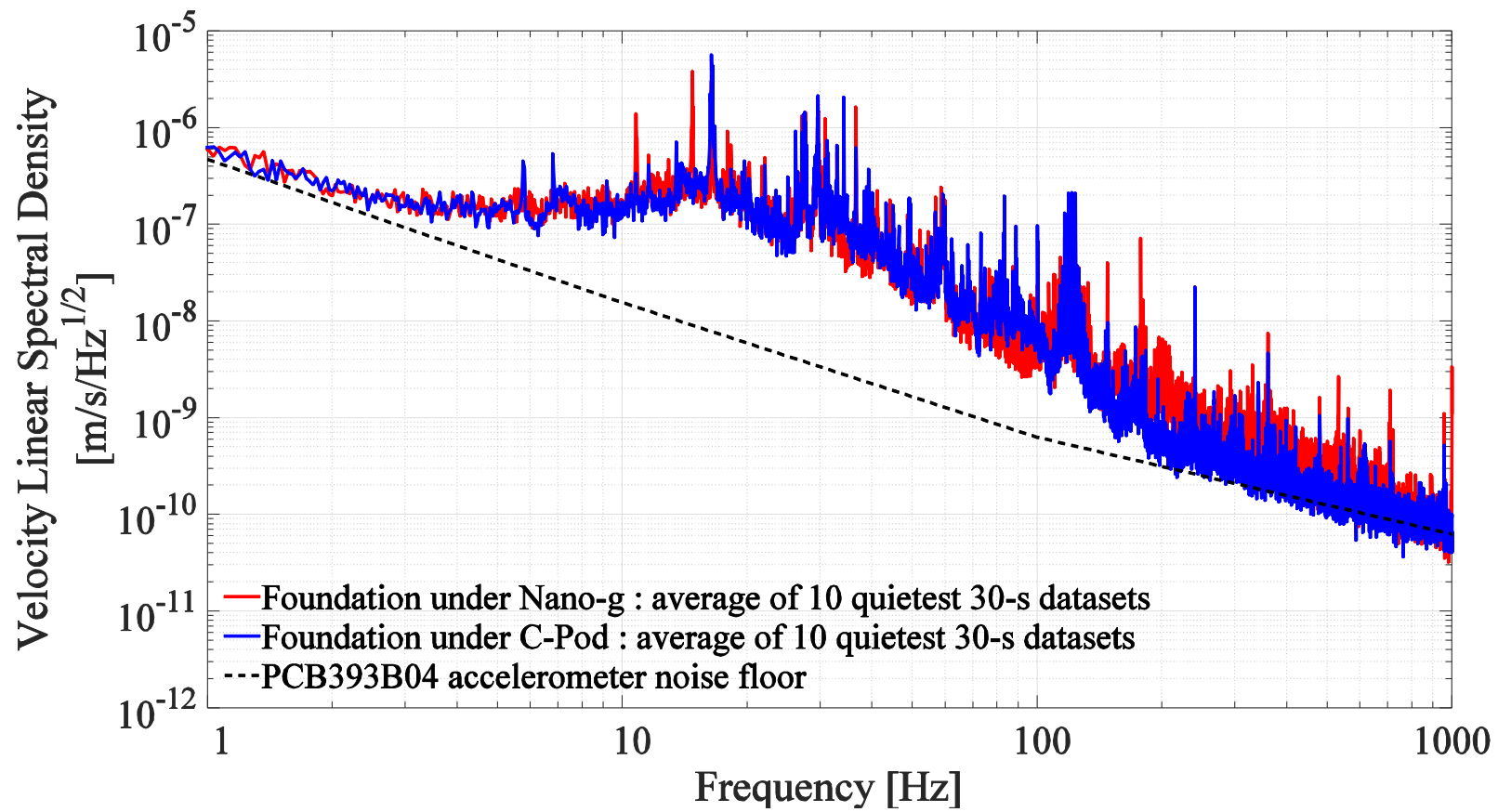


Figure 2.54 : Comparison of the average of the 10 quietest 30-s horizontal velocity spectra on the two isolated foundations

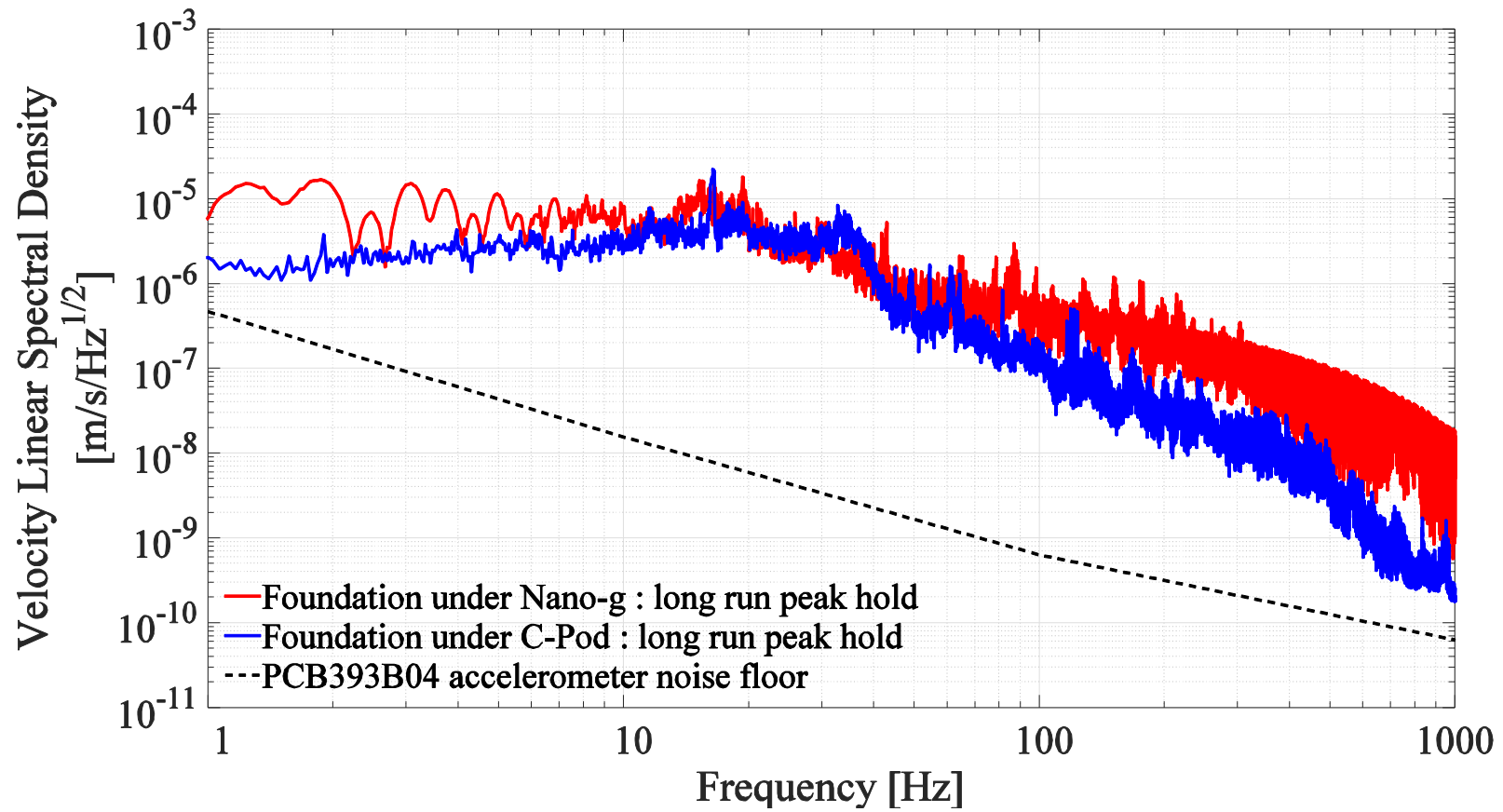


Figure 2.55 : Comparison of the long run peak-hold horizontal velocity spectra on the two isolated foundations

2.7.2 Inertia blocks

In this section, simulations and measurements of the rigid-body and flexural vibrations of the LAIR's massive concrete inertia blocks are presented.

2.7.2.1 Simulation of inertia block vibrational mode frequencies

Based on the nominal properties of the designed inertia blocks and the isolators selected, the rigid body and first six flexural modes of the inertia blocks were calculated using COMSOL eigenfrequency FEM simulations with COMSOL 5.1 and the COMSOL Structural Mechanics module . For all of the simulations presented in this section, the mesh sequence type used was “Physics-controlled mesh” and the element size was set to “extra-fine”.

To model the rigid body modes, effective support stiffnesses $k_{eff} = (2\pi f_0)^2 m$ were calculated in the horizontal and vertical directions based on the calculated inertia block masses (m) and the nominal heavy-load isolator vertical and horizontal resonant frequencies (f_0).

These stiffnesses were inputted into the model using a “Spring Foundation” constraint applied to the isolator support flanges of the inertia blocks, approximating the real support conditions provided by the pneumatic isolators.

The materials properties used in these simulations were a linear volume-weighted average of the concrete properties and the reinforcing bar properties. Although this rule of mixing approach to effective medium theory for reinforced concrete is very crude, the low total volume of reinforcement even in the very heavily reinforced concrete used for the inertia blocks means that the corrections to the material properties of the un-reinforced concrete are likely to be small. The principal consequence of this is that the choice of concrete is important since the

elastic properties of the inertia block composite are dominated by the properties of the concrete. The material properties used for the simulations are summarized in Table 2.12; the key results - rigid body mode frequencies and fundamental flexural mode shapes and frequencies - of the simulations are summarized in Table 2.13 and Figure 2.56. Higher order flexural mode shapes are presented alongside the experimentally measured mode shapes in section 2.7.2.3.

Material	Young's modulus	Density	Poisson's ratio	% composition of inertia block by volume
High strength concrete	30 <i>GPa</i>	2400 <i>kg/m³</i>	0.2	96
Fiber reinforced plastic	55 <i>GPa</i>	2000 <i>kg/m³</i>	0.25	3
Stainless steel	200 <i>GPa</i>	8000 <i>kg/m³</i>	0.28	1
Inertia block reinforced concrete – approximate composite properties	0.96×30 $+0.03 \times 55$ $+0.01 \times 200$ $= 32.5 \text{ } GPa$	0.96×2400 $+0.03 \times 2000$ $+0.01 \times 8000$ $= 2444 \text{ } kg/m^3$	0.96×0.2 $+0.03 \times 0.25$ $+0.01 \times 0.28$ $= 0.2023$	100

Table 2.12 : Material properties used in FEM simulations of the inertia block resonant frequencies

Pod	Vertical Resonant Frequency (total vertical stiffness)	Horizontal Resonant Frequency (total horizontal stiffness)	Calculated rolling Mode frequencies (Hz)			Lowest calculated flexural mode frequencies (Hz)					
			About NS axis	About EW axis	About vertical axis	1 st	2 nd	3 rd	4 th	5 th	6 th
C-pod	0.8 Hz	0.7 Hz	1.19	1.25	1.14	236	288	349	368	392	459
Omegapod	0.8 Hz	0.7 Hz	0.85	0.67	0.94	202	278	324	363	375	382
Nano-g	0.8 Hz	0.7 Hz	0.93 ¹¹	0.85 ¹²	0.9	186	189	281	294	329	355

Table 2.13 : Summary of the results of finite element simulations of the rigid and flexural vibrational modes of the LAIR inertia blocks

¹¹ The broken symmetry of the Nano-g inertia block results in the principal axes of inertia not being aligned with the Cartesian axes of the basement. The principal moment of inertia in the North-South column is along an axis with normalized components 0.93 in the South direction and 0.37 in the East direction.

¹² See the above footnote. The principal moment of inertia in the East-West column is along an axis with normalized components 0.37 in the North direction and 0.93 in the East direction.

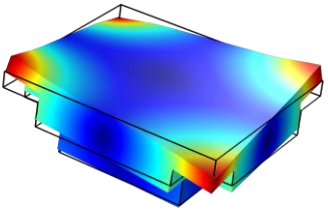
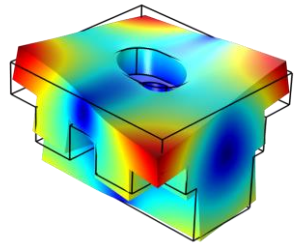
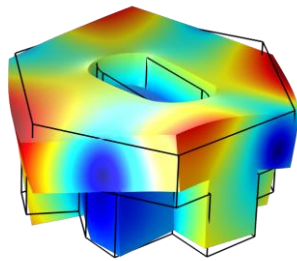
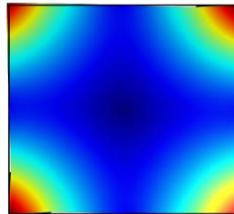
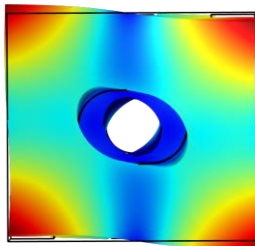
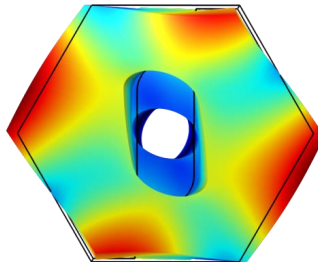
		
		
<p>C-pod fundamental flexural mode :</p> <p>236 Hz</p>	<p>Omegapod fundamental flexural mode:</p> <p>202 Hz</p>	<p>Nano-g fundamental flexural mode :</p> <p>186 Hz</p>

Figure 2.56: Plan and isometric views of the FEA-predicted fundamental flexural mode shapes for the three LAIR inertia block

2.7.2.2 Initial commissioning of inertia blocks

Measurements made by Dr. Yan Pennec and Vincent Wong from the LAIR and Steven Shedd from Integrated Dynamics Engineering (IDE) during the initial commissioning of the inertia block are summarized in this section.

Numeric values describing the rigid body resonance behavior of the inertia blocks - summarized in Table 2.14 - are taken from the IDE commissioning report- [63] . These data show that the inertia blocks have rigid body resonances around 1 Hz in the horizontal and vertical directions. While the vertical mode of the Nano-g inertia block is well damped, the horizontal direction of that block and all the directions of the other blocks are more weakly damped. This is due to the adjustable damping valve fitted to the PD-3001H isolators of the Nano-g inertia block which is not effective for horizontal motions and is not present on the isolators of the other inertia blocks.

Plots of the absolute velocity levels measured on the three inertia blocks created from raw data taken by Vincent Wong and Dr. Pennec are shown in Figure 2.57 and Figure 2.58. The data presented in these plots suffer badly from the noise floor limitation of the accelerometer, a finding which led to the later purchase of a (much more expensive) Wilcoxon 731A.

The data in Table 2.14 were calculated from empirical transfer functions for the inertia blocks' accelerations relative to the foundation accelerations measured by Steven Shedd and reprinted with permission from IDE's commissioning report [63]. These data were acquired at 200 Hz, for an unknown time period at unspecified locations on the top surfaces of the floating inertia blocks. Proprietary IDE vibration sensors were used. These transfer functions show relatively ideal behavior from resonance until ~10-20 Hz at which point features which are not predicted by a 2nd order transfer function appear. These feature are conjectured to be off-

resonance excitations of the inertia block motion by acoustic forces and are analyzed in more detail in section 2.7.2.5 .

Direction	Quantity	C-Pod	Omegapod	Nano-g pod
X (NS)	Resonant Frequency	1.02 Hz	0.81 Hz	0.65 Hz
	Amplification at resonance	26.7 dB	24.2 dB	23.6 dB
Y (EW)	Resonant Frequency	1.02 Hz	0.96 Hz	0.65 Hz
	Amplification at resonance	30.1 dB	28.2 dB	25.5 dB
Z (Vertical)	Resonant Frequency	1.4 Hz	1.2 Hz	0.7 Hz ¹³
	Amplification at resonance	20.5 dB	17.9 dB	1.62 dB

Table 2.14: Summary of rigid-body vibration characteristics of the three LAIR inertia blocks upon commissioning in 2012. The resonant frequencies and amplifications at resonance are taken from Integrated Dynamics Engineering’s commissioning report [63].

¹³ A 2.5 Hz peak with a time constant of 0.476 s - attributed to a rocking mode of the block – can be measured on the Nano-g inertia block for accelerometer locations near the edges but was not observed in IDE’s measurements.

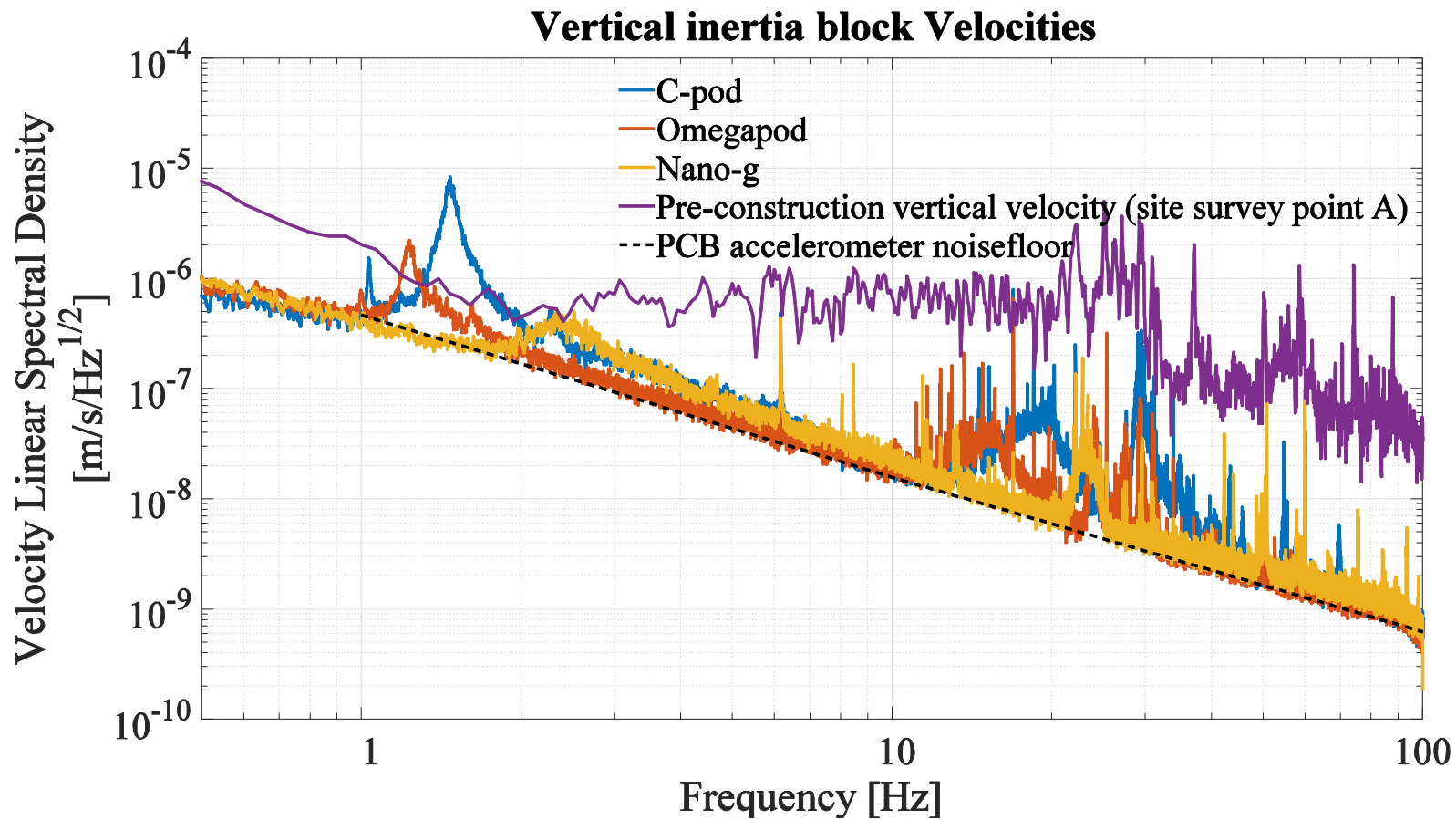


Figure 2.57: Vertical inertia block velocities on the three inertia blocks. A 0.01 Hz wide moving average filter has been applied to reduce the variance of these curves. Substantial improvement from the pre-construction velocity levels is evident, however the noise floor of the PCB 393B04 accelerometer obscures the true performance of the inertia blocks at many frequencies. The resonances of the inertia blocks around 1-2 Hz are evident, as is the superior damping of the resonance of the Nano-g inertia block relative to the other two. In a later section, it will be argued that ~10-40 Hz peaks are due to acoustic forces.

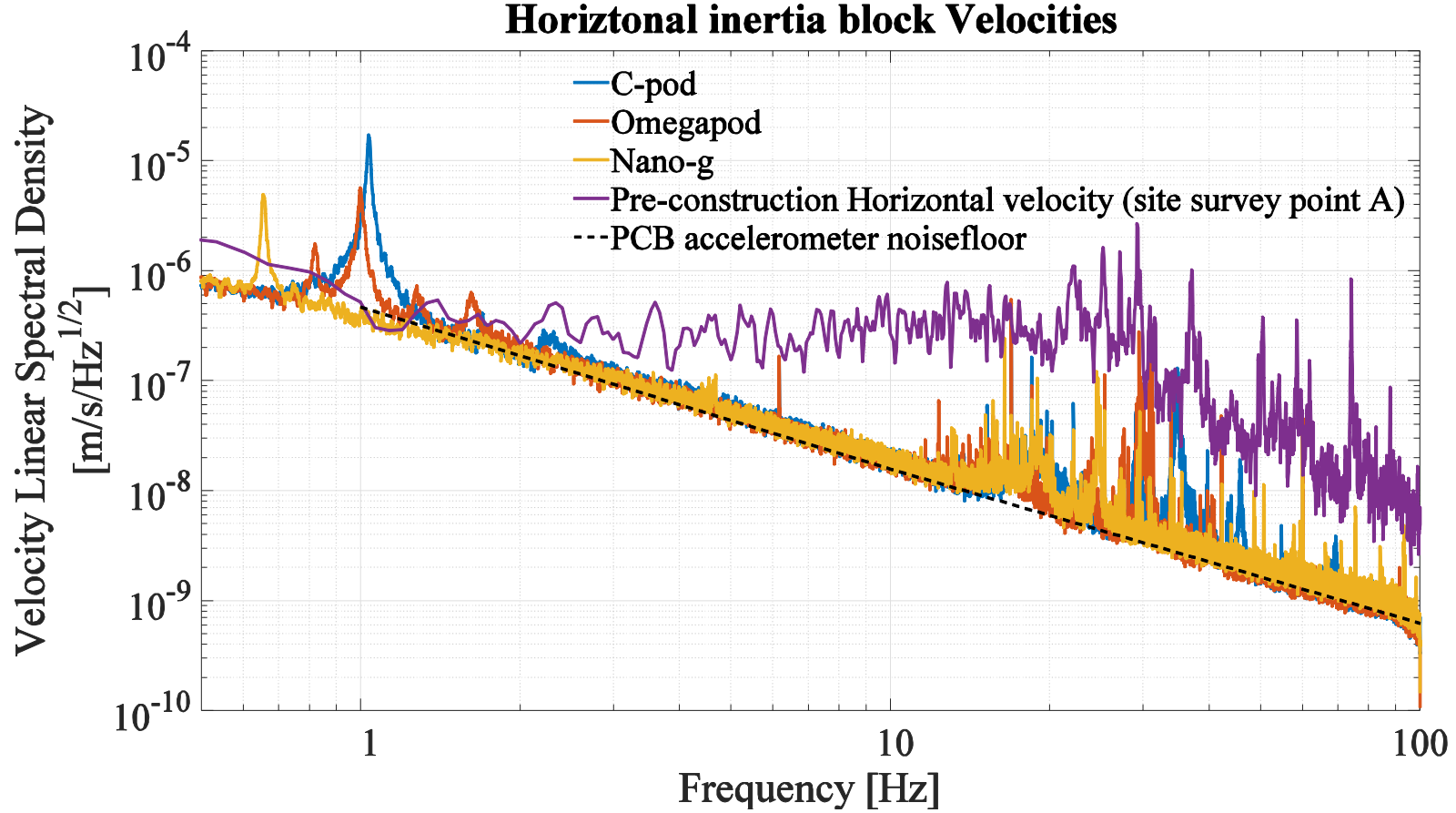


Figure 2.58: Horizontal inertia block velocities on the three inertia blocks. Poor damping of the rigid body modes (peaks ~1Hz) is apparent for all three inertia blocks. The multiple small peaks present around 1Hz in the Omegapod velocity spectrum are likely multiple rigid body modes (horizontal shifting, rocking, vertical mode) coupling to the accelerometer signal.

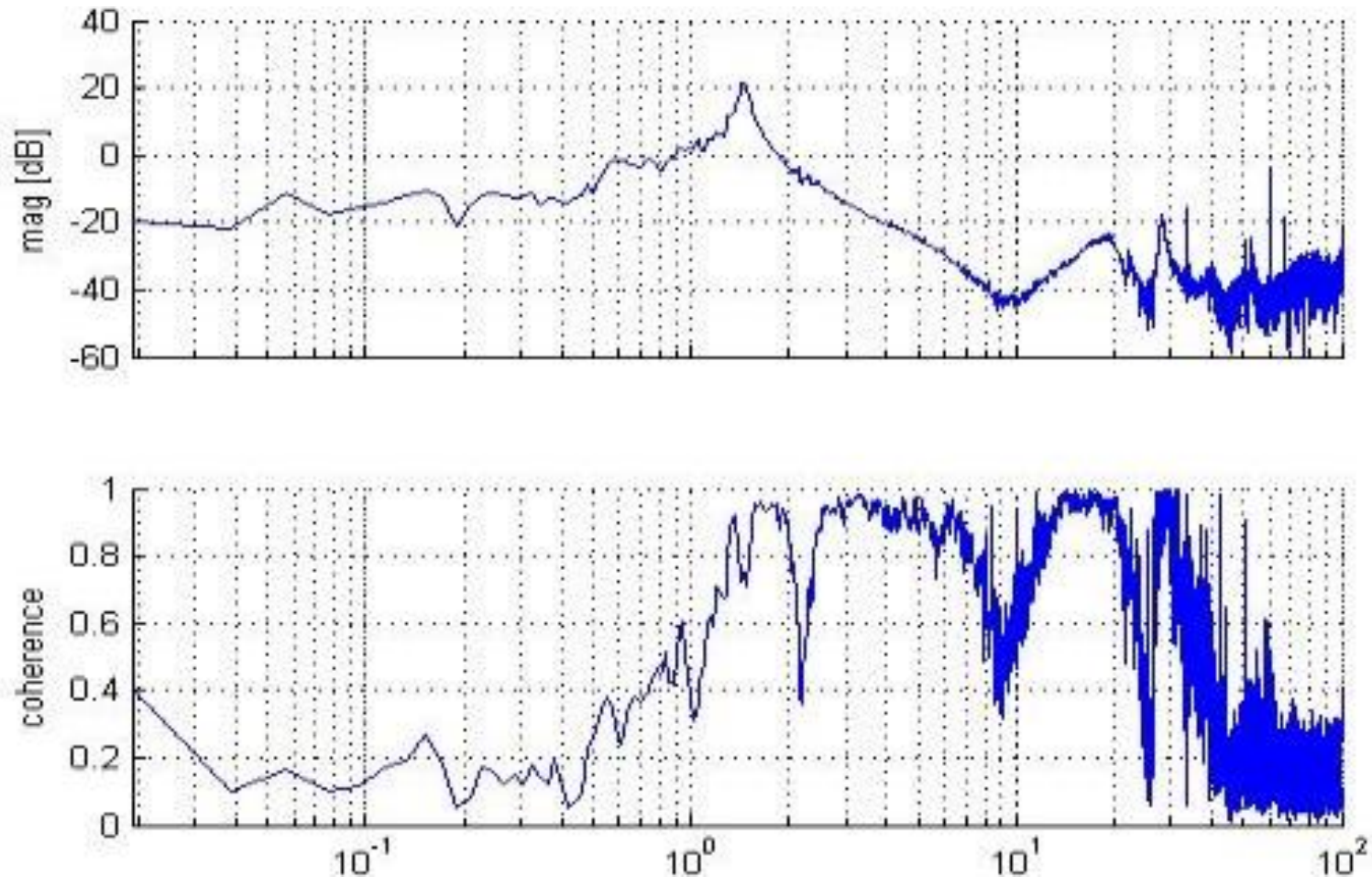


Figure 2.59 : C-Pod inertia block vertical axis transfer function showing a resonant frequency of 1.42 Hz and 20.5 dB amplification at resonance. Image reprinted with permission from [63] (slide 4) © 2012 Steve Shedd/Integrated Dynamics Engineering. As is the case in all the transfer functions shown in this thesis, sensor noise contaminates the measurement below about 1 Hz, yielding poor coherence and an empirical transfer function that does not approach 1 in the low frequency limit. Roughly ideal behavior is evident from low frequencies until ~10 Hz, where it will be argued that acoustic forces become relevant.

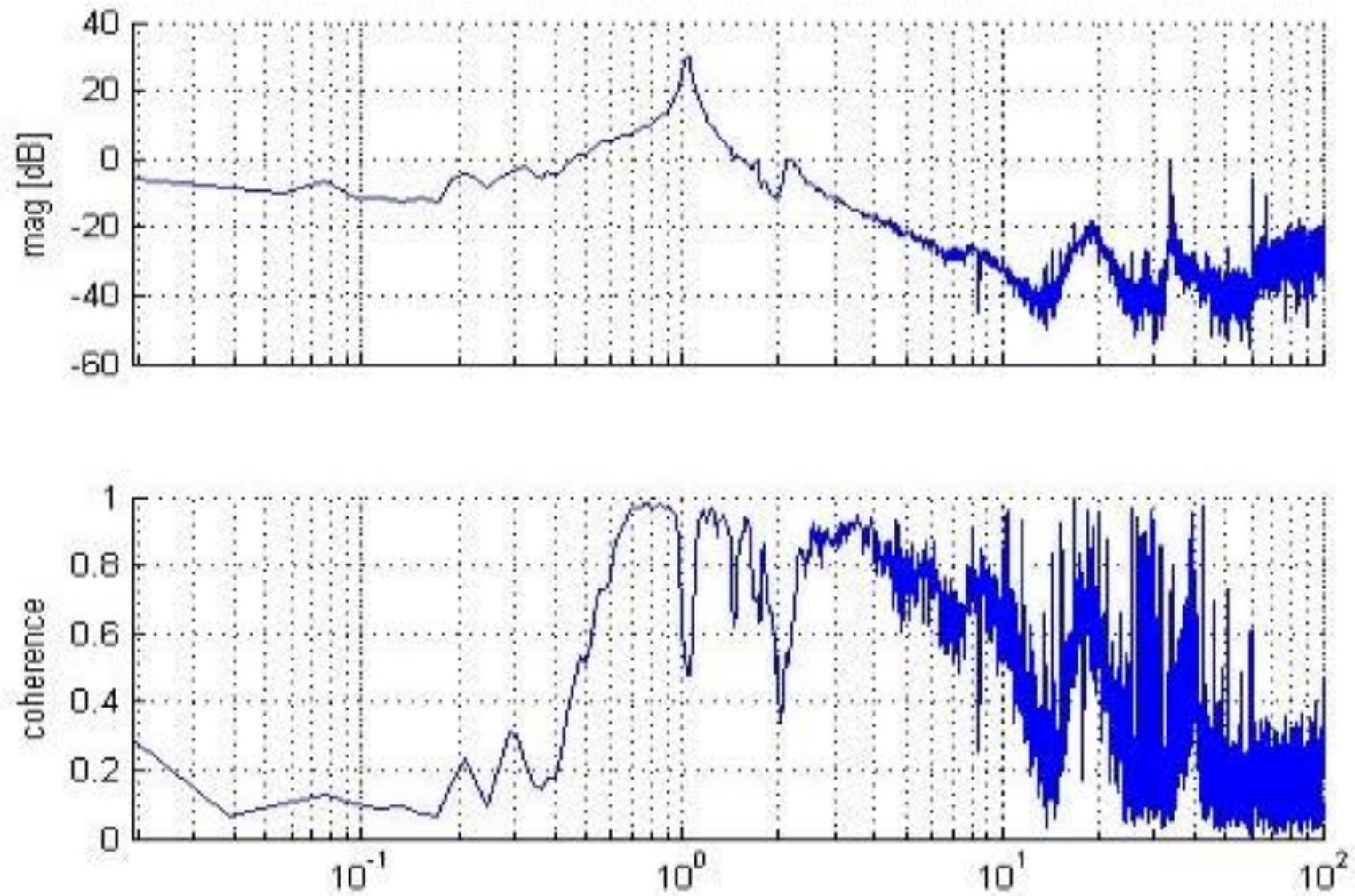


Figure 2.60: C-Pod inertia block East-West-axis transfer function showing a resonant frequency of 1.02 Hz and 30.1 dB amplification at resonance. Image reprinted with permission from [63] (slide 5) © 2012 Steve Shedd/Integrated Dynamics Engineering

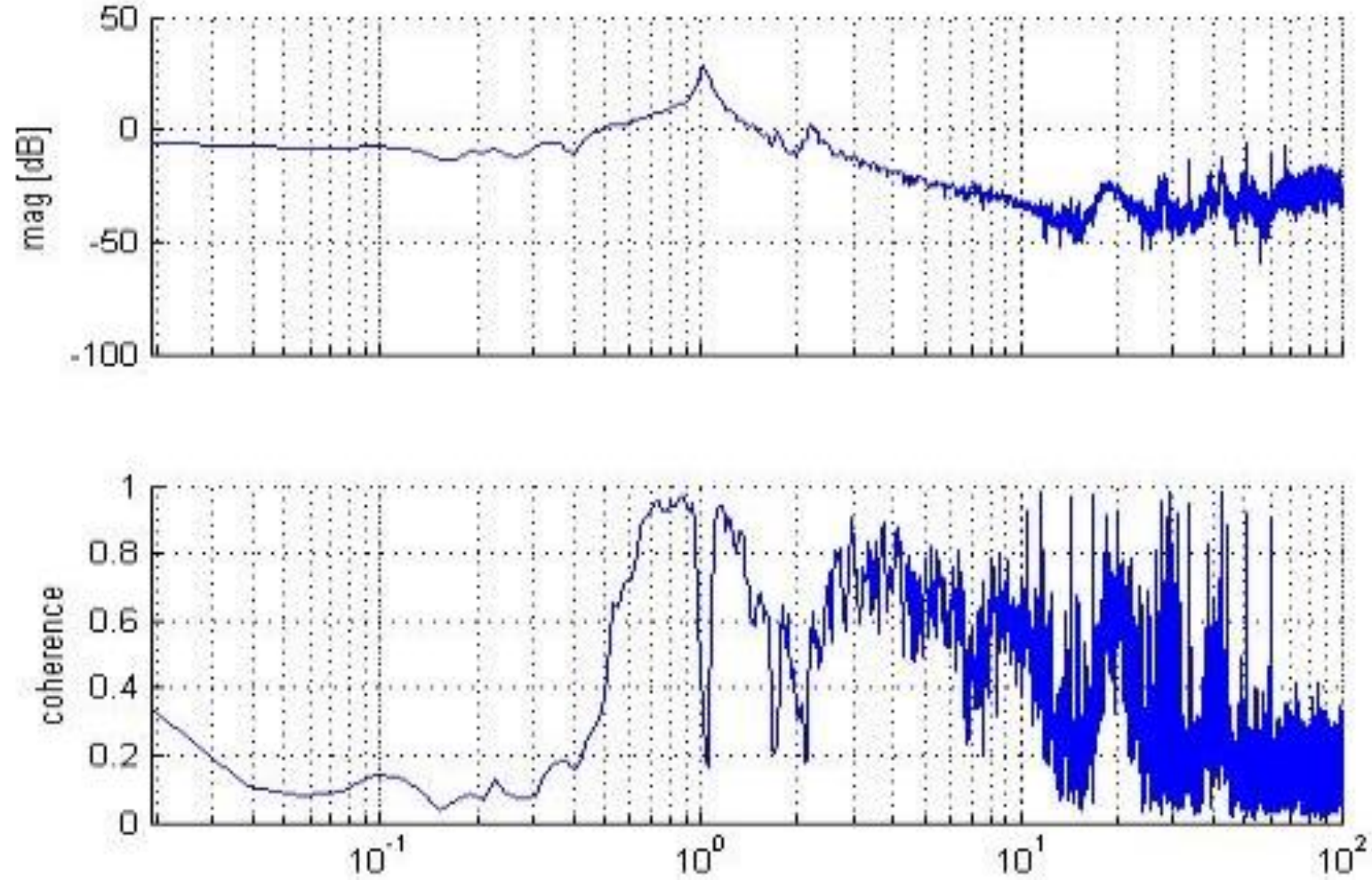


Figure 2.61: C-Pod inertia block North-South axis transfer function showing a resonant frequency of 1.02 Hz and 26.7 dB amplification. Image reprinted with permission from [63] (slide 6) © 2012 Steve Shedd/Integrated Dynamics Engineering

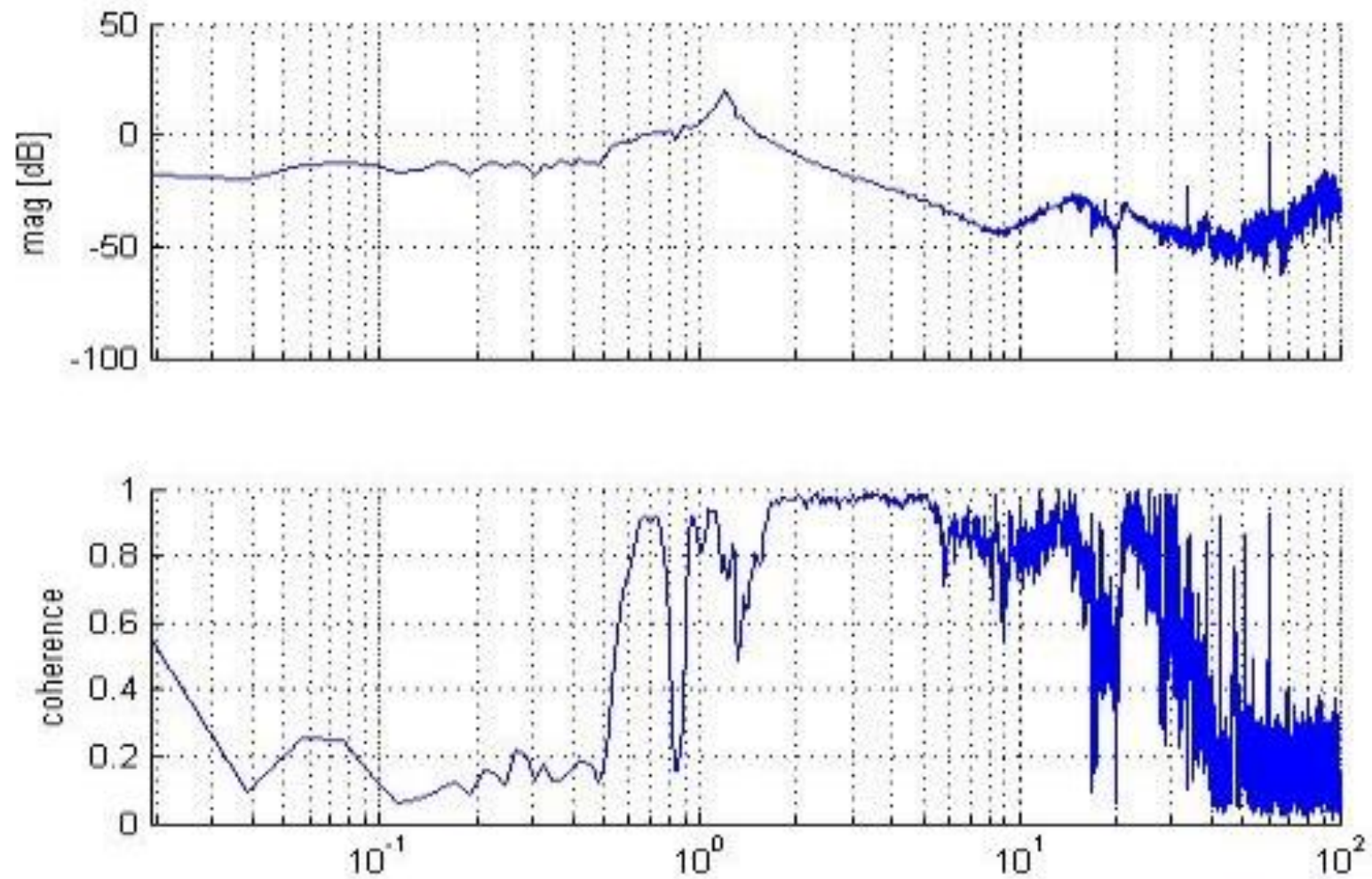


Figure 2.62: Omegapod inertia block vertical axis transfer function showing a resonant frequency of 1.16 Hz and 17.9 dB amplification at resonance. Image reprinted with permission from [63] (slide 12) © 2012 Steve Shedd/Integrated Dynamics Engineering

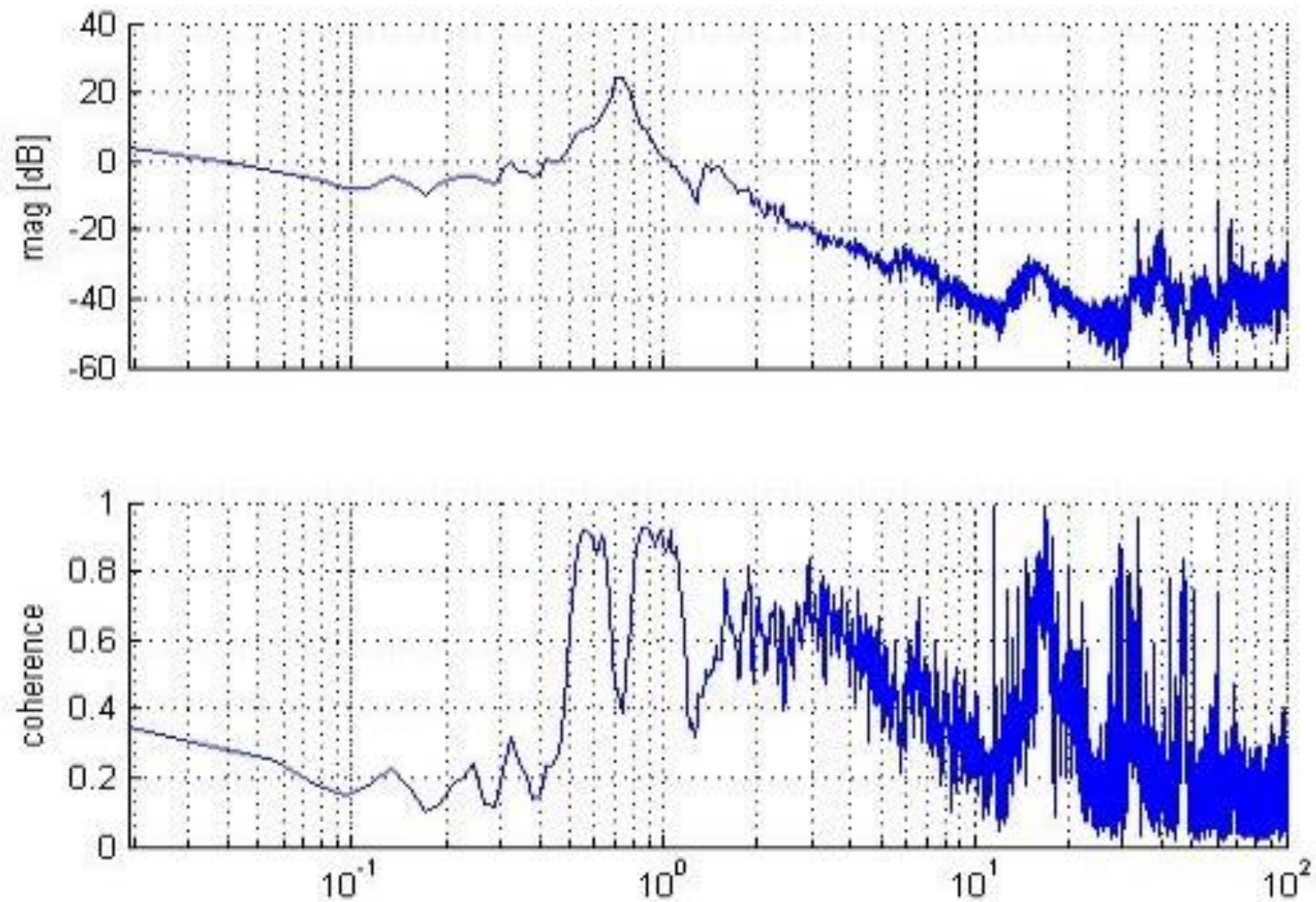


Figure 2.63 : Omegapod inertia block North-South axis transfer function showing a resonant frequency of 0.74 Hz and 24.2 dB amplification at resonance. Image reprinted with permission from [63] (slide 13) © 2012 Steve Shedd/Integrated Dynamics Engineering

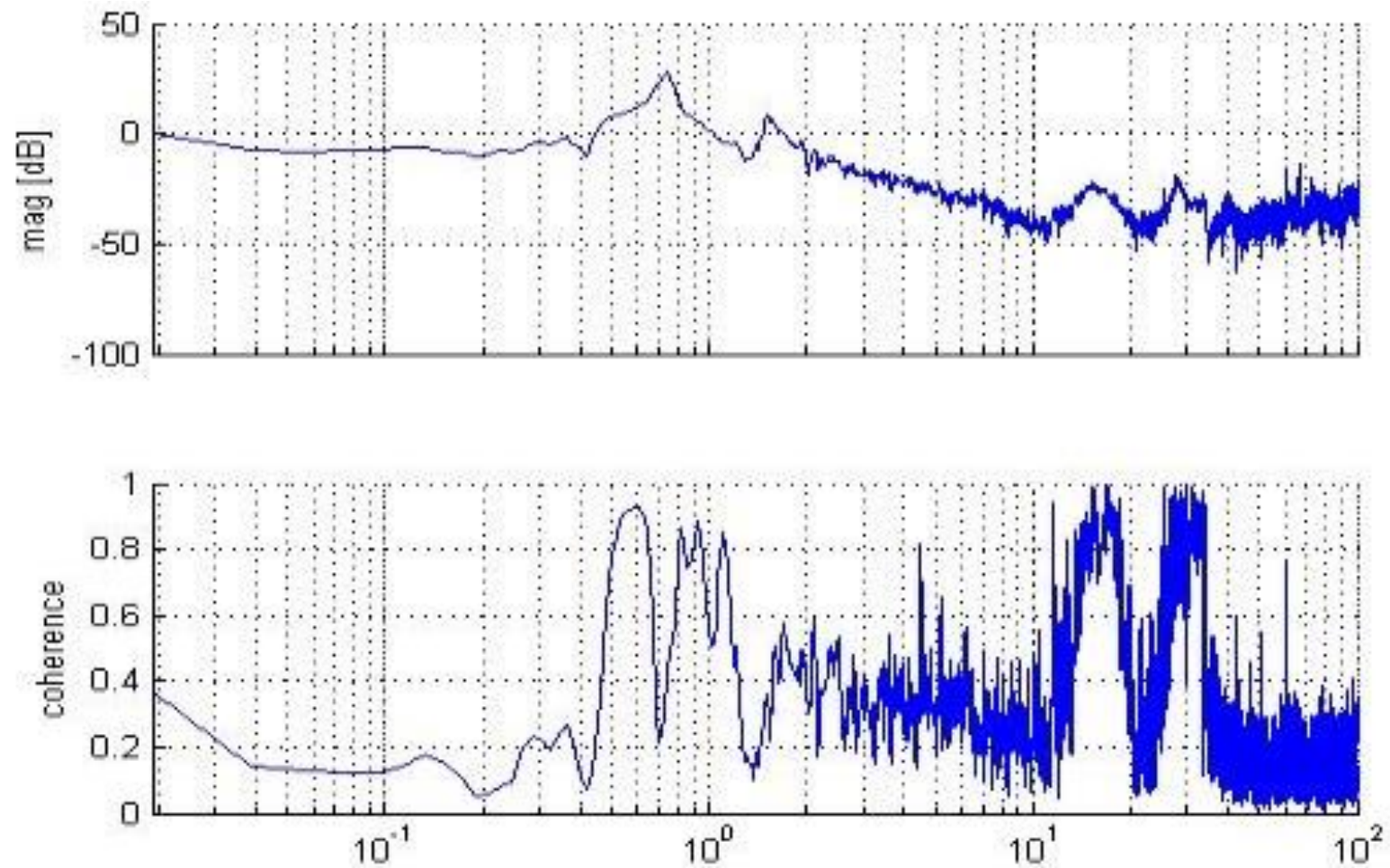


Figure 2.64: Omegapod inertia block East-West axis transfer function showing a resonant frequency of 0.74 Hz and 28.2 dB amplification at resonance. Image reprinted with permission from [63] (slide 14) © 2012 Steve Shedd/Integrated Dynamics Engineering

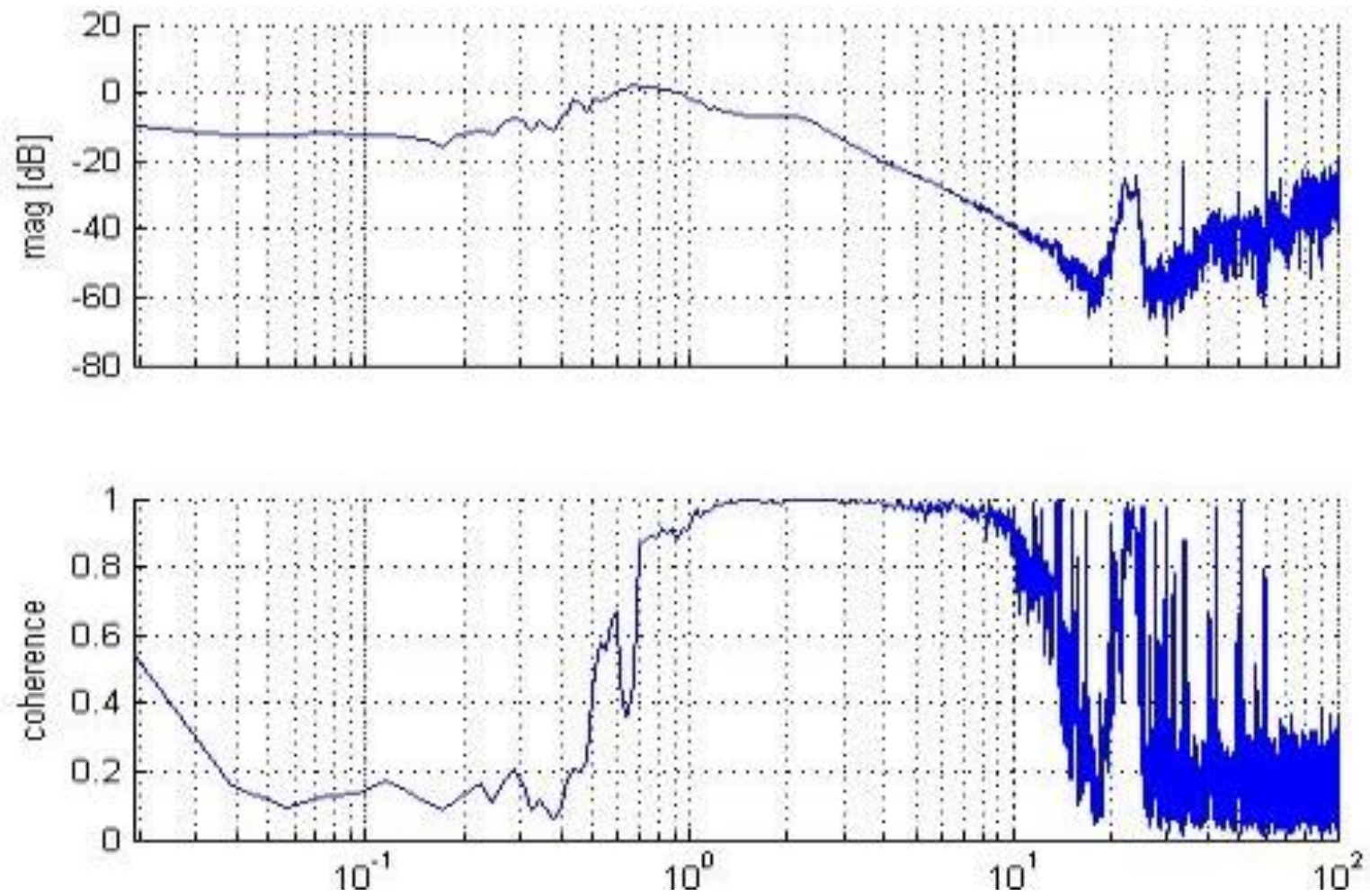


Figure 2.65 : Nano-g inertia block vertical axis transfer function showing a highly damped resonance a 0.7 Hz.Image reprinted with permission from [63]
(slide 23) © 2012 Steve Shedd/Integrated Dynamics Engineering

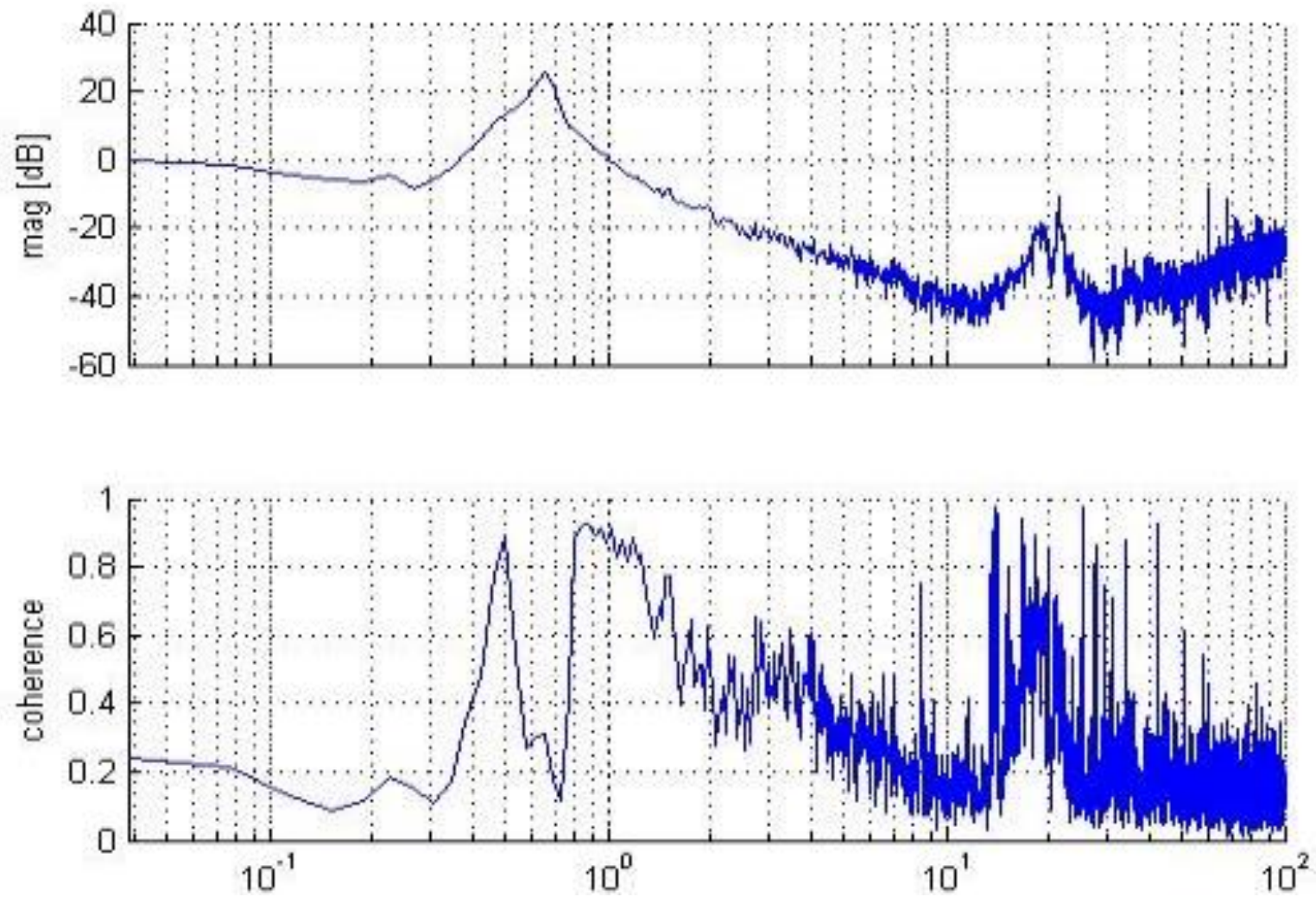


Figure 2.66 : Nano-g inertia block East-West axis transfer function showing a resonant frequency of 0.65 Hz and 25.5 dB of amplification at resonance.Image reprinted with permission from [63] (slide 24) © 2012 Steve Shedd/Integrated Dynamics Engineering

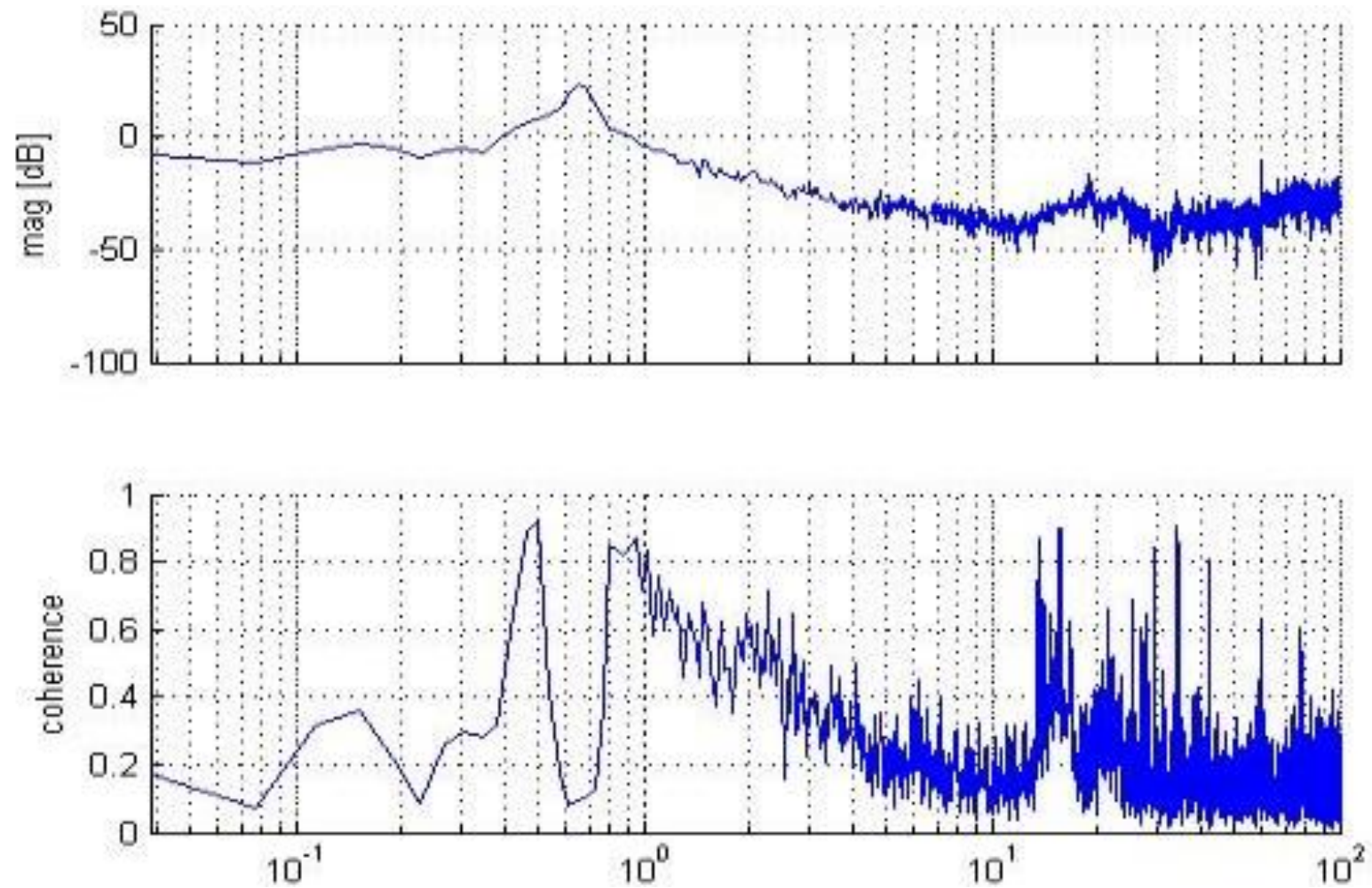


Figure 2.67 : Nano-g inertia block North-South axis transfer function showing a 0.65 Hz resonant frequency and 23.6 dB of amplification at resonance. Image reprinted with permission from [63] (slide 25) © 2012 Steve Shedd/Integrated Dynamics Engineering

Several important observations can be made about this initial commissioning data.

First, the damping of the horizontal motions of the three inertia blocks is lower than the damping of the vertical motion. Furthermore, the adjustable damping valves fitted to the PD-3001H isolators supporting the Nano-g inertia block provide much better Z-axis damping for this block than for the other two. While the lower value of damping provides faster roll off of the isolator transfer function above resonance, additional adjustability of the horizontal damping for all three inertia blocks and of the Z damping for Omegapod and C-pod is desirable in order to have more freedom to optimize the vibration conditions for the individual experiments.

Second, undesirable upwards deviations from ideal second-order behavior show up in the transfer functions beginning around 10 Hz. Cryostats have resonances beginning in this frequency range and this loss of isolation may be particularly detrimental for STM's without an additional stage of vibration isolation in the form of an internal spring suspension, such as the dilution STM discussed in chapter 3. As argued in section 2.7.2.5, the origin of these non-ideal features in the transfer functions are likely due to the highly compliant inertia blocks being perturbed by acoustic pressure forces.

2.7.2.3 Flexural motion of inertia blocks

In this section, the modes of flexural - as opposed to rigid body – vibration of the inertia block are considered. Results of experimental modal data collected principally by Vincent Wong is compared to the finite element simulations of the inertia blocks carried out in section 2.7.2.1.

The experimental mode shape data presented here was acquired by repeatedly exciting the flexural modes of the inertia block and measuring the acceleration response to the excitation as a function of position. The excitation was accomplished by dropping a metal slug from a fixed height onto a thick metal sheet placed on the top surface of the inertia block. A PCB393B04 accelerometer was moved to points on a grid over the surface of the block to measure the acceleration response as a function of position. The variability in the excitation due to slight variations in the drop height and larger variations in the impact was accounted for by measuring the acceleration near to the excitation point with a 2nd reference accelerometer (also a PCB393B04). All signals were sampled at 2 KHz for 2 seconds, timed so the impact of the metal slug came just after the beginning of data-recording.

Early experiments with coarse grids over the entire surface of the block showed intriguing but not entirely clean results. This led to the adoption of an experimental procedure where data was acquired over a finer grid of points over one-quarter of the C-pod and Omegapod inertia blocks and half of the Nano-g inertia block as shown in Figure 2.68, and subsequently mirrored during the analysis stage to produce a symmetric image of the mode shape. This experiment was conceived by Dr. Yan Pennec, Vincent Wong and the author of this thesis. The analysis of this data was carried out by Fourier transforming the acceleration response at each spatial data point and identifying the peak response frequencies corresponding to flexural modes. Then the response amplitude at each modal frequency was normalized by the amplitude at that

frequency measured at the reference accelerometer. Finally, the data was symmetrized as appropriate and plotted as a function of position for each modal frequency. This analysis was carried out by Vincent Wong; the results are presented alongside the COMSOL FEA in Figure 2.71, Figure 2.72 and Figure 2.73.

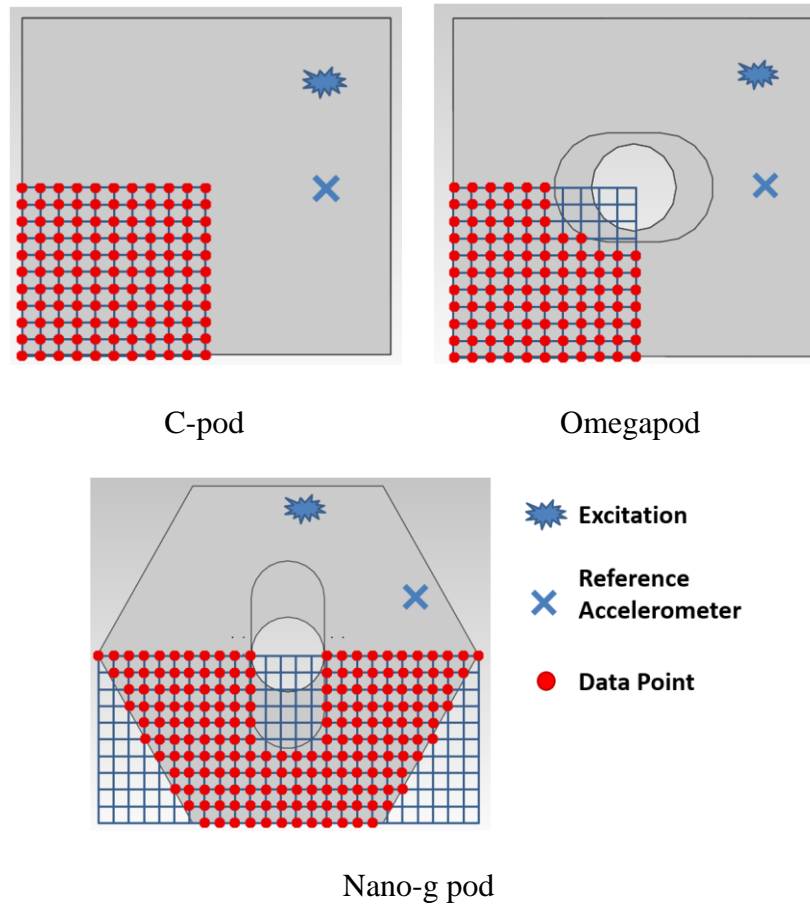


Figure 2.68: Accelerometer and excitation locations for the inertia block mode shape experiments. (Images adapted with permission from [64]–[66] © 2012 Vincent Wong and Yan Pennec)

A typical time trace for one spatial data-point on the C-pod inertia block, and its spectrum, are shown in Figure 2.69 and Figure 2.70, respectively. Inspection of these data indicates that the flexural modes of the inertia blocks have a Q of approximately 50 or damping ratio $\xi = 1\%$ which appears to be comparable to values in the literature [22] [67]. Equivalently, the time constants $\tau = Q/(\pi f)$ are about 50 ms for flexural modes around 200 Hz.

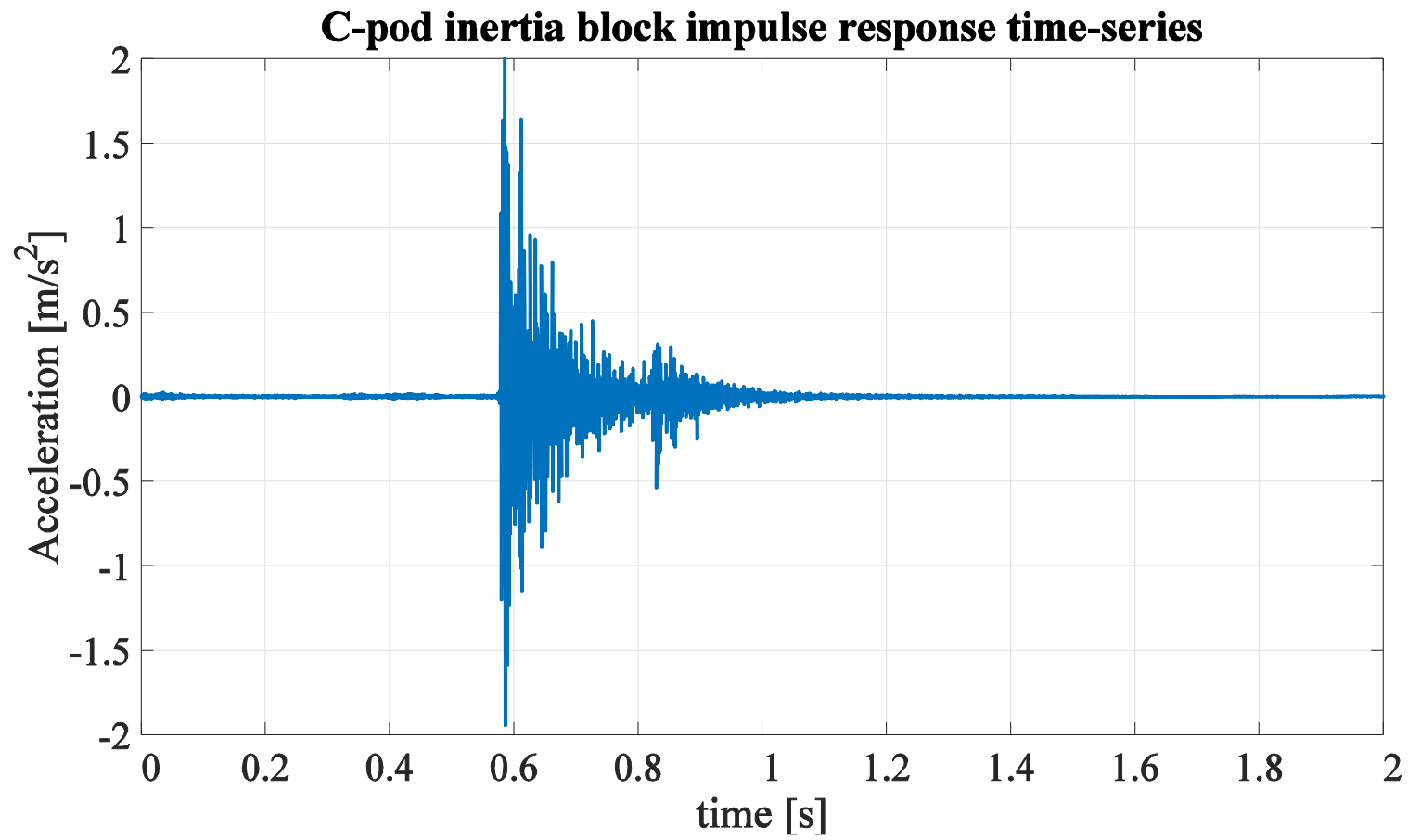


Figure 2.69: Time-series of the response of the C-pod inertia block measured at the south-west corner of the block to an impulse near the north-east corner of the block. The time-constant of the decay is approximately 50ms. A second impact of the metal slug likely caused the re-excitation around 0.85 seconds.

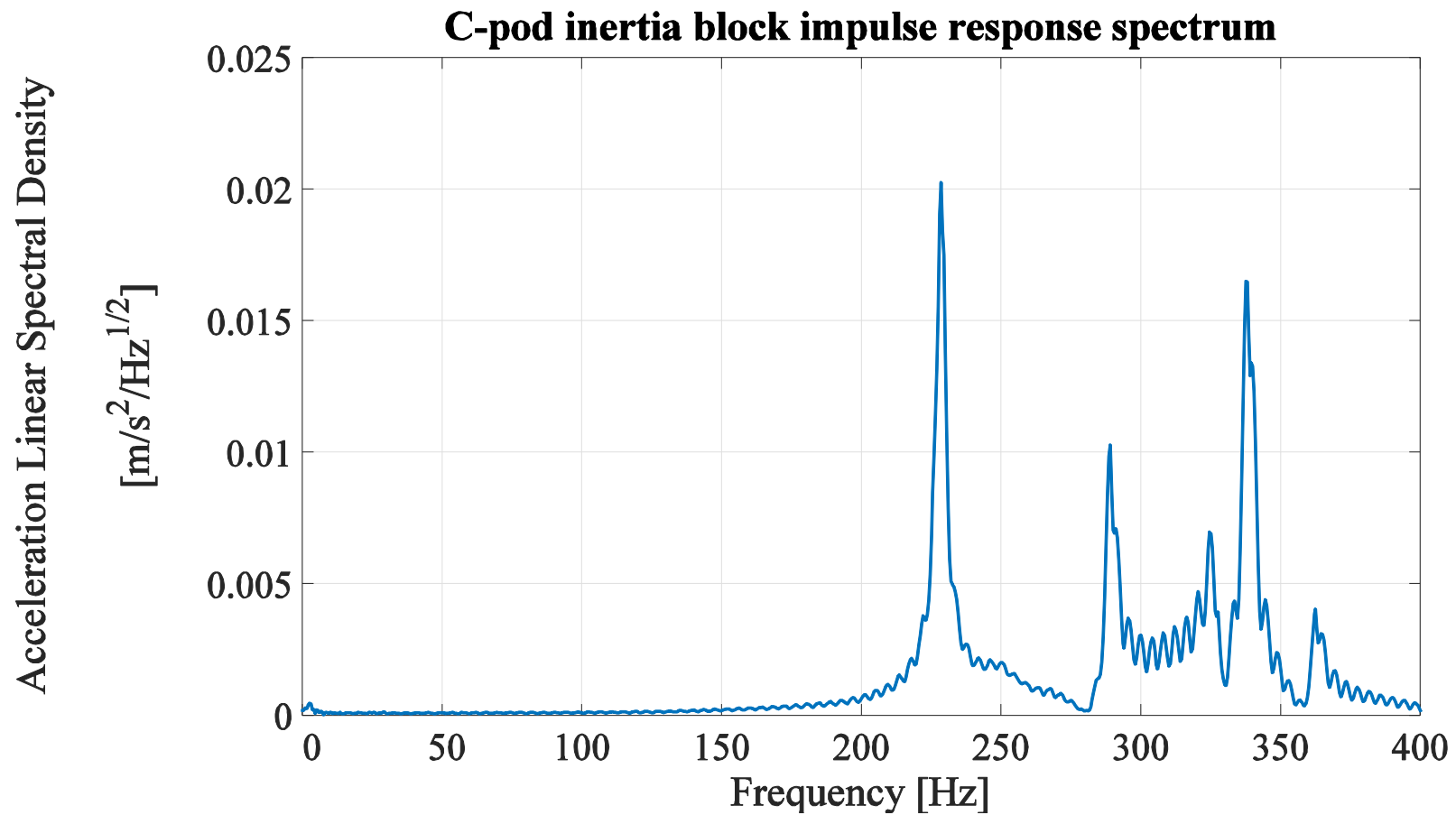


Figure 2.70: Linear spectral density of the impulse response of the C-pod inertia block at the southwest corner to an impulse in the northeast corner.
The 225 Hz peak's FWHM of about 5 Hz corresponds to a Q of approximately 50, or a time constant of about 70ms

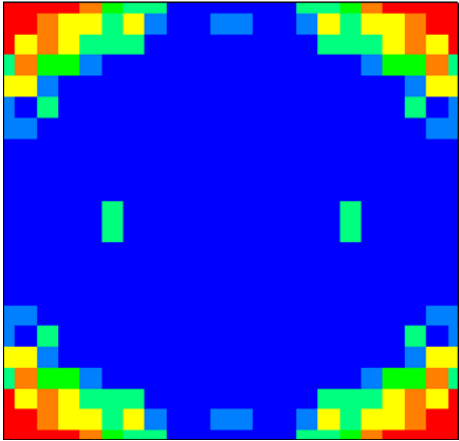
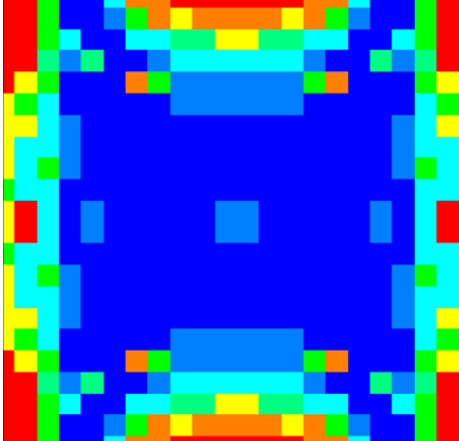
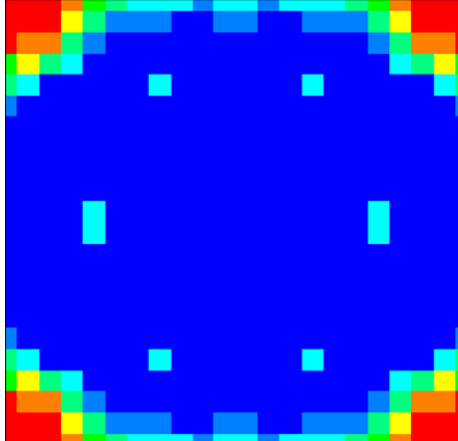
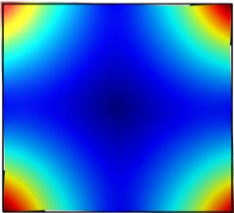
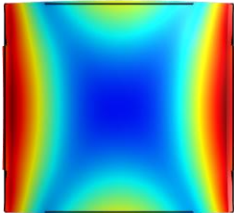
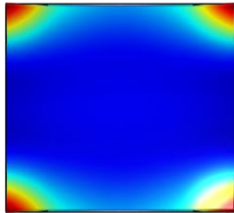
Measured mode shape at 228 Hz	Measured mode shape at 289 Hz	Measured mode shape at 339 Hz
		
		
FEA-predicted mode shape at 236 Hz	FEA-predicted mode shape at 288 Hz	FEA-predicted mode shape at 349 Hz

Figure 2.71 : Comparison of symmetrized experimental mode shapes and frequencies with FEA predictions for the C-pod inertia block. (Upper row images adapted with permission from [64] © 2012 Vincent Wong and Yan Pennec)

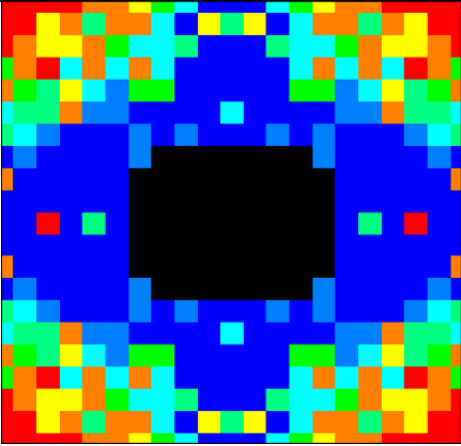
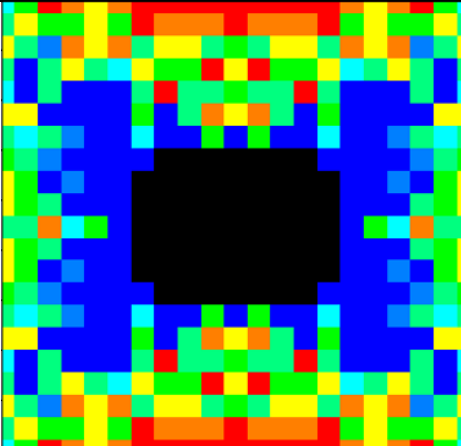
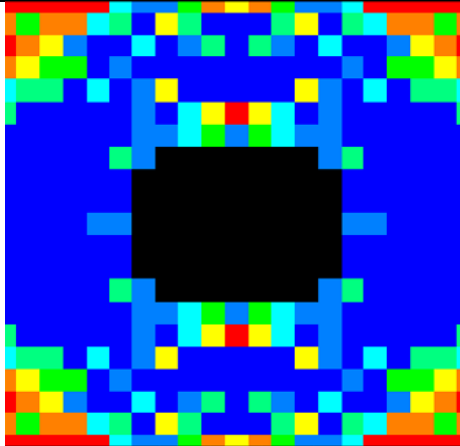
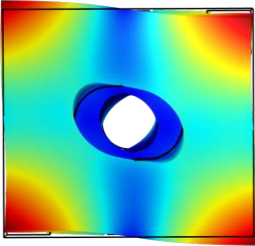
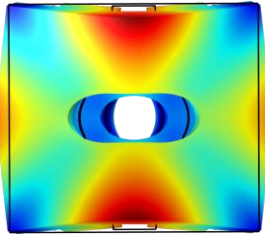
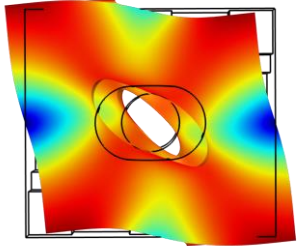
Measured mode shape at 210 Hz	Measured mode shape at 293 Hz	Measured mode shape at 385 Hz
		
		
FEA-predicted mode shape at 202 Hz	FEA-predicted mode shape at 278 Hz	FEA-predicted mode shape at 363 Hz

Figure 2.72: Comparison of symmetrized experimental mode shapes and frequencies with FEA predictions for the Omegapod inertia block (Upper row images adapted with permission from [65] © 2012 Vincent Wong and Yan Pennec)

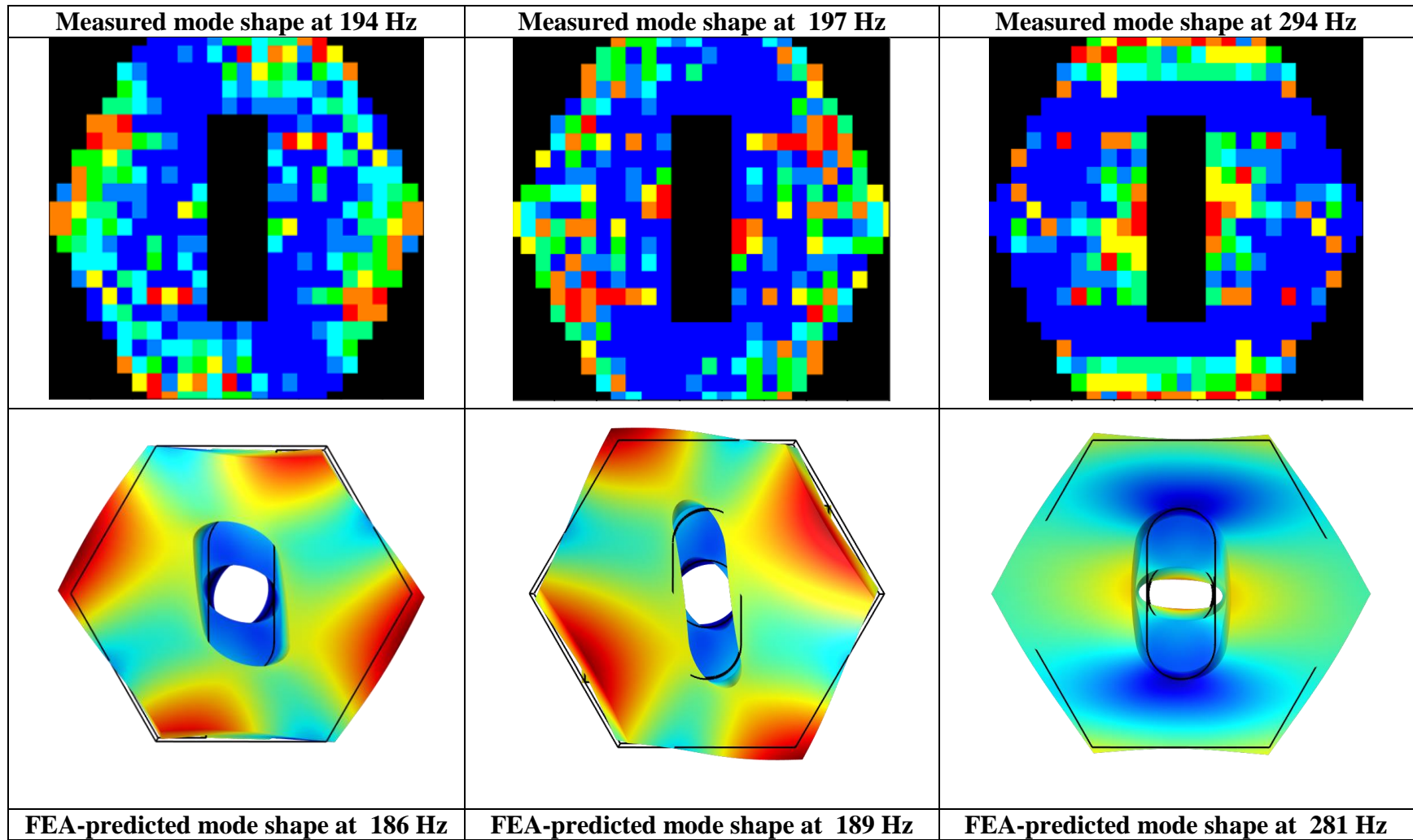


Figure 2.73: Comparison of symmetrized experimental mode shapes and frequencies with FEA predictions for the Nano-g inertia block (Upper row images adapted with permission from [66] © 2012 Vincent Wong and Yan Pennec)

As others have noted [22] , the relatively high Q of the inertia block flexural modes can lead to decreased vibration isolation performance at the modal frequencies. Although the addition of additives to the concrete to improve the damping has been considered, these typically result in decreased stiffness and therefore decreased resonant frequency for a given geometry [67]. The finite element approach used to design the inertia blocks for the LAIR facility with high fundamental resonant frequencies appears effective. Attaining fundamental flexural resonant frequencies well above the majority of the environmental seismic and acoustic energy is desirable as this minimizes the energy available to excite these high- Q resonances. In the following section it will be seen that these flexural resonances are indeed excited to measurable levels under average ambient conditions and quite detrimental levels under the worst ambient conditions.

A further advantage of being able to predict the mode shapes, also noted in [22], is that it may be possible to position the equipment on the inertia blocks near the nodes of the flexural modes such that excitation of the equipment due to the flexural modes is minimized. This has been accomplished to some extent in the LAIR since the STM experiments are mounted close the centers of the inertia blocks while the low order flexural modes tend to have anti-nodes at the edges.

2.7.2.4 Long term vibration measurements

To better characterize the spectral characteristics and amplitude range of the vibrations of the inertia blocks throughout the day and night, several long term measurements of the inertia blocks were made. By gathering data late at night when minimal human activity is taking place, these measurements provide some idea of the “vibrational noise floor” of the LAIR facility.

Conversely, by capturing many large transient vibration events throughout the day, worst case vibration levels for the facility can be approximated. Finally, averaging over many data sets allows very smooth spectra and transfer functions to be computed.

All data in this section was acquired at 5 KHz, in 30-second bursts, once per minute over multiple hours. Block vibrations were measured using the Wilcoxon 731A acceleromer in all cases, which was attached with a threaded stud to a large block of stainless steel, which was in placed on the inertia block either vertically or horizontally. The location of the accelerometer on the inertia block is important for two related reasons : vibrations due to both rigid body rocking modes and flexural modes of the inertia block tend to have higher amplitudes towards the edge of the block. This is because the block edge is further from the center of rotation for the rocking modes and is also typically closer to the anti-nodes of the low order flexural modes described in the following section. Because it was desired to measure transfer functions from the block to the experiments supported on light load isolators at the same time as the block and foundation measurements, the Wilcoxon accelerometer was placed as close as possible to the base of one of the light load isolators. For the Nano-g and Omegapod data, this was by the base of the southwest light load isolator and for the Createc pod, by the south-east isolator. This choice of corners matches the placement of the PCB accelerometers by the bases of the heavy load

isolators for the measurement of the foundation vibration (see Figure 2.22). This choice of measurement locations on the inertia block near the bases of the light-load isolators was made because the vibration at these locations can be considered as the input vibration to the subsequent light-load isolation stage.

Z-velocity spectrograms/RMS velocity plots are presented for the three inertia blocks in Figure 2.74, Figure 2.75 and Figure 2.76. Similar data for the horizontal axis is shown for the Nano-g and C-pod inertia blocks in Figure 2.49 and Figure 2.50. These show order of magnitude variations in the RMS velocity from night time to daytime appearing to come mostly in the form of transient increases with timescales on the order of minutes or tens of minutes.

Peak-hold, time-average and averaged-minimum vertical velocity spectra are shown for each inertia block in Figure 2.77, Figure 2.78 and Figure 2.79; The equivalent horizontal axis data for Nano-g and C-pod is shown in Figure 2.51 and Figure 2.52.

Long-term mean empirical transfer functions, obtained by dividing the long-term mean block velocities by the long-term mean foundation velocities, are shown in Figure 2.84 (vertical direction) and Figure 2.85 (horizontal direction).

Finally, comparisons between the inertia blocks are made for the horizontal and vertical peak-hold levels (Figure 2.88 and Figure 2.91), linear-means (Figure 2.87 and Figure 2.90) and averages of the 10 quietest 30-second data segments (Figure 2.86 and Figure 2.89)

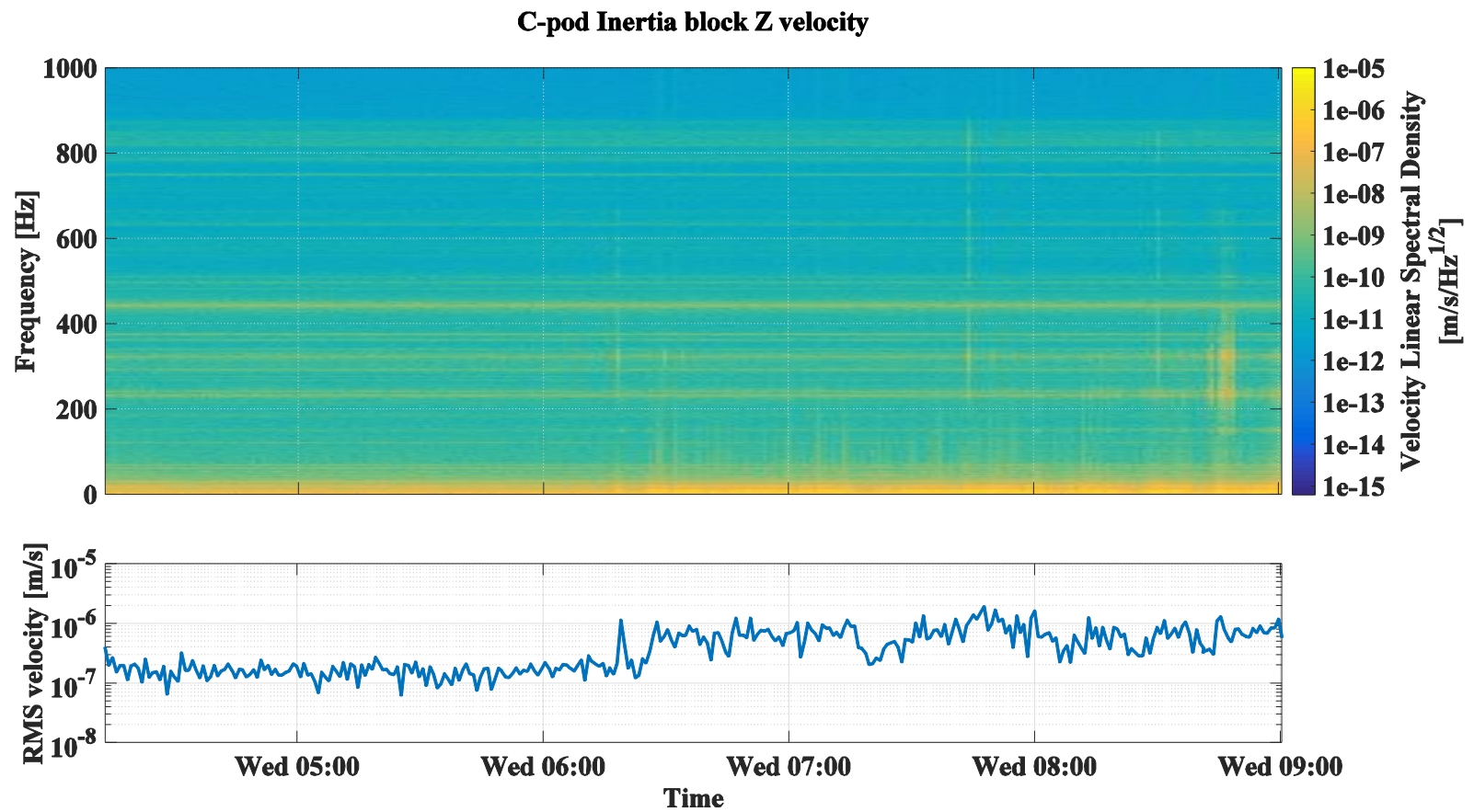


Figure 2.74: Vertical velocity spectrum and RMS velocity on the C-pod inertia block vs time at the beginning of a workday The C-pod is the closest of all the pods to the QMI excavation site which may explain the violent transients and upwards shift in RMS velocity beginning early in the morning.

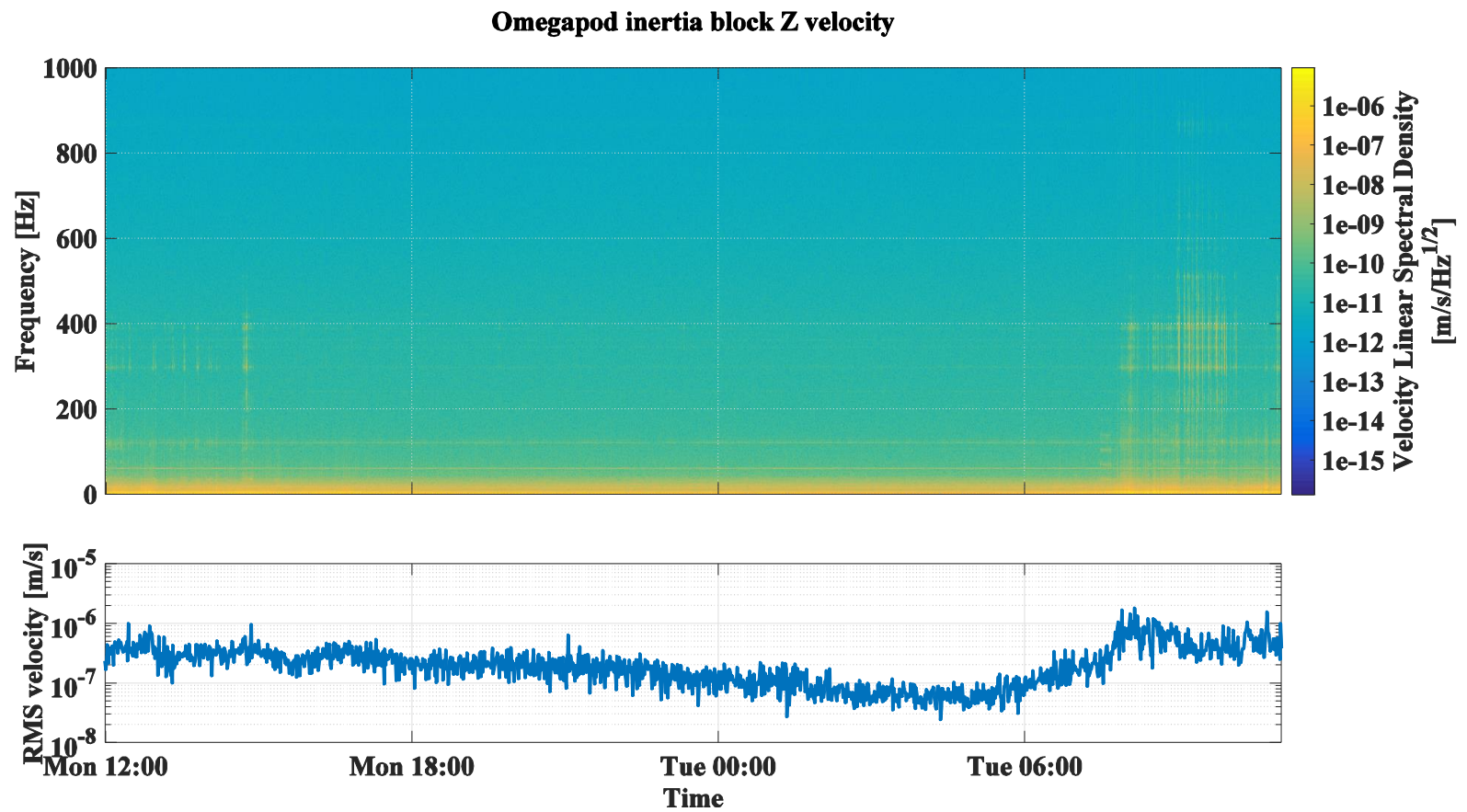


Figure 2.75: Vertical velocity spectrum and RMS velocity on the Omegapod inertia block vs time over nearly 24 hours during the work week.

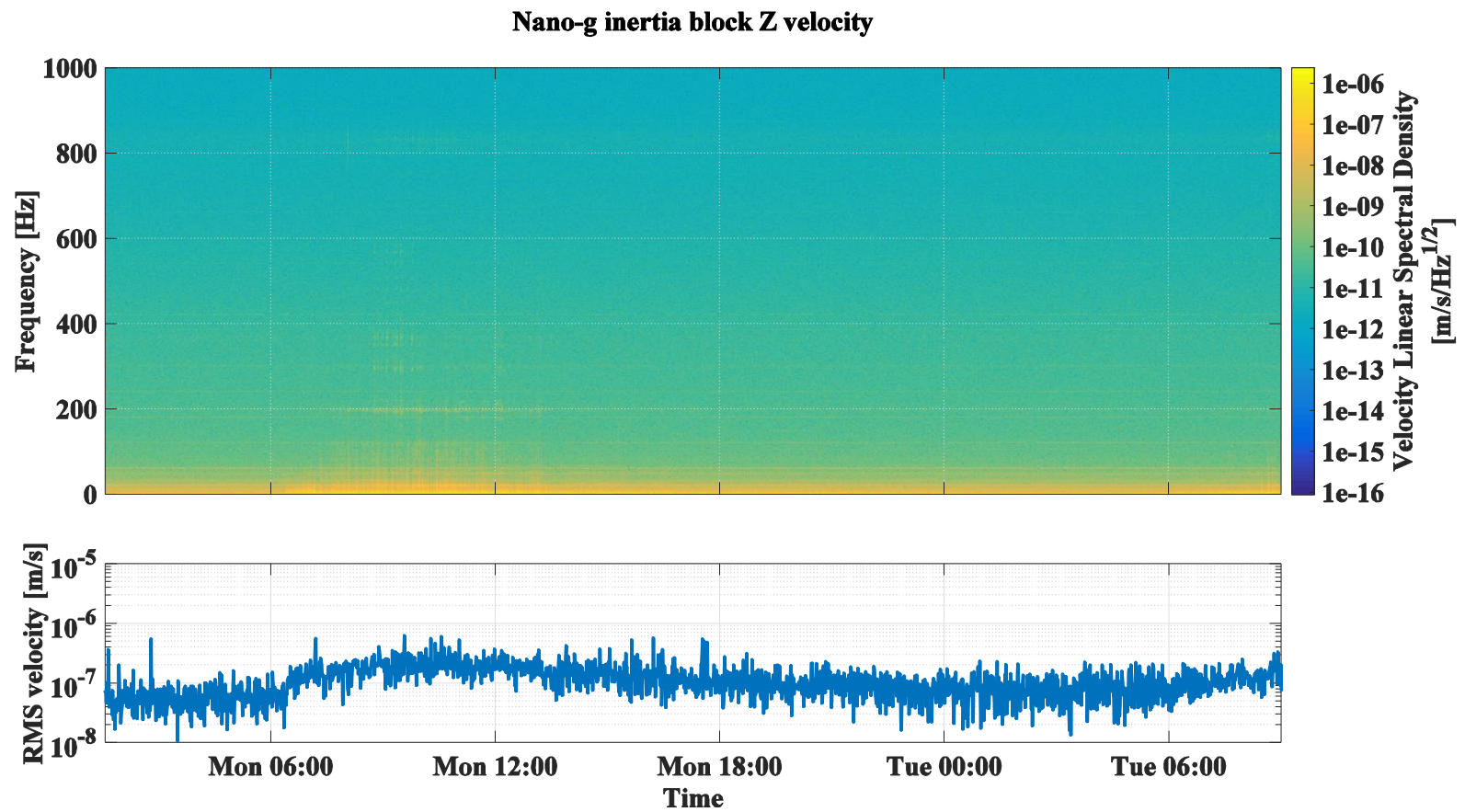


Figure 2.76: Vertical velocity spectrum and RMS velocity vs time on the Nano-g inertia block over more than 24 hours during the work week. The Nano-g inertia block is the furthest from the QMI building site excavation.

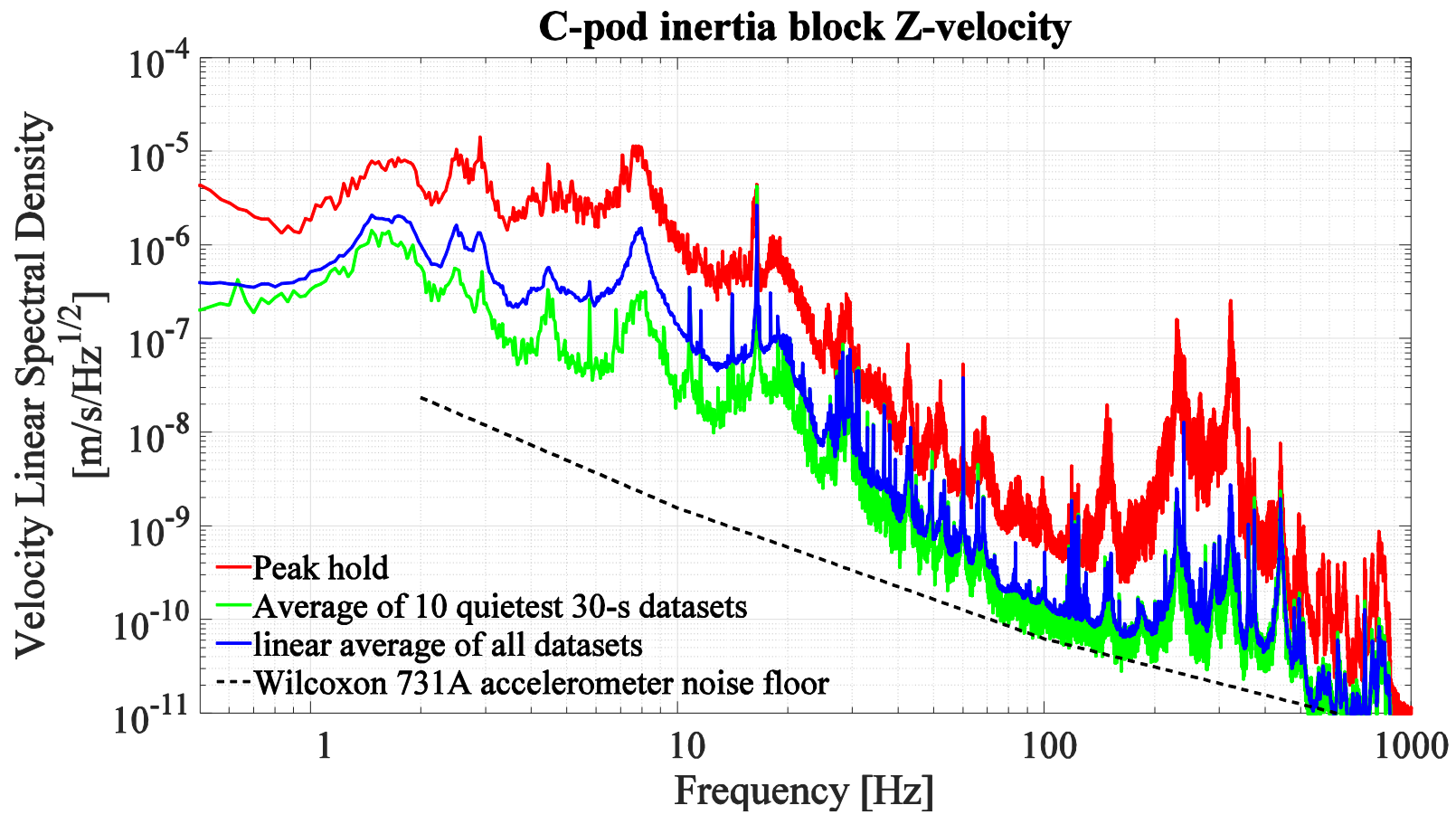


Figure 2.77 : Long term vertical velocity spectra for the C-pod inertia block.

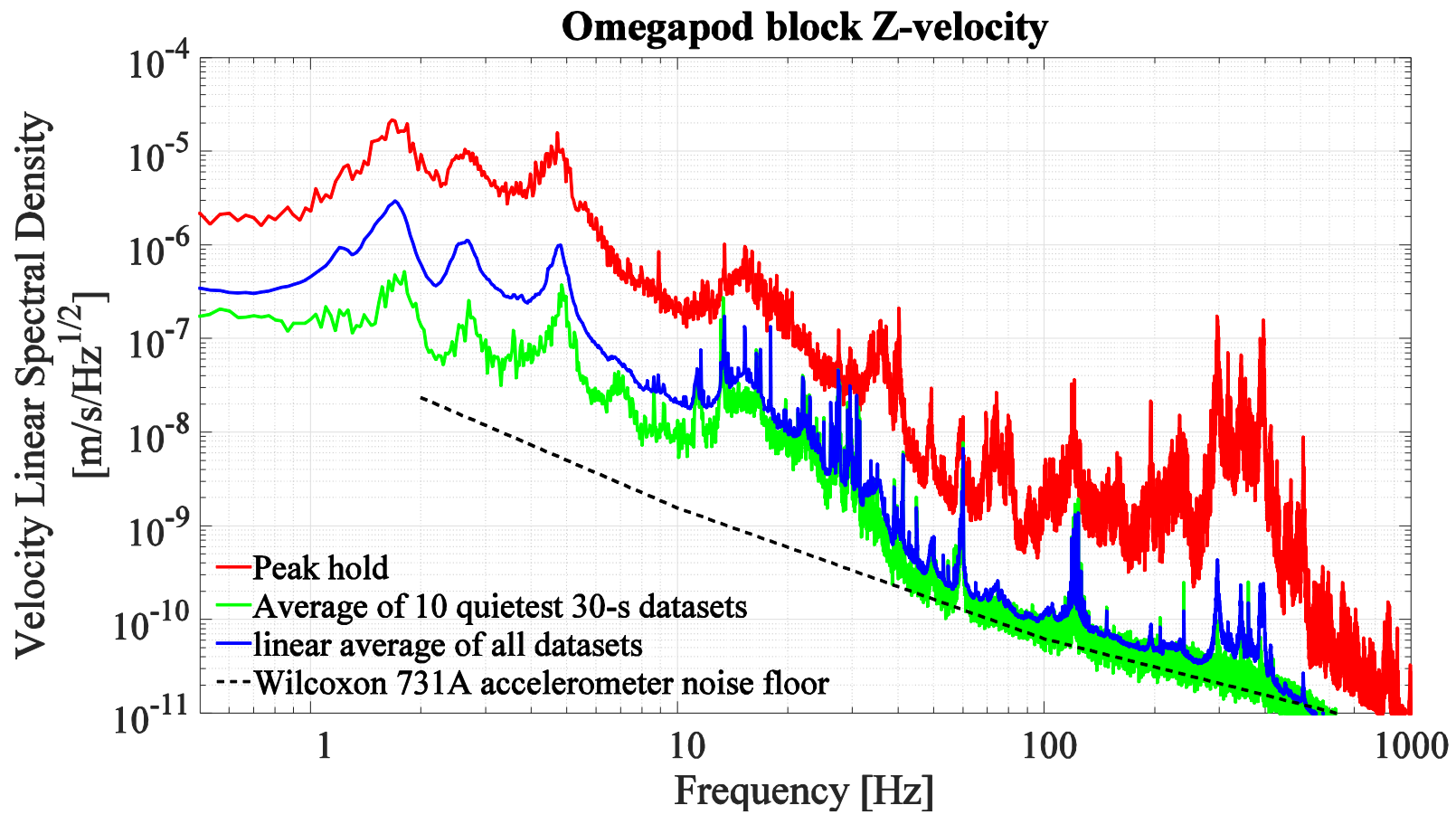


Figure 2.78: Long term vertical velocity spectra for the Omegapod inertia block

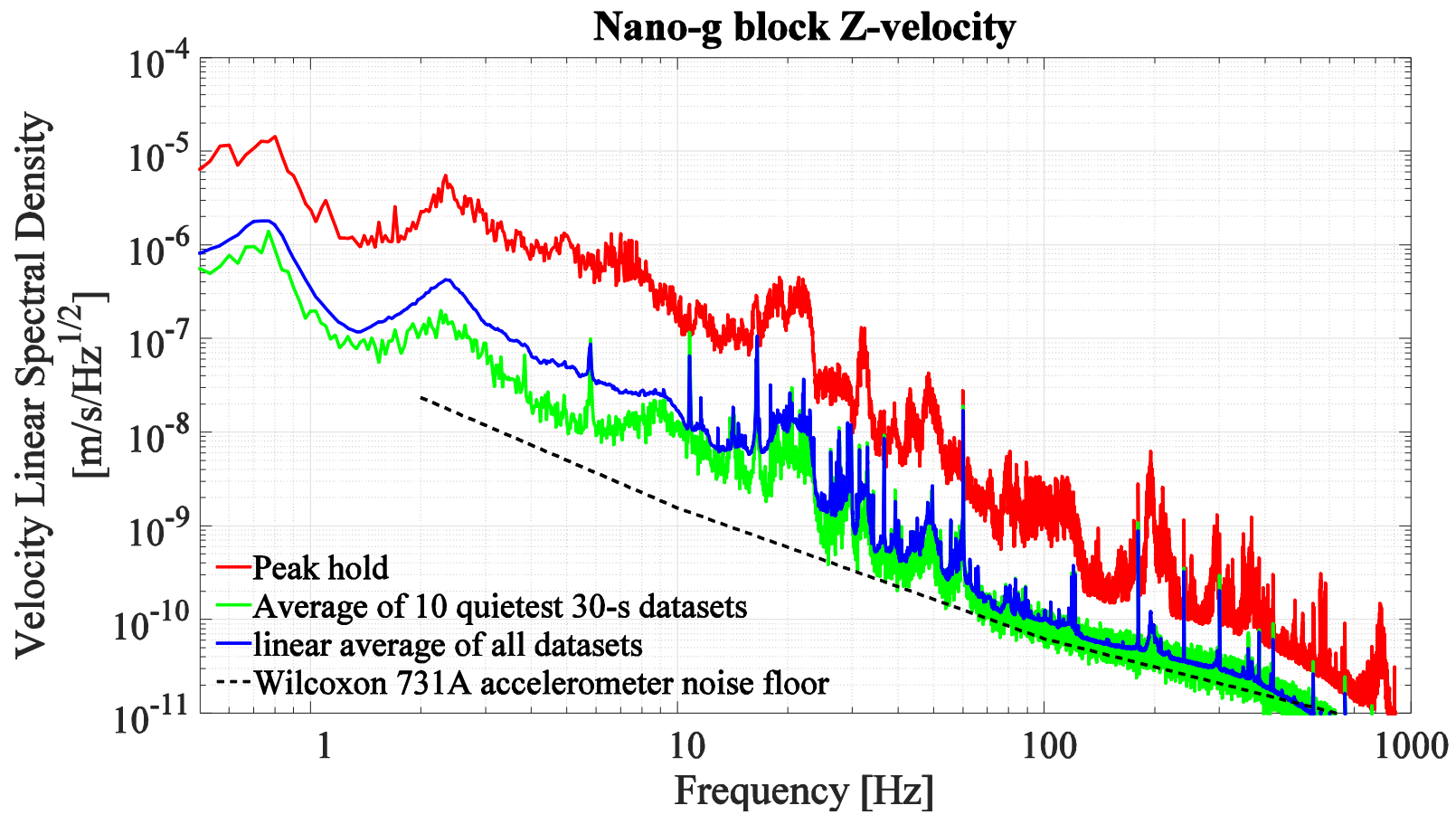


Figure 2.79 : Long-term vertical velocity spectra for the Nano-g inertial block

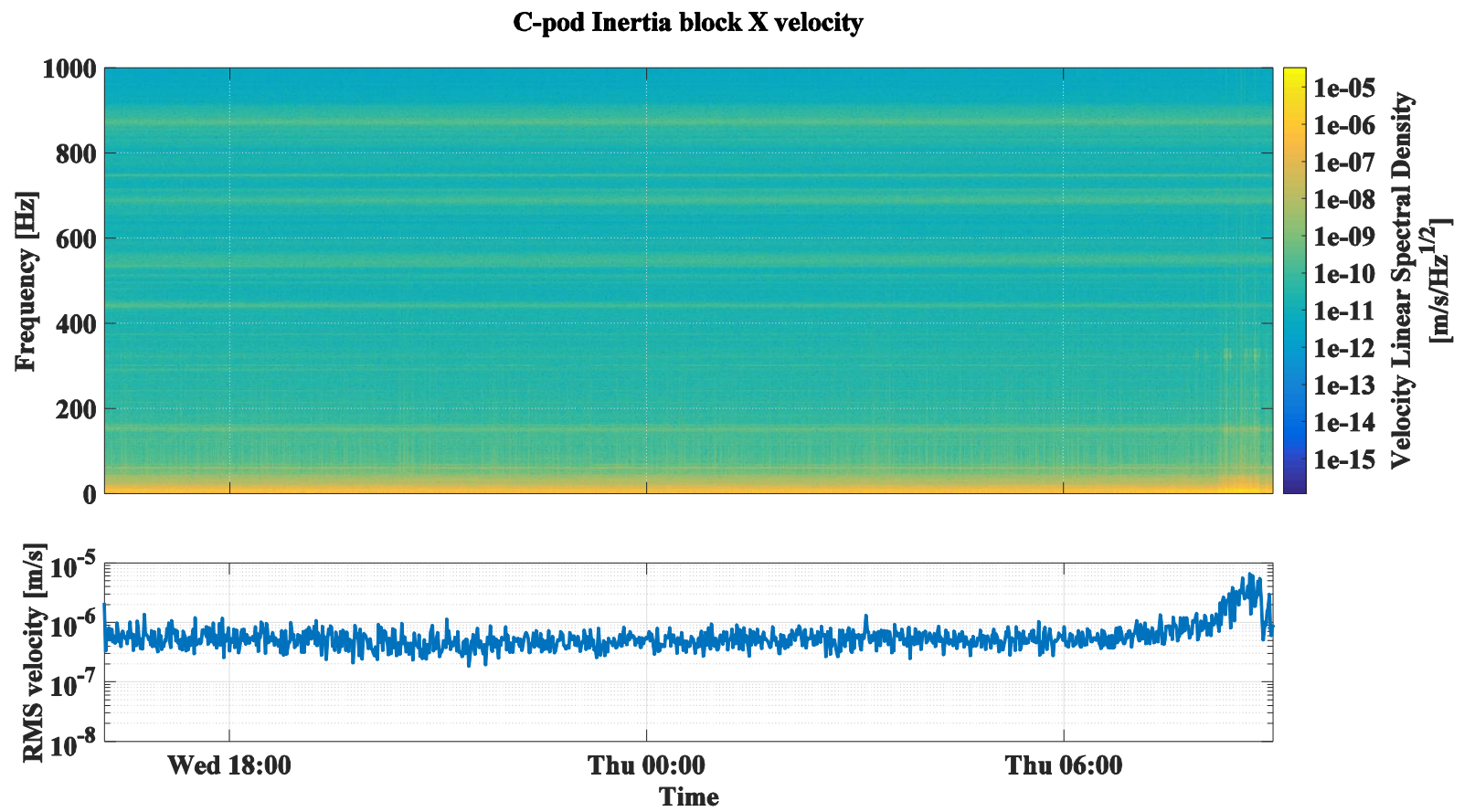


Figure 2.80: Horizontal velocity spectrogram for the C-pod inertia block

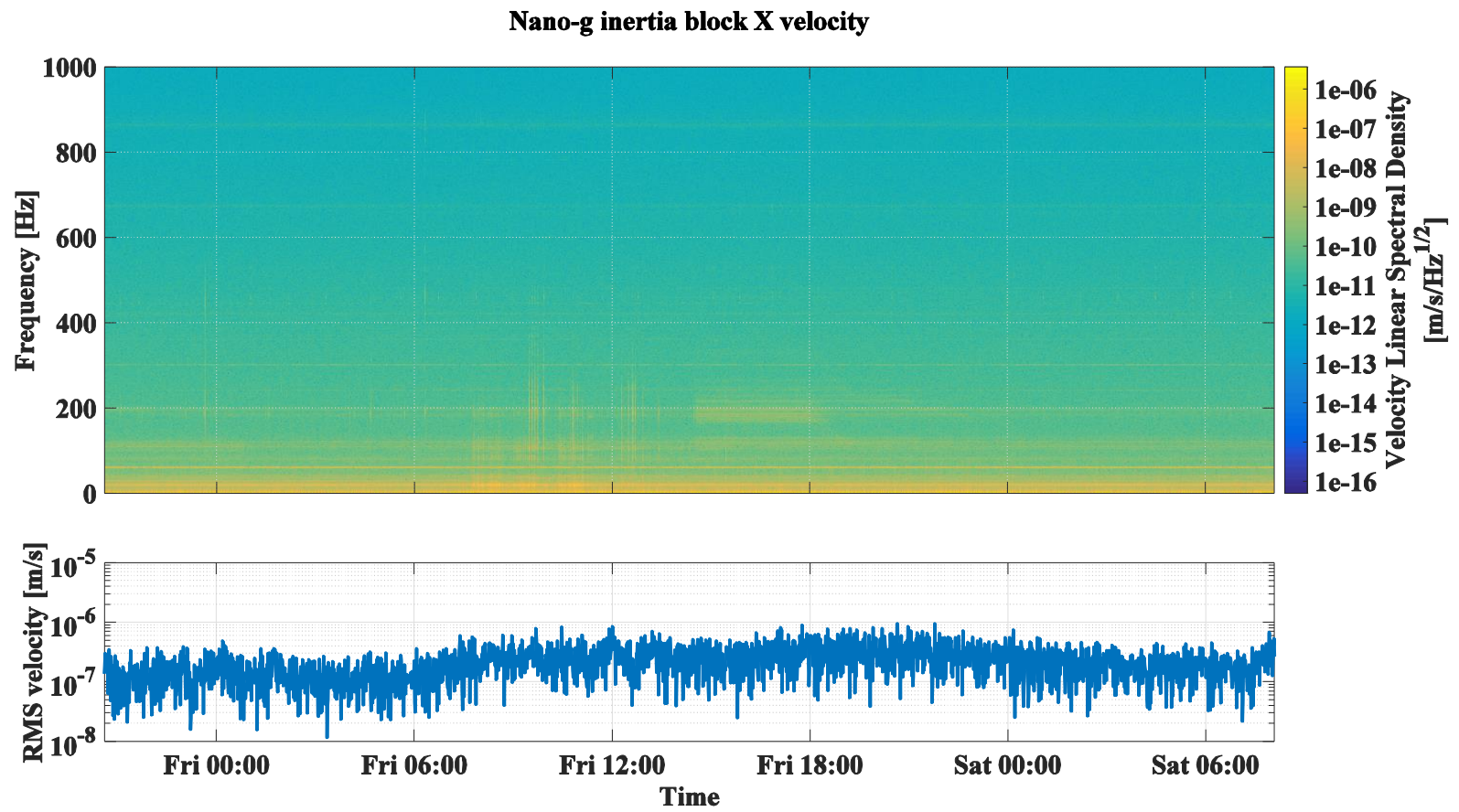


Figure 2.81: Horizontal velocity spectrogram for the C-pod inertia block

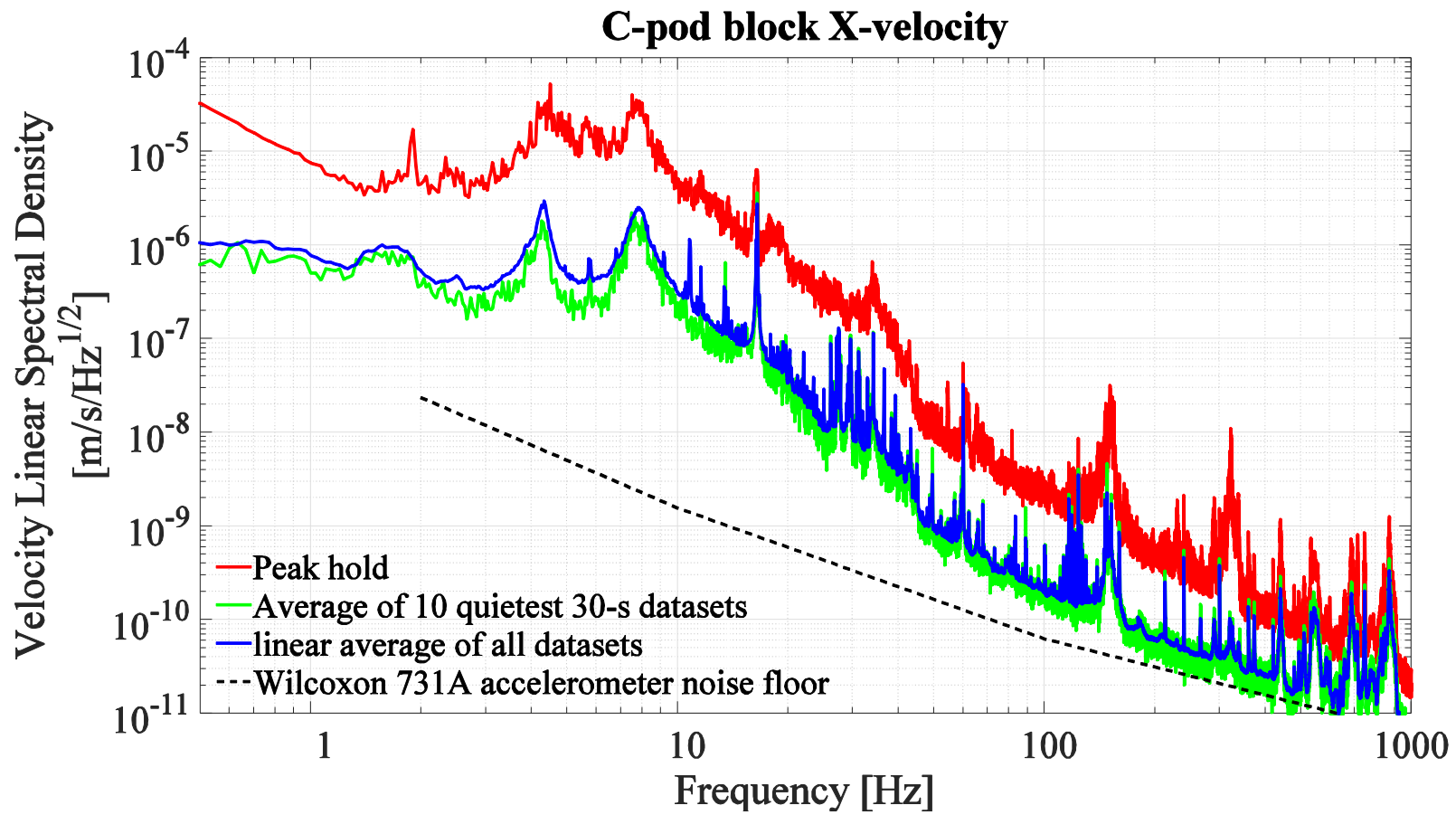


Figure 2.82: Long term horizontal velocity spectra on the C-pod inertia block

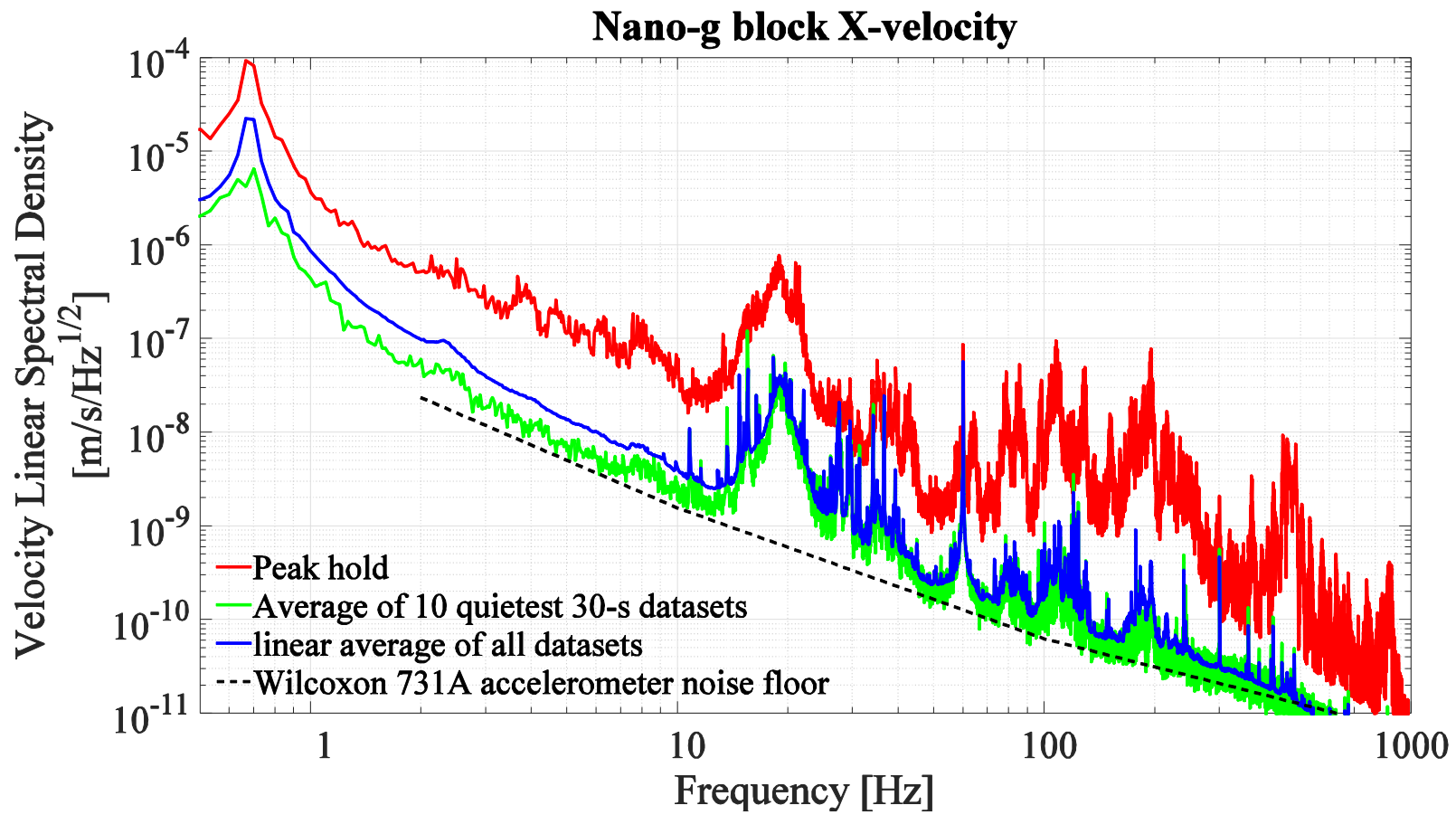


Figure 2.83: Long term horizontal velocity spectra on the Nano-g inertia block

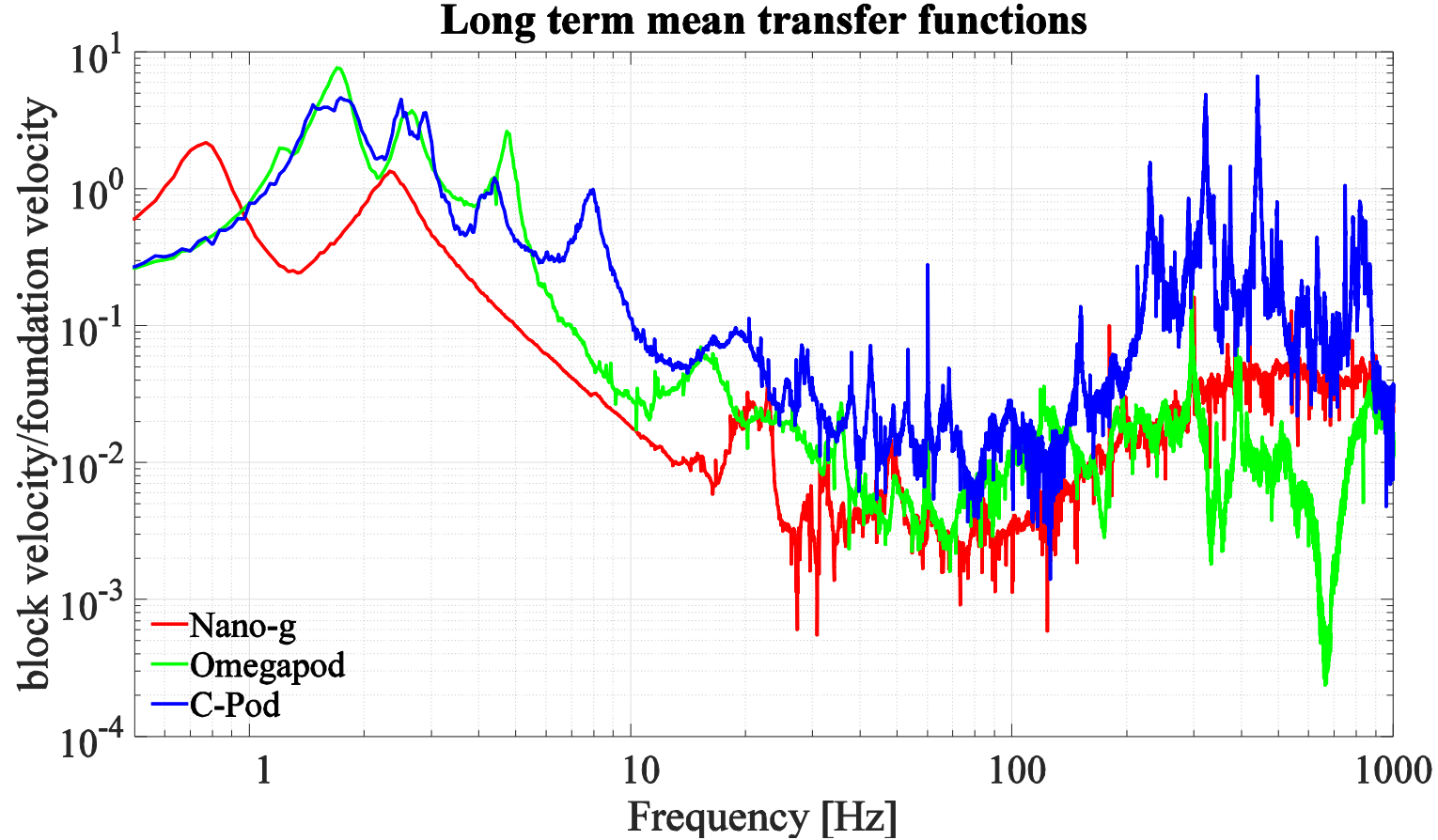


Figure 2.84: Long-term mean vertical axis empirical transfer functions from the foundations to the inertia blocks. It is important to keep in mind that neither the Omegapod nor the C-pod inertia blocks were floating properly when these measurements were made, as indicated by the large peaks in their transfer functions extending up to nearly 10 Hz. The ~2.3 Hz peak in the Nano-g transfer function is due to a rocking mode of the inertia block and is an expected feature..

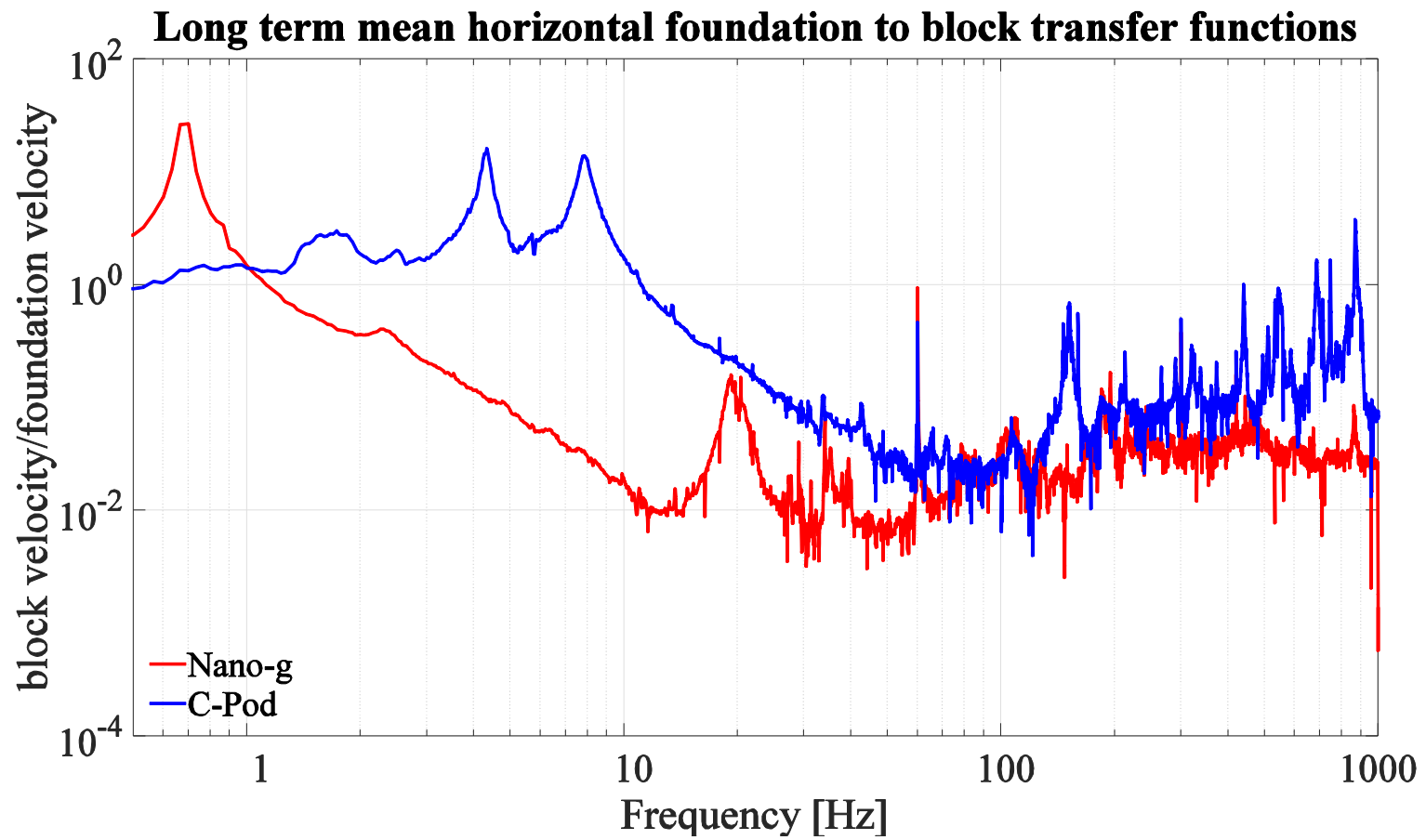


Figure 2.85: Long-term horizontal axis empirical transfer functions for the C-pod and Nano-g inertia blocks

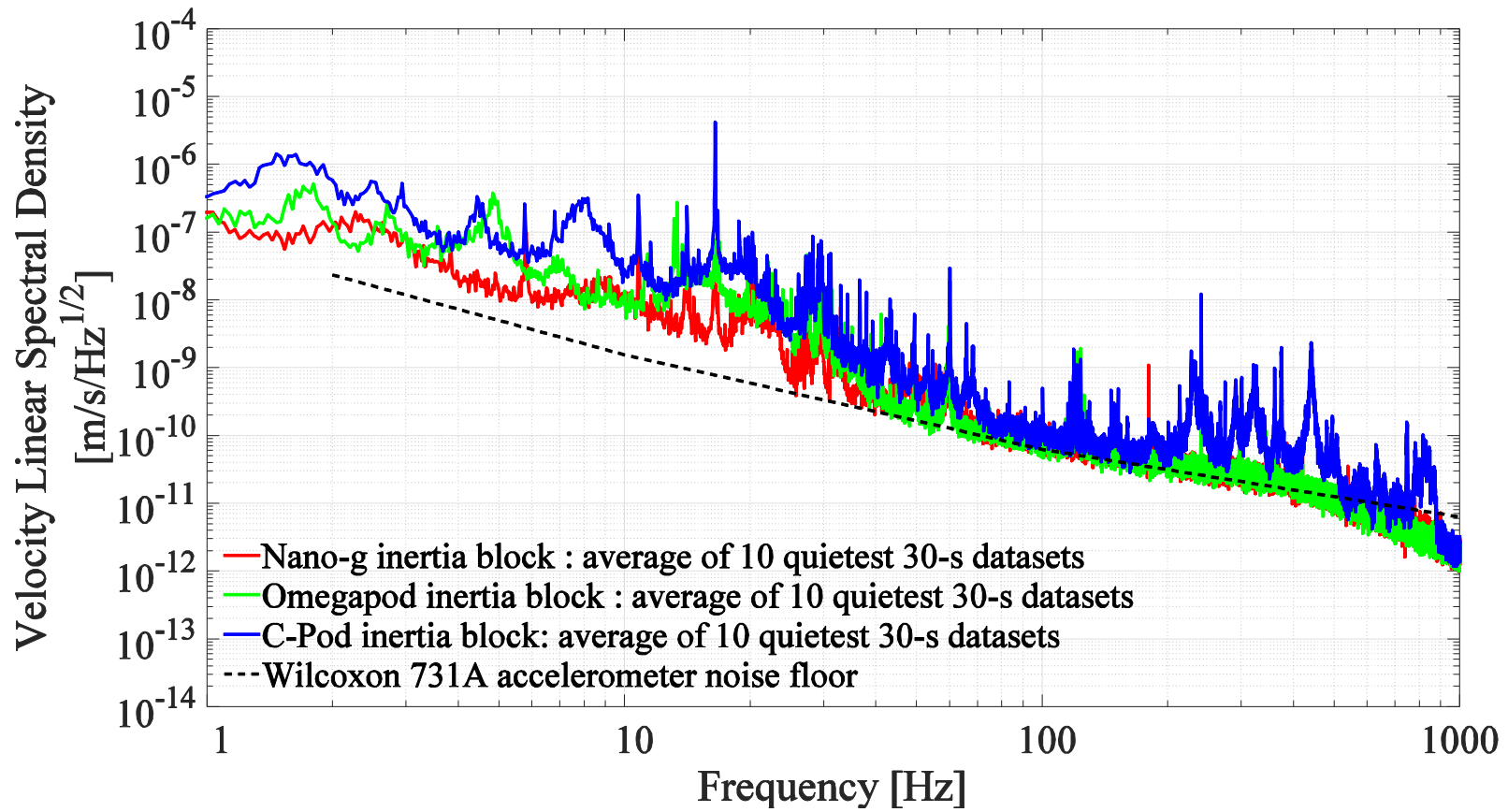


Figure 2.86: Comparison of the average of the 10 quietest 30-s long vertical velocity spectra on the three inertia blocks

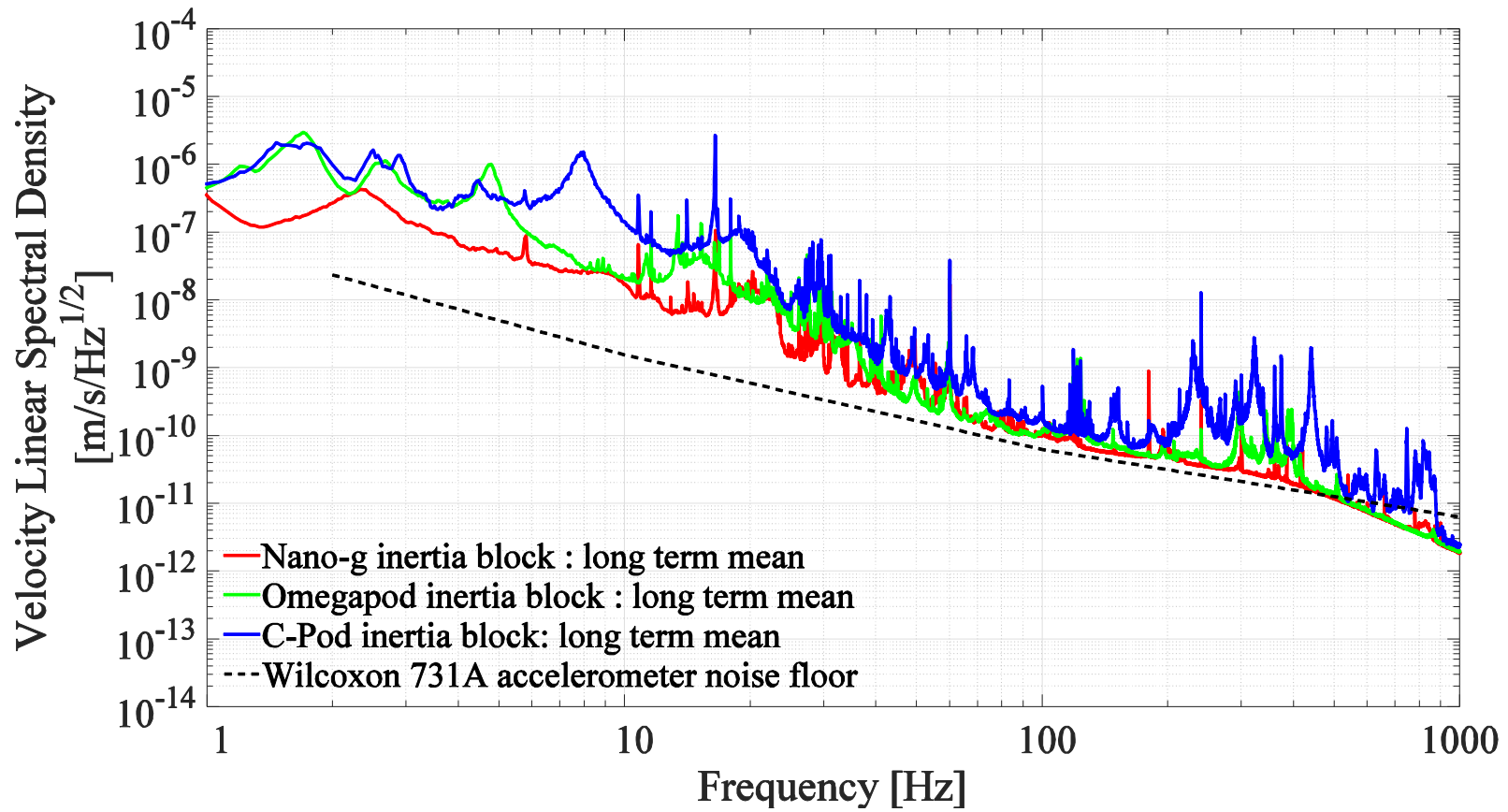


Figure 2.87: Comparison of the long term mean vertical velocity spectra on the three inertia blocks

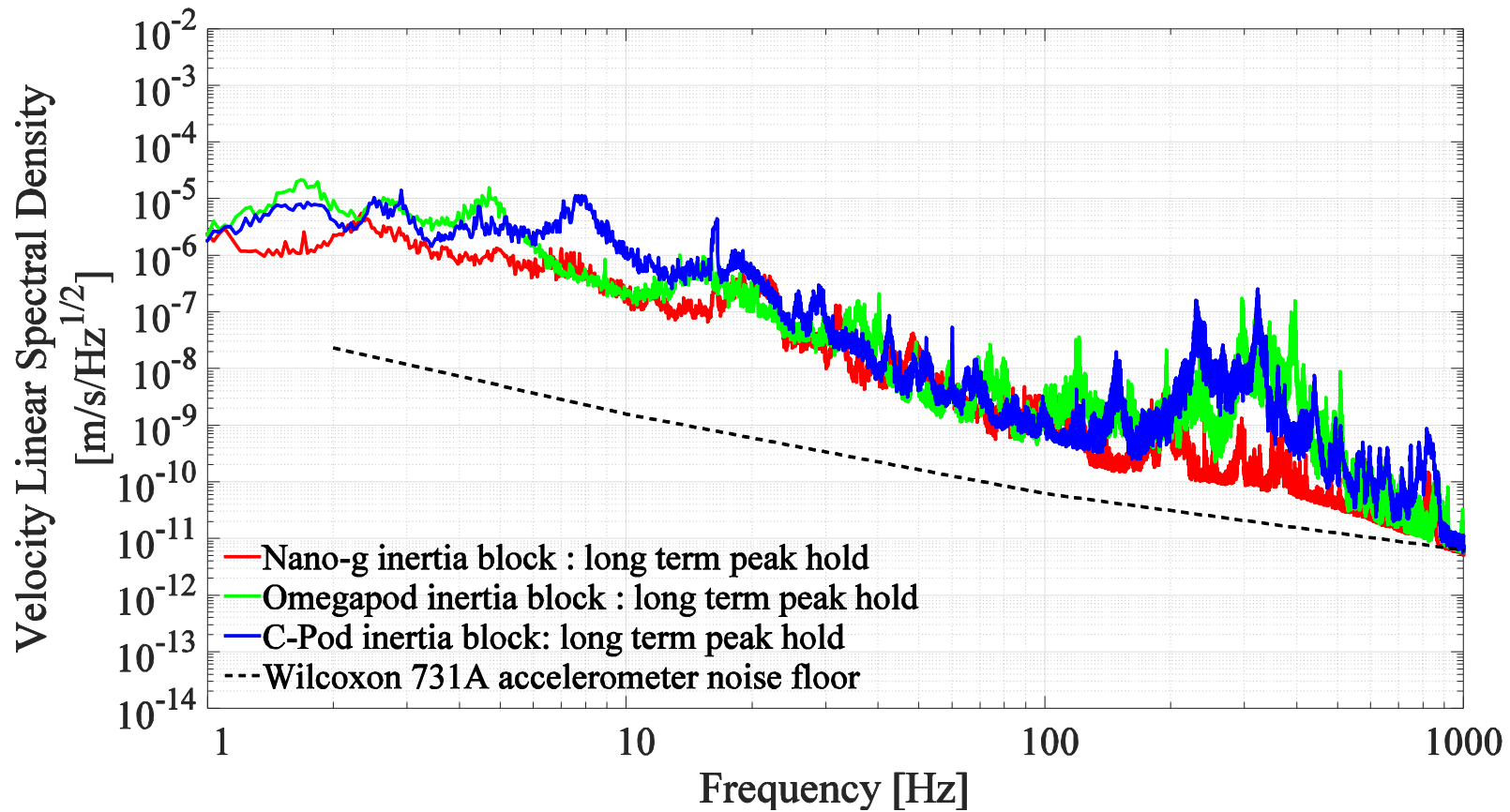


Figure 2.88: Comparison of the long term peak hold vertical velocity spectra on the three inertia blocks. The large peaks in the C-pod and Omegapod spectra above 200 Hz are likely attributable to the flexural modes of those inertia blocks.

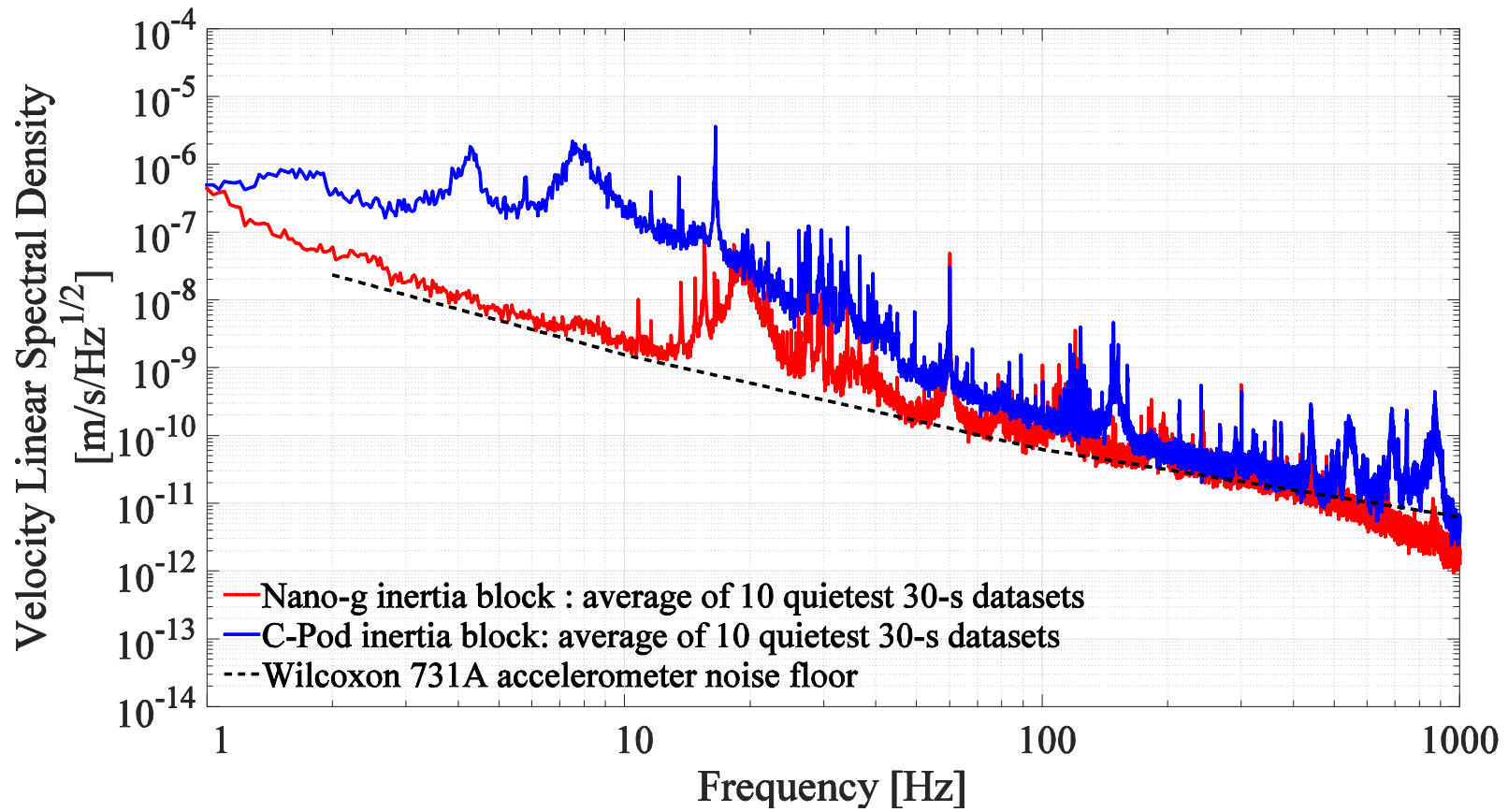


Figure 2.89: Comparison of the average of the 10 quietest 30-s long horizontal velocity spectra on the three inertia blocks

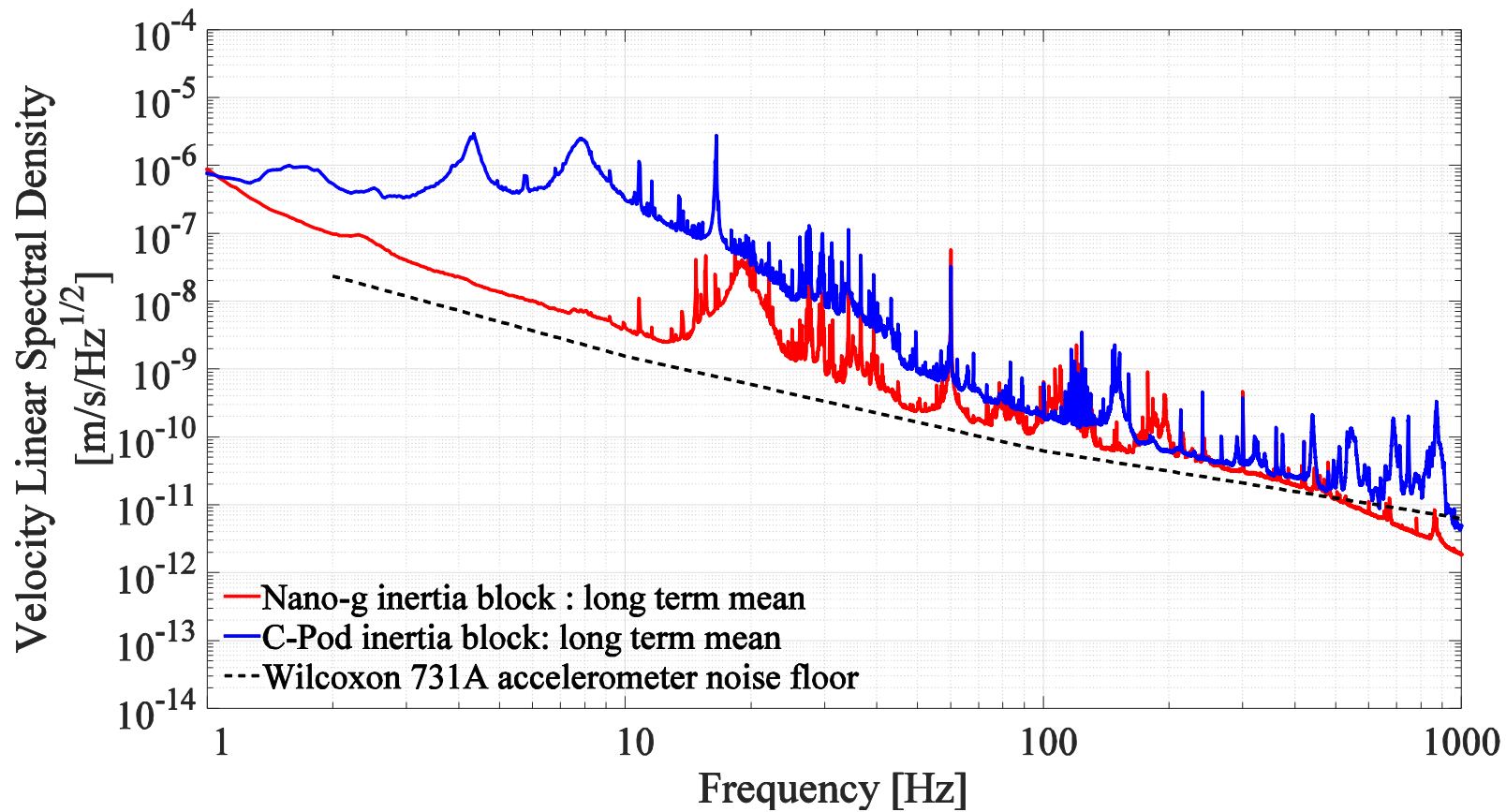


Figure 2.90: Comparison of the long-run mean horizontal velocity spectra on the Nano-g and C-pod inertia blocks

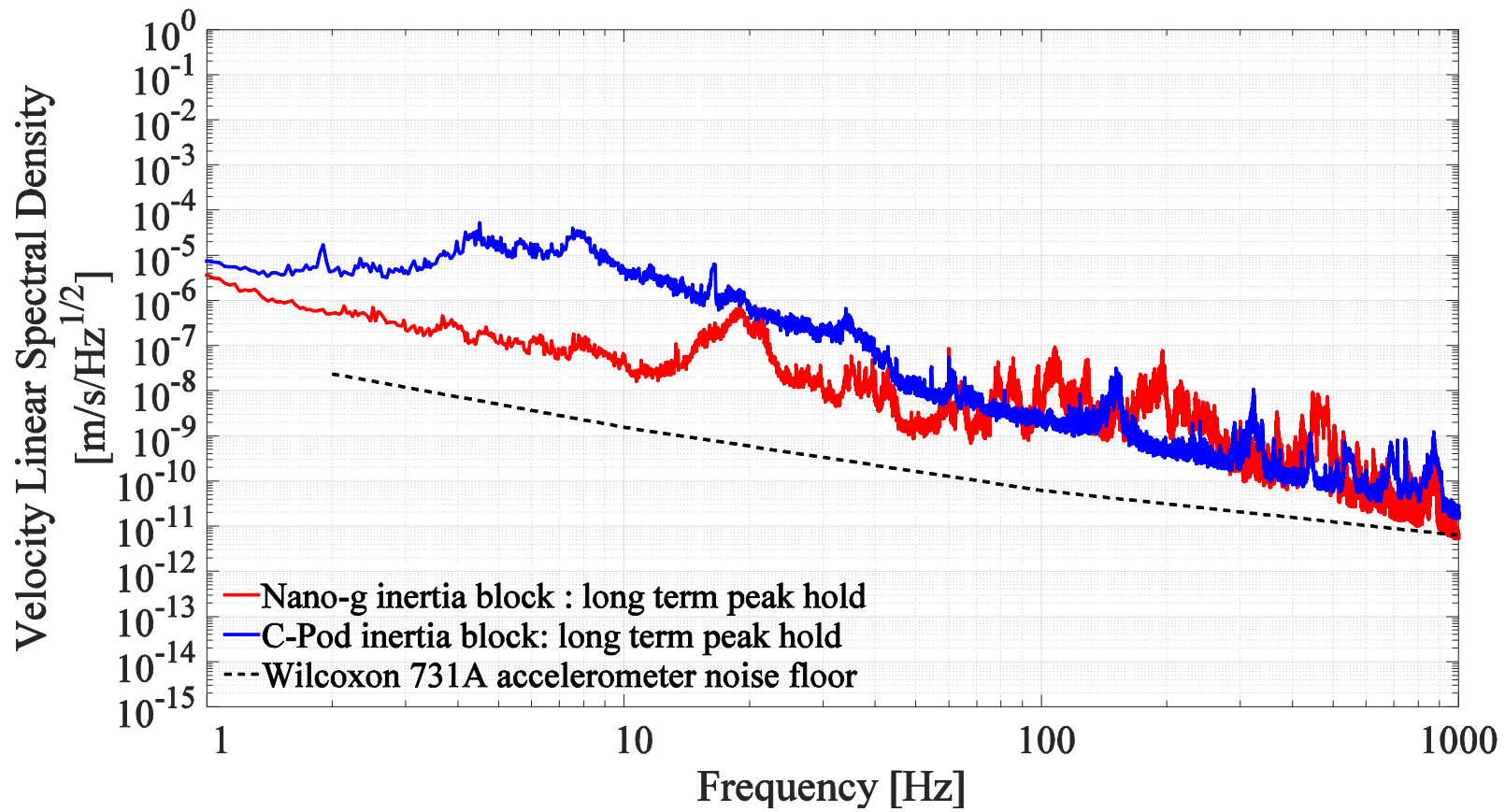


Figure 2.91: Comparison of long term peak-hold horizontal velocities on the C-Pod and Nano-g inertia blocks

This data has the substantial advantage over the initial commissioning data of having been recorded with an accelerometer with a much lower noise floor – the Wilcoxon 731A. Upon examining this data, especially the transfer functions, it is clear that the C-pod and Omegapod inertia blocks were not floating properly throughout the acquisition. This clearly impacts their isolation performance for the worse and makes comparisons between the inertia blocks based on this data of little value. This is unfortunate because comparing the performance of the inertia blocks – the masses of which roughly span the range of sizes in use today worldwide – could have provided valuable information about the importance of the absolute mass of the inertia block to vibration isolation performance.

Since this data was taken, the cause of the poor performance of the Omegapod block has been discovered and remedied. The cup of one of the levelators underneath the block was touching the cone on the block even when the block was fully floated. This was fixed by dropping the cup using the levelator's adjustment screw. A similar solution will be applied to the C-pod inertia block.

Examining the Nano-g data is nevertheless useful, as the inertia block was floating properly. The Nano-g inertia block has a persistent peak at about 2.3 Hz, which is likely a rocking mode despite being at a higher frequency than the predicted rocking modes for this inertia block.

Due to the improper floating of the C-Pod and Omegapod inertia blocks during these data runs, it is not appropriate to draw conclusions about their performance relative to the Nano-g inertia block.

2.7.2.5 Off-resonance acoustic excitation of inertia block rigid body motion

In this section it is argued that acoustic forces acting on the inertia blocks produce measurable motion of the inertia blocks at frequencies in the neighborhood of 20 Hz. At these frequencies, the attenuation of the acoustic enclosures is much lower than at higher frequencies, the amplifying acoustic modes of the enclosures are present, and the lengths of the acoustic waves are similar to the characteristic dimensions of the inertia blocks. It appears that these factors can combine to create a sound field which is efficiently coupled to the inertia block motion and sufficiently intense to result in block motions which are much larger than what would be expected due to the excitation of the inertia block due to ground motion alone.

A simple analytical model of this effect – sometimes referred to as acoustic buffeting, or the sail-effect -is proposed in [23]. Here this model is extended slightly by using the full second order force response transfer function and approximate agreement with experimental data is found. Although acoustic buffeting is often alluded to in the experimental literature – see [5],[16] and [53] for example – to the author’s knowledge, the combined microphone and accelerometer measurements reported here are the first quantitative experimental evidence published regarding this effect.

First hints that this effect might be occurring for the LAIR facility inertia blocks were seen in the unexpected peaks in the inertia block transfer functions presented in section 2.7.2.2. Comparing the Nano-g inertia block velocity spectra to sound pressure spectrum in that pod (Figure 2.92) shows a large region between 20 and 100 Hz where the block velocity spectrum resembles the sound pressure spectrum as much or more than the foundation velocity spectrum; this is especially true near 20 Hz.. This qualitative similarity of the spectral shapes in this region is another hint that acoustic forces may be driving some motion of the inertia block.

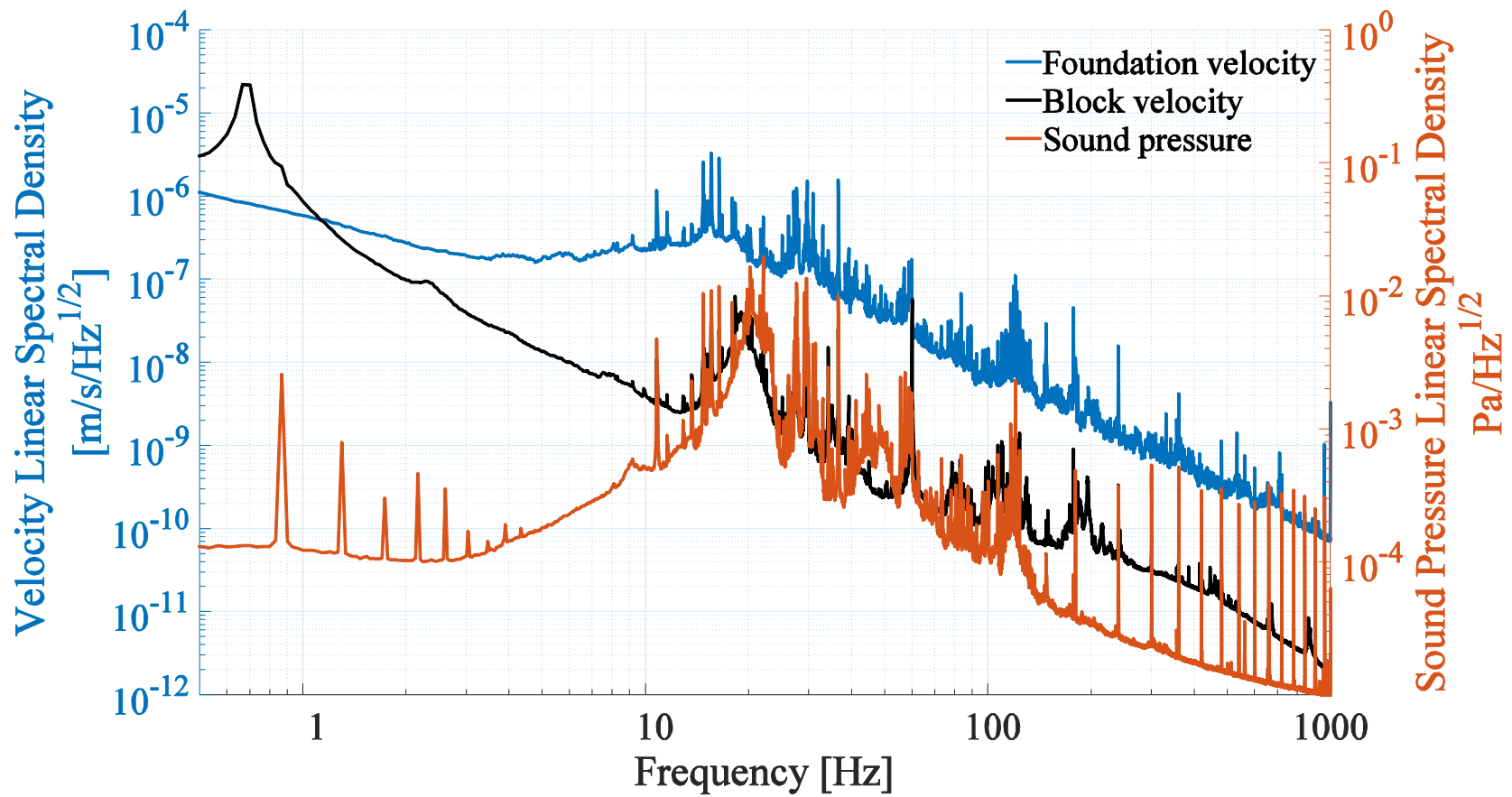


Figure 2.92: Long-term average horizontal velocity spectra on the Nano-g inertia block and foundation compared to the sound pressure level measured near the south surface of the inertia block. These spectra are the long-term linear average spectra detailed in sections 2.6.3 and 2.7.2.4. The inertia block was properly floating and the acoustic vault was closed with nobody inside throughout the data acquisition. The broad peak in the block velocity centered at ~20 Hz seems to correspond with a similar feature in the sound pressure while no similar feature is apparent in the foundation velocity.

To save space, inertia blocks typically extend close to the vertical inner surfaces of their acoustic enclosures. This makes the fundamental horizontal acoustic room modes (and in fact all odd order axial room modes) modes particularly relevant here as these modes will harmonically approach a minimum pressure at one side of the room / inertia block while simultaneously approaching a maximum pressure on the other side, as illustrated in Figure 2.94. Following [23], we can easily develop a simple one dimensional model of the harmonic force on an inertia block with opposing faces of equal areas A separated by a distance L resulting from a harmonic acoustic wave of pressure amplitude

$$P(x, t) = P \cdot \cos\left(\frac{2\pi x}{\lambda}\right) \cdot \cos(2\pi f t)$$

The following model assumes that at time $t = 0$, an acoustic wave impinging on the inertia block has a pressure maximum at the $x = 0$ side of the inertia block. This would at some point be the case for any travelling acoustic wave. Importantly, this is also approximately the case for the pressure-amplitude envelope of the fundamental acoustic room modes in a room whose walls are much closer than one wavelength to the surface of the inertia block. The net acoustic force on the inertia block is approximately

$$\begin{aligned} F_{acoustic}(t) &= F(x = 0, t) + F(x = L, t) \\ &= P(x = 0, t) \cdot A - P(x = L, t) \cdot A \\ &= P \cdot A \cdot \cos(2\pi f t) \cdot \left(1 - \cos\left(\frac{2\pi L}{\lambda}\right)\right) \end{aligned}$$

where the propagation speed c is related to the frequency f and the wavelength λ by $c = f\lambda$.

Thus we have a simple function for the acoustic force on the inertia block, shown in Figure 2.93.

$$F_{acoustic} = P \cdot A \cdot \cos(2\pi ft) \cdot \left(1 - \cos\left(\frac{2\pi Lf}{c}\right)\right) \quad 2.23$$

Parameters used here for modelling the Nano-g inertia block were $A=14.47 \text{ m}^2$ and $L=4.5 \text{ m}$.

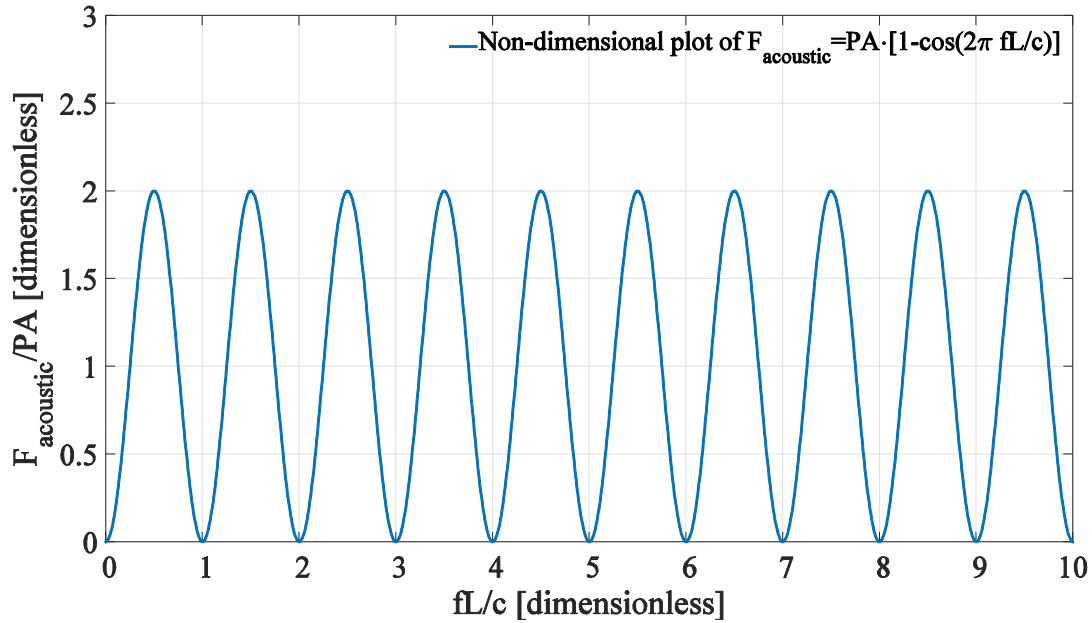


Figure 2.93 : Non-dimensional plot of the acoustic force on an inertia block as a function of the length of the block and of the frequency of the acoustic wave. The force on the inertia block is maximized when $fL/c = n + \frac{1}{2}$ for $n = 0, 1, 2, 3 \dots$ or equivalently, when the block length is an odd multiple of the acoustic *half*-wavelength.

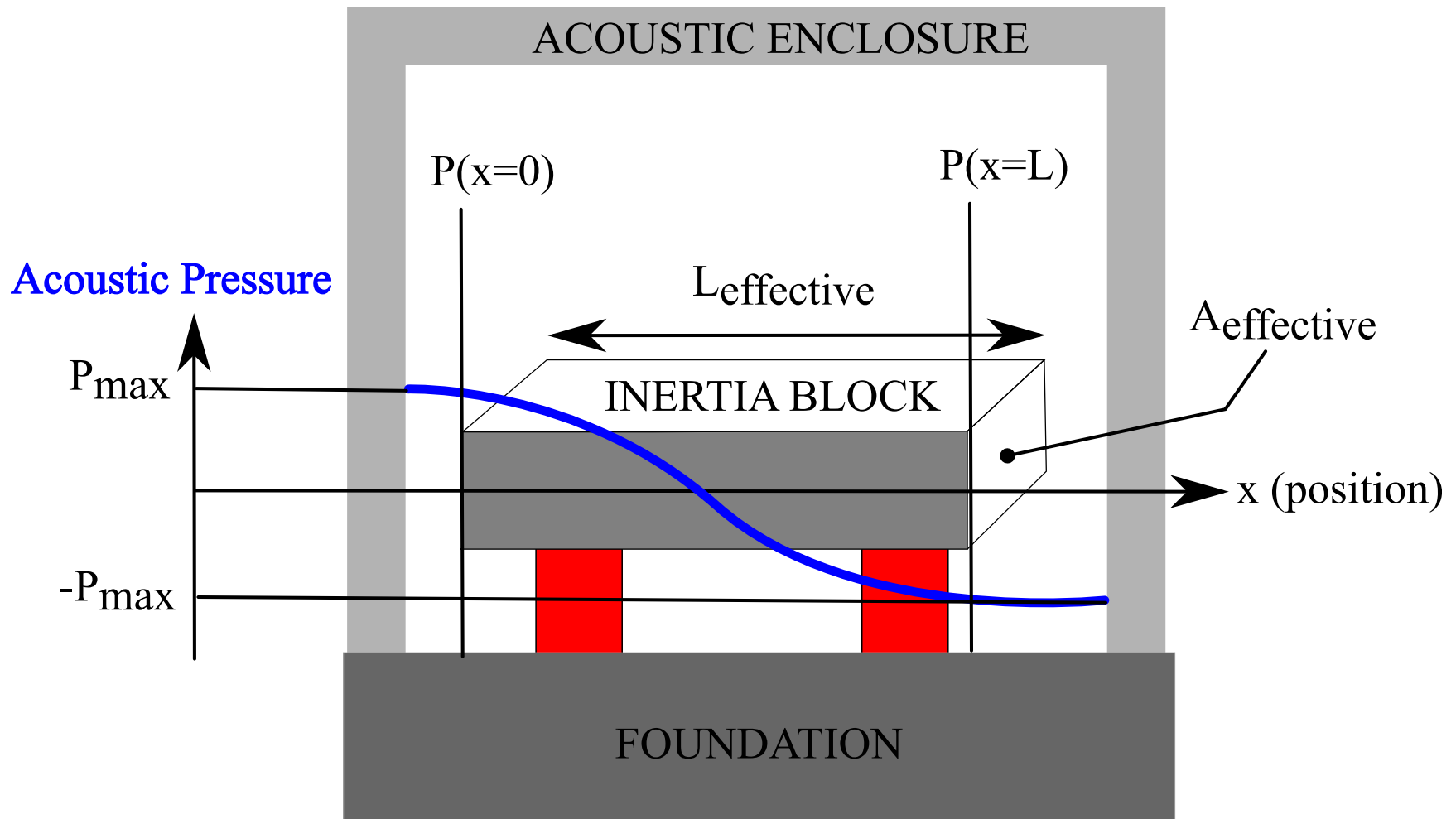


Figure 2.94 : Schematic of the spatial variation in the acoustic pressure of the fundamental acoustic mode of a room containing an inertia block.

With an equation for the acoustic force in hand, it is straightforward to model the velocity response of an inertia block to an acoustic excitation. Fitting the empirical base-excitation transfer function for the pneumatic isolators can yield reasonably accurate values for the system resonant frequency and damping. From these values and the approximately known mass of the inertia block, a force response transfer function H_{force} of the type derived in chapter 1 can be defined for the inertia block. Finally, the total velocity of the inertia block V_{block} can be modelled as:

$$\begin{aligned} V_{block}(f) &= V_{base\ excitation}(f) + V_{acoustic\ excitation}(f) \\ &= V_{foundation}(f) \cdot H_{base}(f) + F_{acoustic}(f) \cdot H_{force}(f) \end{aligned} \quad 2.24$$

where $H_{base}(f)$ is a base-excitation transfer function of the type derived in chapter 1

Examining the empirical transfer function for the Nano-g inertia block isolators (Figure 2.95) motivates a slight complication to this modelling approach due to a secondary peak which appears above the fundamental horizontal resonance. This secondary peak is attributed to a rocking mode of the inertia block. The complication introduced is that to achieve a reasonable fit to the empirical transfer function, a weighted sum of two transfer functions had to be used. Thus the system dynamics are better modelled by:

$$H_{base,overall}(f) = a_1 \cdot H_{base,1}(f, f_{0,1}, \xi_1) + a_2 \cdot H_{base,2}(f, f_{0,2}, \xi_2)$$

$$H_{force,overall}(f) = a_1 \cdot H_{force,1}(f, f_{0,1}, \xi_1) + a_2 \cdot H_{force,2}(f, f_{0,2}, \xi_2)$$

where a_1 and a_2 are linear weights, $H_{base,1}$ and $H_{force,1}$ share a single resonant frequency $f_{0,1}$ and damping ratio ξ_1 and $H_{base,2}$ and $H_{force,2}$ share another resonant frequency $f_{0,2}$ and damping ratio ξ_2 . The best-fit values for these parameters are shown in Figure 2.95. The results of the modelling are presented in Figure 2.96 and Figure 2.97. A inertia block mass of 80T was used.

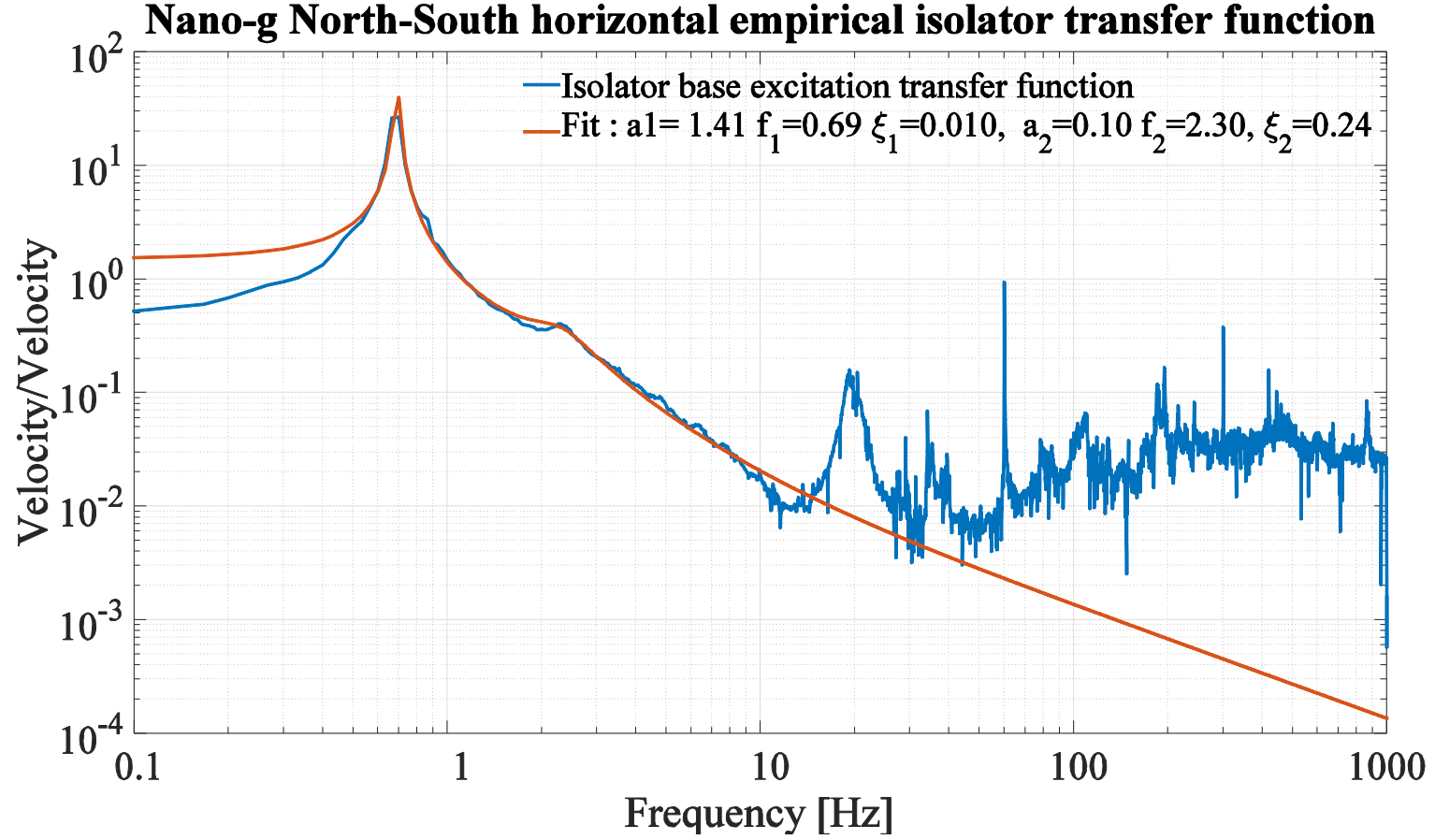


Figure 2.95: Long-term average horizontal axis empirical transfer function and fitted transfer function for the Nano-g inertia block pneumatic isolators. A weighted sum of two 2nd order transfer functions was fit to the empirical transfer function over the region 0.5 – 10 Hz. The slight second resonance at 2.3 Hz is attributed a rocking mode of the inertia block. The conspicuously non-ideal peak in the data at 20 Hz is likely due to acoustic excitation of the inertia block.

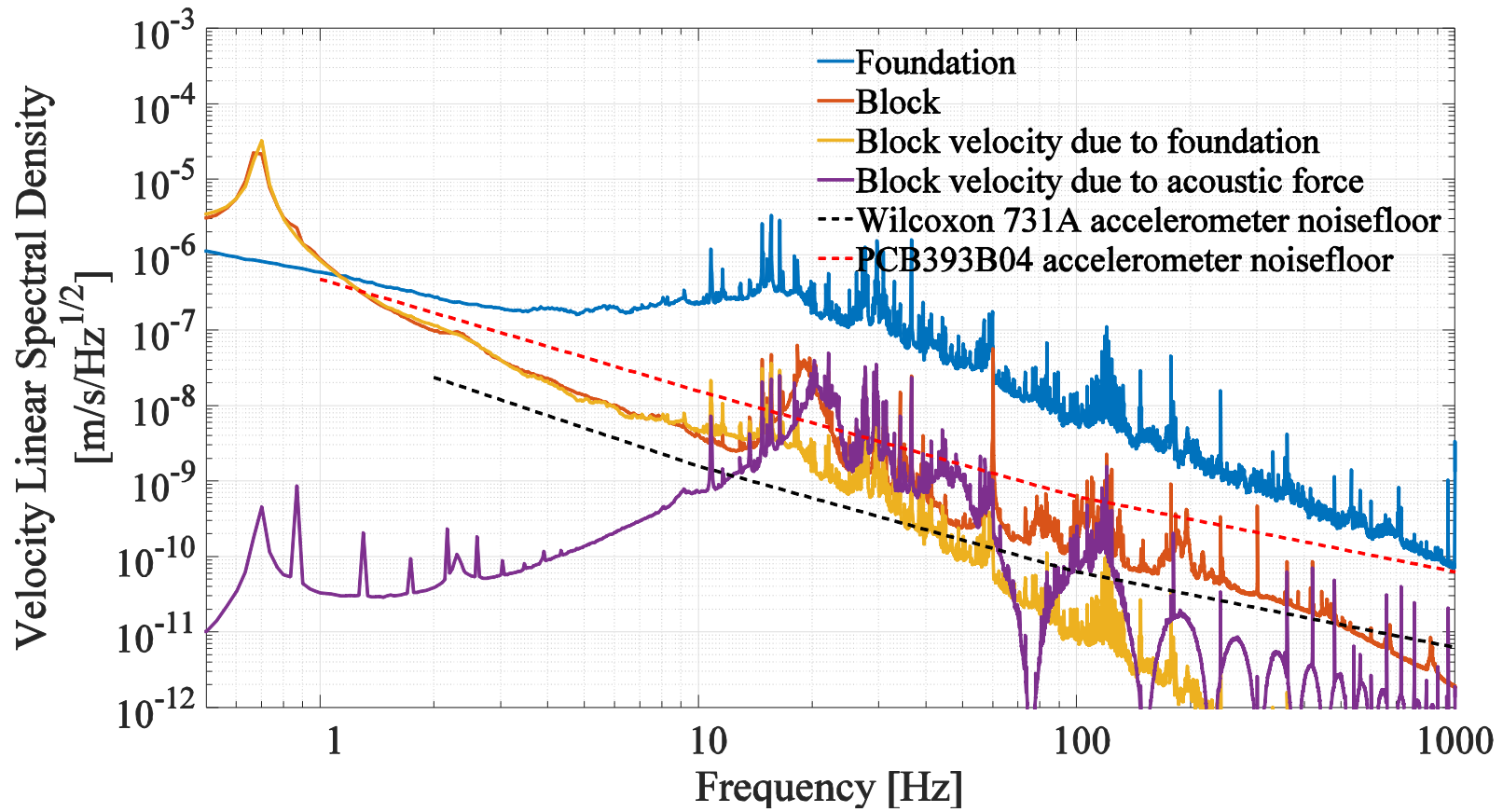


Figure 2.96: Modelled acoustic forcing and base-excitation contributions to the velocity of the Nano-g inertia block

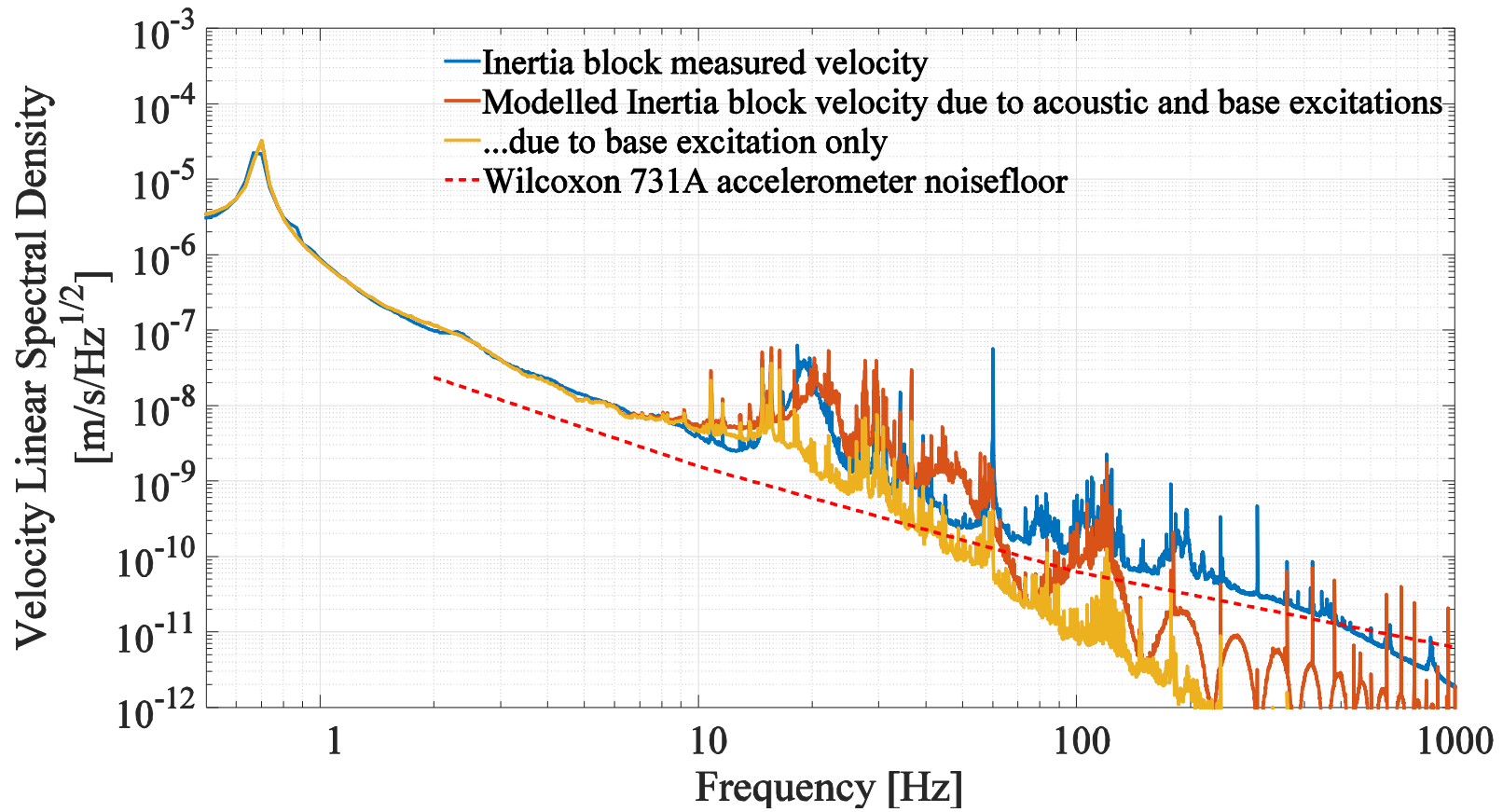


Figure 2.97: Comparison of modelled base excitation and total velocity with the measured velocity of the Nano-g inertia block.

This modelling strongly suggests that the non-ideal behavior of the inertia block near 20 Hz is driven by acoustic forces.

Inaccuracies in the modelled motion are likely the result of the very coarse approximation of the Nano-g inertia block as a cuboid and the simplification of the acoustic field as a plane wave bouncing between the north and south walls where the FEA of the room modes clearly shows otherwise.

A more refined analysis would account for this non-uniform pressure distribution over the more complex hexagonal geometry of this inertia block. An additional refinement to the model would involve refining the higher-frequency part of the force-response transfer function corresponding to rocking motion of the inertia block. This would be accomplished by introducing an effective torsional mass closely related to the moment of inertia of the inertia block as well as an effective acoustic torque. Improvements to this acoustic buffeting model would likely best be implemented using finite element methods.

Additionally, although this analysis has not been carried out for the other inertia blocks, their more approximately cuboidal shapes suggest that the acoustically driven motion of those inertia blocks may conform more closely the simple model used here.

2.7.3 Experiment frames supported by light load pneumatic isolators

The ability of the LAIR facility to meet the vibration criterion set out in section 2.4, depends largely on the behavior of the 2nd stage of vibration isolators – the so-called light load isolators. Unfortunately, the ideal behavior assumed for these 2nd stage isolators in section 2.4 is far from what occurs in practice. During the long run data acquisition in the Omega pod, data was gathered from a PCB393B04 accelerometer mounted on the frame of the STM experiment

housed in that pod. This experiment (an Omicron 4K UHV STM) is supported by three Newport I-2000, which were fully pressurized during the data acquisition. Although the experiment appeared to be floating properly on its pneumatic isolators, isolation was achieved over a limited frequency range, as can be seen by comparing the velocity spectra of the experiment frame and the inertia block (Figure 2.98) or by examining the empirical transfer function (Figure 2.99)

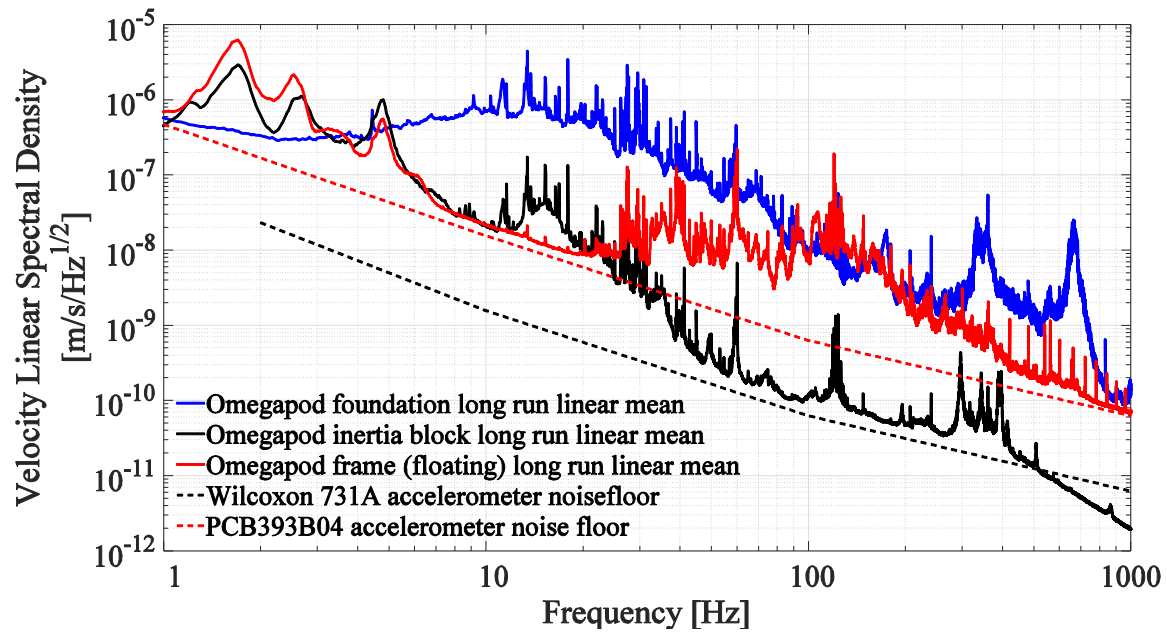


Figure 2.98: Long run linear mean velocity spectra on the Omegapod foundation, inertia block and STM experiment frame. Although the noise floor of the PCB accelerometer obscures the vibration signal on the frame between approximately 8 to 20 Hz, almost no isolation was provided by the light load isolators outside this region

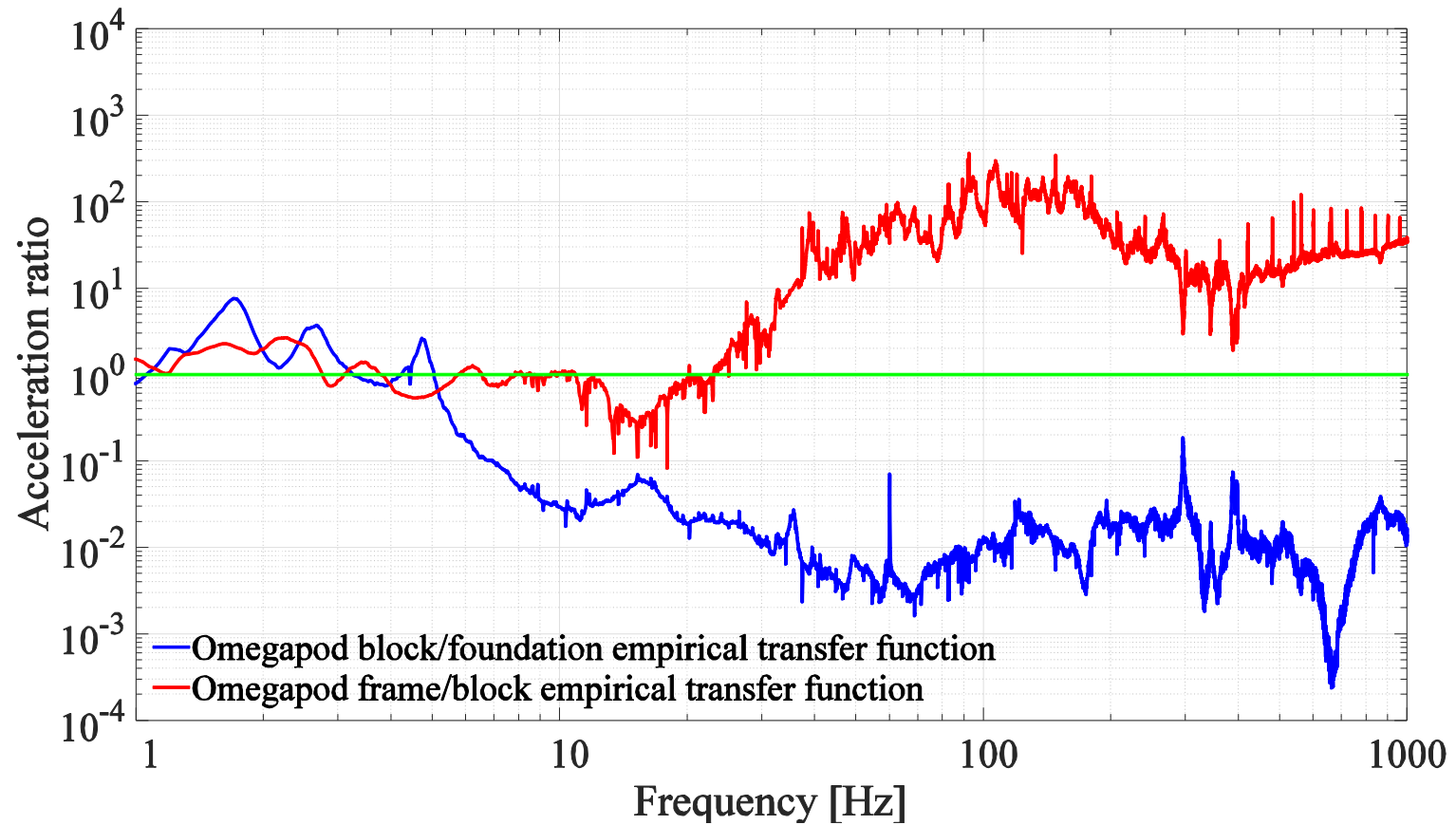


Figure 2.99: Empirical transfer function between the Omegapod inertia block and the Omegapod STM experiment frame Isolation appears to be provided by the light load isolators supporting the frame only in a small region around 10 Hz – although the amount of isolation provided in that region may be higher than shown due to the acceleration signal from the frame dropping to the sensor noise floor between approximately 8-20Hz

As there are some clues in the literature that pneumatic isolators do not perform as well for -small input vibration amplitudes - such as on a substantially isolated inertia block – an attempt was made to investigate the amplitude dependence of the transfer function of the light load isolators. This was done in a binary way, by comparing the transfer function of the light load isolators when the inertia block was floating (i.e. a low input amplitude) to the transfer function when the block was not floating (a high input amplitude) – see Figure 2.100 and Figure 2.101. These data show that at frequencies above 15 Hz, frame vibration is seemingly independent of the vibration level on the inertia block. A possible explanation is that acoustic excitations of the experiment frame are dominating the forces transmitted through the frame. If this is the case, the highly compliant mounting of the frame provided by the light load isolators is actually very detrimental to performance.

Since the force transfer function reduces to

$$\lim_{f \rightarrow 0} H_{force}(f) = \frac{1}{k}$$

in the low frequency limit, to provide better vibration isolation from acoustic disturbances a highly rigid anchoring of the frame to the inertia block would likely be effective. Such a mounting configuration would have a high absolute stiffness (high value of k) and high resonant frequency (ideally >100 Hz), so that large acoustic forces below 100 Hz would be approximately in the low frequency limit.

The lack of substantial isolation of the Omegapod experiment frame above 25 Hz is likely due to the excitation of rigid body, and perhaps flexural, vibration modes of the frame by acoustic forces. The topic of frame vibrations is examined in more detail in chapter 3.

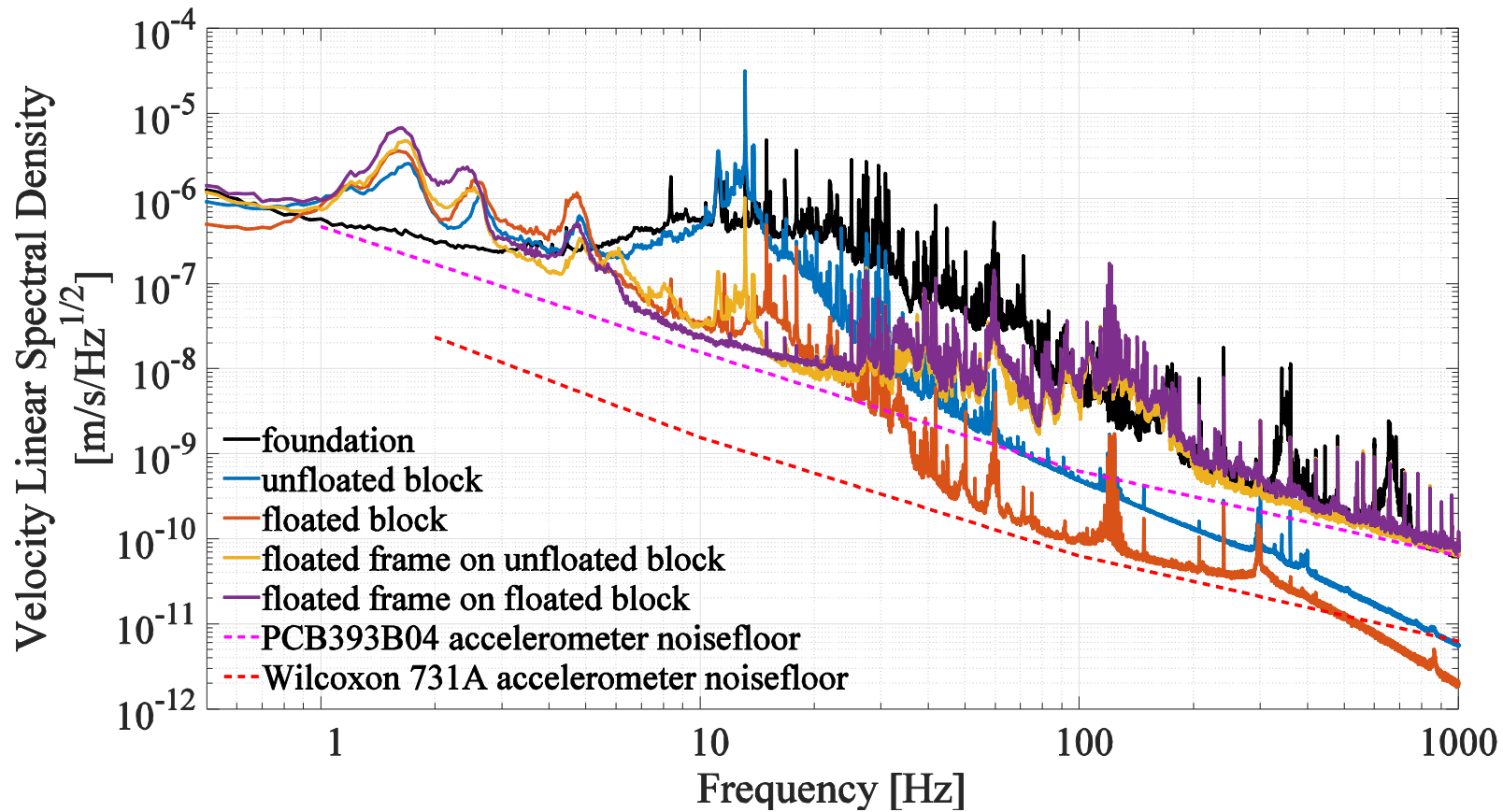


Figure 2.100: Vibration spectra on the OmegaPod STM experiment when floating on its light load isolators for different states of the inertia block The high frequency vibration levels of the frame appear to be substantially independent of the vibration level on the inertia block, suggesting that the dominant excitation mechanism of the frame vibrations at these frequencies is not coupling of vibrations from the block to the frame through the isolators.

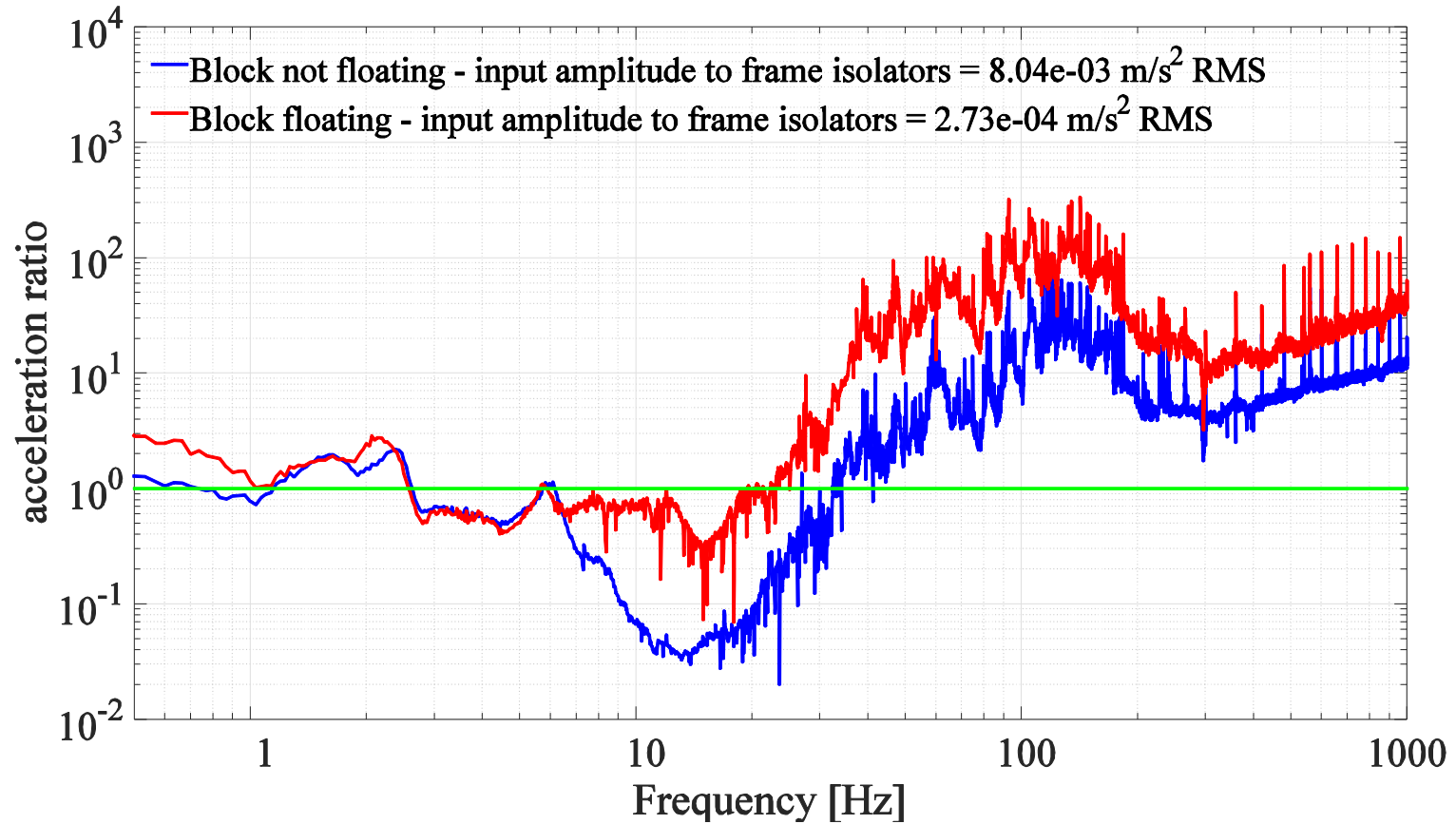


Figure 2.101: Empirical transfer function from the Omegapod inertia block to the frame of the Omicron 4K STM experiment through the experiment's light load pneumatic isolators. Although the red curve is not valid in the region around 10 Hz due to the signal reaching the noise floor of the accelerometer, this data shows that even for large amplitude vibration inputs, the light load isolators provide only roughly ideal behaviour between about 1 and 15 Hz. The peak at ~2.5 Hz is the Z-resonance of the isolator/ experiment structure while the peak just below 6 Hz is most likely a rocking mode of the assembly.

2.8 Comparison to St. Andrews university ultra-low-vibration labs

It is useful to establish how the vibration levels measured in the LAIR facility compare to those measured at a similar facility elsewhere. The Peter Wahl group of the University of St Andrews have kindly shared RMS and peak-hold velocity data for one of the inertia blocks in their newly commissioned ultra-low-vibration labs. These data are compared to the long-term data for the Nano-g inertia block from section 2.7.2.4 in Figure 2.102.

The St Andrews data were taken with a Geospace SN1976 geophone using a Stanford 500x gain preamplifier routed into a Stanford Network analyzer set to averages 20 time-series of 1.024 seconds in length sampled at 800 Hz. Geophone data scaling was performed in MATLAB.

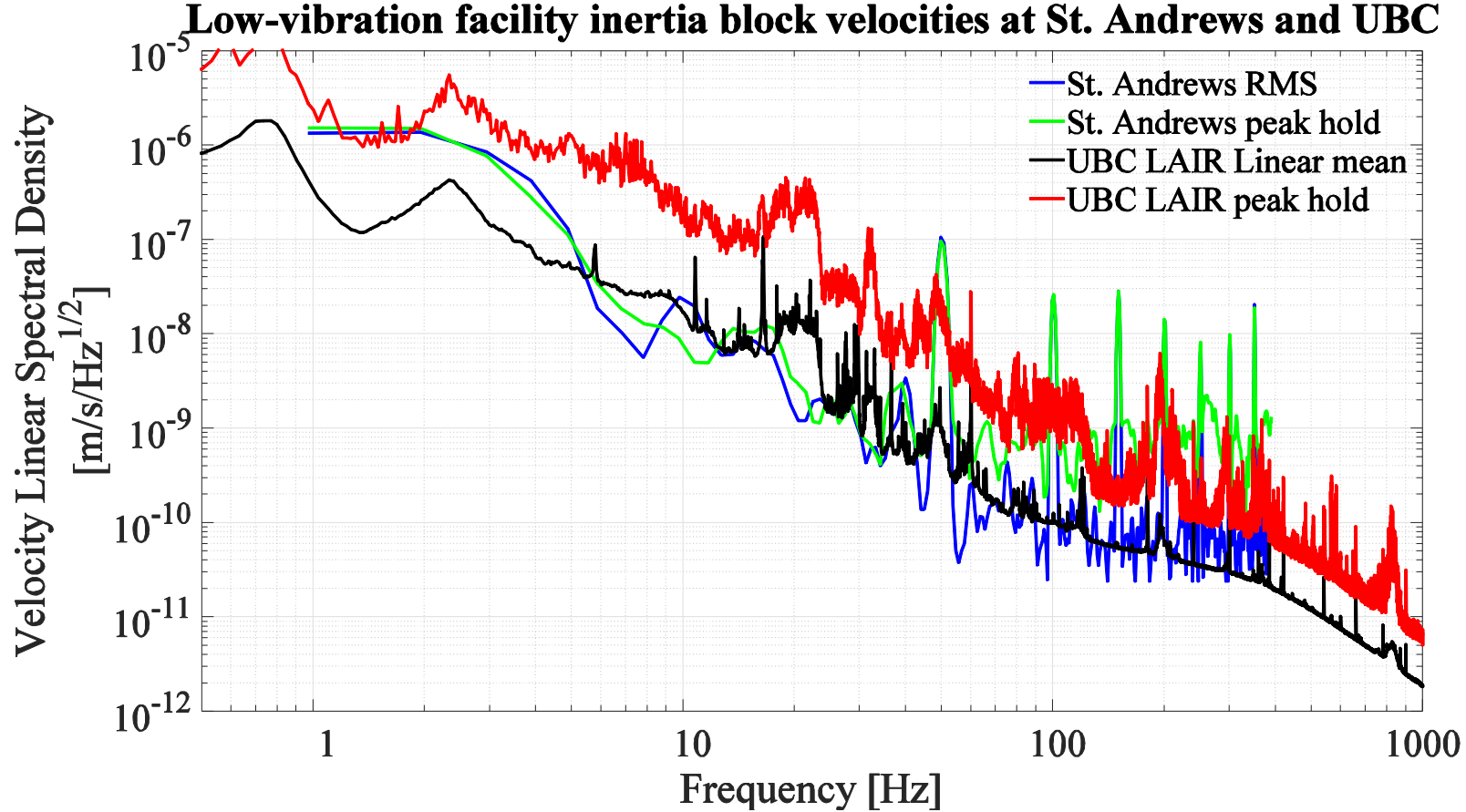


Figure 2.102 : Comparison of peak-hold and averaged velocity spectra for an inertia block at St Andrews with similar data for the Nano-g inertia block at the UBC LAIR facility. The large peaks in the St Andrews data at integer multiples of 50 Hz are electrical pickup in the geophone used and are not representative of the true inertia block velocity at those frequencies. The substantially higher peak-hold spectrum for UBC is likely due to the construction work which was occurring adjacent to the AMPEL building when the data was being acquired. The similar mean velocity spectra suggest that the two facilities are at least roughly comparable in performance over long time periods for which the spectra are not dominated by large amplitude transient vibration events.

Chapter 3: A high-bandwidth, dilution temperature ultra-high-vacuum scanning tunneling microscopy experiment

In this chapter, the UBC dilution refrigerator UHV STM system is briefly described with a focus on the vibrational aspects of the design of microscope head, cryostat and experiment frame.

Accelerometer data and the mechanical noise at the STM tunnel junction for different mechanical configurations of the system are presented, including some simultaneously acquired vibration and STM Z-height noise signals. Finite element analysis is used to show that the engagement or disengagement of a heatswitch can significantly shift the resonant frequency of a problematic mechanical vibration mode of the dilution fridge.

3.1 Microscope head

The design of the scanning tunneling microscope head is presented in this section. The head is a custom-built Pan-style¹⁴ head designed at UBC by Dr. Yan Pennec and myself but which heavily references a detailed design generously provided to us by Professor Seamus Davis of Cornell University. This microscope was assembled and initially tested by Dr. Pennec and Kirill Sapchuk in early 2012 as detailed in Kirill's undergraduate honor's thesis [68]. Although a full description of the engineering and design of this microscope head is outside the scope of this thesis, an overview of the head is shown in Figure 3.1; Details of the scanner tube assembly are shown in Figure 3.2 and of the sample plate in Figure 3.3

¹⁴ See [73] for more details on this style of STM head.

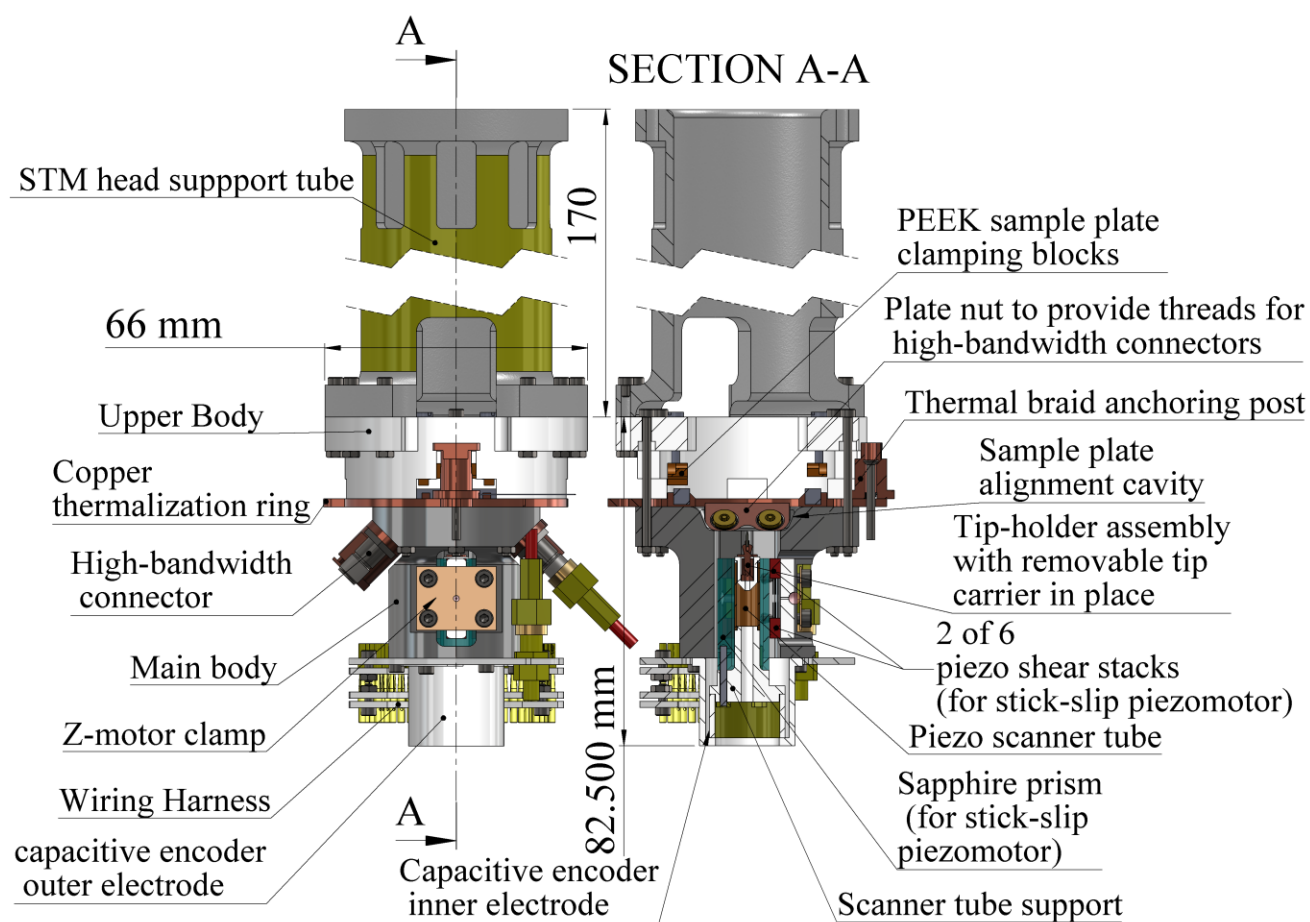


Figure 3.1 : Schematic overview of the microscope head used in the UBC dilution refrigerator STM experiment The tip is approached towards the sample (not shown) by a stick-slip piezomotor, which uses piezoelectric shear stacks to frictionally drag a moving stage (sapphire prism, scanner tube and support, tip) up and down or to rigidly lock it into place as needed. The friction force is set by the adjustment of the beryllium copper Z-motor clamp. The sample plate (not shown) is loaded along the vertical axis into the sample plate alignment cavity; twisting the cap then rigidly locks it against the PEEK clamping blocks.

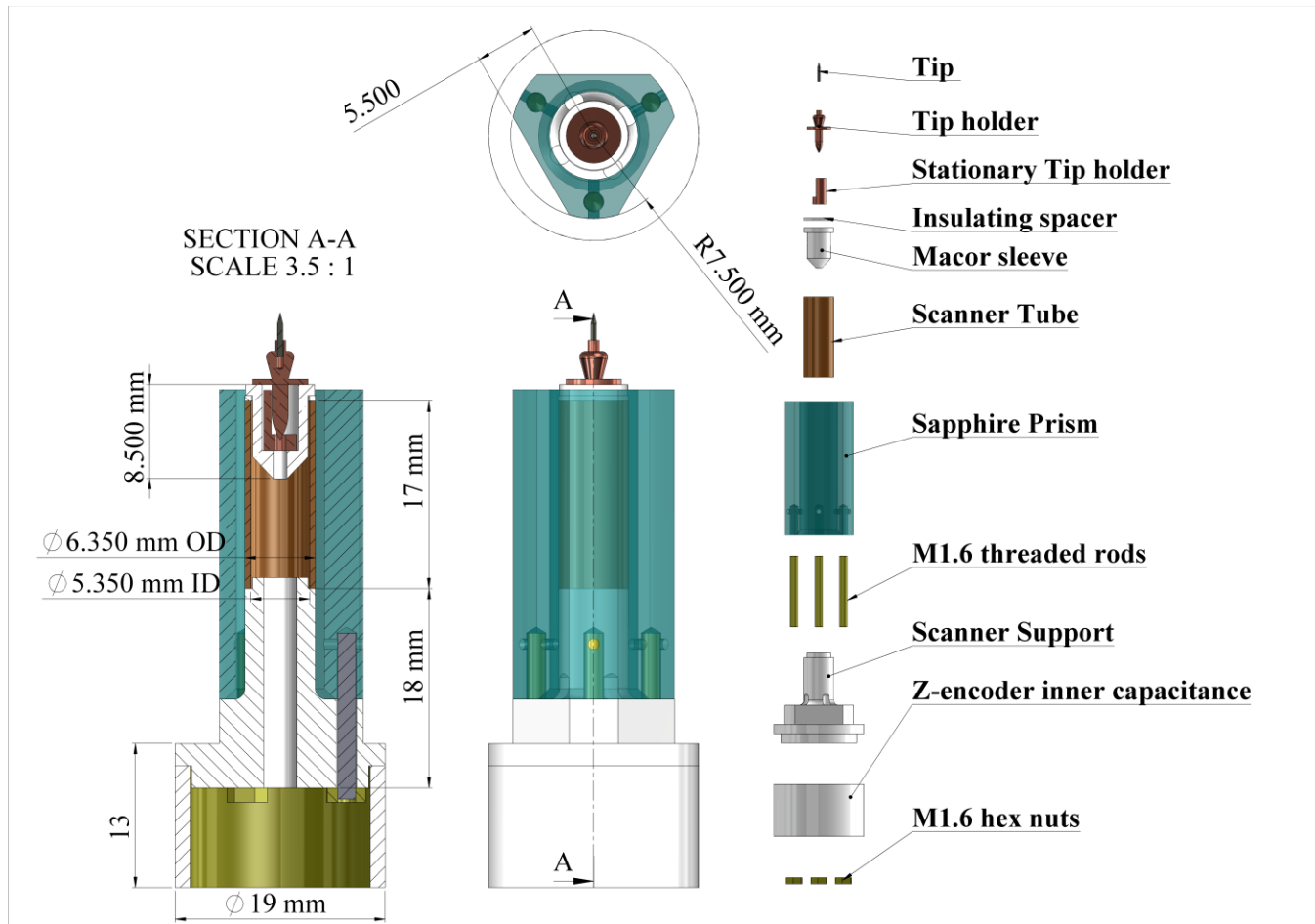


Figure 3.2 : Schematic of the moving stage and scanner tube assembly of the STM All parts shown in white are made from macor. The scanner tube was epoxied to the scanner support with insulating, UHV compatible epoxy and wires for the scanner tube are fed through holes in the scanner support and bonded to the five electrodes of the scanner tube with conductive UHV epoxy. The Z-encoder inner capacitance has been metallized by evaporation of gold. The tunnel current from the tip is carried out of the assembly via a miniature coaxial cable fed through the central hole of the scanner tube and support.

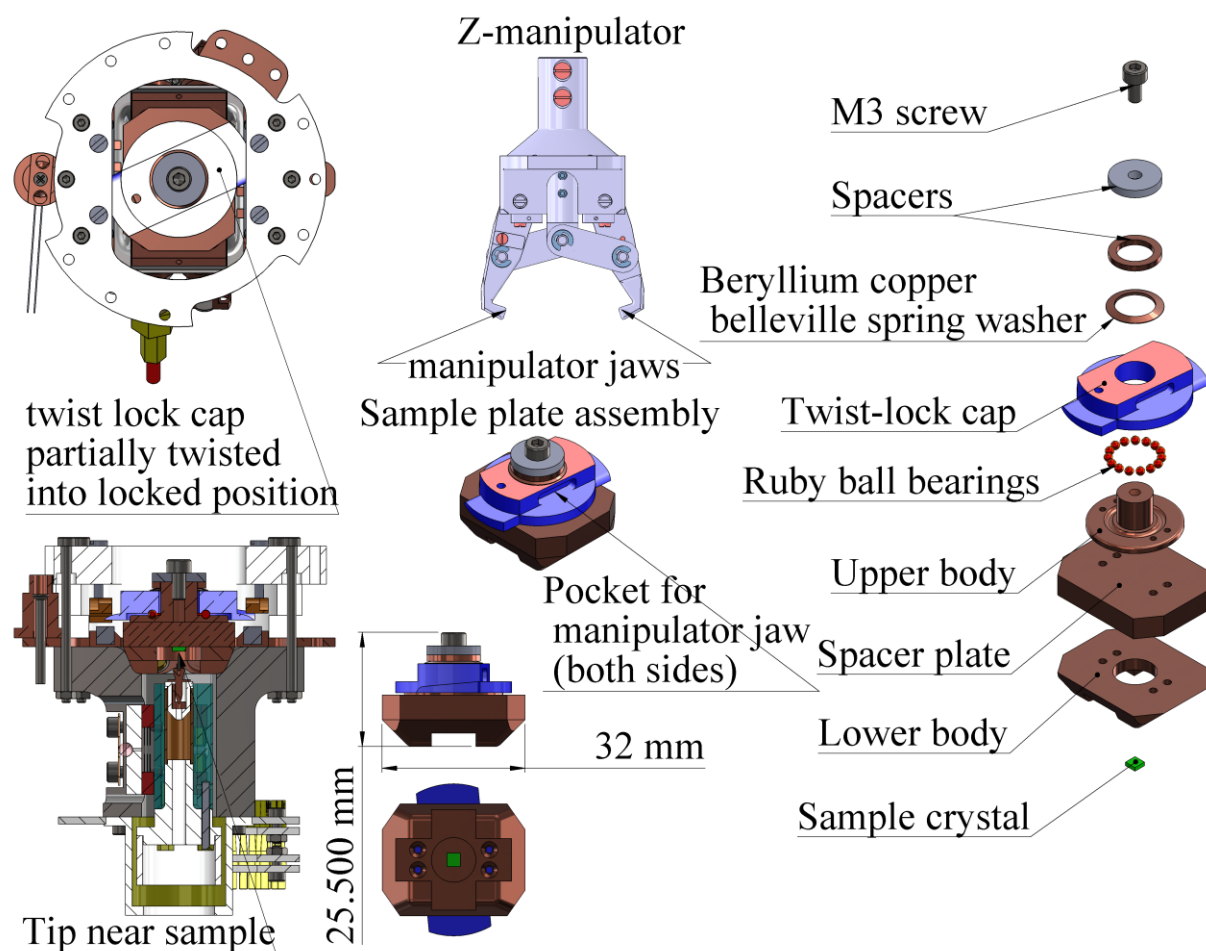


Figure 3.3 : Schematic of sample plate design, transfer mechanism and scheme for locking the sample plate into the head. Pockets in the twist lock cap allow the sample plate to be held by the jaws of the Z-manipulator arm for sample loading and removal. To load a sample into the head, the sample is lowered downwards until the lower body of the sample plate is constrained by the sample alignment cavity in the main body of the STM head. The twist-lock cap can then be rotated relative to the remainder of the sample plate assembly. This causes the sloped “wings” of the twist lock cap to wedge themselves underneath the PEEK clamping blocks attached to the STM upper body, securely locking the sample plate in place. The jaws of the manipulator are then opened and the manipulator can be removed. To remove a sample from the STM head, the process is reversed. A beryllium copper spring washer pre-loads the twist-lock cap against a set of ruby ball bearings, which ensure smooth, low-friction rotation of the cap in the sticky cryogenic UHV environment. The small dragging friction between the spring washer and the top of the twist lock is enough to prevent unwanted rotations without hindering the intentional ones.

3.2 Experiment overview

The experiment consists of the STM head connected via a macor support tube to an ultra-high-vacuum dilution refrigerator (Figure 3.4) built by the Janis Research Company and designed by Janis in collaboration with UBC. The vacuum can of the DR extends into the bore of an American Magnetics 7T (Z) / 2T (X) superconducting vector magnet. During operation, the magnet and DR vacuum can are bathed in the liquid helium which fills the approximately 65L reservoir of the Kadel super-insulated, nitrogen-free dewar (Figure 3.5). This dewar provides a hold time of approximately 10 days when fully filled with helium. The dilution refrigerator is a continuous mixture-circulation type similar to the DR detailed in [5], in that it employs a Joule-Thompson impedance instead of a conventional 1K pot to pre-cool the incoming helium mixture with minimal production of vibrations due to fluid flow. A small number of struts built from thin-walled stainless tubing mechanically connect the ~1K still plate to the 4.2 K vacuum can flange and the mixing chamber plate to the still plate while minimizing the conduction of heat to these stages. Although the low resonance frequencies provided by this construction are undesirable from a vibration perspective, the low cooling powers of these stages require that heat leaks be minimized. To allow rapid pre-cooling of the experiment without introducing a heat exchange gas (which would contaminate the UHV space), a magnetically coupled linear actuator provides a mechanism for thermally coupling these thermally isolated stages to the cooling power of the helium bath. As will be discussed later, the additional stiffness provided by this substantial copper rod provides a useful tool for diagnosing the vibrations of the DR structure. A UHV access bore provides access to the STM head for the in-situ exchange of samples by a manipulator arm. When samples are not being exchanged, thermally anchored rotary shutters block the optical path for the room temperature radiation coming down the UHV access bore.

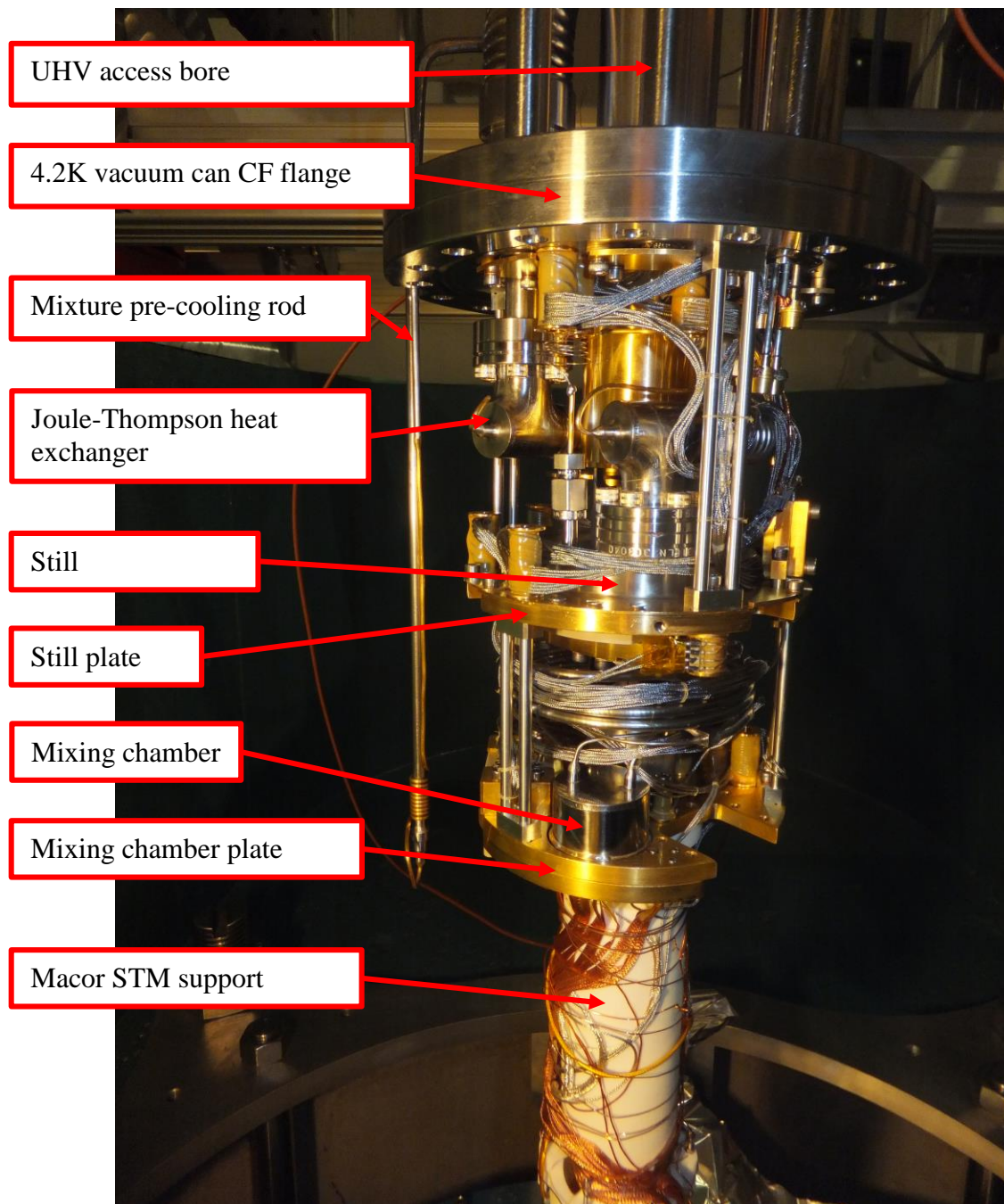


Figure 3.4: A photograph of the dilution refrigerator taken underneath the experiment frame in the access pit of the Nano-g inertia block. Not shown in this picture are : the 1K radiation shield which attaches to the still plate, the UHV vacuum can which seals with a copper gasket to the 4.2 K vacuum can con-flat (CF) flange and contains the entire DR and the STM head, which is attached to end of the macor STM support just below the bottom of the frame.

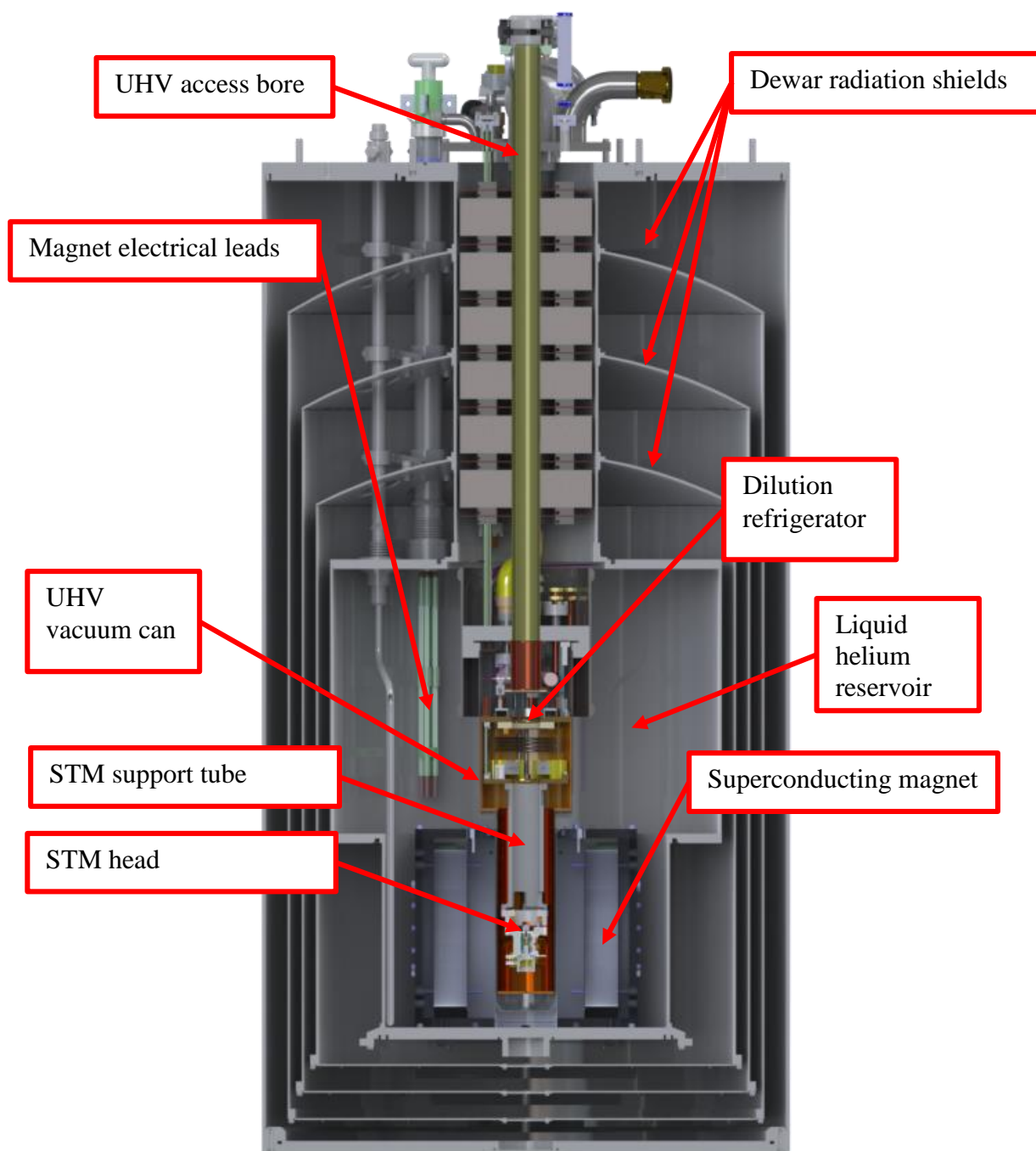


Figure 3.5: Section view of the helium dewar, superconducting magnet, dilution refrigerator and scanning tunneling microscope. Solid models of the DR, magnet and dewar were provided by Janis, AMI and Kadel respectively, and are used with permission. The large mass of the STM and its support combined with the long, slender struts of dilution refrigerator create a low-frequency, vertical-cantilever type mechanical oscillator.

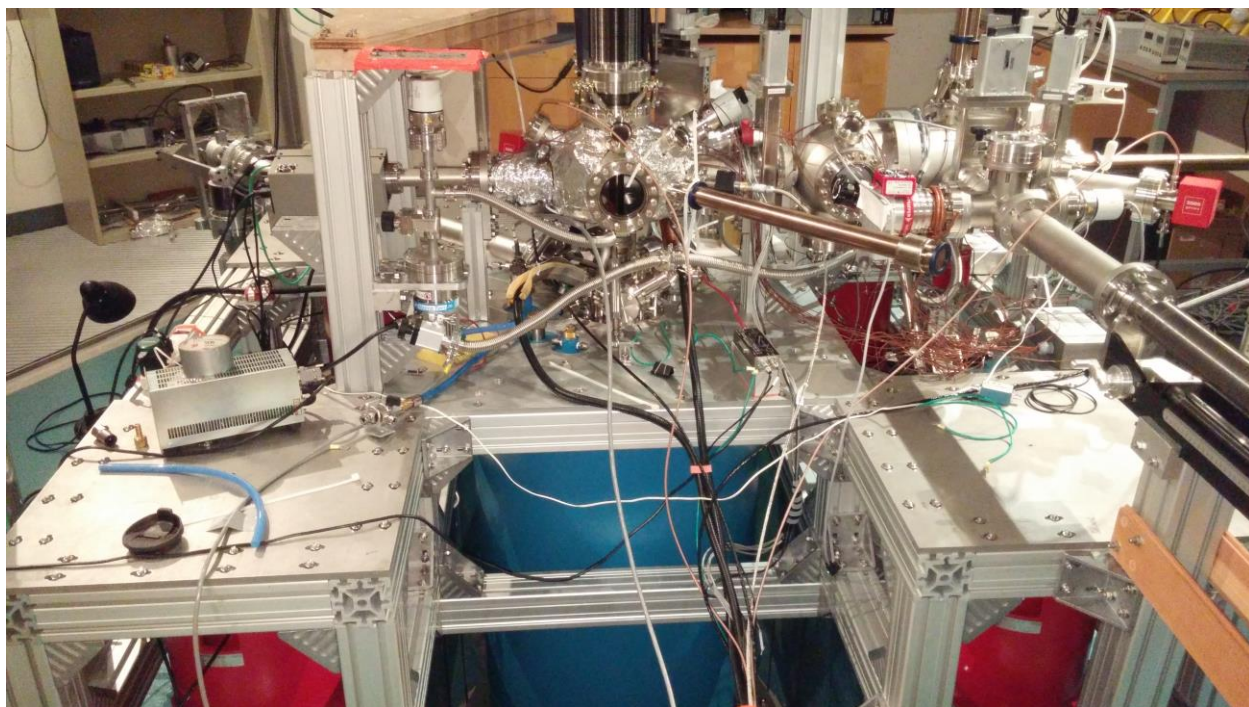


Figure 3.6: Dewar visible underneath experiment frame.

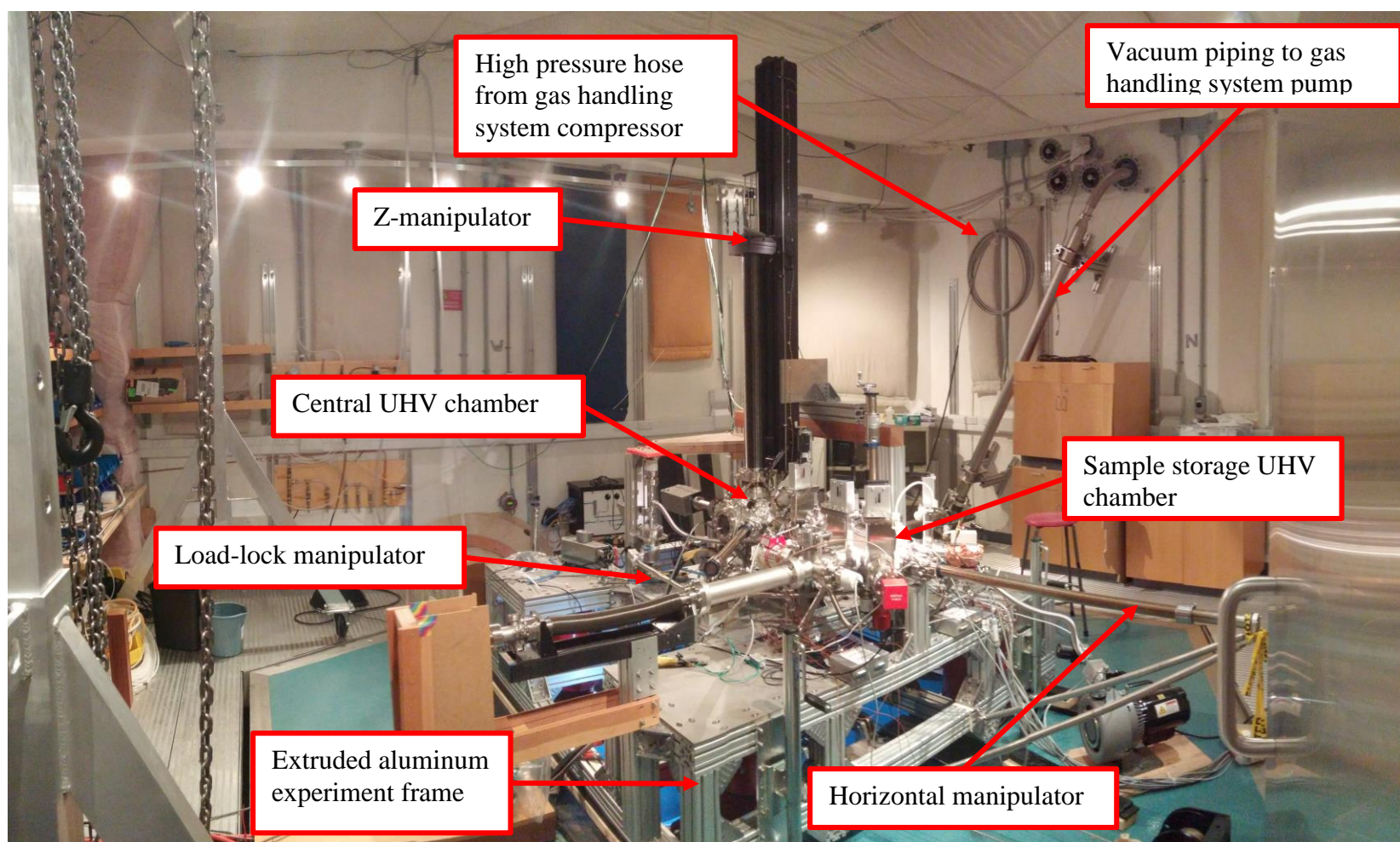


Figure 3.7: Annotated photograph of the UBC dilution fridge STM system on top of the Nano-g inertia block. Additionally visible are the blue painted top surface of the inertia block, the aluminum user access floor surrounding the inertia block and several types of acoustic absorbers on the walls and ceiling.

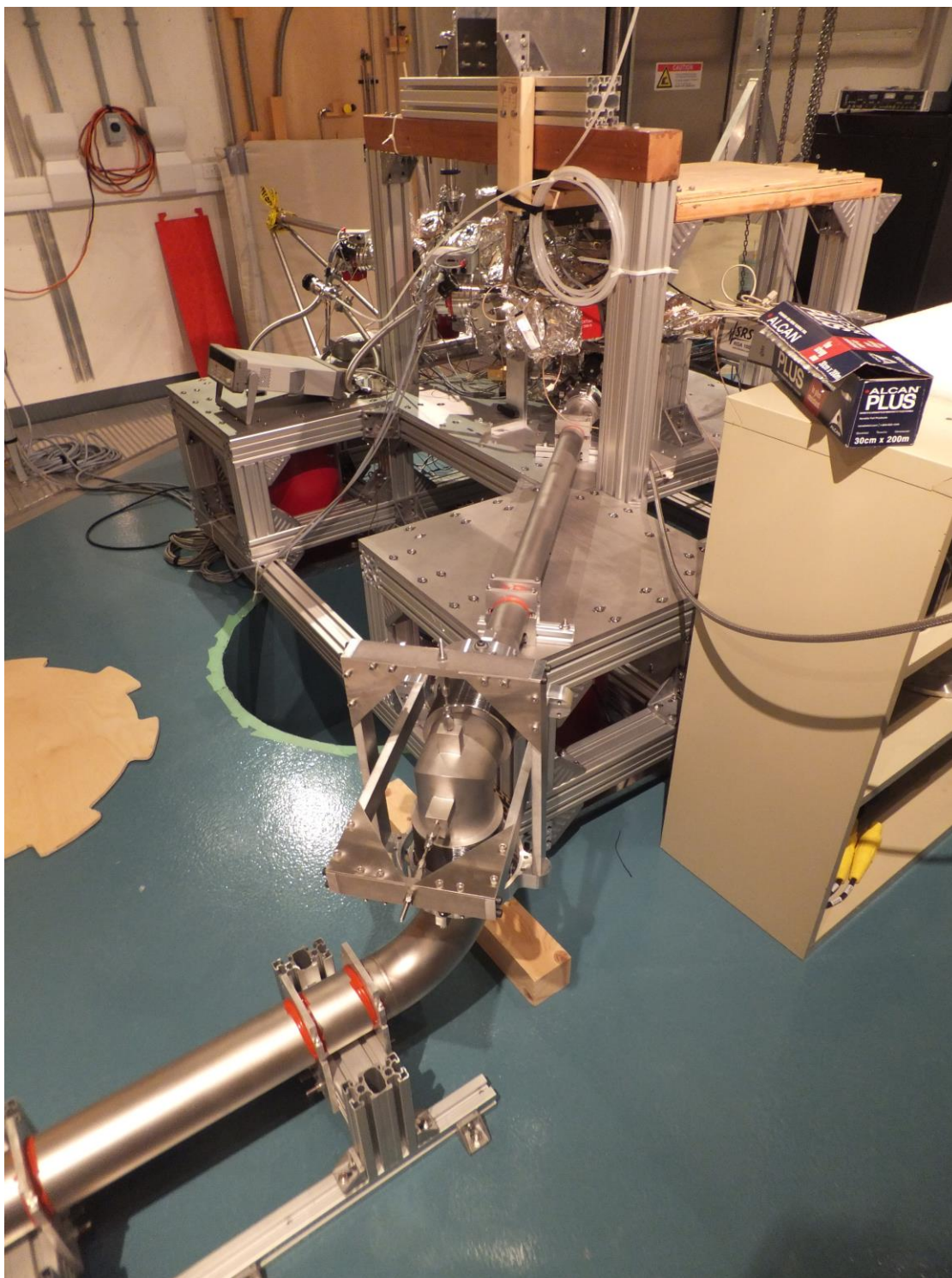


Figure 3.8: Gas handling system pumping line connected to dilution fridge still

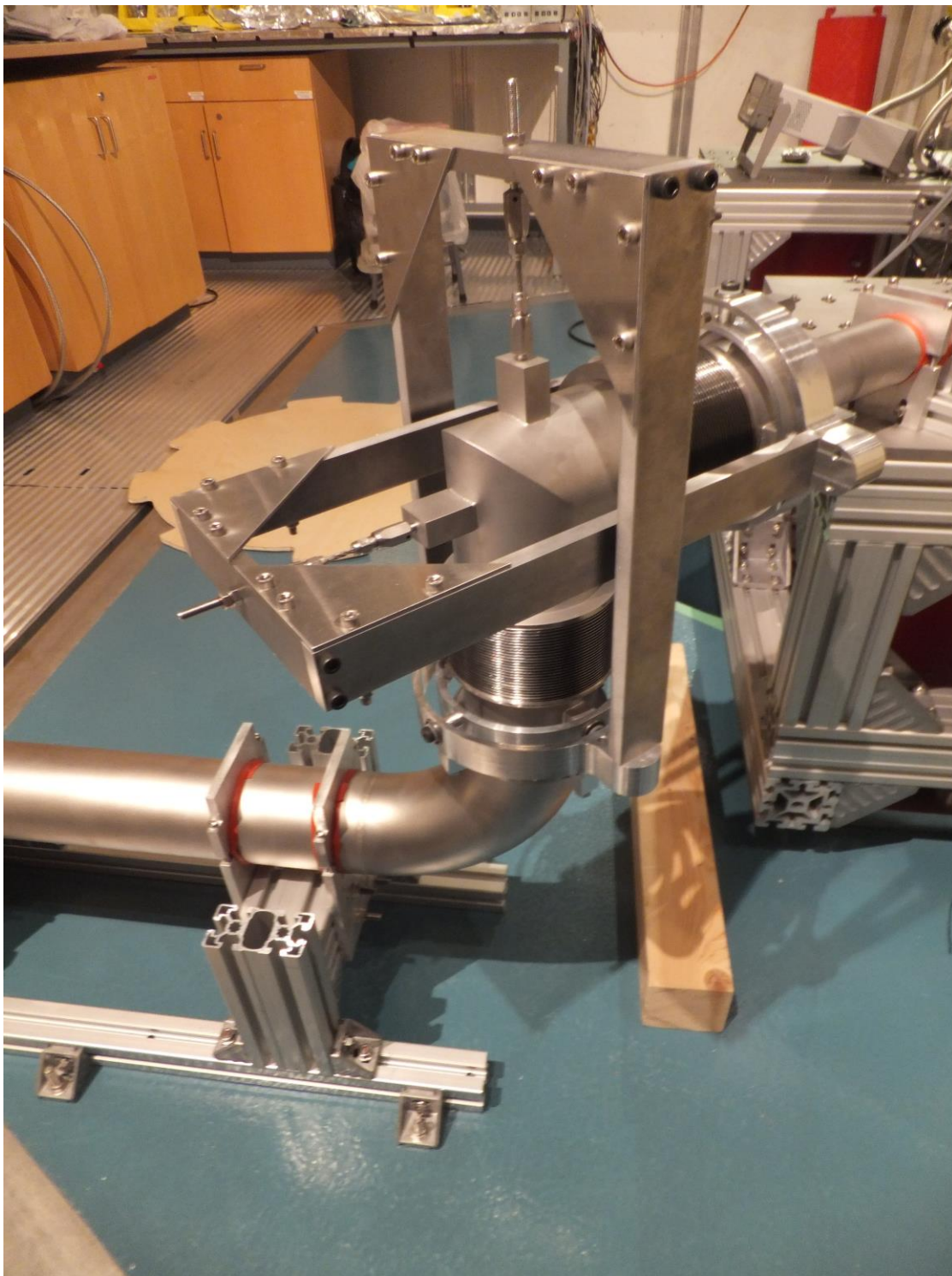


Figure 3.9: Vibration isolating gimbal for dilution fridge pumping line

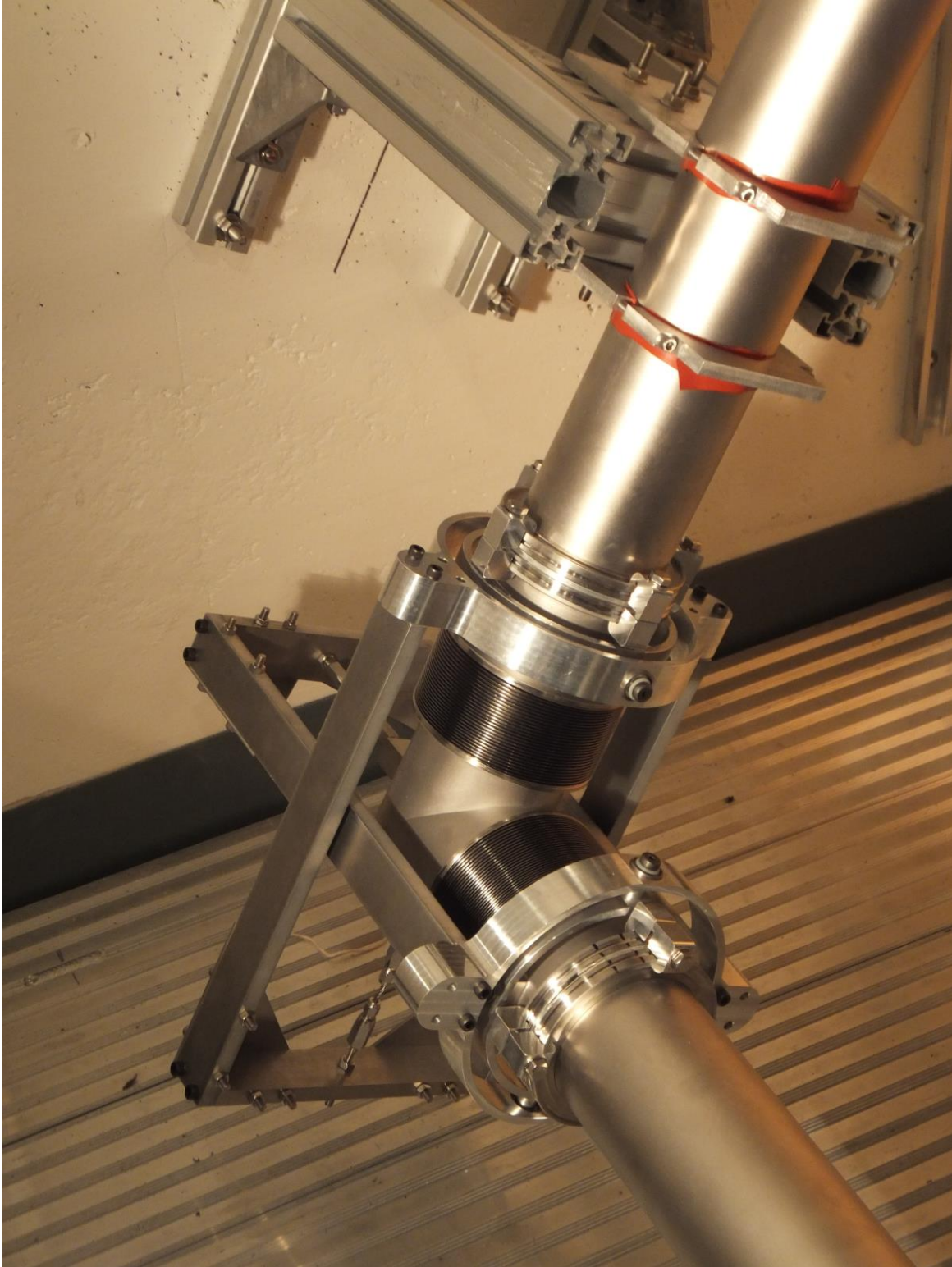


Figure 3.10: 2nd vibration isolating gimbal for dilution fridge pumping line

3.3 Experiment structure vibrations and microscope head performance

Removing the impact of vibrations on the performance of the UBC dilution temperature STM experiment is an ongoing effort. A large reason for this is that the vibration levels on the experiment frame and cryostat are larger than the vibration levels on the inertia block, contrary to the predictions of the simple modelling carried out in section 2.4. This appears to be due to acoustic forces exciting rigid body and possibly flexural motion of the experiment structure.

During the early stages of commissioning the experiment it seemed that floating the light load isolators did not substantially affect the amount of vibration noise present in the microscope's tunneling current signal and the standard operating procedure became to operate the experiment simply sitting on the unfloated light load isolators. More recently (summer 2015), lower intrinsic noise floors¹⁵ have been achieved by operating the experiment at 77K and 4K, revealing the presence of several noise peaks in the tunnel current signal, particularly in the range 10-50 Hz. Troubleshooting these peaks prompted a more careful study of vibration on the experiment frame. Vibration levels were measured on the central plate of the frame with the Wilcoxon 731A. Three conditions were examined (Figure 3.11): the frame sitting on its unfilled light load isolators, floating on the light load isolators and with its corners sitting on 1" thick rubber strips on top of wood 4 x 4's.

The major conclusion of this study was that sitting the frame on the unfloated isolators is the worst possible configuration of the configurations tested, and that the vibration levels on the frame are very sensitive to the exact details of the mounting configuration.

¹⁵ Vibration and diffusion of the atoms on the tip and sample of the microscope contribute broad-band noise to the tunneling current signal which can obscure mechanical noise peaks when the preparation of the tip and sample is not ideal.

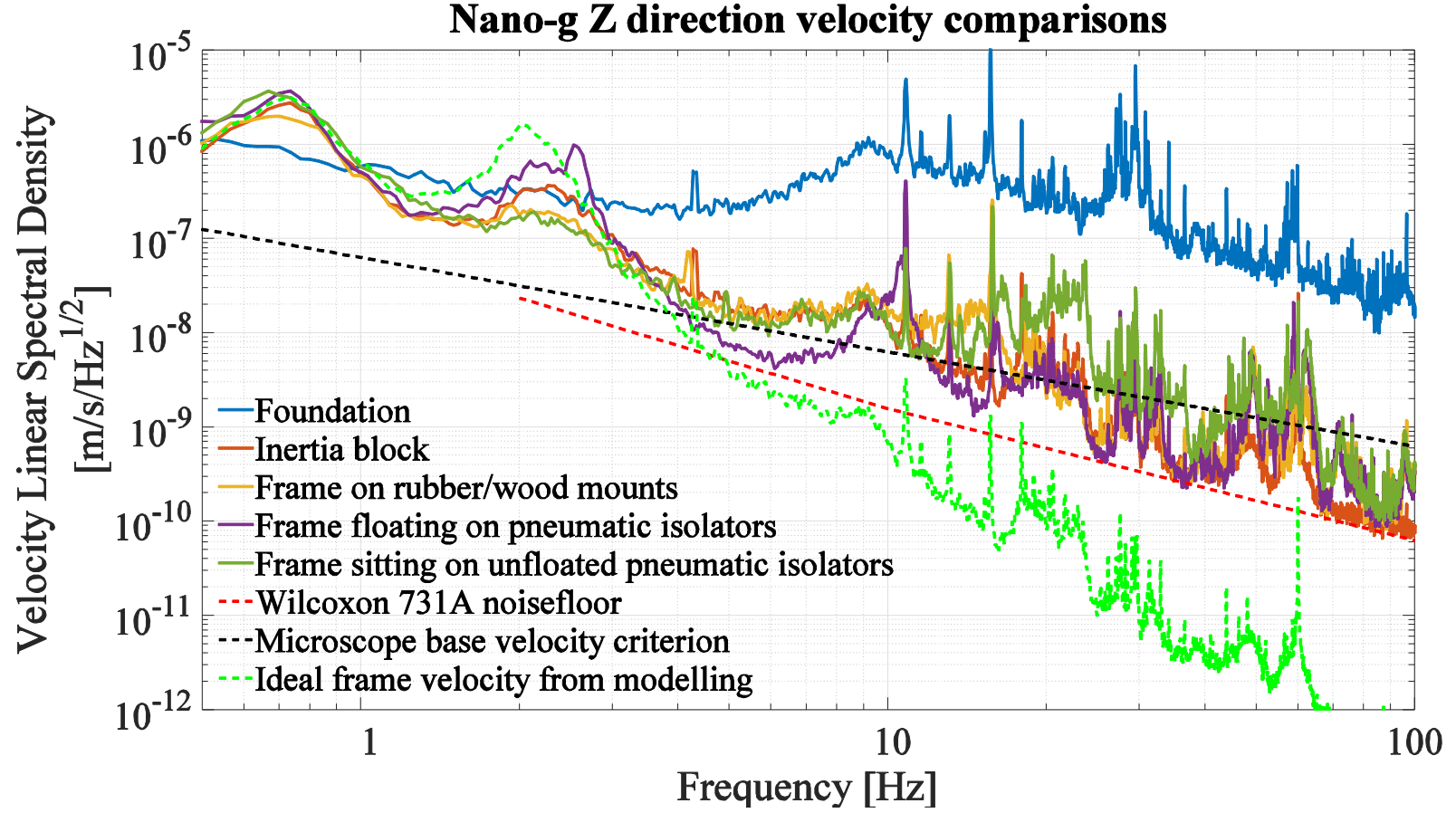


Figure 3.11: Vibration levels measured on the central plate of the dilution refrigerator STM frame under different frame mounting conditions. The frame vibration levels are significantly higher than the ideal starting at frequencies below 10 Hz and this non-ideality is even worse than in the case of the inertia block.

The divergence of the measured vibration levels from those that would ideally be expected due only to base excitations through the isolators suggests that acoustic excitation may again be at play. Any excitations of the frame are also likely to be complicated by the many flexural resonances of that structure.

The acoustic excitation of optical tables – structures which are similar to the dilution STM experiment frame – has been mentioned in at least one location in the literature [52]. In that study, motion attributed to acoustic excitations begins to cause the measured transfer functions to deviate from the ideal above 20-30 Hz.

Assuming a fixed level of motion due to acoustic excitation, it seems reasonable to expect that when an experiment frame is pneumatically suspended on top of an already very quiet floor such as an inertia block, the acoustically driven motion becomes larger than the motion due to base excitation at a lower frequency. Correspondingly, the onset of the deviation of the empirical transfer function from the ideal should occur at a lower frequency on a very quiet floor than for a floor with a higher level of vibration. The ability to float and unfloat the large inertia blocks provides an easy way to test this hypothesis while keeping the set-up of the light load isolator and experiment frame unchanged. Examination of the empirical transfer functions in Figure 3.12 agrees with this line of reasoning.

To complete the picture, acoustic modelling of the same type carried out in section 2.7.2.5 was performed for the frame. The parameters and results of this modelling are shown in Figure 3.13 and Figure 3.14.

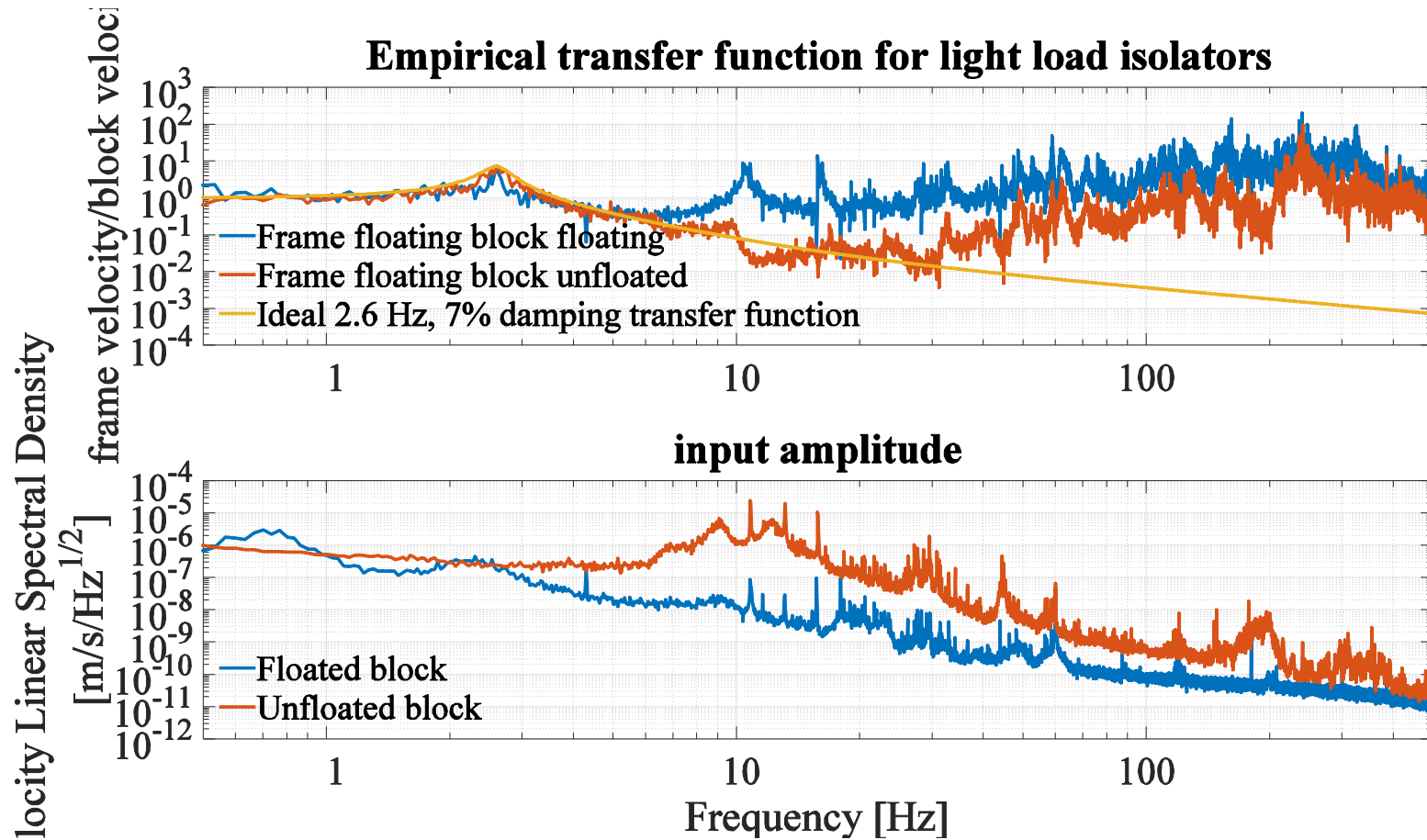


Figure 3.12: Empirical transfer functions from the inertia block to the experiment frame for large (inertia block not floating) and small (inertia block floating) levels on input vibration. For the higher level of input vibration, the transfer function remains ideal to higher frequency (~20-30 Hz) relative to the lower level of input vibration which diverges from the ideal around 5Hz. This is consistent with a fixed amount of acoustically-driven motion which dominates the lower input-amplitude transfer function at a lower frequency than the high input-amplitude transfer function.

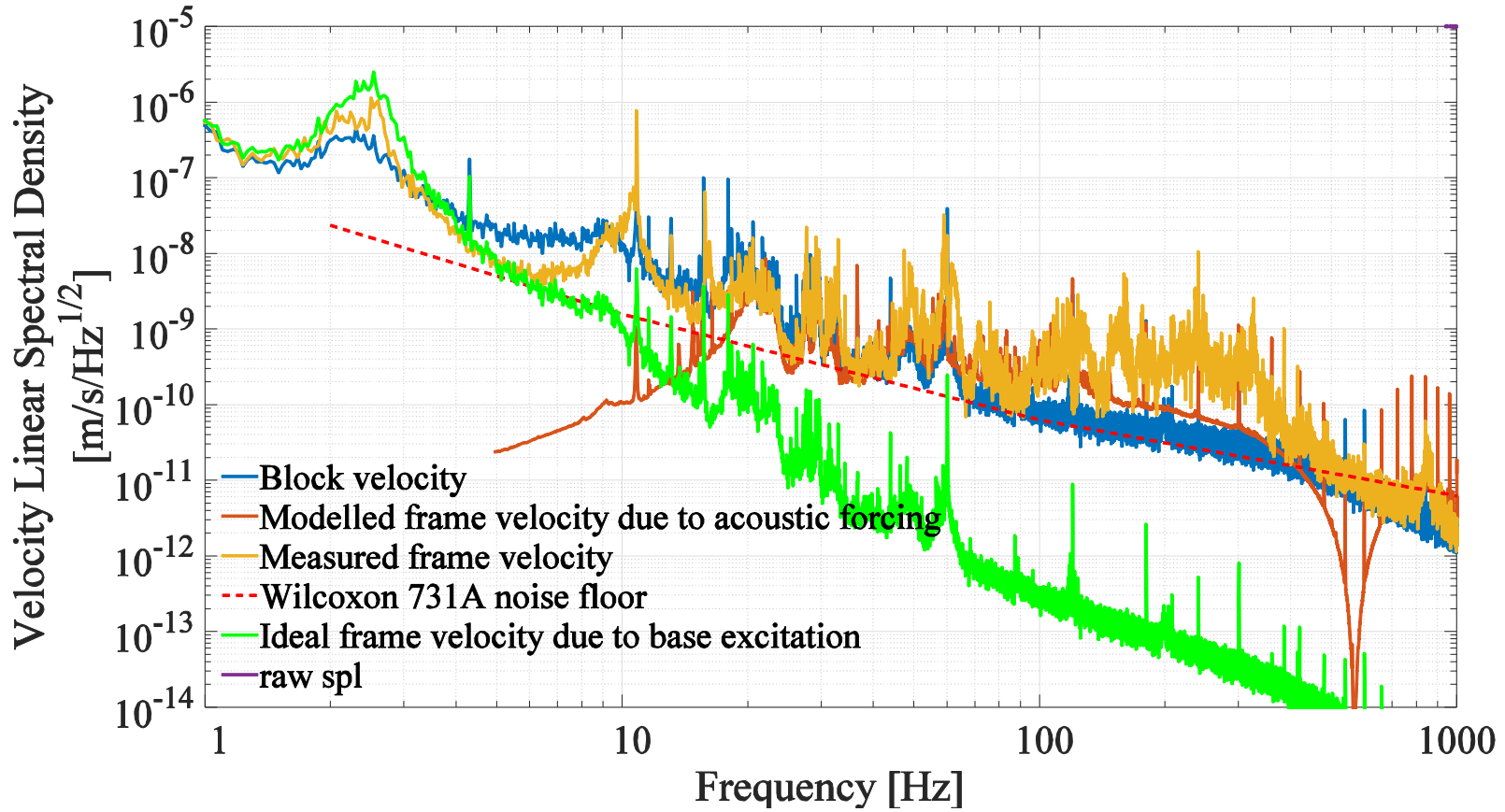


Figure 3.13: Modelled velocity of the dilution STM frame due to acoustic forcing. This modelling treats the frame as a 2.6 Hz oscillator with 7% of critical damping, an acoustic effective surface area of 2 m^2 , acoustic effective length of 0.6m and a mass of 1000 kg. Acoustic forces were computed from the same long term mean data set used for the Nano-g inertia block forcing calculation in section 2.7.2.5. The acoustic excitation of the frame appears to be able to approximately explain a large part of the motion of the frame above ~20 Hz. The conspicuous peak in the frame velocity at ~11 Hz may be a frame resonance.

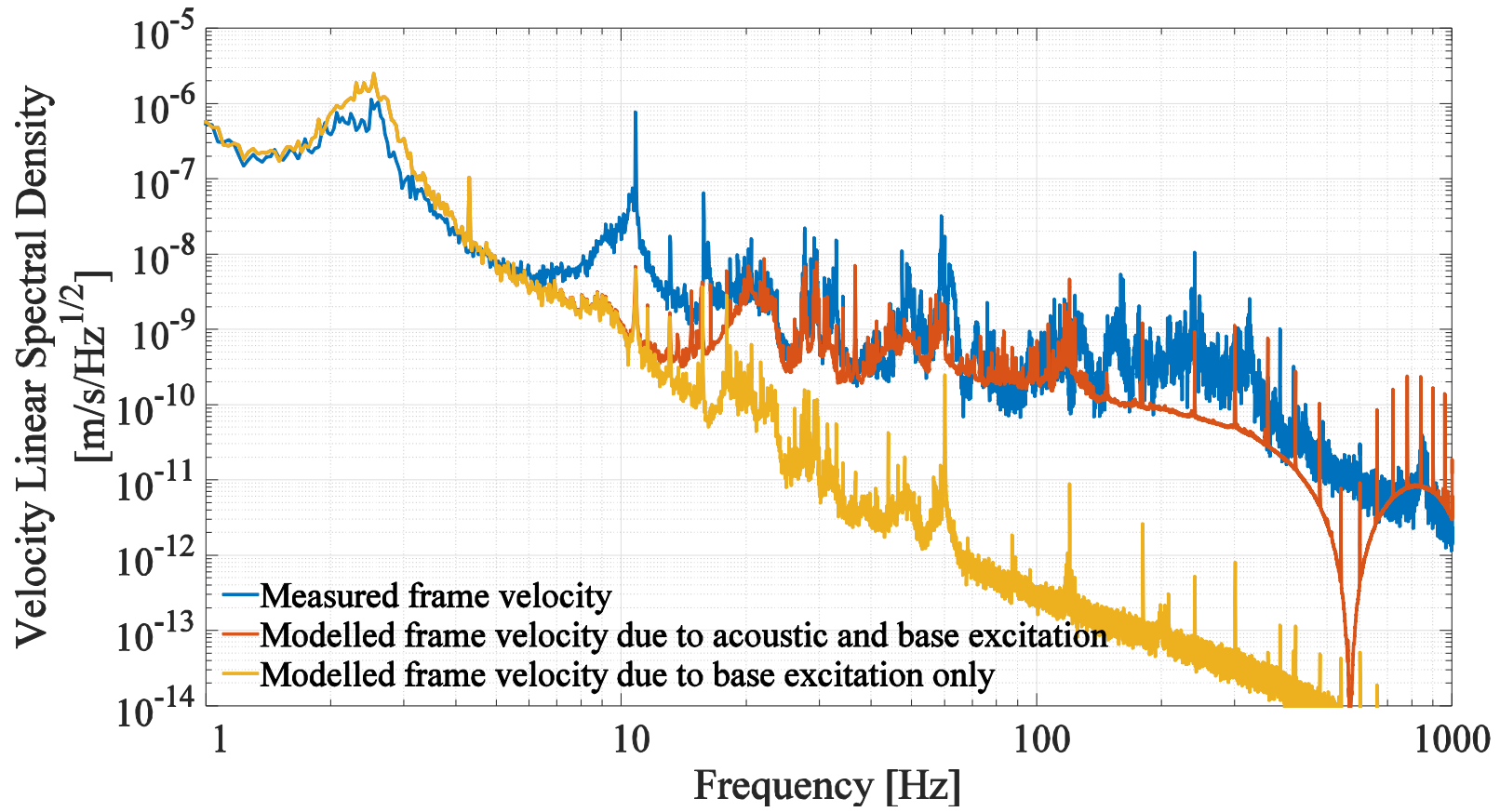


Figure 3.14: Modelled velocity of the dilution STM frame due to combined acoustic and base excitation compared to the ideal base-excitation only modelled velocity. Acoustic forces seem to explain relatively well the measured frame motion above 15 Hz which is not readily explained by base excitation through the isolators.

To gain insight into the coupling of mechanical vibrations to the microscope signal, the vibration levels on the end of the vacuum can near to the mounting position of the microscope head were recorded while simultaneously tunneling onto graphite at room temperature and acquiring Z-height noise data from the STM's feedback loop. This data is shown in Figure 3.16 and Figure 3.17, where the tip motion level is also compared to the $10 \text{ fm}/\sqrt{\text{Hz}}$ vibration criterion established earlier. These data were taken both for the frame sitting on its pneumatic isolator and on the wood/rubber mounts, and show clearly the decrease in vibrations when the wood/rubber mounts are employed.

Horizontal and vertical empirical transfer functions for the tip/sample motion as a function of the vacuum can motion have also been calculated. These empirical transfer functions include the response of the both the dilution fridge and the microscope head since the accelerometers were mounted to the very stiff vacuum can which is connected to the base of the very flexible, low resonant frequency dilution fridge. Nevertheless, the relatively good agreement between the simple modelled sensitivity of the microscope to external perturbations and the empirical transfer functions is encouraging. These empirical transfer functions and the ideal modelled one are compared in Figure 3.17. Note that the empirical transfer functions have only been calculated at the frequencies where clear peaks were visible in both the Z-height and accelerometer data, since the noise floors of both these measurements obscure the mechanical vibration data at most other frequencies¹⁶.

¹⁶ The broadband noise in the tunnel current Z-height feedback signal is likely due to instabilities in the tunneling tip. Meanwhile, the accelerometer signal drops below the noise floor at many frequencies; the large size and mass of the Wilcoxon accelerometer made the use of this superior sensor impractical for this particular experiment.

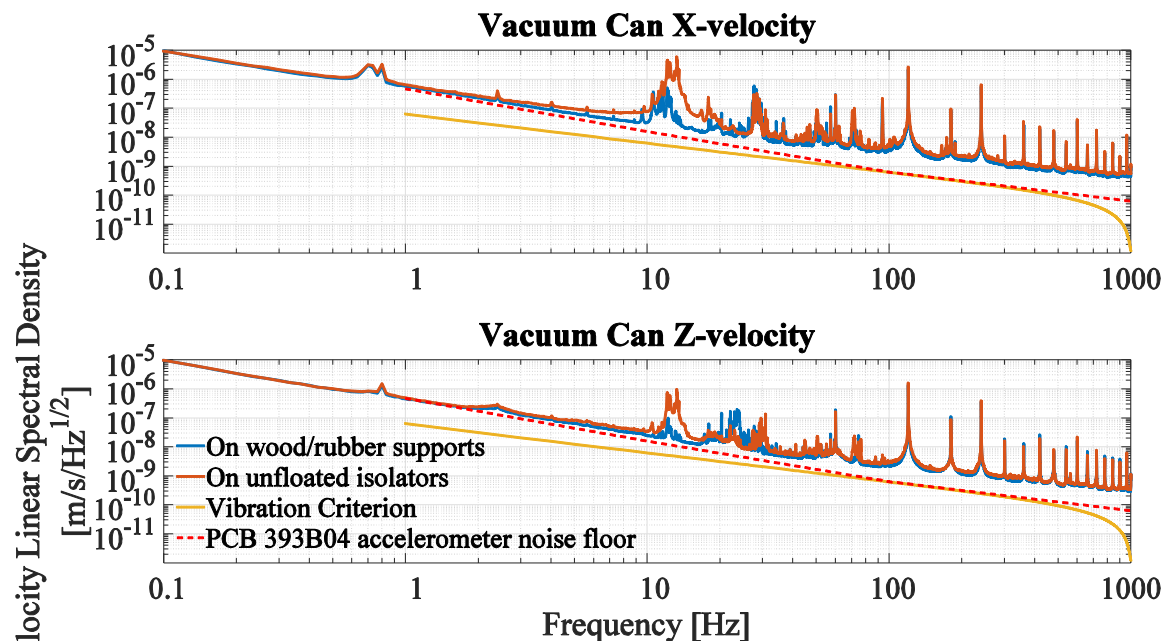


Figure 3.15: Vibration spectra measured at the end of the DR vacuum can compared to the vibration criterion for the STM base established in section 2.4.

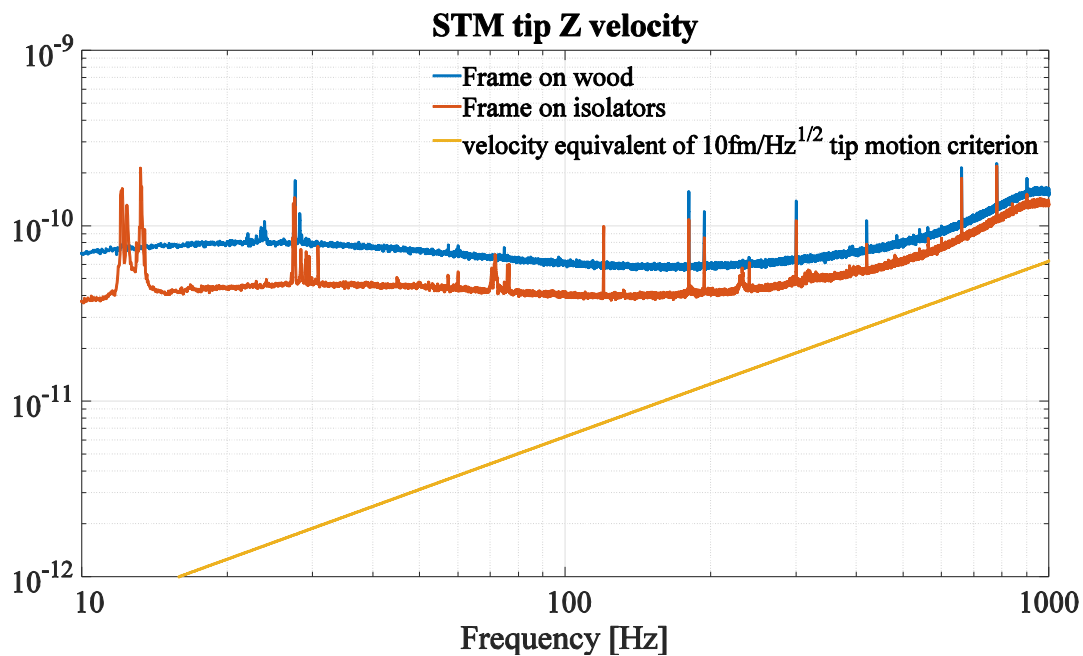


Figure 3.16: Relative Z-velocity of the STM tip to sample while tunneling onto graphite at a 50pA setpoint, 600 mV bias, proportional gain of 20 pm and time constant of 1 ms.

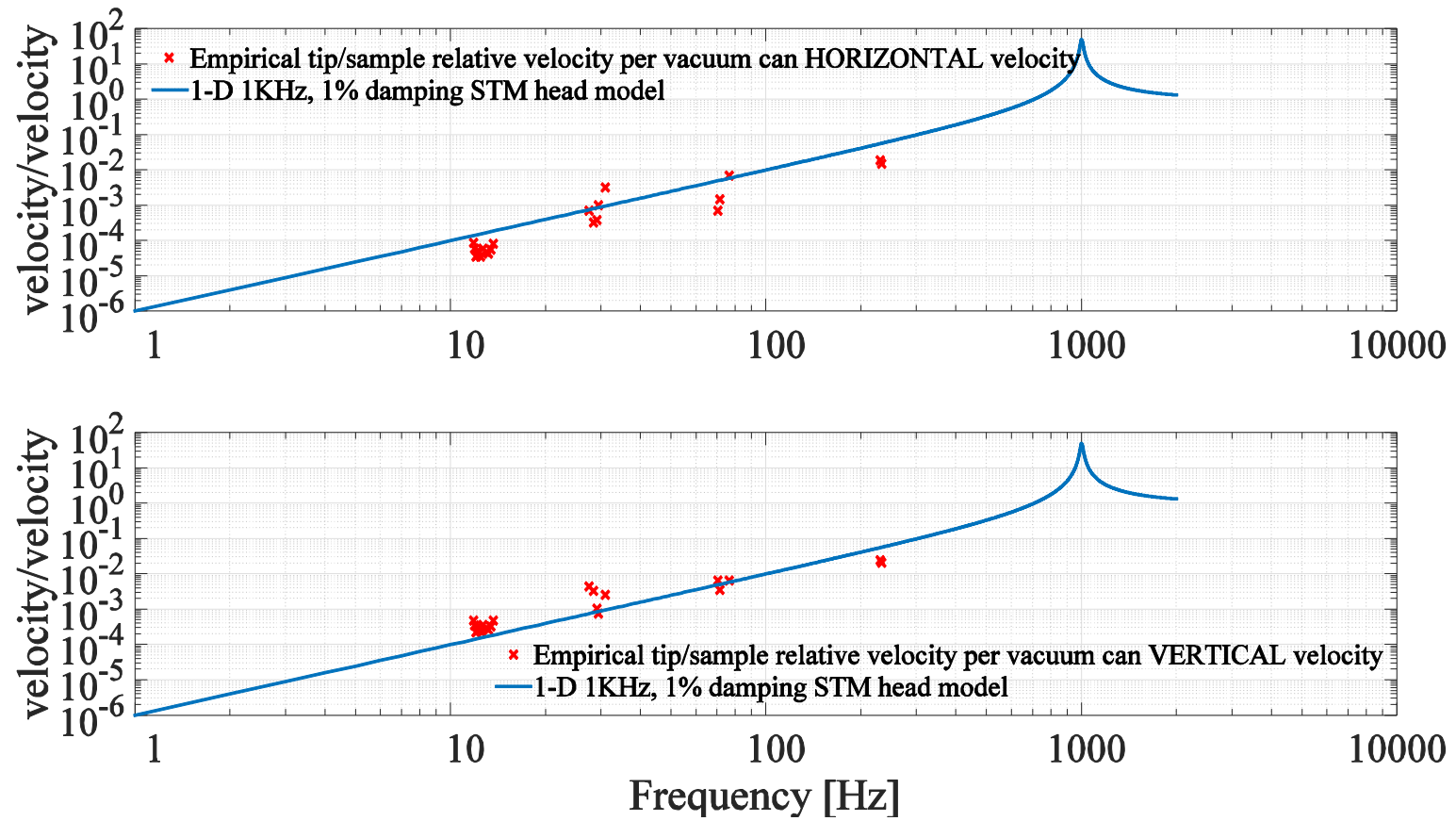


Figure 3.17 Comparison of the empirical transfer functions from the vacuum can to the STM head to the simple model developed in section 2.4 The clusters of data points come from the peaks that show up both in the accelerometer and STM Z-height data.

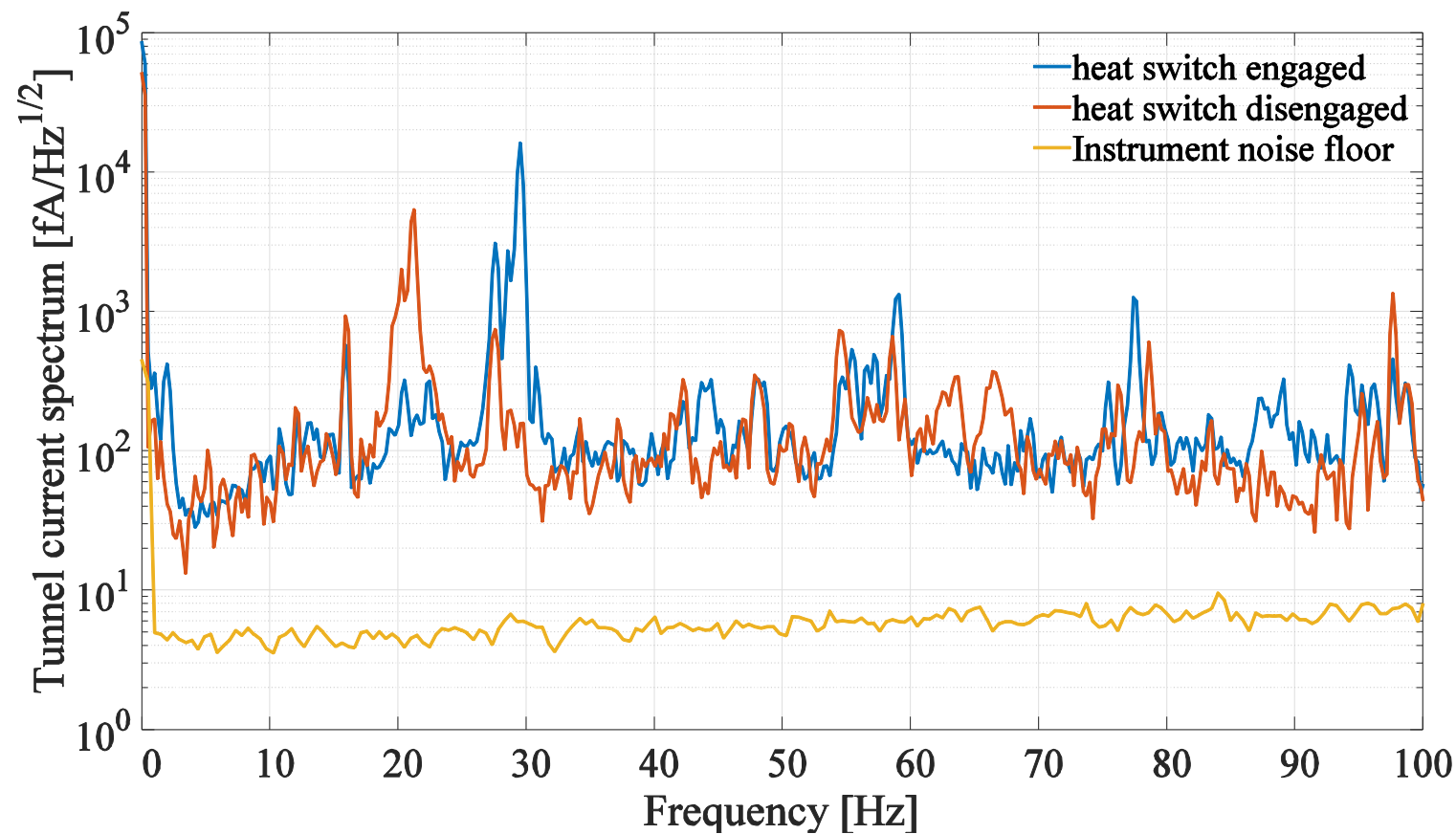


Figure 3.18 : Tunnel current noise-spectrum with and without heat switch rod mechanically connecting the 4K, still and mixing chamber plates.
This data suggests that the 20 Hz peak in the tunnel current noise is due to a resonance of the dilution fridge structure which can be shifted to a higher frequency by increasing the stiffness of the structure by engaging the heat switch.

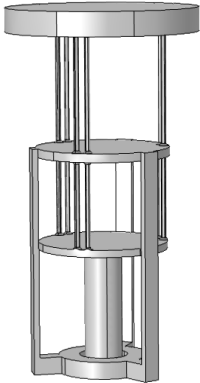
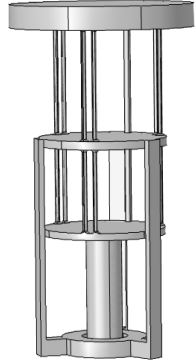
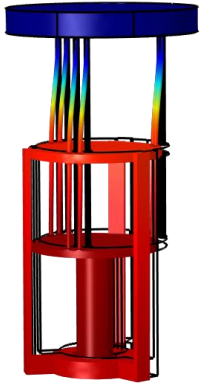
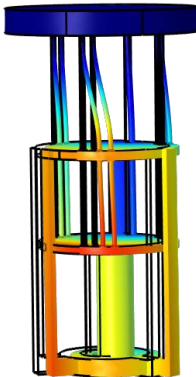
	Heat switch disengaged – 32.15 Hz cantilever mode	Heat-switch engaged – 38.65 Hz cantilever mode
Geometry		
Mode shape		

Figure 3.19 : Finite element analysis of the fundamental cantilever mode of the dilution refrigerator with and without the heat-switch engaged. Simplified geometry is used to facilitate meshing. The mass of the STM and support is modelled as a simple cylinder protruding from the mixing chamber plate, while the mass of the radiation shield is modelled as a disc hanging from three rectangular bars. The engaged heat switch is modelled as a rod connecting the 4K, still and MC plates, the added stiffness of which shifts the resonant frequency of the cantilever mode up from 32.15 to 38.65 Hz, comparable to the experimentally observed shift.

The experimental data in this chapter suggests several parallel courses of action to improve the performance of the STM.

The most direct, and perhaps easiest action that can be taken to improve the STM performance is to add one or more structural members between the 4K and still plates, where the FEA suggests the bulk of the deflection for the cantilever mode of the cryostat is occurring. Ideally this would shift the resonant frequency to a frequency at which there is less excitation energy available, and also increasing the damping of the mode. Although internal friction for most materials tends to decrease at low temperature (see [69] for example), more advanced approaches to damping at cryogenic temperatures such as sliding friction have been employed [70]. The use of a shunted piezoelectric element [71], analogous to a tuned mass damper without the need for a mechanical viscous dashpot element, is another alternative that could work at cryogenic temperatures in UHV.

Further actions could include more rigidly fixing the experiment frame to the block to minimize acoustic excitations of the frame, active isolation of the experiment frame, and improved damping of the acoustics in the room at the problem frequencies.

Chapter 4: Conclusion

This section outlines the conclusions of this research, practical design recommendations arising therefrom, and future research directions which could further advance the state of knowledge and technological capability in the field of ultra-low-vibration facilities. A discussion of the experimental and analytical merits and shortcomings of this work is then given.

4.1 Regarding instrumentation for characterizing low-vibration facilities

Based on the findings of this thesis, conclusions, recommendations and interesting future research directions regarding instrumentation for characterizing low-vibration facilities are outlined in the following subsections.

4.1.1 Conclusions

Order-of magnitude fluctuations in environmental vibration levels – due at least in part to nearby excavation work - were measured to occur in the LAIR facility during the work week.

Valid measurements of the low amplitude acoustic pressure fluctuations and low amplitude vibrations achieved in the LAIR low-vibration facility require the careful selection of measurement equipment. In particular:

- Low-frequency noise in even high-end seismic piezoelectric accelerometers such the PCB 393B04 and Wilcoxon 731A tends to obscure typical vibration signals below approximately 1 Hz.
- The lowest-level ambient sound and vibration signals measured in the LAIR were found to be obscured by the noise floors of the ECM8000 microphone above approximately 100 Hz, by the PCB 393B04 accelerometer at almost all frequencies and by the Wilcoxon

731A accelerometer around 200 Hz. This is due to the effectiveness of the acoustic and seismic vibration isolation measures in the LAIR increasing with frequency, leading to increasingly low ambient signal levels at higher frequencies.

-

4.1.2 Recommendations and future research directions

The large but transient increases in environmental vibration and acoustic levels measured in the LAIR facility during working hours suggest that a truly representative assessment of the vibration levels in a facility must include data taken over long periods both during and outside of working hours. An ideal facility noise and vibration data set would include perhaps 72 hours of data including 48 hours during a work week and 24 hours on a weekend or holiday. This kind of extensive data set is likely to capture at least the most common kinds of transient vibration events occurring in the facility, as well as the magnitude of the increase of vibration levels during the workday. Data from a weekend or holiday when the building is substantially devoid of occupants also enables a differential analysis of which components of the daytime increase in vibration are due to scheduled operation of building mechanical systems and which are due to occupant activity.

At the current levels of vibration performance achieved in the LAIR facility, state of the art low-noise piezoelectric accelerometers such as the Wilcoxon 731A are largely adequate tools for measuring accelerations in the band from approximately 1 Hz to several hundreds of Hz. The principal drawback of these accelerometers is their price; the development of similarly sensitive but much more economical home-built piezo accelerometers such as those detailed [52] or the employment of geophones might enable more widespread deployment of low-noise acceleration

measurements for troubleshooting, optimizing and monitoring the performance of low-vibration facilities such as the LAIR.

As acoustics appear to be the dominant source of vibrational excitation above approximately 15 Hz for inertia blocks and above approximately 7 Hz for experiment frames in the LAIR facility the ability to measure ambient acoustic signals without being limited by the noise floor of the microphone is desirable. The ECM8000 electret microphone used in this study only provided a meaningful signal between approximately 10-100 Hz under the quietest acoustic conditions encountered. Extension the useable bandwidth of the acoustic measurements to higher frequencies through the selection of a microphone with a lower noise floor could help provide more information about the acoustic excitation of frame vibrations which appears to be the dominant source of vibrations out to several hundreds of Hz.

4.2 Regarding acoustic effects on the performance of low-vibration facilities

Based on the findings of this thesis, conclusions, recommendations and interesting future research directions regarding acoustic effects on the performance of low-vibration facilities are outlined in the following subsections.

4.2.1 Conclusions

Several findings made here suggest that acoustic pressure fluctuations play a significant and detrimental role in the performance of the LAIR low vibration facility:

- The empirical transfer functions of both small and large passive pneumatic isolators begin to deviate substantially from the ideal base-excitation transfer function above 10-20 Hz. Simple modelling of the acoustically driven motion of the Nano-g inertia block and

experiment frame suggests that acoustic forces acting on the pneumatically supported stages cause these deviations. As the frequency increases above 10-20 Hz, the modelling suggests that the acoustically driven motion becomes far more important than the motion transmitted through the isolators. This effect appears to substantially reduce the performance of two-stage cascaded passive isolation systems and occurs even in heavily acoustically isolated room studied.

- The transmission of sound through the acoustic doors of the C-Pod double-walled acoustic isolation vault is much larger than the transmission through the walls of the vault. In both cases, the transmission is greatest at low frequencies. Moreover, the low-frequency acoustic resonances of the C-pod vault and the Nano-g vault appear to amplify the ambient acoustic noise which is transmitted into the pod.
- The fundamental acoustic room modes of an approximately cuboidal room can be downshifted by 20% or more when a large, approximately cuboidal inclusion such as an inertia block is present in the room. These modes can be substantially lower than would be predicted only from the largest wall-to-wall distance in these types of rooms. Acoustic Finite Element Analysis appears to be a useful tool for simulating these types of effects.
- The pressure distribution of the fundamental acoustic room modes of approximately cuboidal rooms is such that inertia blocks with dimensions comparable to the room dimensions and large planar faces parallel to the walls of the room are efficiently coupled to the acoustic field at the room's modal frequencies and are therefore subject to important net acoustic forces at these frequencies.
- Measured acoustic pressure spectra increased by more than order of magnitude at the loudest

4.2.2 Recommendations and future research directions

This work suggests several that several approaches to reducing the detrimental effect of acoustic forces on the performance of low-vibration facilities similar to the LAIR may be effective:

Improve acoustic isolation down to low frequencies through the use of heavier, more carefully designed or additional acoustic enclosures.

As the pod doors appear to be an acoustic weak point, ensuring that the attenuation performance of the doors comparable to the rest of the enclosure should be a high priority. Identifying and finding ways to mitigate other potential acoustic weak links such service penetrations may be a valuable direction for future work in this area.

Attenuate acoustic resonances within the enclosures at frequencies down to the frequencies of the fundamental acoustic resonances of the enclosures around 20 Hz.

Effectively damping the resonances of the enclosures will reduce the acoustic forces perturbing the inertia block and experiment frame. Although conventional acoustic treatments are effective above ~100 Hz and large volumes of fibrous material appear to have been moderately effective at damping the acoustic modes of the Nano-g enclosure down to 50 Hz, more sophisticated technologies may be required to achieve effective acoustic damping down to the fundamental modal frequencies of the enclosures.

Candidate technologies which have been experimentally shown to provide substantial damping in the frequency range 20-100 Hz include perforated panel absorbers [61] and compound panel absorbers [58]. Tuned acoustic absorbers employing damped Helmholtz

resonators tuned and coupled to the resonance of an enclosure have also been proposed and studied theoretically [72]. Evaluating and implementing effective low frequency acoustic attenuation treatments and characterizing any resulting reduction in acoustically excited motion of pneumatically isolated inertia blocks and experiment structures is a promising and important direction for future work.

Design inertia blocks and experiment structures which are weakly coupled to the acoustic field inside their acoustic enclosures:

Reducing the surface-area-to-mass ratio of pneumatically suspended stages by using much denser construction materials, adding dense ballasts or minimizing surface area is probably the most straightforward approach to reducing the impact of acoustic forces. Additionally, careful consideration of the geometry of the pneumatically suspended stages relative to the acoustic modes of the room could be beneficial. For example, a cuboidal inertia block rotated by 45 degrees about the vertical axis relative to a surrounding cuboidal acoustic enclosure would likely be subject to substantially reduced acoustic pressure forces by virtue of the block surfaces being further away (on average) from the pressure anti-nodes of the fundamental room modes.

Future work to create new and improved models of the interaction between acoustic forces and both rigid and flexural modes of vibration of inertia blocks and experiment structures could help produce further more specific insights into the design of low vibration facilities and experiments. More exotic approaches, such as feeding-forward measurements incoming acoustic perturbations to an active vibration controller supporting the experiment frame may

also merit investigation should more extreme decreases in vibration levels be deemed necessary for a particular application.

Carefully consider the mechanism by which the experiment frame is mounted on top of the inertia block – a second stage of light load passive vibration isolators may not be the optimal configuration.

The data presented in section 2.7.3 for the Omicron STM frame finds that a floated experiment frame achieves additional isolation only between approximately 2-20 Hz and has much higher vibration levels than the inertia block on which it rests above this frequency range (although this data is potentially suspect as the cross-sensitivity of the PCB 393B04 to acoustic pressure may make this measurement invalid at frequencies where substantial acoustic noise was present). If this data can be believed (and the experiment should be repeated with the Wilcoxon and PCB accelerometers side by side and with simultaneous microphone data to verify if it can), they suggest that an extremely rigid mounting of the experiment frame to the inertia block – such that the rigid body modes of the frame lie above the bulk of the acoustic energy may actually provide the best performance under some circumstances.

The data presented in section 3.3 for the dilution refrigerator STM tell a very different story than the data in section 2.7.3. These data suggest that floating the frame on light-load pneumatic isolators results in frame vibration levels close to or even slightly below the levels on the block out to at least 100 Hz. This level of motion for the Nano-g experiment frame is, broadly speaking, consistent with the acoustically driven motion predicted by modelling. Although such modelling was not carried out for the Omegapod experiment frame, the parameters of the frame structures, isolators and acoustic environments of the two experiments are similar enough that

their differences seem unlikely to explain the 10-100 times higher velocity of the Omegapod frame between 10-100 Hz, suggesting that either the Omegapod frame measurement was flawed or a very important factor has been left out of the analysis.

Although the floating frame configuration was found to provide superior performance to the other two more rigid mounting options studied (unfloated isolators and wood/rubber mounts), it is very likely that these “rigid” options do not come close to approaching the >100 Hz resonant frequency required to keep the response to acoustic forces in the stiffness-dominated (i.e. below resonance) region of the force excitation transfer function. Therefore, the investigation of substantially more rigid mounting schemes may still be of value.

4.3 Regarding vibrations of solid bodies relevant to the performance of low-vibration facilities

Based on the findings of this thesis, conclusions, recommendations and interesting future research directions regarding solid vibrations on the performance of low-vibration facilities are outlined in the following subsections.

4.3.1 Conclusions

The rigid body and flexural vibrations of the structures relevant to the performance of the STM experiments housed in the LAIR is a complex topic spanning the rigid body rocking modes of 150 ton monolithic concrete boxes to the relative vibrations of the tip and sample inside a tea-cup size microscope head. The key conclusions of this thesis in this area are:

- Human activity – especially large scale nearby excavation work - can cause broad-band, order of magnitude increases in the velocity spectrum on the foundations of the monolithic concrete isolation boxes.
- The velocity spectra measured on the foundations of the concrete isolation boxes do not appear to be substantially lower than the pre-construction spectra taken at a similar location on a much thinner and less massive floor. The benefits of decoupling these foundations from the foundations of the remainder of the building remains unclear but do not appear to be large. A more careful study of the vibrations of these foundations relative to those of the surrounding building for comparison with the increased horizontal and decreased vertical vibrations found in [15] may be worthwhile to advance understanding of the vibrational behavior of this type of construction.
- Linear isotropic finite element simulations of reinforced concrete inertia blocks using the volume-weighted material properties of the concrete and the reinforcement are a useful tool for optimizing rigid inertia block designs. These simulations can be validated by performing impulse response measurements over a grid of points on the inertia blocks. The frequencies of the first several flexural modes of three different inertia blocks were predicted with an accuracy better than 10% in most cases. Qualitatively accurate predictions of the mode shapes were also generated.
- Long term measurements of the vibrations of inertia blocks show broad-band variations in the velocity spectra of comparable magnitude to the variations in the foundation velocity and acoustic spectra. The smooth velocity spectra obtained through these measurements clearly show features that can be identified with rigid body modes around 1 Hz, acoustic excitations above 20 Hz, and flexural modes beginning around 200 Hz. The flexural modes of the

smaller inertia blocks appear to excited more readily than the flexural modes of the larger Nano-g inertia block.

- In several instances, both heavy and light-load pneumatic isolators were found to be floating improperly, typically because of a mechanical element such as a levelator connecting the floating stage to the floor when it should not have. In the case of the inertia blocks, these events are hypothesized to be due to the gradual differential settlement of the foundations. Some of the subtler detrimental effects of a levelator touching are unfortunately clear in Figure 2.84 and Figure 2.85, where the low frequency isolation of Omegapod and C-Pod inertia blocks is diminished substantially by resonances approaching 10 Hz that are not there when the blocks are floating properly. These data were taken on inertia blocks that appeared to everyone to be floating properly while measurements immediately showed that this was not the case. Improper floating is not always obvious as an improperly floated stage may still appear to move freely when pushed by hand. Moving freely is a necessary but not a sufficient condition for a pneumatically isolated stage to be floating properly; quantitative measurements of transfer functions should always be used to determine if a pneumatically supported stage is floating properly.
- Excluding the flexural modes, which do seem to more readily excited on the smaller inertia blocks, the differences in performance between the blocks appears to depend largely on the properties of the pneumatic isolators supporting the blocks. A more insightful analysis of the effects of the inertia block mass might be possible with long-term data taken with all three blocks floating properly.
- A ~20 Hz cantilever-like flexural vibrational mode of the dilution refrigerator is the dominant narrow-band noise source in the dilution refrigerator STM tunneling current. This

resonance can be shifted to ~30 Hz by engaging the heat-switch, a significant structural member. This behavior is well reproduced qualitatively with a simplified finite element model of the dilution fridge and heat switch.

4.3.2 Recommendations and future research directions

This work suggests several that several approaches to reducing the detrimental effects of structural vibrations on the performance of low-vibration facilities similar to the LAIR may be effective:

Build dedicated low-vibration facilities away from areas of frequent construction and high levels of human and vehicle activity. The large increases in vibration levels measured during the daytime in the LAIR could likely be avoided in more secluded facilities.

Develop foundation designs which yield substantial vibration isolation. Despite their mass, the foundations of the LAIR isolation vaults do not seem to provide substantial isolation. By exploring more exotic constructions such as placing the foundations on compliant rubber mounts, further isolation may be achievable. Answering this question more fully is an important direction for future work.

Use finite element simulations to optimize the flexural resonant frequencies of inertia blocks and experiment structures. This represents a powerful methodology to avoid undesirable low-frequency structural resonances.

Develop a better understanding of the differences in performance between larger and smaller inertia blocks. A fair comparison has not been made here but a dramatic difference in performance for the larger inertia blocks is not immediately obvious and it is possible that beyond a certain mass the marginal improvement in performance would be much larger if resource were directed towards other areas, such as improved acoustic isolation or active vibration isolation systems.

Benchmark and quantitatively monitor vibration isolation performance. A transfer function plot can immediately reveal problems with a vibration isolation system which may not be perceptible even to an experienced user of that system.

Select pneumatic vibration isolators with improved characteristics. Lower resonant frequencies can be achieved with pneumatic isolators that are taller or that have auxiliary spring gas volumes and mechanism for improved, adjustable horizontal and vertical axis damping are available. In addition to the obvious benefits of better low frequency isolation, lower resonant frequency and higher damping should both help to attenuate acoustically excited rigid body motion of the payload.

Implement active vibration control systems. Active feed-forward control inertia blocks and/or experiment frames based on measurements of incoming acoustic and structure-borne vibrations is likely the most effective way to achieve significantly further decreases in vibration levels.

Improve STM performance by improving the immunity of the STM head to external vibrations. Despite the extremely rigid design employed for the DR STM head, further improvements to the design may still be possible. In particular, the adoption of much finer gauge (i.e. more compliant) wires for the tunnel current, scanner tube and coarse approach piezos has been suggested as a way of reducing vibrational disturbances to the tip sample junction.

Improve STM performance by decreasing the vibration at the STM mounting point of the dilution refrigerator by shifting the 20 Hz resonance to a frequency at which the ambient excitation is weaker. The simplest approach to reducing the 20 Hz noise affecting the STM might be to measure the vibration spectrum at the 4K flange of the dilution refrigerator and – assuming a suitable trough in the spectrum is available – simply shift the fridge resonance downw into that trough by adding weights to the still or mixing chamber plate. Alternatively, additional structural members might accomplish a similar goal by shifting the resonance into a low point in the spectrum situated somewhat above 20 Hz.

Improve STM performance by decreasing the vibration at the STM mounting point of the dilution refrigerator by developing a suitable damping mechanism. Although materials with high internal friction at dilution temperature do not appear to be available, a vibration damping mechanism which is effective at low amplitudes and compatible with the operational constraints of UHV, low-temperature and low thermal conductance may still be possible. Simple sliding friction between mechanical elements has been employed to damp vibrations at cryogenic temperatures [70]. Shunted piezoelectric dampers – analogous to tuned-mass-dampers but with piezoelectric rather than viscous energy removal – have been demonstrated to effective at

mechanical frequencies [71] and can certainly be made compatible with UHV and low temperatures.

4.4 Identified shortcomings of the present work

There are many experimental and analytical weaknesses in the present work. In particular:

- Direct acoustic coupling to the accelerometer signals (i.e. the accelerometers behaving as microphones) was not experimentally proven to be negligible. Direct acoustic coupling to the accelerometers could invalidate all the sail-effect analysis and conclusions.
- Not realizing the blocks were not floating properly during the long term measurements led to failure to get meaningful long-run data for all three blocks
- Poor choice of acquisition time during transmission function sine sweep. The choice of 0.1 Hz frequency steps with only 2s acquisition time yielding 0.5 Hz actual frequency resolution is illogical.
- Less than rigorous analysis of spectral density estimate variances and effective resolutions, particularly when using moving average smoothing.
- Failure to use more sophisticated analysis methods such as phase relationship to extract further information about relationships between two signals or coherence to make more definite statements about causality between signals.
- Insufficient theoretical treatment of acoustic modes and acoustic attenuation through walls.
- No calibrations were performed on either the microphones or the accelerometers. More careful experiments would have pre- and post- calibrations.

Bibliography

- [1] C. J. Chen, *Introduction to Scanning Tunneling Microscopy*. 2008.
- [2] M. Okano, "Vibration isolation for scanning tunneling microscopy," *J. Vac. Sci. Technol. A Vacuum, Surfaces, Film.*, vol. 5, no. 6, p. 3313, 1987.
- [3] D. W. Pohl, "Some design criteria in scanning tunneling microscopy," *IBM J. Res. Dev.*, vol. 30, no. 4, pp. 417–427, 1986.
- [4] "Low Noise Current Amplifier Variable Gain Low Noise Current Amplifier DLPCA-200." Femto FEMTO Messtechnik GMBH.
- [5] Y. J. Song, A. F. Otte, V. Shvarts, Z. Zhao, Y. Kuk, S. R. Blankenship, A. Band, F. M. Hess, and J. a. Stroscio, "Invited Review Article: A 10 mK scanning probe microscopy facility," *Rev. Sci. Instrum.*, vol. 81, no. 2010, 2010.
- [6] C. R. Ast, M. Assig, A. Ast, and K. Kern, "Design criteria for scanning tunneling microscopes to reduce the response to external mechanical disturbances," *Rev. Sci. Instrum.*, vol. 79, 2008.
- [7] S. C. White, U. R. Singh, and P. Wahl, "A stiff scanning tunneling microscopy head for measurement at low temperatures and in high magnetic fields," *Rev. Sci. Instrum.*, vol. 82, pp. 10–15, 2011.
- [8] S. A. Z. Jahromi, M. Salomons, Q. Sun, and R. a. Wolkow, "Prediction of the resonant frequency of piezoelectric tube scanners through three-dimensional finite element modeling of a tube assembly," *Rev. Sci. Instrum.*, vol. 79, no. 7, pp. 2006–2009, 2008.
- [9] J. H. Kindt, G. E. Fantner, J. a. Cutroni, and P. K. Hansma, "Rigid design of fast scanning probe microscopes using finite element analysis," *Ultramicroscopy*, vol. 100, no. 3–4, pp. 259–265, 2004.
- [10] M. Assig, M. Etzkorn, A. Enders, W. Stiepany, C. R. Ast, and K. Kern, "A 10 mK scanning tunneling microscope operating in ultra high vacuum and high magnetic fields," *Rev. Sci. Instrum.*, vol. 84, no. 3, p. 033903, 2013.
- [11] Integrated Dynamics Engineering, "Active and passive Isolation Modules." 2010.
- [12] C. Erin, B. Wilson, and J. Zappe, "an Improved Model of a Pneumatic Vibration Isolator: Theory and Experiment," *J. Sound Vib.*, vol. 218, no. 1, pp. 81–101, 1998.

- [13] J. T. Nelson and W. Blazier, "Influence of Foundation Design on Environmental Vibration," in *Vibration Control in Microelectronics, Optics, and Metrology*, 1991, vol. 1619, pp. 0–8.
- [14] H. Amick, T. Xu, and M. Gendreau, "The Role of Buildings and Slabs-on-Grade in the Suppression of Low-Amplitude Ambient Ground Vibrations," *Proc. 11th Int. Conf. Soil Dyn. Earthq. Eng.*, pp. 877–881, 2004.
- [15] H. Amick, T. Xu, and M. Gendreau, "The Role of Buildings and Slabs-on-Grade in the Suppression of Low-Amplitude Ambient Ground Vibrations," *Proc. 11th Int. Conf. Soil Dyn. Earthq. Eng.*, pp. 877–881, 2004.
- [16] K. Iwaya, R. Shimizu, A. Teramura, S. Sasaki, T. Itagaki, and T. Hitosugi, "Design of an effective vibration isolation system for measurements sensitive to low-frequency vibrations," *J. Vac. Sci. Technol. A Vacuum, Surfaces, Film.*, vol. 30, no. 2012, p. 063201, 2012.
- [17] S. Misra, B. B. Zhou, I. K. Drozdov, J. Seo, L. Urban, a. Gyenis, S. C. J. Kingsley, H. Jones, and a. Yazdani, "Design and performance of an ultra-high vacuum scanning tunneling microscope operating at dilution refrigerator temperatures and high magnetic fields," *Rev. Sci. Instrum.*, vol. 84, 2013.
- [18] E. E. Ungar, "Design of Floated Slabs to Avoid Stiffness Effect of Entrapped Air," *Noise Control Engineering*, vol. 5, no. 1. p. 12, 1975.
- [19] H. Amick, B. Sennewald, N. C. Pardue, C. Teague, and B. Scace, "Vibration of a room-sized airspring-supported slab," pp. 39–47, 1998.
- [20] E. Lörtscher, D. Widmer, and B. Gotsmann, "Next-generation nanotechnology laboratories with simultaneous reduction of all relevant disturbances.," *Nanoscale*, vol. 5, no. 21, pp. 10542–9, 2013.
- [21] H. Bachmann, W. J. Ammann, J. Eisenmann, I. Floegl, G. H. Hirsch, G. K. Klein, G. J. Lande, O. Mahrenholtz, H. G. Natke, H. Nussbaumer, J. H. Rainer, and B. Verlag, *Vibration Problems in Structures - Practical Guidelines*. 1995.
- [22] H. Amick and P. J. M. Monteiro, "Vibration Control Using Large Pneumatic Isolation Systems with Damped Concrete Inertia Masses," *Proc. 7th Intl. Conf. Motion Vib. Control*, no. MoViC 04, pp. 2–11, 2004.
- [23] A. M. Fraumeni, P. Heiland, and N. Judell, "Generic vibration criteria for nanotechnology experiments," *SPIE 5933, Build. Nanoscale Res. Beyond*, p. 59330T–59330T–14, 2005.
- [24] P. W. Smith, "Response and Radiation of Structural Modes Excited by Sound," *The Journal of the Acoustical Society of America*, vol. 34, no. 5. p. 640, 1962.

- [25] “Integrated Dynamics Engineering,” “NLS 100 Acoustic Enclosure.” .
- [26] D. Hils, J. E. Faller, and J. L. Hall, “Practical sound-reducing enclosure for laboratory use,” *Rev. Sci. Instrum.*, vol. 57, no. 10, pp. 2532–2534, 1986.
- [27] D. A. Muller, E. J. Kirkland, M. G. Thomas, J. L. Grazul, L. Fitting, and M. Weyland, “Room design for high-performance electron microscopy,” *Ultramicroscopy*, vol. 106, no. 11–12 SPEC. ISS., pp. 1033–1040, 2006.
- [28] A. Osipov, P. Mees, and G. Vermeir, “Low-Frequency Airborne Sound Transmission through Single Partitions in Buildings - Part 2,” *Noise Vib. Worldw.*, vol. 30, no. 2, pp. 21–26, 2009.
- [29] A. London, “Transmission of reverberant sound through double walls,” *Journal of Research of the National Bureau of Standards*, vol. 44, no. 1. p. 77, 1950.
- [30] J. A. Hoffmann, E. M. Hoskinson, J. W. Alldredge, T. M. Haard, R. E. Packard, and J. C. S. Davis, “Advanced Vibration / Acoustic Isolation Techniques for Low Temperature Systems,” pp. 2–2.
- [31] J. R. Weaver, M. Voorhis, and R. Reifenberger, “Nanometrology Room Design : The Performance and Characterization of the Kevin G. Hall High- Accuracy Laboratory,” *J. IEST*, vol. 52, no. 2, pp. 1–12, 2009.
- [32] F. Levinzon, *Piezoelectric Accelerometers with Integral Electronics*. .
- [33] F. A. Levinzon, “Fundamental Noise Limit of Piezoelectric Accelerometer,” *IEEE Sens. J.*, vol. 4, no. 1, pp. 108–111, 2004.
- [34] “Model 731A / Model P31 system Seismic accelerometer and power amplifier,” *Shock*. Wilcoxon Research Inc.
- [35] “Model 393B04 Seismic , miniature (50 gm), ceramic flexural ICP ® accel ., 1 V / g , 0 . 06 to 450 Installation and Operating Manual.” .
- [36] “NI 446x Specifications,” *Source*, vol. 4462. National Instruments, pp. 1–16.
- [37] “ECM8000 Technical Specifications.” Behringer, p. 8000, 2011.
- [38] “PGM 8 compact live sound mixer - OWNER ’ S MANUAL.” Yorkville.
- [39] H. Singleton, “Microphone Frequency Response Measurement Report,” no. 413. Cross Spectrum Labs, pp. 9–10, 2012.

- [40] A. J. Zuckerwar, T. R. Kuhn, and R. M. Serbyn, "Background noise in piezoresistive, electret condenser, and ceramic microphones.," *J. Acoust. Soc. Am.*, vol. 113, no. 6, pp. 3179–3187, 2003.
- [41] M. H. Hayes, *Statistical Digital Signal Processing and Modeling*. John Wiley, 1996.
- [42] G. Heinzel, A. Rüdiger, R. Schilling, and T. Hannover, "Spectrum and spectral density estimation by the Discrete Fourier transform (DFT), including a comprehensive list of window functions and some new flat-top," 2002.
- [43] S. S. Rao, *Mechanical Vibrations*, 4th ed. New Jersey: Pearson Prentice Hall, 2004.
- [44] "Comsol Multiphysics V5.0." COMSOL, Inc.
- [45] "APEX220 data sheet," no. 716, p. 14305.
- [46] Behringer Inc., "MX602A User ' s Manual," no. December, pp. 1–16, 2001.
- [47] B. Zadler, "Properties of elastic materials using contacting and non-contacting acoustic spectroscopy," 2005.
- [48] D. Wuchinich, "A practical evaluation of harmonic elastic power loss in substantially strained structures," 1998. [Online]. Available: http://www.modalmechanics.com/UIA_1998_presentation.htm. [Accessed: 06-Aug-2015].
- [49] EBL Products Inc, "Lead Zirconate Titanates." [Online]. Available: <http://www.eblproducts.com/leadzirc.html>.
- [50] D. Wehnes, J. Meier, J. Classen, and C. Enss, "Simple and reliable low-temperature STM with piezoelectric coarse approach," *Appl. Phys. A Mater. Sci. Process.*, vol. 66, no. SUPPL. 1, pp. 41–44, 1998.
- [51] L. Gaul and R. Nitsche, "The Role of Friction in Mechanical Joints," *Applied Mechanics Reviews*, vol. 54, no. 2. p. 93, 2001.
- [52] F. B. Segerink, J. P. Korterik, and H. L. Offerhaus, "Vibration transfers to measure the performance of vibration isolated platforms on site using background noise excitation," *Rev. Sci. Instrum.*, vol. 82, no. 6, pp. 1–8, 2011.
- [53] K. Iwaya, R. Shimizu, T. Hashizume, and T. Hitosugi, "Systematic analyses of vibration noise of a vibration isolation system for high-resolution scanning tunneling microscopes," *Rev. Sci. Instrum.*, vol. 82, no. 2011, 2011.

- [54] C. Harrison, R. Butler, and Golder Associates, “Geotechnical desktop study report Brimacombe room 45 - AMPEL, ARPES and LASER lab, University of British Columbia,” 2010.
- [55] E. Kohn, “Discussion: Elastic Properties of a Dense Glacial Till Deposit,” *Can. Geotech. J.*, vol. 3, no. 4, pp. 235–239, 1966.
- [56] G. Wong, “MEASUREMENT AND PREDICTION OF LOW-FREQUENCY NOISE IN INDUSTRIAL WORKROOMS,” 2006.
- [57] J. Higgins, S. Daltrop, and M. Hodgson, “UBC STM Lab Acoustic Analysis,” 2012.
- [58] H. V. Fuchs, X. Zha, X. Zhou, and H. Drotleff, “Creating low-noise environments in communication rooms,” *Appl. Acoust.*, vol. 62, no. 12, pp. 1375–1396, 2001.
- [59] M. Heckl, “The Tenth Sir Richard Fairey Memorial Lecture: Sound transmission in buildings,” *J. Sound Vib.*, vol. 77, no. 2, pp. 165–189, 1981.
- [60] F. P. Mechel, “Design charts for sound absorber layers,” *The Journal of the Acoustical Society of America*, vol. 83, no. 3, p. 1002, 1988.
- [61] J. Lee and G. W. Swenson, “Compact Sound Absorbers for Low Frequencies,” *Noise Control Eng. J.*, vol. 38, no. 3, p. 109, 1992.
- [62] E. Eka Putri, N. S. V Kameswara Rao, and M. a. Mannan, “Evaluation of Modulus of Elasticity and Modulus of Subgrade Reaction of Soils Using CBR Test,” *J. Civ. Eng. Res.*, vol. 2, no. 1, pp. 34–40, 2012.
- [63] S. Shedd, “Vibration Isolation System Field Service Report For UBC C-POD, Omega-POD, and Nano-G Pod,” 2012.
- [64] V. Wong and Y. Pennec, “Characterization of C-Pod slab,” 2012.
- [65] V. Wong and Y. Pennec, “Characterization of Omega Pod slab,” 2012.
- [66] V. Wong and Y. Pennec, “Characterization of Nano-g slab,” 2012.
- [67] L. Zheng, X. Sharon Huo, and Y. Yuan, “Experimental investigation on dynamic properties of rubberized concrete,” *Constr. Build. Mater.*, vol. 22, no. 5, pp. 939–947, 2008.
- [68] K. Sapchuk, “Construction and Commissioning of the UBC Ultra High Vacuum Gigahertz 2D Tesla Ultra Low Temperature Scanning Tunneling Microscope,” no. April, 2012.

- [69] L. J. Bruner, “Low-temperature internal friction in face-centered cubic and body-centered cubic metals,” *Phys. Rev.*, vol. 118, no. 2, pp. 399–410, 1960.
- [70] A. Facco and I.-L. Nazionali, “MECHANICAL MODE DAMPING IN SUPERCONDUCTING LOW β RESONATORS,” pp. 685–694, 1997.
- [71] C. H. Park, “Dynamics modelling of beams with shunted piezoelectric elements,” *J. Sound Vib.*, vol. 268, no. 1, pp. 115–129, 2003.
- [72] F. J. Fahy and C. Schofield, “Note on the Interaction Between a Helmholtz Resonator and an Acoustic Mode of an Enclosure.,” *J. Sound Vib.*, vol. 72, no. 3, pp. 365–378, 1980.
- [73] S. H. Pan, E. W. Hudson, and J. C. Davis, “ ^3He refrigerator based very low temperature scanning tunneling microscope,” *Rev. Sci. Instrum.*, vol. 70, no. 2, p. 1459, 1999.

Appendices

Appendix A : Lists of the lowest 30 FEA-predicted vibrational frequencies for the monolithic isolation enclosures

Mode #	Frequency (Hz)	
	Nano-g enclosure	Omegapod/C-pod enclosure
1	5.45	5.4709
2	6.052	7.5486
3	11.653	12.044
4	13.062	13.616
5	19.868	18.226
6	20.038	19.409
7	28.069	40.057
8	32.344	43.022
9	33.915	46.15
10	40.442	48.279
11	44.05	54.214
12	51.989	56.204
13	55.293	59.385
14	58.679	64.075
15	60.619	64.883
16	62.036	66.83
17	63.076	70.777
18	65.357	75.856
19	71.072	78.894
20	71.685	81.171
21	74.853	82.342
22	77.83	85.245
23	79.403	88.227
24	81.674	89.53
25	87.546	91.435
26	90.387	93.371
27	93.577	94.071
28	95.029	96.924
29	95.367	99.363
30	97.583	102.6

Appendix B : Linear spectral density calculation MATLAB script

```
function [f,A] = LSD(t,a)
%Calculates the Linear Spectral Density of a time varying signal a(t)

%determine sampling rate and number of samples
Fs =1/mode(diff(t));
L = numel(t);

%Detrend the acceleration vector %(THIS LINE ADDED ON 26-7-2015)
a=detrend(a);

%DC balance the acceleration vector
a=a-mean(a);

%create the frequency vector
f = [(Fs/2)*linspace(0,1,floor(1+numel(a)/2))]' ;

%take the fourrier transform
A=fft(a,numel(a));

%truncate Fa to the NFFT/2 + 1 first samples
A=A(1:(1+floor(numel(a)/2))); %do this because the 2nd half of the
samples are just the first half mirrored across Fs/2

%compute the PSD as defined in 'Spectrum and Spectral density estimation
by the DFT' eqn. 24
A= (1/(Fs*L))*2*(abs(A)).^2 ;

%compute the linear spectral density from the DFT
A=sqrt(A);

%fix the first element
A(1)=A(2);end;
```